

GLUCOSE SENSORS BASED ON COPPER THIN FILMS

FACILE AND FLEXIBLE GLUCOSE SENSORS BASED ON COPPER THIN FILMS

By

M. MAKSUD ALAM

M.S. (Electrical and Computer Engineering)

B. Sc. (Electrical and Electronic Engineering)

A Thesis Submitted to the School of Graduate Studies in Partial
Fulfillment of the Requirements for the Degree of

Doctor of Philosophy

in

Electrical and Computer Engineering

McMaster University © Copyright by M. Maksud Alam, November 2023

DOCTOR OF PHILOSOPHY (2023)

Electrical and Computer Engineering

McMaster University, Hamilton, Ontario, Canada

Facile and Flexible Glucose Sensors Based on Copper Thin Films

AUTHOR:

M. Maksud Alam

M.S. (ECE), Purdue University, Indiana, USA

B.Sc. (EEE), CUET, Chittagong, Bangladesh.

SUPERVISOR:

Matiar M. R. Howlader, PhD

Associate Professor, Electrical & Computer Engineering,

SUPERVISORY COMMITTEE CHAIR:

Gurmit Singh, PhD

Professor, Department of Pathology and Molecular Medicine,

SUPERVISORY COMMITTEE MEMBERS:

M. Jamal Deen, PhD

Professor, Electrical & Computer Engineering,

P. Ravi Selvaganapathy, PhD

Professor, Mechanical Engineering,

McMaster University, ON, Canada

EXTERNAL EXAMINAR

Tze Wei (John) Yeow, PhD

Professor, Department of Systems Design Engineering,

University of Waterloo, ON, Canada

NUMBER OF PAGES: xxv, 236

Lay Abstract

While the symptoms are severe and quick for the type – 1 diabetes, there may be no symptoms shown, if some people, especially, have prediabetes (a higher-than-normal blood sugar), gestational diabetes (diagnosed for the first-time during pregnancy, gestation), and type – 2 diabetes (the pancreas does not produce enough insulin and/or cells respond poorly to insulin and take in less sugar). Thus, early detection of diabetes through real-time monitoring of glucose is critical to prevent complications and can save lives. The electrochemical enzymatic electrodes face several drawbacks while dominating the world market for blood glucose monitoring devices. Hence, facile, flexible, inexpensive, and high-performance electrochemical non-enzymatic electrodes are needed for non-invasive glucose monitoring devices. A very simple low-cost fabrication technique has been shown to make the facile, flexible, and inexpensive electrodes to detect sugar in sweat bio-analyte for a non-invasive glucose monitoring system using the native stable Cu oxides (CuNOx), Cu₂O and CuO, layers grown on 35 μ m thin Cu foils keeping under ambient conditions (25°C- and 760-mm Hg) for more than 2 years. Moreover, the foils also annealed at various temperatures such as 160, 230, and 280°C with new temperature profile for reducing the required time of growing stable oxides and producing oxides with larger crystallized structures with higher surface – to – volume ratio. The cyclic voltammetry (CV) with the 3 – electrode configuration of the potentiostat has been used for electrochemical characterization.

Abstract

The electrochemical enzymatic electrodes dominate the world market for blood glucose monitoring devices for controlling, as well as reducing the detrimental effects of diabetes. However, the enzymatic electrodes exhibit constraints restricting their reliance on the enzyme's activity which can be influenced by the external, and the environmental factors such as temperature, pH, and humidity etc. However, the greater thickness of the enzyme layer hinders the performance of the glucose biosensors resulting in signal dampening or loss. In addition, the selectivity of the electrodes is affected by the interferents present in blood. Moreover, the invasive nature of the electrodes is a major problem considering the patient's perspective. In contrast, recent research activities demonstrated that the electrochemical non-enzymatic electrodes possess huge potential for inexpensive and highly sensitive glucose monitoring devices, yet these electrodes are invasive in nature. Therefore, the purpose of this research was to fabricate electrochemical non-enzymatic non-invasive electrodes for sweat glucose monitoring devices.

A very simple low-cost fabrication technique has been shown to make the facile, flexible, and inexpensive electrodes to detect sugar in sweat bio-analyte for a non-invasive glucose monitoring system using the native stable Cu oxides (CuNO_x), Cu_2O , layers grown on 35 μm thin Cu foils keeping under ambient conditions (25°C - and 760-mm Hg) for more than 2 years so that the oxide layers are full-grown, and fully stable. Moreover, the foils also annealed at various temperatures such as 160, 230, and 280°C with new temperature profile for reducing the required time of growing stable oxides and producing oxides with larger

crystallized structures with higher surface – to – volume ratio. The X-ray photoelectron spectroscopy (XPS) and high-resolution transmission electron microscopy (HRTEM) results supported that at 280°C annealing temperature the surface, mostly, transformed into highly electrocatalytic CuO with larger grain sizes, crystallized structures, and the uniform layer of ~ 140 nm.

The electrochemical characterization, and sensing performance of the electrodes have been done by cyclic voltammetry (CV), one of the excellent and well accepted electrochemical methods, with the 3 – electrode configuration of the potentiostat. The CuNOx sensors of having ~10 nm layer of stable Cu₂O exhibited a sensitivity of 603.42 $\mu\text{A mM}^{-1} \text{cm}^{-2}$, a linear range beyond the desired limit of 7.00 mM with excellent linearity ($R^2 = 0.9983$) and a low limit of detection of 94.21 μM . In contrast, the new annealing profile has. the CuNOx sensors annealed at 280 °C using new temperature profile provided twin calibration curves of linear ranges of 0.05 – 1.00 mM and 1.00 – 7.00 mM, that applicable for sweat and blood glucose sensing, respectively, and exhibited a sensitivity of 1795 $\mu\text{A mM}^{-1} \text{cm}^{-2}$, a linear range up to the desired limit of 1.00 mM for sweat glucose sensing with excellent linearity ($R^2 = 0.9844$), and a lower limit of detection of 135.39 μM .

In addition, it has been shown that the peak electro-oxidation current of glucose sensing is linearly related with the square root of the annealing temperature, \sqrt{T} . This can help to figure out the required applied annealing temperature for getting desired peak electro-oxidation current of glucose in a human health monitoring system.

Acknowledgements

I would like to express my gratitude to Dr. Matiar M. R. Howlader for providing me with the opportunity to study as a Ph.D. student at McMaster University. As my supervisor, he built a good research team for me with talented researchers such as Arif Ul Alam, Taufique Z. Redhwan, Martin Klimuntowski, and Victor Mitea. I truly appreciate his efforts in building and maintaining the unique and advanced Micro and Nano Systems Laboratory, where my research work was carried out. Also, his door is always open for me for technical support and valuable discussions. I am grateful for his continuous guidance and support on my research.

I would also like to thank my supervising committee members Dr. M Jamal Deen and Dr. P. Ravi Selvaganapathy for their advice on my research and for taking the time to review my thesis.

I am grateful for the help that I have received from Dr. Nora Martinez and Professor Tadatomo Suga of the University of Tokyo for their help in the XPS experiments for the electrodes. I appreciate Mr. Xiangyu Zhu and Professor Moon J Kim of the Department of Materials Science and Engineering at The University of Texas at Dallas, Richardson, TX 75080, USA for their HRTEM investigation of the copper native oxide specimens.

I sincerely thank my parents for their unconditional support and encouragement over all these years. This thesis is dedicated to them.

Table of Contents

Lay Abstract.....	iii
Abstract.....	iv
Acknowledgements.....	vi
Table of Contents.....	vii
Lists of Figures.....	x
List of Tables.....	xix
List of Abbreviations.....	xvii
List of Symbols.....	xxi
Declaration of Academic Achievement.....	xxiv
Chapter 1 Introduction	
1.1 Human Health Monitoring.....	1
1.2 Necessity of Glucose Monitoring.....	6
1.3 Glucose Biosensors.....	8
1.3.1 Electrochemical Glucose Biosensors.....	9
1.3.2 Enzymatic Glucose Biosensors.....	15
1.3.3 Non-enzymatic Glucose Biosensors.....	19
1.4 Research Motivation.....	20
1.5 Research Contribution.....	22
1.6 Thesis Organization.....	24
Chapter 2 Analyzing Electrochemical Sensing Fundamentals for Health Applications	
2.1 Background.....	27
2.2 Fundamentals of Analytical Chemistry for Electrochemical Sensing.....	30
2.2.1 Chemical Equilibrium.....	31
2.2.2 Thermodynamic Equilibrium.....	32
2.2.3 Gibb's Free Energy.....	34
2.2.4 Equilibrium Constant of Water Dissociation.....	41
2.2.5 pH Scale.....	42
2.3 Effects of Oxygen, and its radicals on Human Physiology.....	44
2.3.1 Oxidation-Reduction (Redox) Reactions.....	45
2.3.2 Effects of Redox Reactions on Human Physiology.....	46
2.3.3 Hemoglobin-dependent Redox Reactions.....	48

2.3.4	Redox Environment in Human Serum Albumin (HAS) & Cells/Tissues.....	49
2.3.5	Thermodynamics of Biological Redox Reactions.....	51
2.3.6	Estimation of Total Reducing Power in Biological Sites.....	53

Chapter 3 Evaluation of Electrochemical Sensing Techniques for Health Applications

3.1	Background.....	55
3.2	Electrochemical Techniques and Fundamentals.....	56
3.2.1	Potentiometric Methods.....	57
3.2.2	Coulometric Methods.....	66
3.2.3	Voltammetry.....	69
3.2.4	Amperometry.....	85
3.3	Research Challenges and Future Perspectives.....	89
3.3.1	Sensor Materials and Functionalization.....	90
3.3.2	Integrated Sensing Systems & Simultaneous Detection of Biomarkers.....	97
3.3.3	Access to Biofluids.....	98
3.3.4	Standardization of Measured Data by Comparing with Standard Methods like ELISA...	99
3.3.5	Analyzing Large Data using Machine Learning.....	100
3.4	Conclusion.....	102

Chapter 4 Nonenzymatic Electrochemical Sensors via Cu Native Oxides (CuNOx) for Sweat Glucose Monitoring

4.1	Background.....	105
4.2	Experimental Procedure.....	108
4.2.1	Chemical & Reagents.....	108
4.2.2	Formation of Native Oxide of Copper.....	108
4.2.3	Preparation of Working Electrode.....	110
4.2.4	Electrochemical Sensing Method.....	111
4.3	Results and Discussion.....	112
4.3.1	Chemical Elemental Characterization.....	112
4.3.2	Morphological and Structural Characterization.....	115
4.3.3	Cyclic Voltammetry of Glucose.....	117
4.3.4	Interference Analysis.....	128
4.3.5	Reproducibility & Reusability.....	130
4.3.6	Stability.....	131
4.3.7	CuNOx Sensing Parameters with Others.....	134
4.3.8	CuNOx Towards Wearable Applications.....	136
4.4	Conclusion.....	137

Chapter 5 High Performance Nonenzymatic Electrochemical Sensors via Thermally Grown Cu Native Oxides (CuNO_x) Towards Sweat Glucose Monitoring

5.1	Background.....	141
5.2	Experimental Procedure.....	145
5.2.1	Chemical & Reagents.....	145
5.2.2	Formation of Thermally grown Native Oxide of Copper & Electrode Preparation.....	145
5.2.3	Electrochemical Sensing Method.....	148
5.3	Results and Discussion.....	149
5.3.1	Chemical Elemental Characterization.....	149
5.3.2	Morphological and Structural Characterization.....	155
5.4	Cyclic Voltammograms and calibration curves.....	158
5.4.1	Sensitivity and LOD.....	159
5.4.2	Effect of Annealing Temperature on Peak oxidation Current & Potential.....	161
5.4.3	Interference Analysis.....	166
5.4.4	Reproducibility & Reusability.....	169
5.4.5	Stability.....	170
5.4.6	CuNO _x annealed at 280°C Sensing Parameters with Others.....	171
5.5	Challenges & Opportunities.....	172
5.6	Conclusions.....	174

Chapter 6 Conclusions and recommendations

6.1	Conclusions.....	176
6.2	Recommendations.....	181

References.....	185
------------------------	------------

List of Figures

Figure 1-1. The schematic of the electrochemical health monitoring systems.....	5
Figure 1-2. The human body organs are severely affected by diabetes.....	7
Figure 1-3. Schematic of the three electrode potentiostat circuit diagram.....	11
Figure 1-4. Schematic of the different components of CV technique.....	14
Figure 1-5. Schematic representation of enzymatic glucose oxidation mechanisms for the three different generations of biosensors.....	17
Figure 2-1. Summary of the changes in Gibbs free energy, chemical equilibrium, and the equilibrium constant [147] for reactions that are (a) product-favored and (b) reactant-favored, when they are at equilibrium. (c) The pH and pOH scales indicate the concentrations of $[H_3O^+]$ and OH, respectively. The chart also shows the pH and pOH values of some common substances at standard temperature (25°C) [148]	40
Figure 2-2. (a) Plants' photosynthesis process; generation of glucose and oxygen from sunlight, water, and carbon dioxide. (b) Dual effects of nitrite on hemoglobin-dependent redox reactions	47
Figure 3-1. A family tree of several interfacial electrochemical techniques is shown. The specific techniques are in red, the experimental conditions are in blue, the analytical signals are in green, and the red-yellowish octagons show the chronological presentation of the techniques.....	56
Figure 3-2. (a) A manual potentiometer with two electrodes (counter electrode and working electrode) is shown schematically. The tapping switch T and the slide-wire variable resistor SW are also indicated. (b) A potentiometric electrochemical cell is depicted. (c) A junction potential between two ionic solutions with different concentrations (0.1 M HCl and 0.01 M HCl) is shown. (d) The waveforms of the applied potential and resulting current of a controlled-potential coulometry are shown. (e) The reduction steps of different species	

present in an aqueous solution of Cu^{2+} are shown in a ladder diagram. The oxidized species are in blue, and the other species are in red. (f) A measured current vs. time curve for a controlled-current coulometry is shown, with the blue area representing the total charge.....60

Figure 3-3. (a) The ladder diagram of the ferricyanide, $\text{Fe}(\text{CN})_6^{3-}(\text{Fe}^{3+})$, reduces to ferrocyanide, $\text{Fe}(\text{CN})_6^{4-}(\text{Fe}^{2+})$ redox half-reaction [1]. (b) Concentration gradients and the diffusion layer width of the reaction from equations (3-15) and (3-16) [1]. Sampled-current voltammetry with stirring (c) Step waveforms applied in a series of experiments, (d) Current-time curves observed in response to the steps, (e) Sampled-current voltammogram [1]. (f) A step potential for excitation in amperometry is applied, where species O is electro-inactive at E1 but is reduced at a diffusion-limited rate at E2. (g) Concentration profiles for various times during the experiment, (h) Current flow vs. time curve [1]72

Figure 3-4. Potential-excitation signals and voltammograms for (a) normal pulse, (b) differential pulse, (c) staircase, and (d) square-wave voltammetry. The black rectangles represent the current sample position. Δi is the current difference between points 2 and 1. The symbols in the diagrams, with typical values for (a), are as follows: τ ($\approx 1\text{s}$) is the cycle time; ΔE_p ($\approx 2\text{mV}$ and increase by $\approx 2\text{mV}$) is a fixed or variable pulse potential, ΔE_s ($\approx 2\text{mV}$) is a fixed change in potential per cycle, and t_p ($\approx 50\text{ms}$) is the pulse time. The current is sampled at the end of each potential pulse for approximately 17 ms before returning the potential to its initial value [1]73

Figure 3-5. (A-G): Concentration profiles (mM) for Fc^+ (blue) and Fc (green) as a function of distance from the electrode (0.5 mm) at various points during the voltammogram. (H): Voltammogram of the reversible reduction of a 1 mM Fc^+ solution to Fc at a scan rate of 100 mV/s. (I): Applied potential as a function of time for a generic cyclic voltammetry experiment, with the initial, switching, and end potentials represented by (A, D, and G, respectively) [104]. (J) Applied potential and voltammogram for ASV at a mercury film electrode, with a copper ladder diagram in the upper figure of Fig. 3-5 (J). Typical

deposition times are 1-30 minutes, with a lower deposition time for higher analyte concentrations [48]81

Figure 4-1. Schematic representation of working electrode preparation. Cross-sectional view of (a) The thin Cu foil at room temperature and pressure (RTP); (b) the foil after attaching with electrical grade scotch tape that covered the oxide layer of one side as well as works as substrate. (c) The dimension of the sensing surface of the electrode for electro-oxidation of glucose using Cyclic Voltammetry. Note: Working electrode and sensing electrode are interchangeably used.....110

Figure 4-2. (a) Wide scan XPS spectrum, and deconvolved high-resolution narrow scan for (b) $\text{Cu}_{2p_{3/2}}$, and (c) O_{1s} spectra of the naturally grown Cu native oxide surface of the electrode.....113

Figure 4-3. HRTEM image shows (a) the growth of Cu oxides is not uniform, (b) the surface morphology affects the growth of the oxide hugely. (c)—(f) EDS images of (b) shows distribution of Cu, O, Pt and C. (g) FFT image of (i), (h) FFT image of Cu metal, red dotted box of (i), and (j) FFT image of Cu_2O , yellow dotted box of (i).....116

Figure 4-4. Cyclic Voltammograms of Cu and Cu native oxide (CuNO_x) electrodes with and without glucose at 30 mVs^{-1} scan rate in 0.1 M NaOH solution.....117

Figure 4-5. (a) Cyclic Voltammograms of $0.1\text{—}7 \text{ mM}$ glucose at 30 mVs^{-1} scan rate in 0.1 M NaOH solution using Cu native oxide electrode, and (b) Magnified version of (a) for the electro-oxidation peak of glucose.....123

Figure 4-6. Calibration curve illustrates the linear relationship between glucose concentration and peak oxidation current (current density) for native oxide (at RTP) electrode with correlation coefficient $R^2 = 0.9983$, at 30 mVs^{-1} scan rate.....124

Figure 4-7. The curve illustrates that (a) Both the peak oxidation current of glucose and associated potential are increasing with the increase of glucose concentrations, and they are exponentially related. (b) The potential at peak oxidation current of glucose is increasing

logarithmically with increase of glucose concentrations. The data has been collected from Fig. 4-5. (a).....127

Figure 4-8. (a) Cyclic voltammograms of 1 mM glucose with 0.1 M NaOH after adding different interferences presence in human sweat. Here, step 1: Blank solution's signal in presence of 0.1 M NaOH. Step 12: Same as in step 1 after taking CV results in presence of all above-mentioned interferants. Step 2 and 11: Response to 1 mM glucose in presence of 0.1 M NaOH. The experiment results in Steps 1 and 2 were discarded from Fig. 4-8(a) to eliminate redundancy. Step 3: Response to 0.132 mM acetaminophen with 1 mM glucose and 0.1 M NaOH. Steps 4 and 7: Responses to 0.1 mM dopamine and 0.02 mM cysteine, respectively. (b) The peak oxidation current and the associated oxidation potential vs. the step order, shown in legends of Fig. 4-8. (a), and Fig. 4-8. (c) Magnified version of Fig. 4-8. (a).....130

Figure 4-9. Repeatability test of the CuNOx in 0.1 M NaOH alkaline solution with 0.1-, 1.0-, 4.0-, and 6.0-mM glucose concentrations. An electrode was used for each concentration in the same solution and the solution was shaken before applying the next CV.....131

Figure 4-10. Stability test of the CuNOx electrode in 0.1 M NaOH alkaline solution with 1.0 mM glucose concentration, (a) the peak oxidation current of glucose vs. days for 12 times with 5 days gap, (b) the CV readings were recorded for a single CuNOx electrode using different Ag/AgCl reference electrodes, (c) the voltammograms of different working electrodes using same Ag/AgCl reference electrode, (d) Magnified version of (b), and (e) Magnified version of (c).....133

Figure 5-1. Schematic representation of the working electrode preparation. (a) The as-received thin Cu foil at room temperature and pressure (RTP); (b) The foil supported by a thermal insulator to protect it from metal contact in the oven; (c) The laboratory oven, which can be used up to 300°C; (d) the thin foil after annealing at 160, 230, and 280°C. The electrode preparation steps (e), (f), and (g) are the same as shown in our previous work [97]; (h) The temperature profile for annealing the Cu thin foil.....146

Figure 5-2. (a) Wide scan XPS spectrum, along with the deconvolved high-resolution narrow scan for $\text{Cu}_{2p_{3/2}}$ of (b) as received copper oxide thin films (at 25°C), (c) those annealed at 230°C , and (d) those annealed at 280°C , utilizing the temperature profile shown in Fig. 5-1(h).....150

Figure 5-3. Peak fitting of (a) O_{1s} , and (b) C_{1s} of the electrodes of as-received (25°C), annealed at 230°C , and 280°C (from left to right)153

Figure 5-4. HRTEM image of the electrode annealed at 280°C presents (a) nearly uniform growth of Cu oxides, (b) an enlarged version of the dotted portion in (a), (c) EDS image of (a) showing Cu distribution, (d) EDS image of (a) showing O distribution, (e) an enlarged version of the dotted portion in (b), (f) the annular bright-field (ABF) image of (e), (g) an enlarged version of the dotted portion in (f), (h) FFT image of the dotted portion in (g), (i) an image of the oxides layer from a different part of the thin film, (j) an enlarged version of the dotted portion in (i), (k) an enlarged version of the dotted portion in (j), and (l) FFT image of the dotted portion in (k).....157

Figure 5-5. Cyclic voltammograms of the CuNOx electrode after annealing at (a) 160°C and (b) 280°C captured at a 30 mVs^{-1} scan rate. Calibration curves of the CuNOx electrode annealed at 25, 160, 230, and 280°C for (c) sweat and (d) blood glucose sensing.....159

Figure 5-6. (a) Voltammograms of 7.00 mM glucose detection using CuNOx electrodes annealed 25, 160, 230, and 280°C at a 30 mVs^{-1} scan rate in a 0.1 M NaOH alkaline environment. (b) The graphs show the relationship between the peak current of glucose oxidation and the oxidation potential at peak current, as shown in Fig. (a), plotted against temperature. (c) The curve fitting of data shown in Fig. (b), excluding 25°C , illustrates that peak electro-oxidation currents and their potentials are linearly related to \sqrt{T}163

Figure 5-7. The curve illustrates the following: (a) Both the peak oxidation current of glucose and the associated potential increase with the increasing glucose concentrations, showing an exponential relationship. (b) The potential at the peak oxidation current of

glucose increases logarithmically with the increase of glucose concentrations. (c) and (d) Semi log graphs of figure (a), and (b), respectively.....164

Figure 5-8. (a) Cyclic voltammograms of 1 mM glucose with 0.1 M NaOH after adding different interferents present in human sweat. Here, Step 1: Signal of a blank solution in the presence of 0.1 M NaOH, which is omitted from Fig. 5-8(a) since the CV results of steps 1 and 12 are the same. Step 12: Identical to step 1, after recording all CV results up to step 11 in the presence of all interferants. Step 2 and 11: Response to 1 mM glucose in the presence of 0.1 M NaOH. Step 3, 5, 7, and 9: Response to 0.132 mM acetaminophen; to 0.01 mM ascorbic acid; to 0.02 mM cysteine and 0.5 mM NaCl, respectively, in the presence of 1 mM glucose and 0.1 M NaOH. (b) The peak oxidation current and the associated oxidation potential vs. the step order, as shown in the legends of Figure 5-8(a), and (c) Magnified version of Fig. 5-8(a).....167

Figure 5-9. Repeatability test of the CuNO_x electrode annealed at 280°C in a 0.1 M NaOH alkaline solution with glucose concentrations of 0.5-, 1.0-, 3.0-, and 7.0-mM. A distinct electrode was used for each concentration in the same solution. The solution was shaken before each subsequent CV measurement.....170

Figure 5-10. Stability test of the CuNO_x electrode annealed at 280°C, conducted in a 0.1 M NaOH alkaline solution with a glucose concentration of 1.0 mM.....171

Figure 6 – 1. Schematic diagram of sweat glucose monitoring systems.....182

List of Tables

Table 1-1: Proposed specifications of the glucose biosensors.....	21
Table 3-1: Potentiometric Sensors for Health Monitoring Applications.....	62
Table 3-2: Coulometry Sensors for Health Monitoring Applications.....	68
Table 3-3: Differential Pulse Voltametric (DPV) Sensors for Health Monitoring Applications.....	76
Table 3-4: Square Wave Voltametric (SWV) Sensors for Health Monitoring Applications.....	78
Table 3-5: Cyclic Voltametric (CV) Sensors for Health Monitoring Applications.....	82
Table 3-6: Amperometric Sensors for Health Monitoring Applications.....	86
Table 4-1: Summary of voltammogram data of Cu, and Cu oxides-based nonenzymatic sensors in presence and absence of glucose from Fig. 4-4 in comparison with that of literature.....	106
Table 4-2: Comparison of CuNO _x sensors with other Cu, and Cu oxides-based nonenzymatic glucose sensors. While the sensors reported in this work are characterized by cyclic voltammetry, the other sensors are characterized by amperometry.....	135
Table 5-1: Peak fitting parameters and percentage relative concentrations for copper oxide thin films in their as received state (25°C), and after annealing at 230°C and 280°C, using the temperature profile shown in Fig. 5-1(h).....	151
Table 5-2: Comparison of CuNO _x @280°C sensors with other non-enzymatic glucose sensors.....	172

List of Abbreviations

3-APBA	3-Aminophenylboronic Acid
5-HT	Serotonin or 5-hydroxytryptamine
AA	Ascorbic Acid
ACh	Acetylcholine
AcChE	Acetylcholinesterase
AChR	Acetylcholine Receptor
ADHD	Attention Deficit Hyperactivity Disorder
AED	Electroanalytical Device
AFP	Alpha-1-fetoprotein
AgNW	Silver Nanowires
AI	Artificial Intelligence
AMI	Acute Myocardial Infarction
ANN	Artificial Neural Networks
AP	Aminophenol
AS	Acidum Salicylicum
ATP	Adenosine Triphosphate
AuNP	Gold Nanoparticle
AuSPE	Gold Screen Printed Electrode
BC	Before Christ
BDD	Boron-doped diamond
BDND	Boron-doped Nanocrystalline Diamond
bi-C	Bio-inspired pyrolytic carbon
BIM	Biomimetic-imprinted Material
BSA	Bovine serum albumin
CAGR	Compound Annual Growth Rate
CD	Cyclodextrin
CD44	Cell Surface Adhesion Receptor
CE	Counter Electrode
CEA	Carcinoembryonic Antigen
Ch	Cholesterol
ChO	Choline Oxidase
CKD	Chronic Kidney Disease
CK-MB	Creatine Kinase-MB isoenzyme
CNS	Central Nervous System
CoPcTS	Cobalt (II) Phthalocyanine Tetrasulfonate
COVID – 19	Corona Virus Disease of 2019
CPE	Carbon Paste Electrode
CRP	C-Reactive Protein
CSF	Cerebrospinal Fluid
cTnI	Cardiac Troponin I

cTnT	Cardiac Troponin T
Cu(acac₂pn)	N,N'-Bis(acetylacetonato)propylenediimine Copper(II)
CuNO_x	Copper Native Oxides
CuNO_x@25°C	Copper Native Oxides annealed at 25°C
CuNO_x @280°C	Copper Native Oxides annealed at 280°C
CV	Cyclic Voltammetry
CVD	Cardiovascular Diseases
Cys	Cysteine
DA	Dopamine
DASM	Dopamine Selective Membrane
Dec	Decade
DET	Direct Energy Transmission
DGN	Dendrite-like gold nanostructures
DHP	Dihexadecyl Hydrogen Phosphate
DI	Deionized
DNA	DeoxyriboNucleic Acid
DOPAC	3,4-dihydroxyphenylacetic Acid
DPV	Differtial Pulse Voltammetry
DSP	Dithiobis(succinimidyl propionate)
EDS	Energy Dispersive X-ray Spectroscopy
FFT	Fast Fourier Transform
EIS	Electrochemical Impedance Spectroscopy
ELISA	Enzyme-Linked ImmunoSorbent Assay
ENFET	Enzyme Field Effect Transistor
Ep	Ephedrine
EtOH	Ethanol
FAD	Flavin Adenine Dinucleotide
FADH	reduced form of flavin adenine dinucleotide
Fru	Fructose
f-SWCNT	Functionalized Singlewalled Carbon Nanotube
FTO	Fluorine doped Tin Oxide
Gal	Galactose
GCE	Glassy Carbon Electrode
GF	Graphene Flake
GO	Graphene Oxide
GO_x	Glucose Oxidase/Glucose 1 – Oxidase
GQD	Graphene Quantum Dot
GSH	Glutathione
GSSG	Glutathione disulfide
HAS	Human Serum Albumin
HBV	Chronic Hepatitis-B
HFrEF	Heart Failure Patients with Reduced Ejection Fraction
HRTEM	High-Resolution Transmission Electron Microscopy
IARC	International Agency for Research on Cancer

IBD	Inflammatory Bowel Disease
IL	Ionic Liquid
ISFET	Ion Sensitive Field Effect Transistor
ITC	Isothermal Titration Calorimetry
ITIES	Interface between two immiscible electrolyte solutions
ITO	Indium Tin Oxide
IUPAC	International Union of Pure and Applied Chemistry
KCl	Potassium Chloride
kDa	kiloDalton
Lac	Lactose
LAPS	Light-Addressable Potentiometric Sensors
LIG	Laser-induced graphene
LMWA	Low-Molecular-Weight Antioxidants
LoD	Limit of Detection
LSV	Linear Sweep Voltammetry
MeCHO	Acetaldehyde
MI	Myocardial Ischemia
MIP	Molecular imprinted polymer
ML	Machine Learning
MOF	Metal-organic framework
MWCNT	Multiwalled Carbon Nanotube
Myo	Myoglobin
NaCl	Sodium Chloride
NADH	Nicotinamide Adenine Dinucleotide (NAD) + Hydrogen (H)
NADPH	Nicotinamide Adenine Dinucleotide Phosphate
NFw	Nano Flower
NH₂-HSM	Amine-functioned hexagonal mesoporous silica
NT	NeuroTransmitters
NT-FET	NanoTube Field Effect Transistor
OMIMPF₆	1-octyl-3-methylimidazolium Hexafluorophosphate
Op-Amp	Operational Amplifier
OPN	Osteopontin
PAH	Poly(allylamine) Hydrochloride
PANI	Polyaniline
PAP	Poly(o-aminophenol)
PC	Porous Carbon
PCA3	Prostate Cancer-specific DNA Sequence
PDA	o-phenylenediamine
PEDOT	Polymer Poly (3,4- ethylenedioxythiophene)
pH	Potential of Hydrogen
PIM	Protein Imprinted Materials
PMB	Polymethylene Blue
PMoV	V-phosphomolybdates
PMPC-SH	Poly (2-methacryloyloxyethyl phosphorylcholine)

PNS	Peripheral Nervous System
POA	Poly(o-anisidine)
POC	Point-of-Care
POM	Polyoxometalates
PPy	Polypyrrole
PSA	Prostate-Specific Antigen
PSMA	Prostate Specific Membrane Antigen
PSTI	Pancreatic Secretory Trypsin Inhibitor
PSS	Poly (styrenesulfonate)
RE	Reference Electrode
rGO	Reduced Graphene Oxide
RSD	Relative Standard Deviation
RTP	Room Temperature and Pressure
SAM	Self-assembled Monolayer
SARS	Severe Acute Respiratory Syndrome
SARS – CoV	SARS – associated Corona Virus
SDS	Sodium Dodecyl Sulfate
SMWNT	Straight Multi-walled Carbon Nanotubes
SPCE	Screen Printed Carbon Electrode
SPE	Screen Printed Electrode
SPR	Surface Plasmon Resonance
SSCF	Sandpaper-supported Copper Framework
SVM	Support Vector Machine
SWCNT	Single-walled Carbon Nanotube
SWV	Square Wave Voltametric
T	Tryptamine
TCCF	Tyrosinase-chitosan Composite Film
TIA	Transimpedance Amplifier
TNBC	Triple-negative Breast Cancer
TNF-α	Tumor Necrosis Factor-alfa
TPA	Terephthalic acid
TYR	Tyrosine
UA	Uric Acid
WE	Working Electrode
WSE	Working SEnse
WHO	World Health Organization
XPS	X-ray Photoelectron Spectroscopy
Xyl	Xylose

List of Symbols

δ	Width of the diffusion layer
τ	Cycle time
A	Electrode surface area
A_V	Voltage Gain
C	Concentration
c	Osteopontin Concentration
C_t	Concentration of a biomarker at time t (hour)
C_0	Concentration of a biomarker at time t (0)
$^{\circ}\text{C}$	Degree Celsius
D	Diffusion constant
E_1	Lowest Potential/Voltage of a CV Scanning
E_2	Highest Potential/Voltage of a CV Scanning
E_{anode}	Potential at anode electrode of an electrochemical cell
$E_{cathode}$	Potential at cathode electrode of an electrochemical cell
E_{cell}	Potential across the electrochemical cell
E_j	Junction potential
E_{ox}	Potential of oxidation half-reaction of a redox reaction
E_{pa}	Peak anodic potential
E_{Red}	Potential of reduction half-reaction of a redox reaction
E_{step}	Potential of Increment of a CV Scanning
ΔE	Change of electromotive force
ΔE°	Change of electromotive force under standard conditions
F	Faraday's Constant
G	Gibb's Free Energy
ΔG	Change of Gibb's Free Energy
ΔG°	Change of Gibb's Free Energy under steady state conditions.
h	Planck's constant
H	Enthalpy

$[H^+]$	Hydrogen ion concentration
$[H_3O^+]$	Hydronium ion concentration
ΔH	Change of Enthalpy
i_{ct}	Counter Current
i_F	Feedback Current
I_{pa}	Peak anodic current
k	first-order rate constant
k_b	Boltzmann constant
k_{bio}	Biodegradation rate of a biomarker in sewers
K_d	Dissociation Constant/Equilibrium constant
k_{total}	Overall transformation rate of a biomarker in sewers
K_w	Water Dissociation Constant
k_{ww}	Abiotic transformation rate of a biomarker
n	Mole of electron
N_A	Mole of an analyte
Q	Net transfer of charge
Q_r	Reaction quotient
R	Universal gas constant
R_i	Input Resistance
R_F	Feedback Resistance
S	Entropy
ΔS	Change of Entropy
T	Absolute Temperature
\sqrt{T}	Squire Root of Absolute Temperature
v	Scan Rate
V^+	Voltage at Non-inverting Input Terminal of an Op-Amp
V^-	Voltage at Non-inverting Input Terminal of an Op-Amp
V_i	Input Voltage
V_{in}	Input Voltage
V_o	Output Voltage

V_{out}	Output Voltage
V_{wr}	Potential Difference between WE and RE
V_{WE}	Potential Difference between WE and Ground
V_{RE}	Potential Difference between RE and Ground
Z_i	Input Impedance

Declaration of Academic Achievement

I, **M. Maksud Alam**, declare that this thesis titled, **Facile and Flexible Glucose Sensors Based on Copper Thin Films**, and works presented in it are my own. I confirm that the research was done under the supervision of Matiar M. R. Howlader, PhD, Associate Professor, Department of Electrical and Computer Engineering, McMaster University.

- Chapter 1: Introduction
- Chapter 2: I conducted the literature review on analyzing electrochemical sensing fundamentals for health applications and summarized the research results.
- Chapter 3: I conducted the literature review on evaluation of electrochemical sensing fundamentals for health monitoring applications in sensing of neurotransmitter, protein, as well as glucose, and summarized the research results in tabular form. Victor Mitea helped me collect published literature on neurotransmitters and protein sensors.
- Chapter 4: I designed the devices and experiments. Taufique Z. Redhwan helped me in the XPS experiments for survey and narrow spectra. Mr. Xiangyu Zhu under supervision of Professor Moon J Kim of the Department of Materials Science and Engineering at The University of Texas at Dallas, USA helped me investigating CuNO_x specimens. I collected all the data and conducted all the data analysis.
- Chapter 5: I designed the devices and experiments. Professor Tadatomo Suga, Meisei University, Japan, helped me investigating the surfaces of the annealed copper thin films by the XPS experiments for survey and narrow spectra. Mr. Xiangyu Zhu under supervision of Professor Moon J Kim of the Department of Materials Science and Engineering at The

University of Texas at Dallas, USA helped me investigating CuNO_x specimens. I collected all the data and conducted all the data analysis.

Chapter 1

Introduction

1.1 Human Health Monitoring

Recent, severe acute respiratory syndrome (SARS), a viral respiratory illness caused by a coronavirus, worldly known as SARS – associated coronavirus (SARS – CoV), transmission as COVID – 19 shows that human race is predominantly under in danger of mass extinction, while connected each other more than ever in history. According to WHO, there have been 767,972,961 confirmed cases of COVID – 19, including 6,950,655 deaths, globally, as of 12 July 2023 [1]. The pandemic acquainted us with the importance of health monitoring. This health monitoring, however, is crucial not only for the diseases which can cause pandemic but also for personal health. Moreover, the diseases due to abnormalities and/or dysfunctionalities of neurotransmitters (NTs), a chemical messenger effects various psychological and neurophysiological purposes such as sleep, emotions, memory, and other cognitive functions, are great concern nowadays [2], [3]. The commotions have been happened in the central nervous systems (CNS) are psychotic (schizophrenia, depression, dementia, etc.), neurodegenerative diseases (Alzheimer’s, Parkinson’s, Huntington’s disease, autism, epilepsy, attention deficit hyperactivity disorder (ADHD), etc.), and other illnesses (glaucoma, arrhythmias, thyroid hormone shortage, congestive heart damage, sudden infant death syndrome, dejection, and anguish, etc.) [4], [5]. Although the Nobel Prize winner German pharmacologist Otto Loewi discovered the first known NT –

acetylcholine (ACh) in 1921, till now total 200 NTs are revealed [3], [6]. However, ACh regulates muscle contraction in the peripheral nervous system (PNS) through acetylcholine receptors (AChR). It also plays a key role in the central nervous system's activities such as behavior, arousal, attention, learning, and memory. The choline acetyltransferase and acetyl coenzyme A synthesize ACh from choline in neurons [7]. Imbalanced ACh regulation in the brain can cause neuropsychiatric disorders such as schizophrenia, Alzheimer's, Parkinson's, and myasthenia gravis [7], [8]. On the other hand, Dopamine (DA) is another neurotransmitter that conveys messages of pleasure in the brain's reward system. Unreasonable levels of dopamine are linked to various diseases, including Schizophrenia, Parkinson's, restless legs syndrome, and attention deficit hyperactivity disorder [9].

Likewise, proteins which provide genetic information through molecular expression that imprinted on nucleic acids define the underlying foundation of biological function [10]. After DNA studies, the researchers are entranced to unraveling the mysteries of proteins because they are at the core of most pathological conditions. C-reactive protein (CRP), an annular pentameric protein made in the liver, is found in blood plasma, increased in response to an offending agent which causes inflammation, and activated the first immune responders. In a healthy human, the normal range of CRP is <5 mg/L, where surgery, trauma, exercise, heatstroke, and childbirth can result in a drastic increase in CRP, ranging from 1 to 500 mg/L [11]. Moreover, the higher CRP values can indicate cardiovascular diseases, pathogenic diseases, inflammatory bowel disease (IBD), and colon cancer [11]. Further, Trypsin, an important enzyme of the digestive system, is produced as the inactive zymogen trypsinogen in the pancreas and activated in the small intestine while

breaking down long proteins into smaller digestible pieces [12]. Trypsin activities are regulated by pancreatic secretory trypsin inhibitor (PSTI) by inhibiting its secretion from the pancreatic acinar cells, which otherwise could damage the pancreas leading to pancreatitis [13]. Therefore, trypsin plays a necessary role, as a specific biomarker, for diagnosis of some important biological disorders as pancreatitis, pancreatic cancer, cystic fibrosis, and biliary cirrhosis [14], [15]. In addition, carcinoembryonic antigen (CEA) is a glycoprotein produced, typically, in gastrointestinal tissue and found in many types of cells associated with tumors [16]. The normal levels of CEA in healthy adults are in the range of $3\text{--}5\text{ ng mL}^{-1}$, although these levels increase up to 10 ng mL^{-1} in some benign diseases [17]. The level of CEA in the blood may be elevated by certain types of cancers, such as colon, rectal, breast, lung, pancreatic, stomach, liver, and ovarian cancer, and non-cancerous conditions like cirrhosis, hepatitis, diverticulitis, IBD, peptic ulcer disease, chronic obstructive pulmonary disease, cholecystitis, and obstructed bile duct. The CEA test is crucial for the diagnosis of colorectal cancer, as well as for monitoring its response to treatment and the risk of reoccurrence [18]. As well prostate-specific antigen (PSA) is a glycoprotein secreted by the prostate gland and found in low amounts, $<4\text{ }\mu\text{g L}^{-1}$, in the blood [19]. Its elevated levels, $>10\text{ }\mu\text{g L}^{-1}$, in the blood can be caused by prostate cancer as well as non-cancerous conditions such as prostatitis, inflammation of the prostate, and benign prostatic hyperplasia, enlargement of the prostate [20].

Furthermore, acute myocardial infarction (AMI), also known as a heart attack, is a common life-threatening cardiovascular disease throughout the world. Serum markers of myocardial cell injury, cardiac markers, are enzymes, as creatine kinase-MB isoenzyme

(CK-MB), and cell contents such as cardiac troponin T (cTnT), cardiac troponin I (cTnI), and heme-containing myoglobin (Myo) are released into the bloodstream after myocardial cell necrosis [21]. The cardiac markers appear at different times after myocardial cell injury and levels decrease at different rates. The AMI results in the rapid release of cTnT (37 kDa) from cardiac muscle cells into the bloodstream which remains elevated up to 14 days after cardiac ischemia, providing the possibility of prognosis of the disease and is the most sensitive and specific marker of choice [21]. While sensitivity and specificity for myocardial cell injury vary significantly among these markers, but the cTnT, a cardiac regulatory protein, is its specific biomarker [21]. The myoglobin, cardiac Myo, increases after the AMI onset. Due to its small size of 17.8 kDa, Myo is quickly released into circulation within 1 – 3 h after symptoms onset and serves as a valuable screening molecule with high sensitivity and predictivity for the AMI detection [22]. However, the tumor necrosis factor- α (TNF- α) is naturally produced by activated macrophages and monocytes and has pleiotropic effects on normal and malignant cells. Though it is a key marker of inflammatory diseases, it is involved in a broad range of physiological and pathological responses, such as atherosclerosis, rheumatoid arthritis, psoriasis, IBD, Alzheimer's disease, and various pulmonary disorders [23]. Moreover, the TNF- α , associated with necrosis or apoptosis, is rapidly upregulated in the brain after injury and important for the understanding of inflammation and discovering drugs that alleviate it [23]. Also, acetaldehyde, also known as ethanal by IUPAC, is an organic colorless liquid or gas and one of the most important aldehydes. Although it occurs widely in nature in plants, it is also produced by the partial oxidation of ethanol by the liver enzyme alcohol

dehydrogenase and is a contributing cause of hangover after alcohol consumption [24]. The International Agency for Research on Cancer (IARC) has listed acetaldehyde as a Group 1 carcinogen [25]. Most importantly, glucose, the main source of energy for the human body, is produced from food, mainly plant based, through digestion. The pancreas produces insulin to help the body to convert glucose into energy in the blood stream for the cells to consume. However, the uncontrolled blood sugar levels due to ineffective insulin use or deficiency can cause diabetes, which can lead to blindness, kidney failure, heart attack, stroke, and serious damage to nerves and blood vessels.

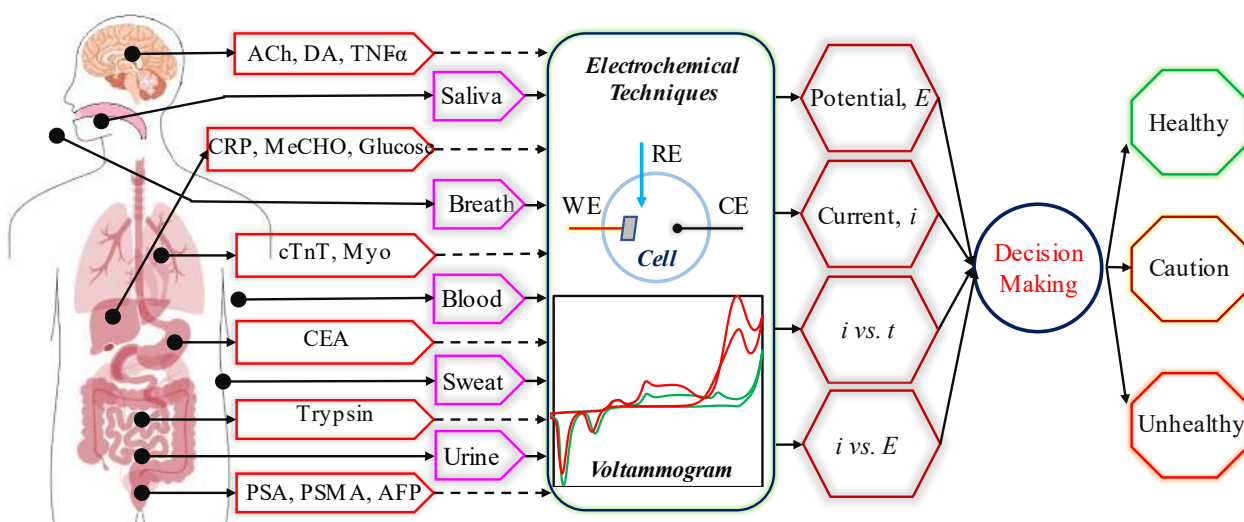


Fig. 1-1, The schematic of the electrochemical health monitoring systems.

These biomarkers have always enchanted researchers due to their effect on human life in general, as shown in Figure 1 – 1. Since the NTs, proteins, and glucose are in the core of human biological functions, they have intrigued researchers into decoding their secrets. Hence, these are feasibly the most intense research subjects as cutting-edge biosensing technology. The Biosensors can be electrochemical, opto-electrochemical, optical, piezoelectric, magnetic, and calorimetric. However, the electrochemical biosensors

have properties those outperforms the other existing sensing systems providing rapid, simple, and inexpensive on-field detection [10]. Moreover, electrochemical measurement protocols are also suitable for mass fabrication of miniaturized devices. In fact, electrochemical biosensors have played a major role in the advancement towards simplified testing for point-of-care usage. Indeed, self-testing glucose strips, based on screen-printed enzyme electrodes, coupled to pocket-size amperometric meters for diabetes, have dominated the market over the past two decades [26]. In this work, we discuss the electrochemical sensors for glucose electro-analysis.

In this chapter, we establish the importance of human health monitoring systems. Next, we discuss the necessity of glucose monitoring for the human body. Then, we discuss conventional methods as well as different electrochemical sensing techniques of glucose sensing. These techniques include cyclic voltammetry (CV) based sensors for electrochemical non-enzymatic glucose sensing. We provide a summary and comparison of the sensor structures, operation conditions, sensing mechanisms, relevant materials, and some key performance parameters such as sensitivity, sensing range, response time and stability of the sensors. Then, the motivation of this research is provided along with the specifications of the fabricated glucose sensors. Finally, the research contribution and thesis organization are presented.

1.2 Necessity of Glucose Monitoring

Diabetes mellitus, or simply diabetes, is a chronic disorder, which is caused by uncontrolled blood sugar (glucose), and it is the result of ineffective use or the deficiency of insulin, a hormone that regulates the movement of sugar into the cells, in the body.

Depending on the sugar level in blood, diabetes symptoms are revealed in the human body. There may be no symptoms shown, if some people, especially, have prediabetes (a higher-than-normal blood sugar), gestational diabetes (diagnosed for the first-time during pregnancy, gestation), and type – 2 diabetes (the pancreas does not produce enough insulin and/or cells respond poorly to insulin and take in less sugar). However, the long-term damage to heart, blood vessels and kidneys may already be happening due to these types of diabetes. On the other hand, the symptoms are severe and quick for the type – 1 diabetes.

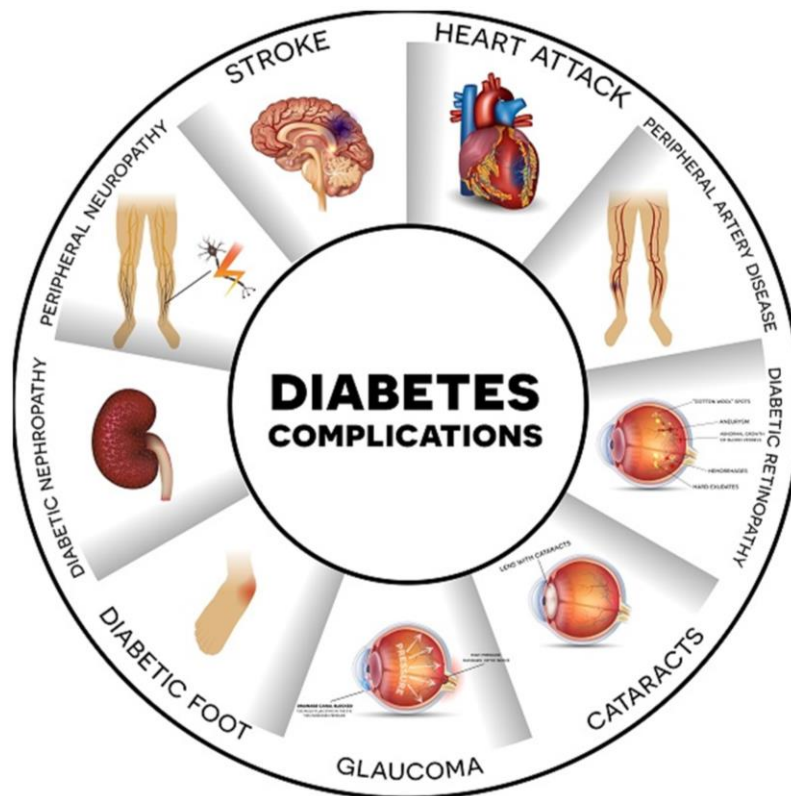


Fig. 1-2. The human body organs severely affected by diabetes [33].

Moreover, type – 1 diabetes is thought to be caused by an autoimmune reaction that means the body attacks itself by mistake which stops the body from making insulin [27]. It is the

seventh leading cause of the death worldwide. According to the WHO, diabetes directly caused an estimated 1.5 million deaths, and 460,000 more deaths due to kidney disease caused by diabetes in 2019 [28]. Furthermore, elevated blood glucose causes around 20% of cardiovascular deaths in 2019 [29]. It has been reported that the illnesses associated with the metabolic syndrome including diabetes act as comorbidities by putting excess strain on the organ systems affected by COVID-19 [30]–[32].

Diabetes causes heart and blood vessel (cardiovascular) disease, nerve damage (diabetic neuropathy), kidney damage (diabetic nephropathy), eye damage (diabetic retinopathy), foot damage, bacterial and fungal infections on skin as well as in mouth, hearing impairment, Alzheimer's disease, and depression related to diabetes, as shown in Figure 1-2 [33], [34]. Alarmingly, type – 1 is commonly diagnosed in children, teens, and young adults while there is no way available to prevent it without taking insulin to survive. Hence, the guidelines for managing type – 1 diabetes are: testing blood sugar; giving insulin; eating regular meals and snacks; balancing food, medication, and physical activity; recognizing the signs of low and high blood sugar [35]. Thus, early detection of diabetes through real-time monitoring of glucose is critical to prevent complications and can save lives.

1.3 Glucose Biosensors

First historical document about diabetes was a papyrus, ancient Egyptian chronological and hieroglyphically written document dating back in 1552 BC by a physician Hesy-Ra, mentioning ‘to regulate.....excessive urine’ discovered by Georg Ebers in 1862, and stated by Ebbell (in 1937) and Tattersall (in 2010) [36]. Nwaneri describes diabetes mellitus as a silent epidemic [36]. Since its discovery, a surfeit of

biosensors has been developed to provide diagnostic information, monitoring, and medication. In a review by Hassan et al. 2021 detailing the advances of glucose sensors showed that the research on glucose biosensors and monitoring systems significantly increased in recent years [37]. There are optical and electrochemical glucose biosensors, usually. Several methods of optical glucose biosensors have been introduced such as fluorescence, absorptiometry, and surface plasmon resonance (SPR), where optical fiber is the main glucose sensing materials to be used by the principles of absorption, illumination, light scattering, or refraction principles [38]–[45]. While this type of biosensors provides many advantages (remote sensing, low cost, free of electrical interference, and fast response time in comparison to conventional methods), there are some associated drawbacks too, which hinders their usages in general, such as interference from ambient light, requirement of high-energy light sources, and limited linear range, which limit their usages [46], [47].

1.3.1 Electrochemical Glucose Biosensors

Electrochemical, also known as electroanalytical, biosensing is a rapidly growing field in global healthcare research. This involves studying the flow of electrical current induced by chemical reactions and measuring the subsequent electrical energy produced [48]. Given that biological systems rely on chemical processes, electrochemical sensing is critical for the fast, reliable, and real-time detection of target molecules and disease diagnosis. In comparison to the lab-based techniques, electrochemical sensing methods are quick, adaptable, portable, cost-effective, and do not require skilled professionals [49], [50]. These methods can be conveniently used in point-of-care settings. Moreover, electrochemical techniques have been extensively used in detecting biomarkers, analytes,

and contaminants in healthcare, environmental monitoring, food packaging, and other applications [51], [52]. However, a few of them proved to be accurately applicable to detect glucose in bio-analytes [53]. In addition, the electrocatalysts are needed to be highly active, and efficient to design an efficient, reliable, stable, and innovative sensing device [54]. Furthermore, recent developments in the field of nanotechnology and synthesis of advanced functional materials have facilitated new strategies for the tailoring of novel materials with desired morphologies and exceptional physicochemical properties [55].

Electrochemical Cell & Measurement Circuitry (Potentiostat)

Electrochemical sensing techniques, a subset of analytical chemistry, focus on analyzing analytes in a solution [56]. Moreover, the techniques can be categorized into bulk and interfacial methods [1]. The former measures properties related to the total concentration of dissolved ions, while the latter concentrates on potential, current, or charge at the interface [57]. However, the interface comprises an electronic conductor (electrode) and an ionic conductor (electrolyte). An electric potential prompts the current to flow through the interface, representing the rate of change of charges (electrons or holes) flowing through the electrode [56]. On the other hand, an electrochemical cell features complex environments with multiple interfaces [58]. The modern potentiostat systems are 4 – probe instruments with working (WE), counter (CE), reference/auxiliary (RE), and working sense (WSE) electrode. Depending on the electrochemical techniques and experiments set up, the 4 – probe instruments can be used as 2 –, 3 –, or 4 – electrode measurement configurations because each individual technique may have multiple possible experimental setups. In a two-electrode electrochemical cell configuration, the sense leads measure the complete

voltage dropped by the current across the whole electrochemical cell that means WE, electrolyte, and CE, since the CE also works as the RE and so the applied potential is the one across the whole cell. When the user defined potential is applied, the current flows through the electrolyte and the potentials of the solution in between WE and CE interfaces change [59]. The change of the potentials is the function of the chemistry of the electrolyte in the cell in terms of solution composition, the electrode materials, and the relative areas of the electrodes.

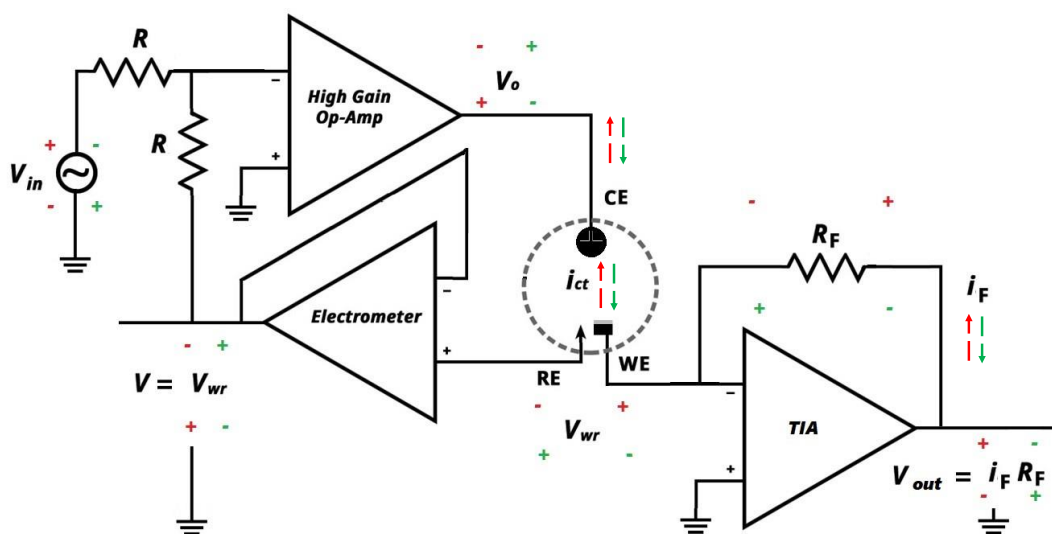


Fig. 1-3. Schematic of the three electrode potentiostat circuit diagram.

Recently, the standard 3-electrode configuration, shown in Figure 1-3, of an electrochemical cell has gained tremendous popularity to conduct necessary experiments. This setup allows users to experiment, only, with the interface of WE and solution, while the electrochemical activities at the CE and its adjacent interface can be ignored [59]. The function of a potentiostat circuitry, see in Figure 1-3, is to make the ‘potential difference

(voltage) static' i.e., constant between the WE and the RE, V_{wr} , by regulating current, i_{ct} , through CE, electrolyte, and WE. The high gain operational amplifier (Op-Amp), the input Op-Amp, is considered an infinity gain, $A_V = \frac{V_o}{V^+ - V^-} = \infty$, amplifier, ideally. Mathematically, the infinity gain is only possible when the input voltage, $V^+ - V^-$, is zero. In addition, the input of an Op-Amp is constructed of several differential amplifiers, a very high input impedance/resistance amplifier, that makes the input impedance/resistance is infinite, ideally, of an Op-Amp. Hence, the zero-input voltage, $V^+ - V^- = 0$, and the infinity-input impedance/resistance, Z_i or $R_i = \infty$, are considered as so called 'Virtual Ground', while the practical circuit ground means the potential difference is zero, and the current is infinity, short-circuited current. When, the input applied voltage $V_i = 0$ and the Op-Amp is ideal or *offset null* procedure is done correctly then the $V_o = 0$, which resulted in no current in between CE, and WE, as a result the $V_{wr} = V_{WE} - V_{RE} = 0$, so there is no changes in voltage at the inverting terminal of the high gain Op-Amp. If the applied voltage, V_i , is any positive value, the red polarity, there is no current through the inverting terminal of the high gain as well as electrometer, which is basically a voltage follower where $\pm V_{in} = \pm V_{out}$, Op-Amps due to the virtual ground. Thus, the output V_o drives toward the negative power supply, not shown in the diagram, which resulted in the current i_{ct} upwards from WE to CE, the red-dotted arrow. Ideally, there is no current through the non-inverting terminal of electrometer as well as the inverting terminal of the transimpedance amplifier (TIA), a current follower where $i_{ct} = i_F$. However, the voltage $V_{wr} = V_{WE} - V_{RE}$ is positive, that produces the voltage at non-inverting terminal of electrometer negative. Therefore, the $V = -V_{wr}$ will reduce the total applied voltage at the inverting input terminal

which will reduces the V_O until $V_{wr} = V_{WE} - V_{RE} = 0$. In contrast, if the applied voltage, V_i , is any negative value, the circuit will work as the green polarities and directions have been shown, see Figure 1-3, to make the voltage V_{RE} equals to V_{WE} . It is assumed that the voltage drop in the cell is negligible considering the solution of high ionic conductivity and/or the RE at a minimum distance of the WE.

The potentiostat & Cyclic Voltammetry (CV) Technique

The standard 3 – electrode electrochemical configuration has been used in this work to detect analyte (glucose/sugar) using the CV technique. Since the configuration studies the interface of the WE and bulk solution only, and the user have the freedom to keep the potential difference between the WE and the RE static, the current, I_F , and voltage, $V_{out} = I_F R_F$, values provide the charge with time that was passed across the interface of WE and bulk solution as a function of the voltage difference between the WE and RE, and time [59]. The CV is a potentiodynamic electrochemical measurement technique in which a cyclic potential scan is performed between two peak potentials E_1 and E_2 , as shown in applied potential section of Figure 1-4. The scan potential is not smooth, rather a staircase potential with height of each step potential is E_{step} . At the end of each step, the current has been sampled or recorded. Hence, the number of points per scan of the current versus potential curve is $\frac{2 \times (E_2 - E_1)}{E_{step} + 1}$. Moreover, the sampling time, the time between two consecutives steps, determines the scan rate, and denoted as Vs^{-1} . However, the interval time is determined by $\frac{Scan\ Rate}{E_{step}}$. The voltammogram, the curve of the current i_{ct} , see Figure 1-3, against the voltage difference between the WE and RE, gives the CV trace, shown in

Figure 1-4, I vs E section. In addition, the voltammogram can be reversible, quasi-reversible, and irreversible depending on the characteristics of the reduction and oxidation chemical reaction of the analyte, as shown in the section of voltammogram in Figure 1-4.

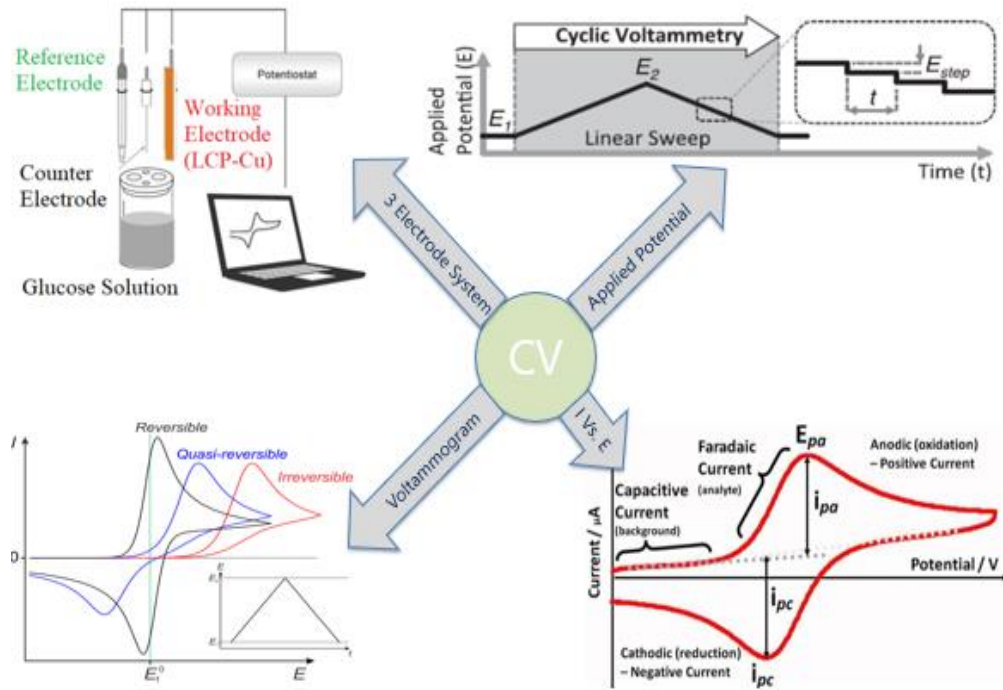
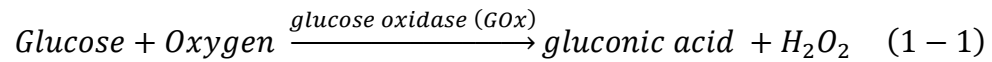


Fig. 1-4. Schematic of the different components of CV technique.

Electrochemical glucose biosensors are the crucial tool of a blood glucose monitoring device. Moreover, these biosensors are extensively used due to their sensitivity, reproducibility, and manufacturability in huge volume and at low cost [60]. In 1962, Clark and Lyons, at the Children's Hospital in Cincinnati, proposed the first enzymatic electrochemical glucose biosensors [61]. However, in the last 60 years, huge effort has been commanded to enhance the performance of these biosensors. Electrochemical glucose biosensors encompass two types: enzymatic and non-enzymatic biosensors.

1.3.2 Enzymatic Glucose Biosensors

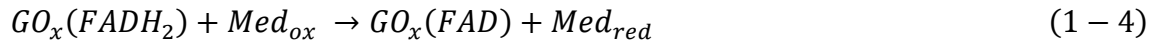
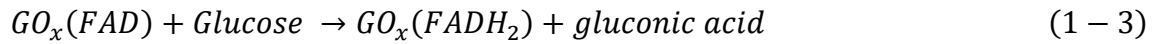
For the first time, Clark and Lyon presented, in a patent, the principle of electrochemical enzymatic glucose biosensors explaining the science behind the conversion of electro-inactive substrates into electroactive products using enzymes [61]. Moreover, the commercial blood glucose monitoring systems, mostly, use electrochemical enzymatic glucose biosensors. All current blood glucose monitoring systems are enzyme-based, and marketed by Abbott Laboratories, Roche Diagnostics, LifeScan, Medtronic, Dexcom Inc., Tandem Diabetes Care Inc., Insulet Corporation, and Terumo Corporation [62], [63]. The global diabetes care devices market is expected to grow from US\$ 28,942.1 million in 2022 to US\$ 42,119.3 million by 2028; it is estimated to grow at a compound annual growth rate (CAGR) of 6.4% from 2022 to 2028 [63]. Enzymatic glucose biosensors, introduced by Clark and Lyons in 1962, in which oxygen consumption was monitored according to the enzyme-catalyzed oxidation of glucose in the



presence of oxygen, as given in equation (1-1). However, the variation in background oxygen interferes with the reactants and products of the equation. Hence, Updike and Hicks developed an electrode system using two electrodes which can measure the differential current and remove background oxygen noises [64]. Moreover, Guilbault and Lubrano developed the first enzymatic amperometric glucose biosensor in 1973, where variable oxygen reduction current is omitted and the anodic production of hydrogen peroxide was monitored, as shown in equation (1-2) [65].



The redox center of the enzyme, glucose oxidase/glucose 1 – oxidase, GO_x is flavin adenine dinucleotide, FAD , which is protected by a thick protein layer deep in the enzyme. The $GO_x(FAD)$ is interacted with glucose and reduced to $GO_x(FADH_2)$ and produces glucolactone, according to equation (1-3) [66]. In contrast, an electron acceptor and oxidation mediator, Med_{ox} , oxidizes GO_x to produce the oxidized form $GO_x(FAD)$, as given in equation (1-4) [66].



However, electron transfer to the active center of GO_x is most important function of the mediator, Med_{ox} , to regenerate, $GO_x(FAD)$, for further electro-oxidation of glucose. Depending on the mediator, Med_{ox} , there are 3 – generations of electrochemical enzymatic glucose biosensors; O_2 as a physiological mediator, an artificial (synthetic) electron acceptor, and direct oxidation by an electrode, as show in Figure 1-5.

First Generation Enzymatic Glucose Biosensors

This type of glucose biosensors regenerate $GO_x(FAD)$ using O_2 as a mediator and detects glucose analyzing the consumption O_2 , or the generation of H_2O_2 [67]. However, the monitoring of generation of $GO_x(FAD)$ has been done using the anodic oxidation and cathodic reduction of H_2O_2 , where the prior enhances regenerate/replenish the O_2 , which helps the enzymatic cycle [68]. Though these biosensors are stable, simple, and easily

miniaturized, the electroactive interferences arise due to the relatively higher potential requirement of H_2O_2 , since some of the interferents such as ascorbic acid (AA) and uric acid (UA) are highly active at higher potential energies and hamper its properties such as the selectivity and accuracy [69], [70]. Several technologies have been proposed to solve the interference problem [37].

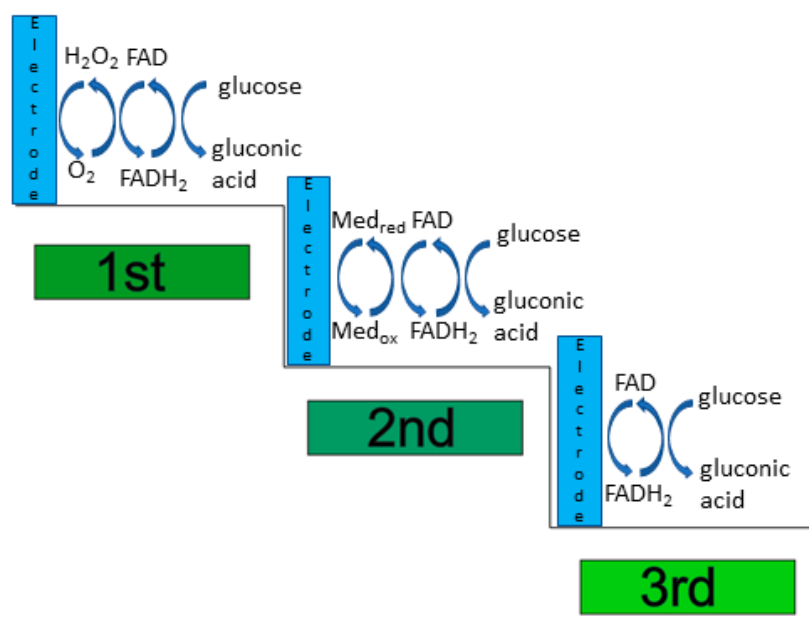


Fig. 1-5. Schematic representation of enzymatic glucose oxidation mechanisms for the three different generations of biosensors (adapted from Ref. [37]).

Additionally, a drawback of the first-generation electrochemical enzymatic glucose biosensors is the dependency on O_2 that used as the Med_{ox} [64], [71]. However, the physiological concentration of glucose is much higher than the concentration O_2 which causes errors in the glucose sensing [72]. Some of the ways to solve the problem are a two-

dimensional cylindrical electrode [73], an oxygen-rich carbon paste enzyme electrode [74]–[76], and an air diffusion biocathode that used oxygen directly from the air [77].

Second Generation Enzymatic Glucose Biosensors

Instead of O_2 , an artificial, synthetic, Med_{ox} mediates to keep the GO_x cycle going in second generation of glucose biosensors to transport electrons, [78]. Various types of the artificial Med_{ox} are proposed by various scholars such as directly attached or trapped in the GO_x immobilized mediator [79], [80], diffusible in and out of the GO_x center solution-state mediator [72], a redox-conducting polymer mediator able to transport its electrons in and out of the GO_x active site [81], [82]. In the catalytic process, step 1, the glucose transfers electrons to the FAD active center of GO_x which reduces $GO_x(FAD)$ to $GO_x(FADH_2)$; step 2, $FADH_2$ transfers electrons to the artificial mediator, Med_{ox} , to be reduced to Med_{red} ; step 3, the transport of electrons through the artificial mediator to the electrode [72]. One of the most prominent drawbacks of the mediator is maintaining closeness with both the surface of the electrode and the enzyme for longer use. To overcome the problem, complex methods of tethering are required [83]. In addition, the dissolved oxygen could be participating with the mediator and producing H_2O_2 .

Third Generation Enzymatic Glucose Biosensors

The third generation of enzymatic glucose biosensors adopts an ambitious technology direct energy transmission (DET) between the enzyme and the electrode [84], [85]. Heller and Degani presented the fundamental idea of DET of connecting the enzyme active site covalently to the surface of the electrode using a redox polymer [86]. This technology could be reduced problems associated with mediators, the intervention of

electroactive interferences, and the dependence on dissolved oxygen. The concepts become reality due to hugely researched on nano and porous materials where surface area and ability to entrap and encompasses the enzyme of electrodes increased [87], [88]. As the DET has increased the performance of glucose biosensors compare to the prior generations, the ambient conditions, temperature, pH, and humidity, as well as the thickness of the enzyme can regulate the enzyme's performance such as selectivity, and sensitivity [85], [89]–[92].

Regardless of all these developments, stability is the main concern issue among others several problems and hinders the prospects of the enzymatic glucose biosensors. Enzymatic glucose biosensors suffer from several constraints such as pH ranges of 2-8, temperatures below 44°C, and ambient humidity levels, a fourth generation of biosensors has been developed and known as non-enzymatic glucose biosensors where glucose directly electro-oxidized on the electrode surface [83].

1.3.3 Non-enzymatic Glucose Sensors

Instead of an unstable and relatively thick complex enzyme, the direct electro-oxidation of glucose occurs on non-enzymatic electrodes. In century ago, the principle behind the nonenzymatic glucose biosensors was discovered by Walther Loeb by observing the direct electro-oxidation of glucose in sulfuric acid while producing gluconic acid at a lead (Pb) anode [93]. This occurred long before the fabrication of the Clark oxygen electrode [61], though extensive research into the non-enzymatic approach coincided with enzymatic development. Direct electro-oxidation and electroreduction of glucose in alkaline ($\text{pH} > 11$) and acidic ($\text{pH} < 2$) solutions have also been investigated [83]. Despite

decades of research into non-enzymatic systems, however, the problems associated with this approach have prevented the practical application of the sensors. This is due to the slow kinetics arises from the absorption of glucose oxidation intermediates (e.g., CO) or solution active species (e.g., Cl^-) which can lead to blockage of electrode activity, but also the lower selectivity compared to enzymatic amperometric glucose biosensors by real sample constituents, and the limited number of systems that are applicable to physiological pH [37], [83]. However, non-enzymatic amperometric glucose sensors present long-term stability, which is the main drawback of the enzymatic biosensors due to the inherent nature of enzymes. However, noble metals and their composites have been used specifically as electrode materials for non-enzymatic sensors due to their high electrocatalytic activity, and high sensitivity to the electrooxidation of glucose [83].

1.4 Research Motivation

While there is no preventative treatment or cure for diabetes, the most effective way of managing the disease is monitoring the glucose level and controlling it. It has been proven that monitoring and controlling sugar in blood can prolong life expectancy [94], [95]. In addition, glucose monitoring can be used to optimize patient treatment strategies, and provide an insight into the effect of medications, exercise, and diet on the patient [96]. Although blood-glucose monitoring is the gold-standard medium for glucose sampling, measurements carried out in this fluid are invasive [38]. Blood-glucose concentrations are typically in the range of 4.9–6.9 mM for healthy patients, increasing to up to 40 mM in diabetics after glucose intake [97].

Much research has been carried out to develop non-invasive glucose sensors for monitoring purposes. However, most of them are enzymatic electrodes. This research is devoted to developing a facile and flexible electrode for sweat glucose monitoring system that is capable of on-demand measurement of glucose in sweat accurately. Such an electrode should realize the following objectives:

- High accuracy: The electrode should be characterized with high sensitivity, repeatability, stability, and selectivity.
- Real-time response: The electrode in the system should respond fast to obtain results on-site towards the detection of the target analyte.
- Low-cost: A low-cost electrode can be afforded by people living in developing and underdeveloped regions and can also be distributed over a wide geographical area.

Table 1-1: Sensing performance of the electrodes

Parameters	CuNOx@25°C	CuNOx@280°C
Sensitivity	603.42 $\mu\text{A mM}^{-1} \text{cm}^{-2}$	1795 $\mu\text{A mM}^{-1} \text{cm}^{-2}$
Sensing range	0.05 – 7.00 mM	0.05 – 1.00 mM [Sweat] 1.00 – 7.00 mM [Blood]
Accuracy/LoD	94.21 μM	135.39 μM
Response time	~120s	~120s
Stability	96.91% (55 Days)	96.91% (50 Days)
Surface Area	1 cm^2	1 cm^2
Cost	< \$0.25	< \$0.25

To accomplish the abovementioned objectives, this research focuses on the development of an electrode to sense glucose in sweat where sweat glucose range is 0.277–1.11 mM [94], [98]. The sensing performance of the electrodes are listed in Table 1-1.

1.5 Research Contribution

The research work conducted in this thesis focuses on developing a facile, flexible, easy-to-use, low cost, and accurate electrochemical non-enzymatic glucose sensing electrode which will be useful for sweat monitoring systems. The major contributions of this work are summarized as follows.

- ✓ **The fabrication of a facile, flexible, and inexpensive glucose biosensors using the stable native cuprous oxide (Cu_2O) of 35 μm thin Cu foil at ambient conditions (25°C).** A very simple low-cost fabrication technique has been shown to make a facile, flexible, and inexpensive electrode to detect sweat glucose for a sweat glucose monitoring system. Since, the metallic Cu is unstable, the native stable Cu oxide, cuprous oxide (Cu_2O), layer has been grown on 35 μm thin Cu foil keeping at ambient conditions (25°C) for more than 2 years to make sure that the full-grown oxide layers are fully stable. The CV electrochemical sensing performance of the electrodes was characterized in terms of their effective surface area, scan-rate, and pH of the solution. A linear glucose sensing response in the range of 0.05–7.00 mM with a limit of detection of 94.21 μM was obtained.
- ✓ **The introduction of a new temperature profile to annealed Cu thin foils to grow uniform Cu native oxide layer with larger CuO crystalline structures and grain sizes.** A very simple but effective temperature profile has been introduced to anneal the 35 μm

thin Cu foil for growing native cupric oxide (CuO) on the surface of the films. The X-ray photoelectron spectroscopy (XPS) and high-resolution transmission electron microscopy (HRTEM) results shows that at 280°C annealing temperature the surface, mostly, converted into CuO and the uniform layer grow till 140 nm.

- ✓ **The fabrication of the high-performance thermally grown native CuO glucose sensing electrode for sweat as well as blood glucose monitoring system.** A very simple low-cost fabrication technique has been shown to make a facile, flexible, inexpensive, and high-performance electrode to detect sweat as well as blood, twin calibration curves, glucose for a sweat and blood sugar monitoring system, respectively. At ambient conditions (25°C), it is needed almost 2 years to get stable Cu₂O while the oxide layer is not uniform. However, at 280°C with new temperature profile a thick uniform CuO layer, with larger CuO crystalline structures and grain sizes, has been grown where CuO is highly electrocatalytic and good electro-conductor compared to Cu₂O. The CV electrochemical sensing performance of the electrode was characterized in terms of their effective surface area, scan-rate, and pH of the solution. The twin calibration curves have been found; a linear range of 0.05 – 1.00 mM for sweat and 1.00 – 7.00 mM for blood glucose monitoring with a limit of detection of 135.39 µM was obtained, where the range of sweat glucose is 0.277 – 1.11 mM for diabetic patients [94], [98], and blood glucose range 4.90 – 6.90 mM [97].
- ✓ **Discover the linear relation of the peak electro-oxidation current of the glucose with the square root of the temperature, \sqrt{T} .** It has been shown that the peak electro-oxidation current of glucose is linearly related with the annealing temperature. This can help to figure

out the required applied annealing temperature to get a higher peak electro-oxidation current of glucose.

Publications

- ✓ M. M. Alam, A. U. Alam, and M. M. R. Howlader. "Sweat Glucose Sensing by Directly Bonded Thin Films." In 2019 6th International Workshop on Low Temperature Bonding for 3D Integration (LTB-3D), pp. 76-76. IEEE, 2019.
- ✓ M Maksud Alam, Victor Mitea, Matiar M. R. Howlader, Ravi P. Selvaganapathy, and M. Jamal Deen," Analyzing Electrochemical Sensing Fundamentals for Health Applications." Advanced Sensor Research (2023), DOI: 10.1002/adsr.202300100. M.
- ✓ M. M. Alam and M. M. R. Howlader, "Nonenzymatic electrochemical sensors via Cu native oxides (CuNOx) for sweat glucose monitoring," Sens Biosensing Res, vol. 34, p. 100453, Dec. 2021, doi: 10.1016/J.SBSR.2021.100453.
- ✓ M. Klimuntowski, M. M. Alam, G. Singh, and M. M. R. Howlader, "Electrochemical Sensing of Cannabinoids in Biofluids: A Noninvasive Tool for Drug Detection," ACS Sens, vol. 5, no. 3, pp. 620–636, 2020, doi: 10.1021/acssensors.9b02390.
- ✓ M Maksud Alam, and Matiar M. R. Howlader," High performance nonenzymatic electrochemical sensors via thermally grown Cu native oxides (CuNOx) towards sweat glucose monitoring." Analyst (2023), DOI: 10.1039/D3AN01153D.

1.6 Thesis Organization

In Chapter 1, an introduction to the importance of human health, and glucose monitoring is presented. Recent research activities in electrochemical enzymatic and non-enzymatic glucose sensors are discussed. Then, the motivation of developing facile,

flexible, inexpensive, and high-performance electrodes for sweat glucose monitoring systems is presented. Finally, a summary of the main contributions of this research and the structure of this thesis are described.

In Chapter 2, analyzed crucial topics in chemical reactions in electrochemical sensing environments such as the dynamics of chemical energy, the roles of acidic and alkaline fluids, chemical reaction tendencies, thermodynamic equilibria, Gibbs free energy, water dissociation, and the pH scale have been discussed. Moreover, the significance of oxygen-derived radicals and nonradical reactive species in biochemical reactions, cellular responses, and clinical outcomes have been discussed in context of the impact of oxidation reduction reactions on human psychology, redox reactions in hemoglobin, redox environments in human serum albumin and cells/tissues, and thermodynamics of biological redox reactions have analyzed.

In Chapter 3, evaluation of electrochemical sensing methods in context of healthcare applications has been presented. Moreover, the recent advances in electrochemical techniques, research challenges and future perspectives in health applications have been discussed.

In Chapter 4, A very simple low-cost fabrication technique has been presented to make a facile, flexible, and inexpensive electrode to detect sweat glucose for a sweat glucose monitoring system using the native stable Cu oxide (Cu_2O) layer on 35 μm thin Cu foil keeping at ambient conditions (25°C) for more than 2 years to make sure that the full-grown oxide layers are fully stable. Detailed fabrication approaches, material characterization methods, and sensor characterization set ups used in this research are

given. Efforts are devoted to studying the sensing mechanisms, and to characterize the sensor performance in terms of effective surface area, scan-rate, pH of the solution, and sensing performance with common interfering ions.

In Chapter 5, A very simple low-cost fabrication technique has been presented to make a facile, flexible, inexpensive, and high-performance electrode to detect sweat as well as blood, twin calibration curves, glucose for a sweat and blood sugar monitoring system using a thick uniform CuO layer of 35 μm thin Cu foil annealed at 280°C with new temperature profile. Detailed fabrication approaches, material characterization methods, and sensor characterization set ups used in this research are given. Efforts are devoted to studying the sensing mechanisms, and to characterize the sensor performance in terms of effective surface area, scan-rate, pH of the solution, and sensing performance with common interfering ions.

In Chapter 6, this thesis is concluded with a summary of the research and several recommendations for future improvements for sweat glucose monitoring system.

Chapter 2

Analyzing Electrochemical Sensing Fundamentals for Health Applications

This chapter is part of our work published as ‘M Maksud Alam, Victor Mitea, Matiar M. R. Howlader, Ravi P. Selvaganapathy, and M. Jamal Deen, “Analyzing Electrochemical Sensing Fundamentals for Health Applications.” *Advanced Sensor Research* (November 2023), DOI: 10.1002/adsr.202300100.’

2.1 Background

Electrochemical biosensing is a rapidly growing field in global healthcare research. This involves studying the flow of electrical current induced by chemical reactions and measuring the subsequent electrical energy produced [48]. Given that biological systems rely on chemical processes, electrochemical sensing is critical for the real-time detection of target molecules and fast, reliable disease diagnosis. In comparison to lab-based techniques, electrochemical sensing methods are fast, adaptable, portable, cost-effective, and do not require skilled professionals [49]. These methods can be conveniently used in point-of-care settings. Electrochemical sensors have extensively used in detecting biomarkers, analytes, and contaminants in healthcare, environmental monitoring, food packaging, and other applications [51][52]. For instance, low-cost and portable glucose blood sensor strips based on electrochemical sensing generate over \$5 billion in revenue annually [26].

Among various reviews, the series titled “Dynamic Electrochemistry: Methodology and Application” in the *Analytical Chemistry Journal* is particularly notable for its impact

in the field of electrochemical sensing. This series includes contributions from Ryan et al. from 1992 [99] and 1994 [100], and Anderson et al. in 1996 [101], 1998 [102], and 2000 [103]. Covering a decade, these reviews highlight both fundamental advancements and practical applications in electrochemistry, particularly in the field of electroanalytical chemistry. Topics covered in this series range from ultramicroelectrodes, analytical voltammetry, and electrode kinetics to surface electrode phenomena, modified electrodes, bioelectrochemistry, characterization of various redox couples, spectroelectrochemistry, and instrumentation [100], [103]. Although this series offers an extensive overview, our current review is more focused on the application of these techniques in health monitoring, recognizing the growing interest in health assessment through electrochemical methods. Similarly, Bakker et al. in 2002 concentrated only on electrochemical sensors, emphasizing those based on potentiometric and voltametric techniques, and their applications in areas like immunosensors, DNA sensors, electrochemiluminescence sensors, and amperometric gas sensors [56]. In 2003, Stetter et al. reviewed insights on various sensors, including chemical sensors, electrochemical sensors, and the broader purview of the Electrochemical Society (ECS) [104]. Given the rapid advancements of electrochemical sensors in health monitoring, our review aims to comprehensively address the bioanalyte environments within the human body, factors influencing them, and the electrochemical techniques suitable for their detection.

Review articles on electrochemical sensing in health applications cover a wide range of subjects, from pharmaceutical compounds, metals, pathogenic bacteria, and biomolecules to neurotransmitters and glucose [105]-[106]. One outstanding review delves

into modern electroanalytical techniques, highlighting their roles particularly in the pharmaceutical and metal industries [105]. Another key article emphasizes the capabilities of electrochemical sensors for real-time, in situ chemical assessments, highlighting the significance of microfluidics, immunomagnetic separation, and multiplexing in microbial detection [107]. A unique review casts light on electrochemical biosensors and their ability in converting biological activities directly into electronic signals [108]. Further, a review on electrochemical sensors underlines their adaptability in detecting diverse signals across fields like agriculture, food, and biomedicine [109]. A subsequent review investigates up-to-date electrochemical methodologies, spotlighting the platforms that synergize nanomaterials and biorecognition elements for immediate detection [110]. Another article offers a detailed exploration of glucose biosensors built on nanomaterials, outlining their operational strategies and prospective directions [106]. Cyclic voltammetry (CV), recognized as a paramount voltametric technique, has been detailed in a review [111], granting readers a comprehensive view of the core attributes of electrochemical techniques. However, there is a gap in articles that simplify the basics, strengths, and limitations of each method. Crucially, the electrochemical identification of bio-analytes in biofluids, essential for advancements in non-invasive biosensing technologies, depends on understanding foundational concepts like biological redox reaction thermodynamics [90], [105], [107]–[111]. Addressing this void and catering to the increasing demand, a timely review could provide clarity on the principles and physics underlying each method. To effectively employ these techniques, an in-depth understanding of reactions at the electrode and the electrical dynamics at the electrode-solution interfaces is essential [58].

In this chapter, we summarize crucial topics necessary to understand chemical reactions in an electrochemical cell environment and the concept of reactions on sensing electrodes. In section 2.2, the concepts that have been summarized are chemical reaction tendencies, thermodynamic equilibria, Gibbs free energy, water dissociation, the pH scale. In section 2.3, the influence of oxygen-derived radicals and nonradical reactive species on human psychology, oxidation reduction reactions, redox reactions in hemoglobin, redox environments in human serum albumin and cells/tissues, and thermodynamics of biological redox reactions have been discussed.

2.2 Fundamentals of Analytical Chemistry for Electrochemical Sensing

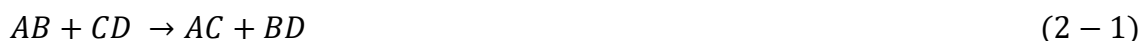
Electrochemical sensing techniques, a subset of analytical chemistry, focus on analyzing analytes in a solution [56]. They generate signals representing properties of an analyte, such as mass, volume, concentration, or absorbance, facilitating both qualitative and quantitative analyses [104]. Historically, the "classical" technique, which measures signals proportional to analyte concentration, was widely used [48]. Electrochemical techniques can be categorized into bulk and interfacial methods [58]. The former measures properties related to the total concentration of dissolved ions, while the latter concentrates on potential, current, or charge at the interface [57]. The main concern in electrochemical techniques is the charge transport through the interface and the factors affecting it [100]. The interface comprises an electronic conductor (electrode) and an ionic conductor (electrolyte). An electric potential prompts the current to flow through the interface, representing the rate of change of charges (electrons or holes) flowing through the electrode

[56]. The electrode phase includes solid metals (e.g., Pt, Au), liquid metals (Hg, amalgams), carbon (graphite), and semiconductors (indium-tin oxide, Si), while the electrolytes are liquid solutions containing ionic species (H^+ , Na^+ , Cl^-) in water or a nonaqueous solvent [48]. Electrochemical cells feature complex environments with multiple interfaces [58].

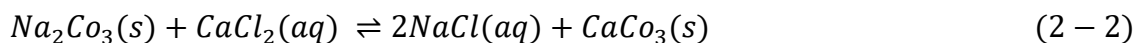
As illustrated in Figure 1-1, the relationship between the signal and analyte concentration is a theoretical function that depends on experimental conditions and the measuring instrument used. Now, we will discuss some chemical reactions and thermodynamics, including oxidation-reduction (redox) reactions, which govern the sensing performance, to gain insights into electrochemical sensing techniques.

2.2.1 Chemical Equilibrium

Until the 18th century, chemical reactions were believed to proceed only in one direction, as demonstrated by equation (2-1), where substances AB and CD react to produce AC and BD as the products [112].



These chemical reactions were understood through the lens of chemical affinities. For instance, substances A and B were thought to have affinities for C and D, respectively. Moreover, the idea of a reverse reaction was dismissed. However, after 1798, French chemist Claude Berthollet made a significant discovery while studying the salt water of Natron Lakes during Napoleon's military expedition to Egypt [113].



This groundbreaking scientific discovery emphasizes the reversible nature of chemical reactions, as indicated by the equilibrium arrow " \rightleftharpoons ", as shown in equation (2-2). Berthollet found that the direction and final composition of a reaction depend on the relative amounts of reactants and products. Initially, the mass of Ca^{2+} in the solution decreases, while the mass of CaCO_3 precipitates increases. Once the reaction reaches a steady state with no net changes, it is in equilibrium. This concept plays a vital role in interfacial interactions in electrochemical cells. Rogers et al. 2012 highlighted the importance of chemical equilibria in machine learning for chemical analysis, introducing the term "perturbed isotherms" to describe non-isothermal experimental conditions influenced by temperature and thermal history [114].

2.2.2 Thermodynamic Equilibrium

Chemical equilibria are influenced by individual molecular interactions and thermodynamics, which studies energy changes during chemical reactions [115]. According to Berthollet, the equilibrium chemical reaction represented by $aA + bB \rightleftharpoons cC + dD$, where a, b, c, and d are the stoichiometric coefficients of the respective substances, does not guarantee a favorable forward reaction and may depend on initial conditions. Depending on initial conditions, the reaction may shift to the left, to the right, or exist in a state of equilibrium, as seen in Figure 2-1(a) and (b) [48]. The aim of chemical thermodynamics is to understand the conditions affecting a reaction's equilibrium position. The Le Chatelier-Braun principle describes how external factors, such as temperature,

pressure, volume, or concentrations of reacting substances, lead to predictable system changes to reach a new equilibrium state [116][117].

Ligand-protein recognition has potential in assays [118], inflammation [119], cancer [120], and Alzheimer's disease [121] treatments. Zhang et al. (2019) developed a label-free electrochemical sensor for the biomarker CD44, detecting human serum and cancer cells [118]. Lerner et al. (2021) created a carbon nanotube FET (NT-FET) for detecting osteopontin (OPN), a prostate cancer biomarker [122]. While traditional methods like ELISA are sensitive, they struggle with OPN quantification [122], [123]. The NT-FET sensor's response curve was well fitted by a modified Hill-Langmuir equation, shown in equation (2-3), which describes ligand-receptor binding in thermodynamic equilibrium [122], [124].

$$\frac{\Delta I}{I} = A \left\{ \frac{(c/K_d)^n}{1 + (c/K_d)^n} \right\} + Z \quad (2 - 3)$$

Where $\frac{\Delta I}{I}$ is the measured responses of devices, c is the OPN concentration, A is the response when all binding sites are occupied, Z is an overall offset to account for the response to pure buffer, K_d is the dissociation constant, and n is the Hill coefficient describing cooperativity of binding. However, ligand-protein interactions, such as ligand binding, can impact cell environment thermodynamics, affecting water molecules near binding sites [125].

2.2.3 Gibb's Free Energy

Thermodynamic changes involve alterations in free energy due to interactions among biomarkers, ligands, solutes, and solvent molecules. These interaction energies depend on fluctuating interatomic distances and orientations, which vary over time in accordance with the conformational dynamics [115]. Under any external conditions, the overall free energy determines the direction of a chemical reaction, be it in the forward or reverse direction. With constant pressure and temperature, Gibbs' free energy (named after J. Willard Gibbs, 1839-1903) is represented by $G = H - TS$, where H , T , and S represent the enthalpy, the temperature in Kelvin, and the entropy, respectively [126].

Enthalpy measures energy flow as heat absorbed or released during a reaction. Endothermic reactions absorb heat and have positive enthalpy, while exothermic reactions release heat with negative enthalpy. Entropy relates to molecular freedom, disorder, and complexity. Change in Gibbs free energy ($\Delta G = \Delta H - T\Delta S$) is widely used, with ΔH , T , and ΔS representing changes in enthalpy, temperature in Kelvin, and entropy, respectively. Changes in Gibbs free energy, enthalpy, and entropy are calculated as differences between product and reactant values.

Wallerstein et al. (2021) studied the impact of small ligand structure changes on galectin-3C's carbohydrate recognition domain, focusing on binding enthalpy and entropy [115]. They analyzed various interactions in an isothermal environment, finding that minor structural differences affected binding thermodynamics, free ligand chemical potential, and complex structures [115]. Using isothermal titration calorimetry (ITC), they determined

binding enthalpy (ΔH), binding-competent protein fraction (n), and dissociation constant (K_d) through a single-site binding model [127]. The heat released or absorbed during the i^{th} injection is given by the following equation (2-4) [128].

$$\Delta Q_i = Q_i - Q_{i-1} + \left(\frac{V_i}{V_o}\right) \left\{ \frac{(Q_i - Q_{i-1})}{2} \right\} + Q_{off} \quad (2-4)$$

where V_i is the volume of the i^{th} injection, V_o is the cell volume, Q_{off} is an offset parameter that accounts for the heat of mixing, and $Q_i = \left(\frac{\Delta H V_o}{2}\right) \left\{ \alpha - \sqrt{\alpha^2 - (4nM_iX_i)} \right\}$ represents the heat following the i^{th} injection, where $\alpha = nM_i + X_i + K_d$ and M_i and X_i are the total concentrations of protein and ligand, respectively, in the cell at any given point during the titration.

Thus, the change in Gibbs free energy can be expressed as equation (2-5) for equation (2-1). Here, $[A]$ and $[A_o]$ represent the concentrations of substance A at any point during the reaction and under standard-state conditions, respectively [126].

$$\begin{aligned} \Delta G &= \Delta G^o + RT \log_e \frac{\left\{ \frac{[C]}{[C_o]} \right\}^c \left\{ \frac{[D]}{[D_o]} \right\}^d}{\left\{ \frac{[A]}{[A_o]} \right\}^a \left\{ \frac{[B]}{[B_o]} \right\}^b} = \Delta G^o + RT \log_e Q_r; \text{ where, } Q_r \\ &= \frac{\left\{ \frac{[C]}{[C_o]} \right\}^c \left\{ \frac{[D]}{[D_o]} \right\}^d}{\left\{ \frac{[A]}{[A_o]} \right\}^a \left\{ \frac{[B]}{[B_o]} \right\}^b} \end{aligned} \quad (2-5)$$

R represents the universal gas constant ($8.314 \text{ JK}^{-1}\text{mol}^{-1}$), T denotes the temperature in Kelvin, and Q_r signifies the reaction quotient. Standard states are defined as gases with unit partial pressures, solutes with unit concentrations, and a value of 1 for pure solids and pure

liquids. The change in Gibbs free energy, ΔG , is zero under standard state conditions or at thermodynamic equilibrium. Hence, the equation (2-5) can be reduced to $\Delta G^o = -RT \log_e \frac{[C_{eq}]^c [D_{eq}]^d}{[A_{eq}]^a [B_{eq}]^b} = -RT \log_e K_d$, where $K_d = \frac{[C_{eq}]^c [D_{eq}]^d}{[A_{eq}]^a [B_{eq}]^b}$ under standard state conditions or at thermodynamic equilibrium, where K_d is the equilibrium constant or the dissociation constant. The authors found that protein-ligands with similar structures exhibit similar thermodynamic signatures [115]. Wallerstein et al. (2021) calculated the entropy (ΔS) of the protein-ligand chemical reaction in a cell using equation (2-5), $\Delta G^o = -RT \log_e K_d$ and $-T\Delta S = \Delta G - \Delta H$. They demonstrated that, for isothermal protein-ligand reactions, the complexes exhibit overall similar thermodynamic signatures, which might be expected due to the similar structures of the ligands [115].

Wallerstein et al. (2021) found several insights on isothermal ligand-protein interactions: 1) chemical potentials in the free state depend on structural differences; 2) binding thermodynamics differences relate to ligand-protein complex variations; 3) binding enthalpy differences can be explained by fewer interactions; 4) total entropy differences come from opposing contributions. More flexibility leads to unfavorable entropic contributions, and galectin-3C's backbone exhibits reduced entropy when bound [115].

Isothermal interactions involve entropy-entropy compensation in protein conformation, while enthalpy-entropy compensation is more prominent at higher temperatures [115], [129]. Vodyanoy et al. (2015) examined erythrocyte vesicle thermodynamics at higher temperatures [129][130][131]. At 37°C, red blood cells are oval and flexible, but at 52°C, they transform into crenated spheres with tiny spicules. Elevated temperatures cause

spontaneous vesiculation in some erythrocyte membranes, disrupting normal protein and lipid interactions [129]:[130][131]. Good (1967) demonstrated that vesiculation mechanisms in red blood cells are consistent across species and depend on the physical state of water within the cells and cell membranes [132]. Vodyanoy et al. (2015) analyzed vesicle loss kinetics in red blood cells during temperature increases due to physical exercise or exposure to external heat [133], [134]. Erythrocytes reduce volume and surface area through vesiculation, with the number of vesicles remaining constant under steady-state conditions [129]. Under these conditions, an equilibrium exists between vesicles generated by erythrocytes and vesicles destroyed by Kupffer cell mechanisms [135], [136].

The thermodynamic analysis of transformations in living cells is an important tool for the quantitative study of energy transductions that occur during these changes [129]. It allows the definition of the nature and function of the chemical processes underlying these transformations [137]. For two temperature points, T_1 and T_2 measured in Kelvin, the logarithmic form of the Arrhenius equation, $k = Ae^{\left(\frac{-E_a}{RT}\right)}$, yields the activation energy, E_a , which represents the thermal activation level of transitions from the intact vesicle at T_1 to the destroyed vesicle at T_2 within the context of first-order activation kinetics, as shown in equation (2-6) [129], [138].

$$\begin{aligned} \log A = \log k_1 + \frac{E_a}{2.303R} \times \frac{1}{T_1} &= \log k_2 + \frac{E_a}{2.303R} \times \frac{1}{T_2} \quad \therefore E_a \\ &= \frac{2.303T_1T_2 \log \frac{k_2}{k_1}}{T_2 - T_1} \end{aligned} \quad (2 - 6)$$

Where A represents the pre-exponential Arrhenius factor, k stands for the first-order rate constant of vesicle destruction process, and R denotes the universal gas constant. The value of k depends on the thermodynamic activation parameters of this transition state and can be represented by the Eyring equation, $k = \frac{k_b T}{h} e^{\left(-\frac{\Delta G}{RT}\right)} = \frac{k_b T}{h} e^{\left(\frac{\Delta S}{R}\right)} e^{\left(-\frac{\Delta H}{RT}\right)}$, where ΔG is the standard Gibbs free energy of activation, h is the Planck's constant, ΔS is the standard entropy of activation, ΔH is the standard enthalpy of activation, k_b is the Boltzmann constant, R is the gas constant, and T is the absolute temperature in Kelvin [139]. The authors, Vodyanoy et al. (2015), derived a linear relation between the logarithm of the Arrhenius frequency factor and the entropy of activation obtained from the Eyring equation for the transitional state, as shown in equation (2-7) [129].

$$\log A = \log \left(\frac{ekT}{h} \right) + \frac{\Delta S}{2.303R} \quad (2-7)$$

From equation (2-6) and (2-7), the entropy is derived as $\Delta S = 2.303R \left\{ \log A - \log \frac{k_b}{h} - \log(eT) \right\}$ and the enthalpy can be calculated as $\Delta H = E_a - RT$, and the Gibbs free energy can be calculated as $\Delta G = \Delta H - T\Delta S$.

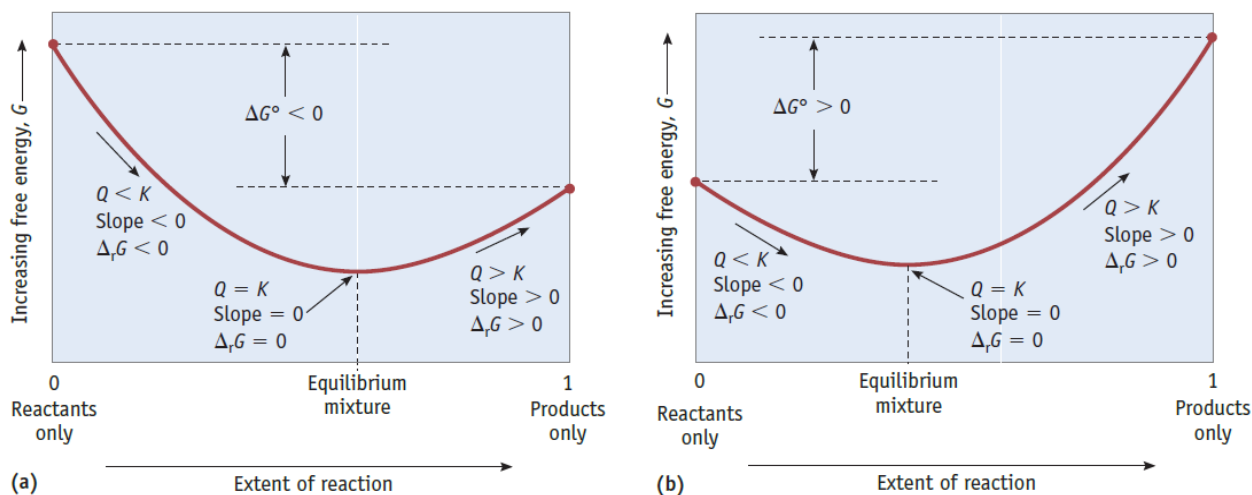
Elevated temperatures affect the release of potassium ions (K^+) and acetylcholinesterase (AcChE) from human erythrocytes, as well as methemoglobin formation during erythrocyte transformation and vesiculation [140]. At higher temperatures, erythrocyte vesiculation and hemolysis are endothermic, absorbing heat with positive enthalpy change ($\Delta H > 0$) [129]. However, entropy changes (ΔS) during these processes are negative ($\Delta S < 0$), typically associated with decreased molecule's rotational

and translational freedom [129]. This negative entropy ($\Delta S < 0$) often involves dehydration of aqueous solvent moieties and ion release, forming the interface between them [141]. The discocyte–echinocyte transition also has a negative entropy change due to increased cell membrane curvature [142]. The energy from entropy change, $T\Delta S$, correlates enthalpy change, ΔH , resulting in small Gibbs free energy, $\Delta G = \Delta H - T\Delta S$, compared to both ΔH and $T\Delta S$ [129]. This is thermodynamic phenomenon known as enthalpy–entropy compensation [143]–[146].

A chemical reaction is thermodynamically favorable when its enthalpy decreases and its entropy increases. The Gibbs free energy, $\Delta G = \Delta H - T\Delta S$, indicates that a reaction is thermodynamically favorable, unfavorable (where the reverse reaction is favorable), or at equilibrium when ΔG is negative, positive, or zero, respectively, as shown in Figure 2-1(a) and (b). As a reaction approaches equilibrium through forward or reverse progression, the concentrations of its species experience change. For both Figure 2-1(a) and (b), the equilibrium mixture points, as described by equation (2-1), can be represented by equation (2-8), where all the species' concentrations are at equilibrium.

$$A_{eq}B_{eq} + C_{eq}D_{eq} = A_{eq}C_{eq} + B_{eq}D_{eq} \quad (2 - 8)$$

At elevated temperatures, erythrocyte vesiculation and hemolysis processes are endothermic, with a positive change enthalpy ($\Delta H > 0$) and a negative change of entropy ($\Delta S < 0$). Consequently, the Gibbs free energy, $\Delta G = \Delta H - T\Delta S$, is positive ($\Delta G > 0$), making the protein-lipid interaction thermodynamically unfavorable [129].



$[\text{H}_3\text{O}^+]$ (M)	$[\text{OH}^-]$ (M)	pH	pOH	Sample Solution
10^1	10^{-15}	-1	15	
10^0 or 1	10^{-14}	0	14	1 M HCl
10^{-1}	10^{-13}	1	13	gastric juice
10^{-2}	10^{-12}	2	12	lime juice
10^{-3}	10^{-11}	3	11	1 M $\text{CH}_3\text{CO}_2\text{H}$ (vinegar)
10^{-4}	10^{-10}	4	10	stomach acid
10^{-5}	10^{-9}	5	9	wine
10^{-6}	10^{-8}	6	8	orange juice
10^{-7}	10^{-7}	7	7	coffee
10^{-8}	10^{-6}	8	6	rain water
10^{-9}	10^{-5}	9	5	pure water
10^{-10}	10^{-4}	10	4	blood
10^{-11}	10^{-3}	11	3	ocean water
10^{-12}	10^{-2}	12	2	baking soda
10^{-13}	10^{-1}	13	1	Milk of Magnesia
10^{-14}	10^0 or 1	14	0	household ammonia, NH_3
10^{-15}	10^1	15	-1	bleach
				1 M NaOH

acidic

neutral

basic

(c)

Fig. 2-1. Summary of the changes in Gibbs free energy, chemical equilibrium, and the equilibrium constant [147] for reactions that are (a) product-favored and (b) reactant-favored, when they are at equilibrium. Reproduced by permission. www.cengage.com/permissions, Copyright 2015, Copyright Holder Cengage Learning, <https://www.cengage.ca/>. (c) The pH and pOH scales indicate the concentrations of $[H_3O^+]$ and OH^- , respectively. The chart also shows the pH and pOH values of some common substances at standard temperature (25°C) [148]. Reproduced (Adapted) under the terms of the CC BY 4.0 license, <https://creativecommons.org/licenses/by/4.0>, Copyright 1999-2013, Copyright Holder OpenStax, <https://openstax.org/>.

In contrast, under isothermal conditions, protein-ligand interactions, involving enthalpy-entropy compensation, are thermodynamically favorable, because the Gibbs free energy, $\Delta G = \Delta H - T\Delta S$, is negative, while the change in enthalpy is negative ($\Delta H < 0$) and the change in entropy is positive ($\Delta S > 0$) [115].

2.2.4 Equilibrium Constant of Water Dissociation

Key chemical reactions include precipitation, acid-base, complexation, and oxidation-reduction (Redox) reactions. Water, as an amphoteric solvent, can act as a base and an acid by accepting and releasing protons, and it can also interact with itself, as demonstrated by equation (2-9).



The equilibrium constant of water, known as the dissociation constant of water, determines is acidic or basic state in acid-base reactions. It can be calculated from equations (2-7), (2-9), and (2-10) at 25°C [148].

$$K_w = [H_3O^+][OH^-] = 1.00 \times 10^{-14} \quad (2-10)$$

The value of K_w changes with temperature, such as 6.809×10^{-15} at 20°C, 1.469×10^{-14} at 30°C, and 1.008×10^{-14} at 25°C. All values are close enough to the value in equation (2-10) that it is used.

2.2.5 pH Scale

For pure water at room temperature, which is neutral (neither acidic nor basic), $[H_3O^+] = [OH^-]$. The hydrogen ion concentration, $[H^+]$, can be easily determined from the hydronium ion concentration, $[H_3O^+]$, as $K_w = [H_3O^+][H_3O^+] \Rightarrow [H_3O^+] = 1.00 \times 10^{-7}$, using equation (2-11) with equation (2-10). Additionally, the p-function of $[H_3O^+]$ or the pH of pure water at 25°C can be expressed as equation (2-11).

$$pH = -\log_{10}[H_3O^+] = 7.00 \quad (2-11)$$

The *pH* and *pOH* values of common substances, based on the concentrations of $[H_3O^+]$ and OH^- respectively, are shown in Fig. 2-1(c) at standard temperature (25°C). However, there is no pH for vegetable oil or alcohol because they are not in aqueous solution (solution containing water) at 25°C [149].

Wastewater pH is crucial for in-sewer biomarker stability [150]. Wastewater based epidemiology (WBE) estimates community chemical usage or exposure by analyzing

biomarkers in sewage [151], [152]. Li et al. (2021) used a first-order kinetics model to simulate biomarker degradation considering pH and other factors in sewers [150]. The first order model for biomarker transformation rates is given as the following equation (2-12) [153]–[157].

$$\ln \frac{C_t}{C_0} = -k_{total} \times t = -(k_{ww} + k_{bio}) \times t = -\left\{k_{ww} + \left(k'_{bio} \times \frac{A}{V}\right)\right\} \times t \quad (2-12)$$

Where C_t (µg/L) is the concentration of a biomarker at time t (h), and C_0 is the initial biomarker concentration at $t(0)$ in the reactor. k_{total} (1/h) represents the overall transformation rate of a biomarker in sewers, which consists of abiotic transformation (k_{ww} , 1/h) in the bulk wastewater and biodegradation (k_{bio} , 1/h) driven by biofilms. It is assumed that suspended solids have negligible biological activity compared to biofilms, and thus, k_{ww} is mainly determined by chemical hydrolysis in the bulk wastewater. Biodegradation is considered a surface process, which is correlated with $\frac{A}{V}$ in a sewer section, i.e., $k'_{bio} \times \frac{A}{V}$. Meanwhile, k'_{bio} (m/h) includes k'_{bioan} and k'_{bioa} , indicating the biodegradation under anaerobic and aerobic conditions, respectively. k_{ww} , k'_{bioan} and k'_{bioa} are estimated based on the experimental results obtained from the control reactor, rising main reactor, and gravity sewer reactor, respectively.

In summary, hydrolysis accelerates at higher pH levels, enhancing biomarker removal, while lower pH levels suppress both biodegradation and chemical hydrolysis [150]. The dominant effect of pH on in-sample and in-sewer biomarker stability has been observed. pH affects micropollutant removals in aquatic environments by altering physio-

chemical properties and biodegradation potential [158]–[163]. The dissociation of compounds (indicated by pKa) should also be considered, as protonation and deprotonation processes at different pH levels can affect abiotic transformation and biomarker stability [150].

2.3 Effects of Oxygen, and its radicals on Human Physiology

In electrochemical sensing, either sensor materials or biomarkers undergo oxidation. Oxygen-derived radicals and nonradical reactive species play major roles in biochemical reactions, cellular responses, and clinical outcomes [164]–[170]. Since oxygen's discovery, its importance and potential toxicity have been acknowledged. In 1969, the discovery of superoxide dismutase (SOD) in almost all aerobic cells highlighted the superoxide theory of oxygen toxicity, sparking research on aging, development, diseases, and cell signaling [171], [172]. These species are radicals due to their unpaired electrons, leading to high reactivity. Oxygen itself is a biradical, [164]–[170] but its reactivity is limited by spin restriction. Non-radical compounds also include various substances, some highly reactive despite not being radicals.

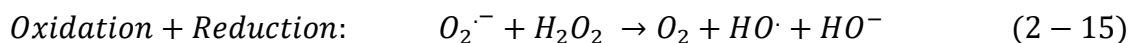
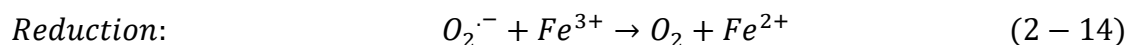
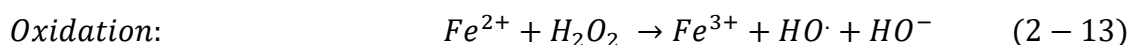
Chemically, oxidants or oxidizing agents accept electrons, while reductants or reducing agents donate electrons for each compound [170], [173]. Reduction involves electron gain, while oxidation involves electron loss [174]. When a reductant donates its electrons, it causes another substance to be reduced, and when an oxidant accepts electrons, it causes another substance to be oxidized [175]. Redox reactions, where reducing agents donate hydrogen or remove oxygen, form the basis for many biochemical pathways,

cellular chemistry, biosynthesis, and regulation [176]. Understanding these reactions is crucial for studying biological oxidation and radical/antioxidant effects.

In biological environments, reductants and oxidants are better termed as antioxidants and pro-oxidants, respectively [170], [175]. Pro-oxidants, including radicals and nonradicals, are called reactive oxygen species (ROS) that can cause damage to biological targets such as lipids, DNA, and proteins, as well as to the cell's defense systems, which are composed of enzymes and reducing equivalents or antioxidants [174].

2.3.1 Oxidation-Reduction (Redox) Reactions

The transition metals in the first row of the D block in the periodic table contain unpaired electrons and can participate as radicals, except for zinc. They can be converted into relatively stable oxidants [164]. The most abundant transition metals, such as copper and especially iron, are major players in the Fenton reaction, as shown in equation (2-13), and the metal-mediated Haber-Weiss reaction, as shown in equation (2-14) [177], [178].



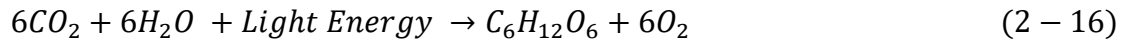
In 1894, Fenton described the oxidation of ferrous ions (Fe^{2+}) into ferric ions (Fe^{3+}), producing hydroxyl radicals ($HO\cdot$), in interaction with H_2O_2 , explaining oxidative damage in biological environments [178], [179]. Loosely bound or removable metals, like these metal ions, participate in redox processes, but metals with one oxidation state hidden in

proteins or storage complexes cannot [180], [181]. At physiological pH, most iron is oxidized to Fe^{3+} and bound to biological chelates, but some cases involve metals in a higher oxidation state [181], [182]. Reducing equivalents with suitable oxidation potential and the nature of iron-binding chelates can strongly affect the occurrence of the Fenton reaction in biological surroundings [183].

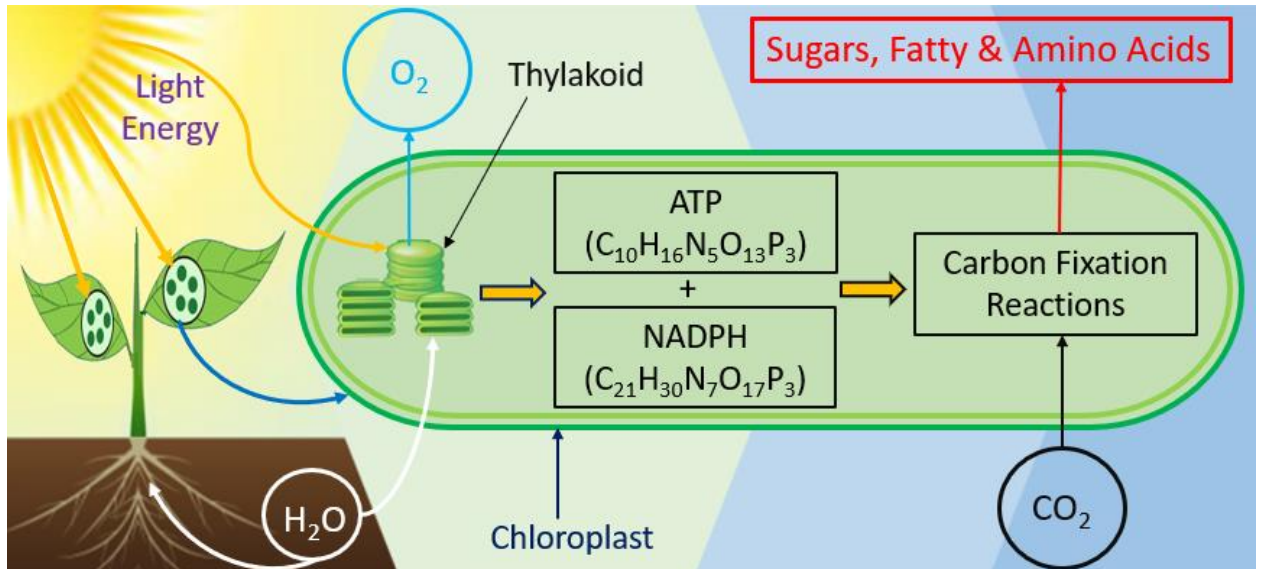
In contrast, the metal-mediated Haber-Weiss reaction, as shown in equation (2-14), involves the superoxide radicals, $\text{O}_2^{\cdot-}$, reducing ferric ions into ferrous ions. These ions are more soluble and enable the Fenton reaction, which is responsible for many of the deleterious effects of oxygen radicals [181], [182]. The combination of the Fenton and metal-mediated Haber-Weiss reaction is thermodynamically possible, representing the *in vivo* Haber-Weiss reaction but it is extremely slow [174].

2.3.2 Effects of Redox Reactions on Human Physiology

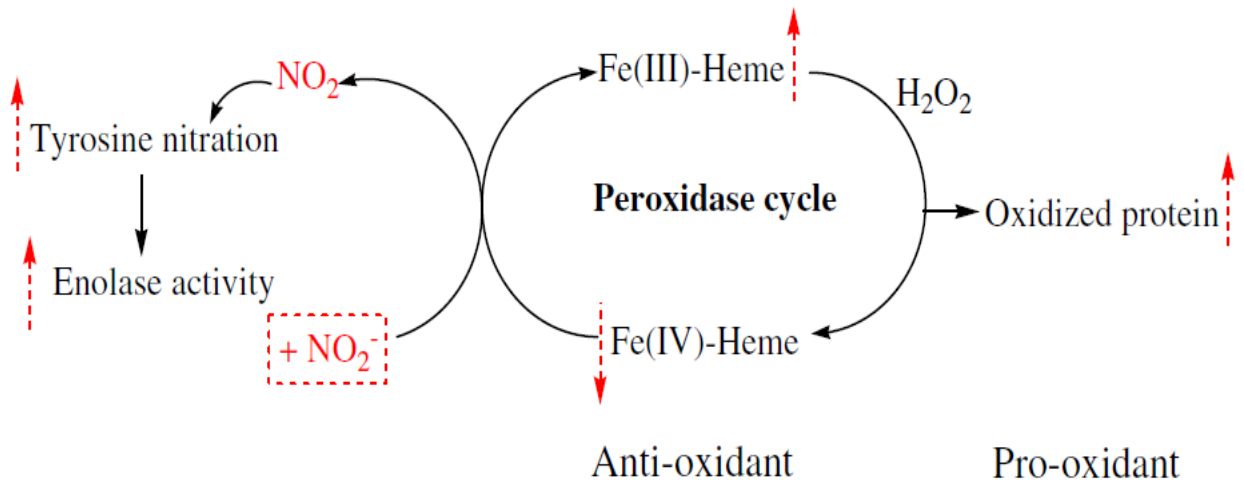
The human body derives energy from glucose, which is primarily stored in plants through the Calvin Cycle, a light-independent step shown in Fig. 2-2(a). This cycle uses ATP (Adenosine Triphosphate), NADPH (Nicotinamide Adenine Dinucleotide Phosphate), and CO_2 to produce carbohydrate molecules like glucose in the stroma. ATP and NADPH are essential energy-rich molecules generated during photosynthesis in plants, algae, and some bacteria. ATP acts as the primary energy currency for cellular processes, while NADPH serves as a coenzyme in anabolic reactions, providing electrons for biosynthesis pathways and maintaining redox balance. Both light-dependent and light-independent reactions can be summarized by equation (2-16), typically a redox reaction.



Within the plant cell, water is oxidized, losing electrons to oxygen, while carbon dioxide is reduced after gaining electrons, forming glucose.



(a)



(b)

Fig. 2-2. (a) Plants' photosynthesis process; generation of glucose and oxygen from sunlight, water, and carbon dioxide. (b) Dual effects of nitrite on hemoglobin-dependent redox reactions [184]. Reprinted with permission. Copyright 2014 Elsevier Inc.

2.3.3 Hemoglobin-dependent redox reactions

Heme proteins, such as myoglobin (Mb) and hemoglobin (Hb) have various biological functions, including oxygen storage, transport and reduction, electron transfer, and redox catalysis [185]. However, they can also induce oxidative damage and contribute to pathophysiology of certain disease states, such as vasospasm following subarachnoid hemorrhages and renal dysfunction following rhabdomyolysis [185]–[189]. These pathologies are associated with the heme group interacting with peroxides, which initiates oxidative reactions that include the formation of free radical species and hypervalent states of the heme iron that attack cellular components [188]–[192]. On the other hand, the free radical nitrite (NO_2^-), which originates from nitric oxide (NO) metabolism, is responsible for the endothelial dysfunction in humans and is correlated with an increased cardiovascular risk load [193], [194].

In the peroxidase cycle of hemoglobin-dependent redox reactions, as shown in Fig. 2-2 (b), H_2O_2 can oxidize ferric Mb/Hb (Fe^{3+}) to highly reactive ferryl Mb/Hb (Fe^{4+}), which can cause damage to biological molecules like Mb/Hb through a series of oxidative side reactions [188], [189][184]. Some antioxidants, such as NO_2^- at physiological pH, can act as reducing agents, preventing oxidation by removing ferryl Mb/Hb (Fe^{4+}) [184], [194]–[196]. However, at low concentrations, NO_2^- can promote a pro-oxidant effect on

Hb–H₂O₂-induced protein oxidation and reduce HepG2 cell viability [184]. In the reduction of ferryl Mb/Hb (Fe^{4+}) to ferric state (Fe^{3+}), NO_2^- is oxidized to a nitrating agent, NO₂. NO_2^- -triggered tyrosine nitration might make an important contribution to the reduction of enolase inactivation, revealing a potentially protective mechanism in hemoglobin-dependent redox reactions [184]. It is now clear that NO_2^- can act as both an antioxidant and a promising therapeutic agent to protect against myocardial ischemia-reperfusion injury through mediating NO homeostasis [195], [196].

2.3.4 Redox Environment in Human Serum Albumin (HSA) & Cells/Tissues

Serum is an oxidizing environment containing 17 disulfide bonds such as cystine, homocystine, cystamine, and glutathione disulfide (GSSG), as well as one unpaired cysteine (Cys₃₄) [197], [198]. The free cysteine (Cys₃₄) is the most abundant protein in plasma, at levels of 0.6 – 0.8 mM. In healthy subjects, it can be found as free in the reduced albumin (about 70% of HSA), HSA_{red}, or linked as a mixed disulfide with cysteine as a reversible oxidized form (about 25 – 30%), or in minor amounts with other natural thiols like cysteinylglycine, homocysteine, and glutathione (GSH) in the oxidized albumin, HSA_{ox}, or a tiny amount (about 3 – 4%) as an irreversible oxidized form, such as sulfinate and sulfonate [199]–[201]. Under pathologic conditions, such as kidney or liver diseases, the level of oxidized albumin increases up to 70%. High values are also possible in athletes after extreme exercise [202]–[208]. Thus, it is evident that the presence of 70–80% reduced Cys₃₄ in albumin coexists with 70–80% of oxidized low molecular mass thiols presented

as disulfides.[199] Hence, oxidized albumin is considered a short-term biomarker of oxidative stress [199].

Extracellular fluids like HSA are oxidizing environments, while reducing mediums are prevalent inside cells [199]. The movement of electrons from oxidizable organic molecules to oxygen (redox couple) provides the energy required to maintain the ordered state of a living organism, resulting in an overall reducing environment in cells and tissues [209]. Changes in the reducing/oxidizing environment or the redox environment affect the responsiveness of redox couples to electron flow, determining a cell's Redox environment [209]. Bücher introduced cellular redox biochemistry, which determines the states of various redox couples in cells and estimates the actual cellular reduction potentials (Ist-Potential) for the NAD^+/NADH and $\text{NADP}^+/\text{NADPH}$ couples [210]. According to Schafer and Buettner, the redox environment is the summation of the products of the reduction potential and reducing capacity of all the redox couples found in biological fluids, organelles, cells, or tissues, as shown in equation (2-17) [209].

$$\text{Redox Environment} = \sum_{i=1}^{n(\text{Couple})} E_i \times [\text{Reduced Species}]_i \quad (2 - 17)$$

where, E_i is the half-cell reduction potential for a given redox pair and $[\text{Reduced Species}]_i$ is the concentration of the reduced species in that redox pair.

A representative redox couple, such as the GSSG/2GSH couple, could be used as an indicator of changes in the redox environment since it is the most abundant redox couple in a cell, providing a large pool of reducing equivalents and serving as the cellular redox

buffer [209]. However, the ratio of interconvertible oxidized and reduced forms of a specific redox couple is not sufficient for all redox couples, such as GSSG/2GSH couple [209]. To have complete information about a redox couple, the redox state should include the reducing capacity (how large is the pool for the redox buffering system) of a redox couple along with the half-cell reduction potential. Schafer and Buettner proposed a notation for the redox state/status of a redox pair, such as GSSG/2GSH, which includes half-cell reduction potential, E_{hc} , of the reduced species, in this case GSH, with its concentration, [GSH], shown as follows.

$$\{E_{hc}(\text{GSH}); [\text{GSH}]\} = \{-180 \text{ mV}(\text{GSH}); 3.5 \text{ mM}\}$$

2.3.5 Thermodynamics of Biological Redox Reactions

The reduction potential, measured in voltage, can be determined using the Nernst equation developed by Walter H. Nernst in 1889. The reducing capacity, which is the total charge stored or the number of electrons available, can be estimated by determining the concentration of the reduced species in a redox couple [174]. The net transfer of charge, Q in coulombs, for a half-reaction in a redox reaction involving one mole of reactants, can be expressed as equation (2-18).

$$\begin{aligned} Q &= nF; \text{ where, } n = \text{mole of } e^-, F = \text{Faraday's constant} \\ &= 96485 \text{ C/mol of } e^- \end{aligned} \quad (2-18)$$

Thus, the change in Gibbs free energy, ΔG in kJ/mole, to move the charge, Q , over a potential change, ΔE , is given by equation (2-19).

$$\Delta G = -Q(\Delta E) = -nF(\Delta E); \quad (2-19)$$

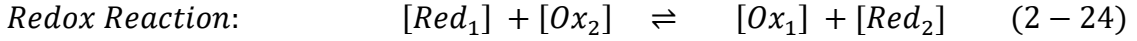
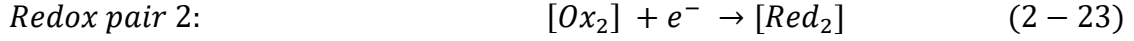
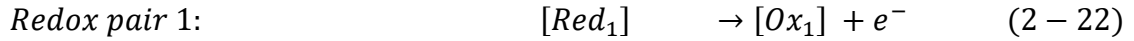
where "-" denotes the favorable direction of a reaction, as shown in Fig. 2-1(a) and (b). According to equation (2-19), a reaction is thermodynamically favored when ΔG is negative, whereas a redox reaction is favored when E is positive. The Nernst equation, which measures an electrode's potential at 25°C, can be deduced as equation (2-20) using equations (2-5) and (2-19).

$$\begin{aligned} -nF(\Delta E) &= -nF(\Delta E^o) + RT \log_e Q_r \\ \Rightarrow \Delta E &= \Delta E^o - \frac{RT}{nF} \log_e Q_r = \Delta E^o - \frac{59.16 \text{ mV}}{n} \log_{10} Q_r \end{aligned} \quad (2-20)$$

The term ΔE^o , which represents the electromotive force under standard conditions, is the difference in the standard reduction potentials of the two half-cells involved in the process. The superscript "°" implies the thermodynamic standard-state conditions. At thermodynamic equilibrium, $\Delta G = 0$, and consequently, $\Delta E = 0$. Equation (2-21) can be derived from equation (2-20) under these conditions.

$$\Delta E^o = \frac{RT}{nF} \log_e K_d = \frac{59.16 \text{ mV}}{n} \log_{10} K_d \quad (2-21)$$

However, equation (2-21) can be applied in biological sites, such as cells, where the system is reversible and all factors affecting the system are known and can be controlled [175], [176], [211]. Cells are not in thermodynamic equilibrium because, within them $\Delta E \neq 0$ and the systems are not fully reversible [174], [209]. Therefore, the Nernst equation can be applied for the biological systems described in the set of equations (2-22), (2-23), and (2-24) as demonstrated in equation (2-25).



$$\therefore \Delta E = E_2 - E_1$$

$$= \left(E_2^o - \frac{59.16 \text{ mV}}{n} \log_{10} \frac{[Red_2]}{[Ox_2]} \right) - \left(E_1^o - \frac{59.16 \text{ mV}}{n} \log_{10} \frac{[Red_1]}{[Ox_1]} \right) \quad (2-25)$$

Where E_2 is the half-cell reduction potential of the electrode associated with the redox pair that is reduced, E_{Red} . Furthermore, E_1 , is the half-cell reduction potential of the electrode associated with the redox pair that is oxidized, E_{Ox} . Consequently, the voltage, ΔE , is the overall potential difference of an electrochemical cell.

2.3.6 Estimation of Total Reducing Power in Biological Sites

Reducing power, unlike redox potential, is not a thermodynamic parameter, but it plays a significant role in conveying information about the overall capability of a cell, biological fluid, or tissue to donate electrons and the concentration of reducing equivalents responsible for this ability [174]. Among many compounds, the major contributors to the reducing power of a resting cell are the low-molecular-weight antioxidants (LMWA), which can be measured to determine the reducing power in cellular and biological environments [174]. Hence, estimating the reducing power may indicate the total LMWA status of a biological system.

There are indirect and direct methods to estimate total LMWA activity [212]. Indirect methods measure consequential factors of redox capacity, such as oxidation products

formed or concentrations of major redox couples in the biological environment, using fluorescent or spectrophotometric techniques, or inhibition methods that involve adding a radical species to the sample. Direct methods, both chemical and electrochemical, utilize an electrode and an external probe to measure the current, which is proportional to the concentrations of the LMWA [174]. Chemical methods are primarily colorimetric techniques that measure a redox-active couple whose reduced and oxidized states have different physical properties, such the ferric-reducing antioxidant power (FRAP) assay, which is based on the reaction of the ferric/ferrous redox couple with antioxidants in the sample and results in the creation of a blue color [212].

Chapter 3

Evaluation of Electrochemical Sensing Techniques for Health

Applications

This chapter is part of our work published as ‘M Maksud Alam, Victor Mitea, Matiar M. R. Howlader, Ravi P. Selvaganapathy, and M. Jamal Deen, “Analyzing Electrochemical Sensing Fundamentals for Health Applications.” *Advanced Sensor Research* (November 2023), DOI: 10.1002/adsr.202300100.’

3.1 Background

Electrochemical techniques, including voltammetry, are essential and popular measurement methods for various modern cutting-edge research fields in biological sites, such as cells, fluids, and tissues. [213]. Voltammetry is applicable for both lipophilic and hydrophilic antioxidants in biological fluids and tissue homogenates, offering several advantages [174]. It can be used without sophisticated extraction and treatment to obtain the reducing-power profile, which provides information about the type and concentration of LMWA [214]. This methodology for quantifying overall LMWA has been used in various clinical situations and pathological disorders, including diabetes [215]–[217], ulcerative colitis [218], brain degenerative diseases and head trauma [219], [220], skin status and pathologies [219]–[222], and irradiation therapy [214], as well as in the study of the aging process [219], [220], and stages of embryonic development [215], [223]. Biological fluids, such as seminal fluid, cerebrospinal fluid, saliva, sweat, urine, plasma, and gastric juice, possess reducing power derived from their LMWA content [224],

Electrochemical techniques provide necessary knowledge concerning the thermodynamic, kinetic, and analytical features of the tested compounds. We have discussed different electrochemical measuring methods to evaluate the promising aspects, challenges, and prospects of applying them in a biological sample.

3.2 Electrochemical Techniques and Fundamentals

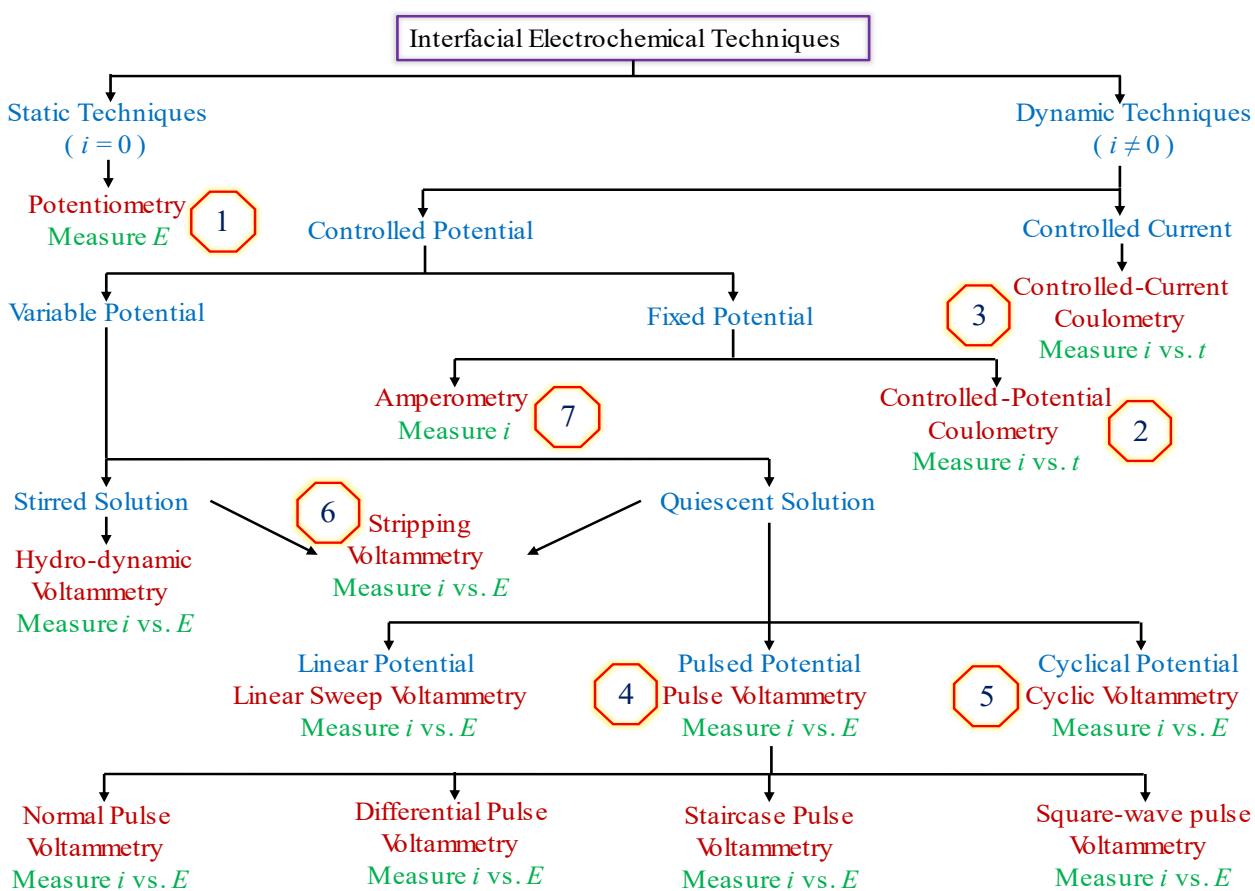


Fig. 3-1. A family tree of several interfacial electrochemical techniques is shown. The specific techniques are in red, the experimental conditions are in blue, the analytical signals are in green, and the red-yellowish octagons show the chronological presentation of the techniques.

Interfacial electrochemical sensing techniques are a broad field that can be classified based on specific techniques, experimental conditions, and output signals, as shown in Fig. 3-1. In this section, we will provide an overview of the sensing performance metrics for each type of sensor by giving some exemplary examples used for detecting neurotransmitters, proteins, and glucose from biofluids for diseases, particularly Schizophrenia, Alzheimer's, and Parkinson's.

3.2.1 Potentiometric Methods

Potentiometric sensors are suitable for determining concentrations higher than 10^{-5} M, which is the range required in most cases. For example, the normal blood glucose level in a human body is between 4.9 and 6.9 mM. Potentiometry is compatible with multichannel array type sensory instruments and requires a simple operating circuit. Thus, non-enzymatic potentiometric glucose sensors are attractive for integration with conventional ion-selective electrodes, such as pH meters. However, selectivity is a key issue for these sensors. Only a few attempts have been made to create a non-enzymatic potentiometric glucose sensor, as reported by Shoji and Freund [225]–[226]. They used polymeric membranes with boronic acid units, which have an affinity for diol saccharides containing two units. The sensor responded to glucose but showed even higher sensitivity to fructose than to glucose [227].

The cell potential is measured under static conditions with little or no current flowing through the electrolyte, so the compositions remain constant and are suitable for quantifying the analyte. In 1889, the first quantitative potentiometric method was invented

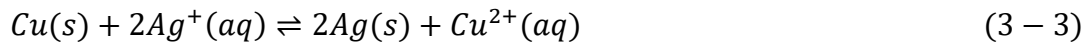
based on the Nernst equation, which relates a cell's potential to the concentration of electroactive species in it [48]. A potentiometer, shown in Fig. 3-2 (a), is used to determine the potential. The species are oxidized at the anode and reduced at the cathode electrode. When the switch, T is open, the potential across R_{cb} can be determined by equation (3-1).

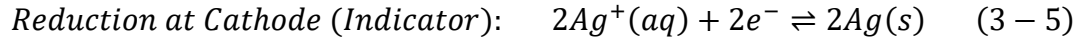
$$\begin{aligned} E_{cb} &= \frac{R_{cb}}{R_{ac} + R_{cb}} \times E_{PS} = \frac{R_{cb}}{R_{ab}} \times E_{PS} = \frac{E_{PS}}{R_{ab}} \times R_{cb} \\ &= i_{ab} \times R_{cb}; \quad E_{PS} \text{ is supply voltage} \end{aligned} \quad (3-1)$$

When T is closed, the potential across the cell, E_{cell} , can be calculated using equation (3-2) if the current through the cell, $i_{cell} = i$, is zero. Usually, the potential depends on the current flowing through the cell.

$$E_{cell} = E_{cb} = \frac{R_{cb}}{R_{ab}} \times E_{PS} = \frac{E_{PS}}{R_{ab}} \times R_{cb} = i_{ab} \times R_{cb} \quad (3-2)$$

The switch T is briefly closed, and the current through the ammeter, which is in the nanoscale, is observed. The slide wire variable resistor is readjusted until the ammeter current is zero to obtain the cell potential. There are two half-cells, shown in Fig. 3-2 (b), each containing an electrode immersed in a solution of ions whose activities determine the electrode's potential. A salt bridge containing an inert electrolyte, such as NaNO_3 , is used to complete the electron flow path. Porous plugs are used to allow ions to freely move through the bridge. The overall cell reaction and half-reactions of the half-cell reactions are given below.



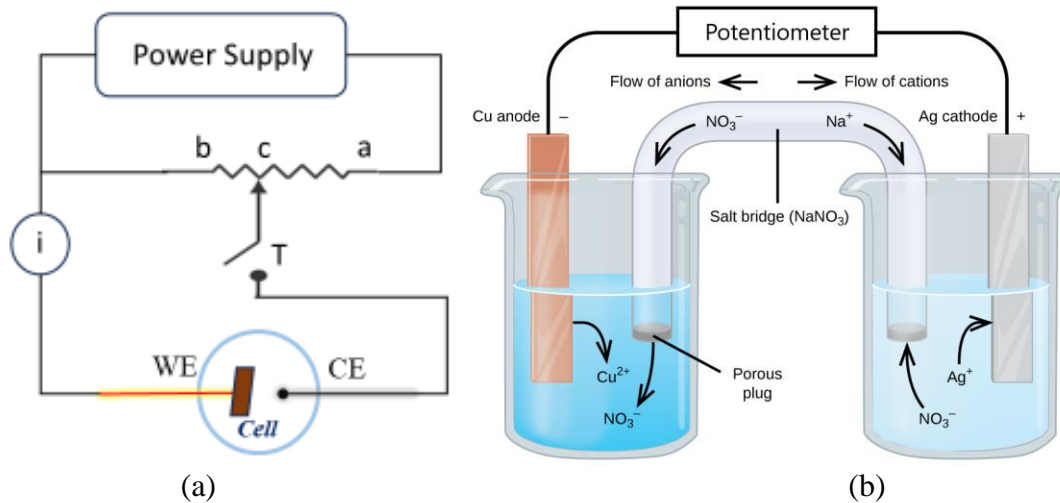


The cell potential can be calculated by combining equations (2-21), (3-4), (3-5), and (3-6).

If both electrodes were placed in the same solution, the reduction of Ag^+ to Ag would occur on the Cu surface and no electrons would pass through the potentiometer. Equation (3-7) is used to deduce the potentiometric electrochemical cell potential, and equation (3-8) can be used to determine any unknown value among E_{cell} , a_{Ag^+} , and $a_{Cu^{2+}}$ if other two are known. and $a_{Cu^{2+}}$, can be determined if other two are known.

$$\begin{aligned} E_{cell} &= E_{Red} - E_{Ox} = E_{cathode} - E_{anode} \\ &= \left(E^o - \frac{RT}{nF} \log_e Q_r \right)_{Red} - \left(E^o - \frac{RT}{nF} \log_e Q_r \right)_{Ox} \end{aligned} \quad (3-6)$$

$$\begin{aligned} E_{cell} &= \left(E_{Ag^+/Ag}^o - \frac{0.05916}{1} \log_{10} \frac{1}{a_{Ag^+}} \right)_{Red} \\ &\quad - \left(E_{Cu^{2+}/Cu}^o - \frac{0.05916}{2} \log_{10} \frac{1}{a_{Cu^{2+}}} \right)_{Ox} \end{aligned} \quad (3-7)$$



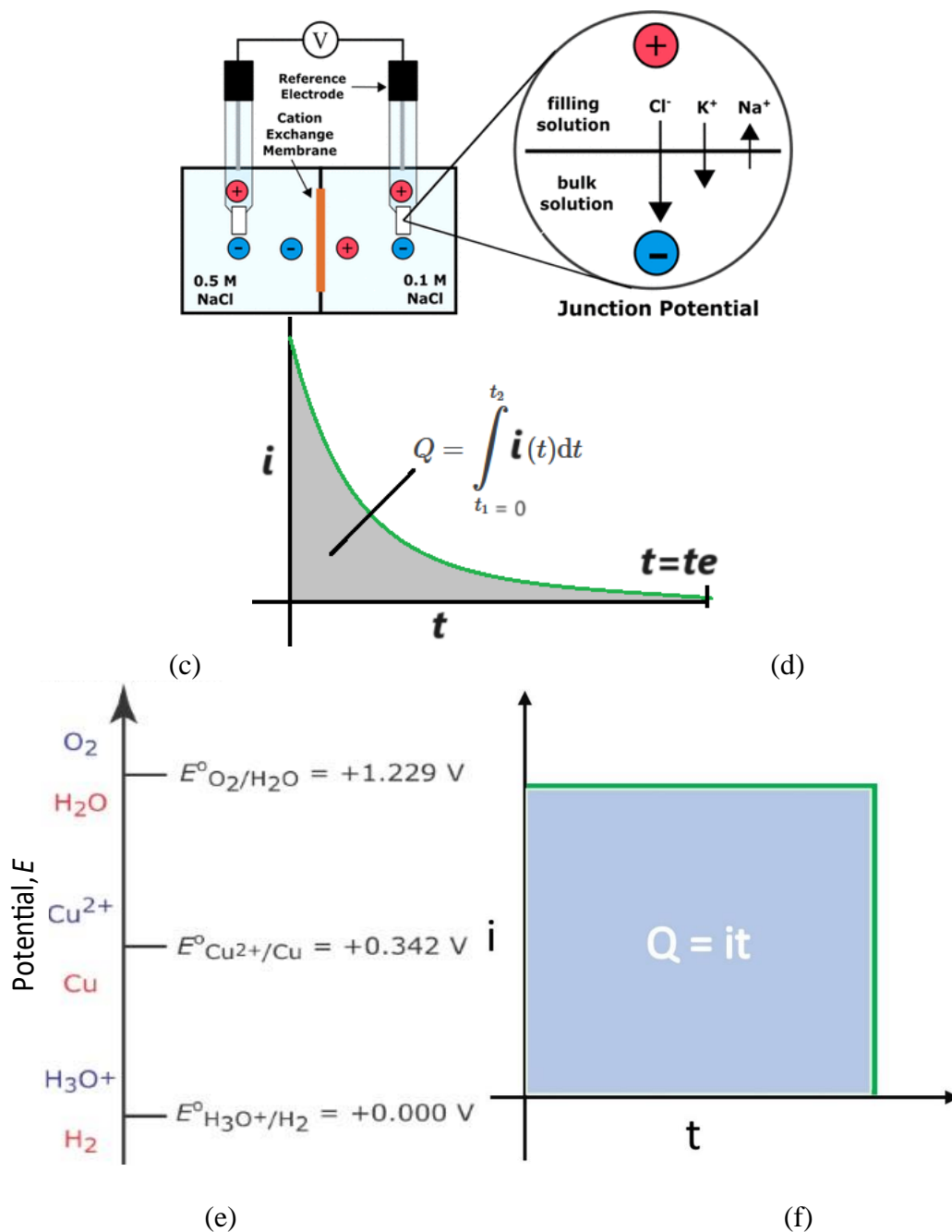


Fig. 3 – 2. (a) A manual potentiometer with two electrodes (counter electrode and working electrode) is shown schematically. The tapping switch T and the slide-wire variable resistor SW are also indicated. (b) A potentiometric electrochemical cell is depicted. Reproduced (Adapted) under the terms of the CC BY 4.0 license,

<https://creativecommons.org/licenses/by/4.0>. [148] Copyright 1999-2013, Copyright Holder OpenStax, <https://openstax.org/>. (c) A junction potential between two ionic solutions with different concentrations (0.5 M NaCl and 0.1 M NaCl) is shown. Reprinted (adapted) with permission. [228] Copyright 2018 American Chemical Society. (d) The waveforms of the applied potential and resulting current of a controlled-potential coulometry are shown. (e) The reduction steps of different species present in an aqueous solution of Cu^{2+} are shown in a ladder diagram. The oxidized species are in blue, and the other species are in red. Reproduced (Adapted) with permission. [229] Copyright 1999-2023, Copyright Holder David Harvey (<https://sites.google.com/depauw.edu/dth/home>), and Libretexts (<https://LibreTexts.org>). (f) A measured current vs. time curve for a controlled-current coulometry is shown, with the blue area representing the total charge.

Disadvantages of Potentiometric Methods

The standard state potentials of equation (3-7) depend on temperature and the medium, as different activities of the same redox couple can vary in different media. For example, the potential for the $\text{Fe}^{3+}/\text{Fe}^{2+}$ redox couple is +0.735 V in 1 M HClO_4 , +0.70 V in 1 M HCl , and +0.53 V in 10 M HCl [48]. The issue can be addressed by using a matrix-dependent formal potential.

$$E_{\text{cell}} = E_{\text{cathode}} - E_{\text{anode}} + E_j \quad (3 - 8)$$

Additionally, the junction potential, caused by concentration differences at the interface or bridge between solutions, is a major challenge. A junction potential arises at the interface between two ionic solutions, as shown in Fig. 3-2 (c) if there is a difference in the

concentration and mobility of the ions. For example, H^+ has higher mobility than Cl^- . This potential at 0.5 M and 0.1 M NaCl are 10.2 and 18.1 mV, respectively [228]. This potential can be as large as 30-40 mV [48]. To address this issue, a salt with equal cation and anion mobilities, such as KCl, is used with a saturated concentration. However, the junction potential cannot be eliminated, so the cell equation (3-7) must be rewritten as equation (3-8).

Table 3-1: Potentiometric Sensors for Health Monitoring Applications

Type	Electrode Materials	Disease	Bio-Analyte	Normal Range [Physiological]	Linear Range	LOD	Sensitivity	Ref.
Neurotransmitter	Oxatub [7]arenes as ionophores	Schizophrenia, Alzheimer, & Parkinson	ACh	0.2 – 1.31 uM [230]	–	0.1 uM	57.2 mV/dec	[8]
	PANI-MIP/MWCNT	Alzheimer	ACh	0.2 – 1.31 uM	11.6 – 34.9 uM	34.5 uM	83.86 mV/dec	[7]
	PAH/SiO ₂ -Np-AChE	Alzheimer	ACh	0.2 – 1.31 uM	0.2 – 1.0 nM	30 uM	7.7 mV/mM	[231]
	SWCNT-TF	Alzheimer	ACh	0.2 – 1.31 uM	0.01 – 100 mM	10 uM	19 mV/dec	[232]
	DASM/PEDOT/PSS	Parkinson, & schizophrenia	DA	50×10^{-9} M [233]	$10^{-5} - 10^{-1} M$	5.8 uM	53.85 mV/dec	[9]
Protein	Anti-CRP/ZnO NTs/Au coated Glass	Acute Inflammation	CRP	<5 mg/L	0.01 – 1.0 mg/L	1 ng/L	13.17 mV/dec	[11]
	Polydopamine	Pancreatic pathology	Trypsin	--	0.08 – 4.0 U/mL	30 mU/mL	--	[234]
	Alkanethiol-SAM/Au coated Si	Cancer	CEA	<2.5 ng/mL	2.5 – 75.0 ng/mL	--	--	[235]
	C-PVC/PIM/GO	Prostate cancer	PSA	<10 ng/mL	0.2 – 12.5 ng/mL	2 ng/mL	-44.2 mV/dec	[20]
Glucose	Poly Aniline	Diabetes	Glucose	4.90-6.90 mM	4.0 – 15 mM	--	--	[225]
	Poly Aniline Boronic Acid	Diabetes	Glucose	4.90-6.90 mM	6.0 – 18 mM	--	--	[226]
	GOx-functionalized ZnO nanowires as MOSFET gate	Diabetes	Glucose	4.90-6.90 mM	1.0 – 100 uM	--	--	[236]
	GOx/SiO ₂ /Al ₂ O ₃ film on n-type Si substrate (LAPS)	Diabetes	Glucose	4.90-6.90 mM	0 – 4 mM	-	--	[237]
	GOx-functionalized SiO ₂ as ENFET gate	Diabetes	Glucose	4.90-6.90 mM	0.05 – 1.8 mM	25 µM	--	[238]
	GOx/Si-SiO ₂ -Si Structure ISFET	Diabètes	Glucose	2.78–5.55 mM [Urine][60]	0.8 – 6.70 mM	--	20 mV/dec	[239]

Useful Acronym: Acetylcholine (**ACh**); Decade (**dec**); Polyaniline (**PANI**); Molecular imprinted polymer (**MIP**); Multiwalled carbon nanotubes (**MWCNTs**); Poly(allylamine) hydrochloride (**PAH**); Silicon dioxide nanoparticles (**SiO₂-Np**); Single-walled carbon

nanotube thin-film (**SWCNT-TF**); Dopamine selective membrane (**DASM**); Polymer poly (3,4- ethylenedioxythiophene) (**PEDOT**); Poly (styrenesulfonate) (**PSS**); C-reactive protein (**CRP**); Carcinoembryonic antigen (**CEA**); Protein Imprinted Materials with charged PVC binding sites (**C-PVC/PIM**); Prostate specific antigen (**PSA**); Self-assembled monolayers (**SAMs**); Graphene oxide (**GO**); Glucose oxidase (**GOx**); Light-addressable potentiometric sensors (**LAPS**); Enzyme field-effect transistors (**ENFETs**); ion-sensitive field-effect transistor (**ISFET**).

First, we will focus on neurotransmitters as summarized in Table 3-1. Acetylcholine, a neurotransmitter, regulates muscle contraction in the peripheral nervous system (PNS) through acetylcholine receptors (AChR). It also plays a key role in central nervous system (CNS) activities such as behavior, arousal, attention, learning, and memory. It is synthesized from choline by choline acetyltransferase and acetyl coenzyme A in neurons [7]. Imbalanced ACh regulation in the brain can cause neuropsychiatric disorders such as schizophrenia, Alzheimer's, Parkinson's, and myasthenia gravis [7][8]. Potentiometric enzyme-based detection of ACh has been presented in several literature sources [7], [8][231][232] but the electrode represented in [231] is better fit with the physiological range but has a high limit of detection (LOD), making it less suitable. The potentiometric ACh sensors listed in Table 3-1 do not meet the requirements.

Dopamine (DA) is another neurotransmitter that conveys messages of pleasure in the brain's reward system. Imbalanced levels of dopamine are linked to various diseases, including Schizophrenia, Parkinson's, restless legs syndrome, and attention deficit hyperactivity disorder. In 2021, He et al. developed a DA enzyme electrode with a linear range of 0.1 μM to 0.1 M, although the physiological range of dopamine is only 50 nM.

For protein sensors, we will provide a few examples, including C-reactive protein (CRP), trypsin, CEA, and PSA, due to their roles in inflammation and metastasis. The

electrochemical potentiometric technique is primarily used for enzymatic detection of important proteins in the human body, such as CRP, trypsin, CEA, and PSA, as shown in Table 3-1. CRP, a protein made in the liver, is found in blood plasma and increases in response to an offending agent, activating the first immune responders. In a healthy human, CRP levels are less than 5 mg/L [11]. However, surgery, trauma, exercise, heatstroke, and childbirth can result in a drastic increase in CRP, ranging from 1 to 500 mg/L. Higher CRP values can indicate cardiovascular diseases, pathogenic diseases, IBD, and colon cancer [11]. An enzymatic anti-CRP layer was immobilized on ZnO nanotubes grown on Au-coated glass to sense CRP. The electrode showed the best response at pH 7, where the optimum pH of the antibody is 7.2. The poor response at pH levels below and above 7 might be due to less activity and detachment of the immobilized antibody [11]. The electrode had the maximum response at 55°C, but the responses decreased at temperatures below or above 55°C due to less charge mobility and denaturation of the immobilized antibody. However, the electrode's linear range of 0.01 to 1.0 mg/L doesn't cover the required range of 1 to 5 mg/L.

Trypsin is produced as the inactive zymogen trypsinogen in the pancreas and is activated in the small intestine to break down long chains of proteins into smaller, more easily digestible pieces. A potentiometric polymeric membrane, made using MIP on ISE, is fabricated to sense trypsin in an enzymatic, label-free manner [234].

CEA is a large glycoprotein that is typically produced in gastrointestinal tissue and is absent or present in low amounts (less than 2.5 µg/L in non-smokers, less than 5.0 µg/L in smokers) in the blood of healthy adults. The level of CEA in the blood may be elevated

in certain types of cancer, such as colon and rectal, breast, lung, pancreatic, stomach, liver, and ovarian cancer, and in non-cancerous conditions like cirrhosis, hepatitis, diverticulitis, inflammatory bowel disease, peptic ulcer disease, chronic obstructive pulmonary disease, cholecystitis, and obstructed bile duct. The CEA test is crucial for the diagnosis of colorectal cancer, as well as for monitoring its response to treatment and the risk of reoccurrence. A CEA-sensing enzymatic layer of hydroxyl-terminated alkanethiol was created in reference [235]. The thiol molecules of the hydroxyl-terminated alkanethiol layer are chemically bonded to a substrate of a gold-coated silicon chip, and template biomolecules are co-adsorbed and later removed to create footprint cavities. The potential changes upon re-adsorption of the CEA biomolecules are measured potentiometrically [235].

PSA is a glycoprotein secreted by the prostate gland and is found in low amounts (less than 4 $\mu\text{g/L}$) in the blood [20]. Elevated levels (greater than 10 $\mu\text{g/L}$) of PSA in the blood can be caused by prostate cancer as well as non-cancerous conditions such as prostatitis (inflammation of the prostate) and benign prostatic hyperplasia (enlargement of the prostate) [20]. An enzymatic biosensor with a negative slope of sensitivity, good linear range, and low detection limit has been developed for PSA [20].

Potentiometric sensors have been used to detect blood glucose, which is the main source of energy for the human body and is produced from food through digestion. The pancreas produces insulin to help the body convert glucose in the bloodstream into energy. However, uncontrolled blood sugar levels due to ineffective insulin use or deficiency can cause diabetes, which can lead to blindness, kidney failure, heart attack, stroke, and serious

damage to nerves and blood vessels. Non-enzymatic electrodes made of polyaniline or polyaniline boronic acid could be used for glucose sensing in human blood, but the authors were not given information about their limits of detection or sensitivities [225][226]. Other potentiometric glucose sensors use the glucose oxidase (GOx) enzyme, as shown in Table 3-1. As shown in Table 3-1, it's evident that GOx is not an effective enzyme for detecting glucose in blood because its linear range deviates from the desired range of 4.90-6.90 mM [236][237][238]. However, the linear range of GOx is not suitable for detecting glucose in blood, but it is effective for glucose sensing in urine [239].

3.2.2 Coulometric Methods

In dynamic methods such as coulometry, current is passed to alter the concentration of species. Coulometry involves complete oxidation or reduction of the analyte at the electrode. The equation (2-17) can be represented as equation (3-9) by substituting N_A for the moles of the analyte in the cell. To calculate N_A , complete electrolysis must be performed, and 100% current efficiency is required to calculate the charge,

$$Q = nFN_A \quad (3 - 9)$$

Coulometry can be further divided into controlled-potential and controlled-current methods.

Controlled potential (chrono) coulometry

A step potential is applied across the cell. As a result, the current, as shown in Fig. 3-2(d), decreases with time as the concentration of the analyte decreases due to oxidation-

reduction reactions. The total charge can be found using equation (3-10). The method is accurate if no potential-dependent redox reaction is associated, assuming 100% current efficiency.

$$Q = nFN_A = \int_0^{t_e} i(t)dt; \quad \text{where, } i \text{ is variable} \quad (3-10)$$

To select an appropriate potential value, a case study using a platinum working electrode to reduce Cu^{2+} as Cu is explained below. The favorable potential is close to 0.342 V, as seen in Fig. 3-2 (d), but must be greater than 0 V to avoid current from water. The potential required to reduce 99.99% of Cu^{2+} can be calculated using equation (3-13) if the initial concentration of Cu^{2+} is known. A small volume, high surface area, and high stirring rate are suggested to reduce the time needed for the reduction process [48].



$$E = E_{\text{Cu}^{2+}/\text{Cu}}^0 - \frac{0.05916}{2} \log_e \frac{1}{[\text{Cu}^{2+}]} \quad (3-12)$$

$$E = E_{\text{Cu}^{2+}/\text{Cu}}^0 - \frac{0.05916}{2} \log_e \frac{1}{0.0001 \times [\text{Cu}^{2+}]} \quad (3-13)$$

Controlled-Current Coulometry

The excitation (red) and charge (blue) are shown in Fig. 3-2 (f). The method requires less time for both electrolysis (10 minutes) and processing, and has a rate constant, as shown in equation (3-14). However, there are two drawbacks, the current decreases with time due to the rate reactions.

$$Q = nFN_A = it_e; \quad \text{where, } i \text{ is constant} \quad (3 - 14)$$

Another one, the current efficiency may be reduced while regulating the potential to keep the current constant. To ensure 100% current efficiency, a mediator is needed. Additionally, the determination of the end point is another challenge of the method where titrimetry is required.

Table 3-2: Coulometry Sensors for Health Monitoring Applications

Type	Electrode Materials	Disease	Bio-Analyte	Normal Range [Physiological]	Linear Range	LOD	Sensitivity	Ref.
Protein	GOx/Au/Pt-Ag Co-metallization	Testicular/Ovarian/Liver Cancer	AFP	10 – 20 ng/ml	--	0.4 ng/mL		[240]

Useful Acronym: Gold (**Au**); Platinum (**Pt**); Silver (**Ag**), Alpha-1-fetoprotein (**AFP**).

There are limited reports on coulometric sensors for health monitoring. An enzymatic approach to detect alpha-1-fetoprotein (AFP) using H_2O_2 and a sensing layer of glucose oxidase (GOx) was published in [240]. AFP is normally produced by a fetus's liver and yolk sac and decreases significantly within a year after birth. AFP is not generally found (0 ng/mL to 20 ng/mL) in healthy adults. Higher values (>20 ng/mL) show the possibility of testicular and ovarian cancer. Adults with cirrhosis and chronic hepatitis also possess higher levels of AFP in their blood. AFP levels of >400 ng/mL may indicate liver cancer. Moreover, a higher value of AFP could be a sign of the rare genetic condition ataxia-telangiectasia. In this coulometric sensor, the sensing performance of the device was enhanced by metallizing the electrode and adding microfabricated solution processing channels. After incubation for 120 min, a detection limit of 0.4 ng/mL was achieved.

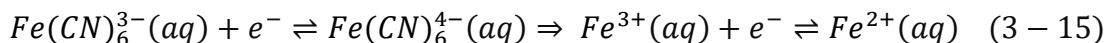
However, the main drawback of this approach, as it is based on coulometric sensing, is the time required to obtain the result.

3.2.3 Voltammetry

In 1959, Jaroslav Heyrovsky won the Nobel Prize in Chemistry for inventing the first voltametric method in the early 1920s, commonly known as polarography. Voltammetry measures current as a function of a time-dependent applied potential, which is displayed as a voltammogram. The voltammogram provides information on the quantitative and qualitative characteristics of the analyte in a sample [241]. The faradaic current in a potentiostat arises from the faradaic process, which requires the transfer of electronic charge and involves atoms, ions, or molecules from or to the bulk solution [242]. Besides the faradaic current from the analyte, other types of currents may exist in the cell, such as background currents from electrolysis of impurities, the electrolyte, the electrode material, and capacitive (charging) current. The latter is the only non-faradaic current and depends on the interface that acts as an electrical capacitor under applied voltage.

Factors Affecting Voltammogram

The reduction potential of ferricyanide, $Fe(CN)_6^{3-}$ as (Fe^{3+}) , to ferrocyanide, $Fe(CN)_6^{4-}$ as (Fe^{2+}) is shown in equations (3-15) and (3-16) and the associate ladder diagram in Fig. 3-3 (a). In this representation, $x=0$ refers to the surface of the working electrode.



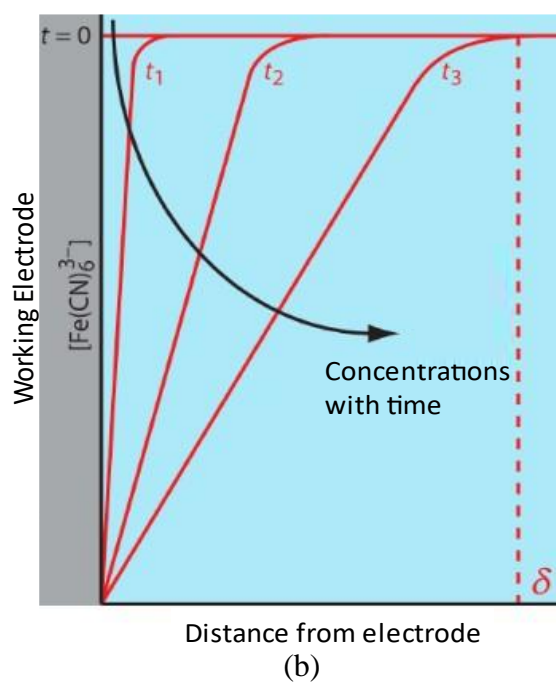
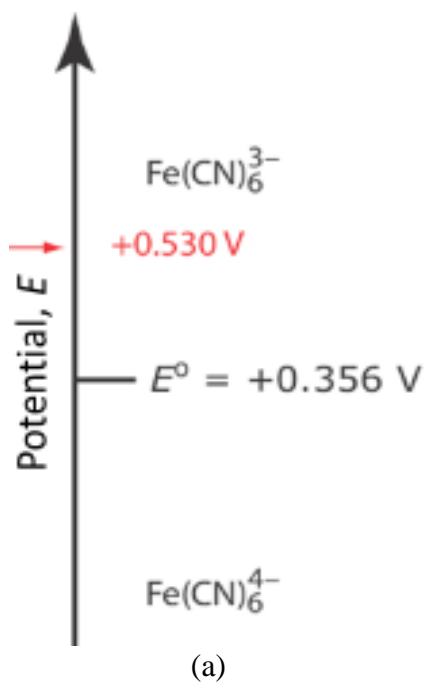
$$\begin{aligned}
 E &= 0.356 \text{ V} - 0.05916 \log_e \frac{[Fe(CN)_6^{4-}]_{x=0}}{[Fe(CN)_6^{3-}]_{x=0}} \\
 &= 0.356 \text{ V} - 0.05916 \log_e \frac{[Fe^{2+}]_{x=0}}{[Fe^{3+}]_{x=0}} \quad (3-16)
 \end{aligned}$$

$$[Fe(CN)_6^{3-}]_{x=0} = [Fe(CN)_6^{4-}]_{x=0} = 0.5 \text{ mM} \quad (3-17)$$

The electrode surface concentration is used since an equilibrium position is established at the surface. If the initial concentrations of $Fe(CN)_6^{3-}$ and $Fe(CN)_6^{4-}$ are 1.0 mM and 0 mM, respectively, the concentrations will not change if a potential of +0.530 V is applied to the working electrode. Hence, there will be no faradaic current flow through the cell. However, if the applied potential is +0.356 V, some $Fe(CN)_6^{3-}$ will be reduced to $Fe(CN)_6^{4-}$, reaching the equilibrium condition where the concentrations of both ions are equal at the electrode surface but not in the bulk solution (as per equation (3-17)). This results in a huge amount of faradaic current flowing and eventually reaching zero. The form of the analyte at the electrode surface depends on the applied potential, and its concentration may not be the same at the electrode surface and in the bulk solution [243]. This difference in concentration creates a concentration gradient between the solution at the electrode surface and the bulk solution, which results in a faradaic current flow until even concentrations are reached. The faradaic current is proportional to the rate of charge transfer of the redox reaction and the rate of the chemical reaction [243]. The rate of a cell reaction is determined by two factors: mass and electron transport. The three modes of mass transport are diffusion, migration, and convection. The faradaic current when mass transport occurs alone is given in equation (3-18).

$$i = nFAD \frac{(C_{bulk} - C_{x=0})}{\delta} = K_o(C_{bulk} - C_{x=0}); \text{ where, } K_o = \frac{nFAD}{\delta} \quad (3 - 18)$$

Where, δ is the width of the diffusion layer, A is the electrode surface area, D is the diffusion constant, and C is the concentrations. The nature of electron transfer between the electrode and adjacent species also affects the current. If the electrons flow quickly, it means the redox reactions are at equilibrium, ensuring electrochemical reversibility, but if they flow slowly, it means the reactions are irreversible. The Nernst equation can only be applied to reversible redox reactions. In contrast, the charging current, which is short-lived, occurs when the electrode's potential suddenly changes from one state to another. The positive or negative surface charge attracts opposite ions at the vicinity of the surface, forming a structured electrode solution interface called the electrical double layer (EDL).



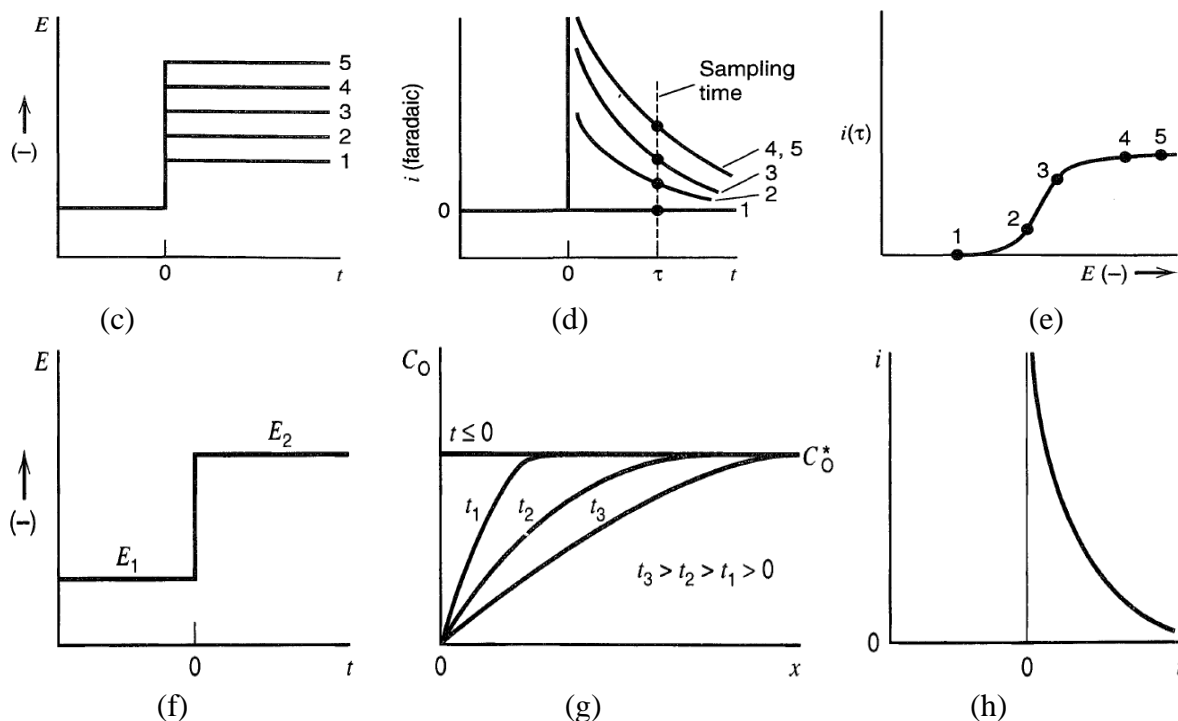


Fig. 3-3. (a) The ladder diagram of the ferricyanide, $Fe(CN)_6^{3-}$ (Fe^{3+}), reduces to ferrocyanide, $Fe(CN)_6^{4-}$ (Fe^{2+}) redox half-reaction [48]. (b) Concentration gradients and the diffusion layer width of the reaction from equations (3-15) and (3-16) [48]. Reproduced (Adapted) with permission. Copyright 1999-2023, Copyright Holder David Harvey (<https://sites.google.com/depuw.edu/dth/home>), and Libretexts (<https://LibreTexts.org>). Sampled-current voltammetry with stirring (c) Step waveforms applied in a series of experiments, (d) Current-time curves observed in response to the steps, (e) Sampled-current voltammogram [58]. (f) A step potential for excitation in amperometry is applied, where species O is electro-inactive at E_1 but is reduced at a diffusion-limited rate at E_2 . (g) Concentration profiles for various times during the experiment, (h) Current flow vs. time curve [58]. Reproduced (Adapted) with permission. Copyright 2001, Copyright Holder John Wiley & Sons, Inc, <https://www.wiley.com/en-ca>.

Pulse (Sampled-Current) Voltammetry

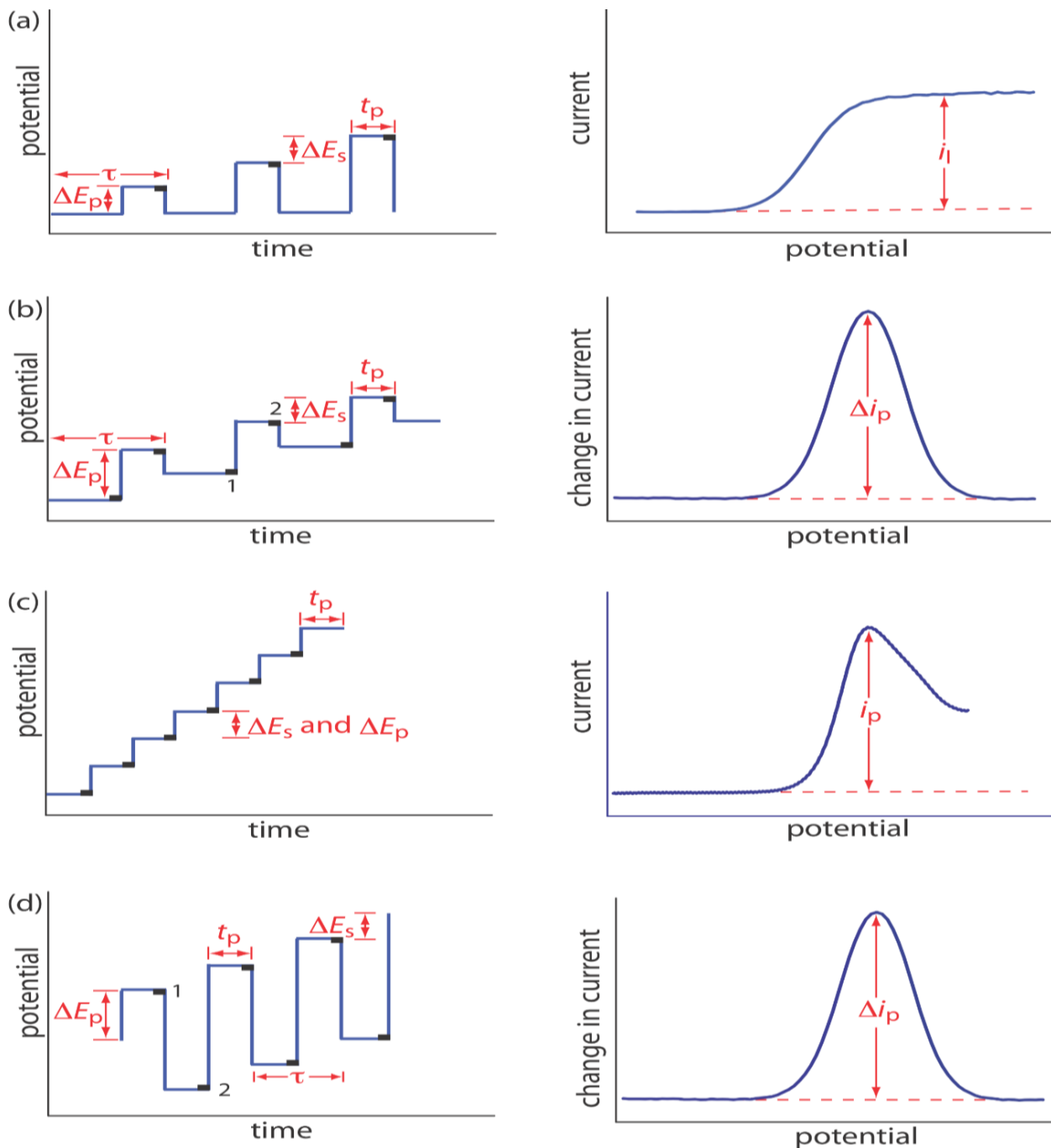


Fig. 3-4. Potential-excitation signals and voltammograms for (a) normal pulse, (b) differential pulse, (c) staircase, and (d) square-wave voltammetry. The black rectangles

represent the current sample position. Δi is the current difference between points 2 and 1. The symbols in the diagrams, with typical values for (a), are as follows: τ (≈ 1 s) is the cycle time; ΔE_p (≈ 2 mV and increase by ≈ 2 mV) is a fixed or variable pulse potential, ΔE_s (≈ 2 mV) is a fixed change in potential per cycle, and t_p (≈ 50 ms) is the pulse time. The current is sampled at the end of each potential pulse for approximately 17 ms before returning the potential to its initial value [48]. Reproduced (Adapted) with permission. [137] Copyright 1999-2023, Copyright Holder David Harvey (<https://sites.google.com/depauw.edu/dth/home>), and Libretexts (<https://LibreTexts.org>).

Normal (linear sweep) voltammetry (LSV) is discussed in the cyclic voltammetry (CV) section, although it is the first voltammetry method. Pulse or sampled-current voltammetry is a popular choice among scientific communities, as shown in Fig. 3-3 (c), (d), and (e) 13. To provide a general understanding, Fig. 3-3 (c), (d), and (e) are discussed briefly below.

A redox reaction is observed under stirring when a series of step potentials is applied, as shown in Fig. 3-3(c). Initially, the potential doesn't result in any faradaic current flow. As the step potentials increase, some species become electroactive and can be reduced, but not completely to zero surface concentration. The last two step values work in the mass-transfer-limited region, which is diffusion rate dependent and not influenced by potential. The current is sampled at time τ for each step and a voltammogram is shown in Fig. 3-3 (e). This type of experiment is called sampled-current or normal pulse voltammetry, as shown in Fig. 3-4 (a), which results in improved sensitivity and lower detection limits. In differential pulse polarography, shown in Fig. 3-4 (b), the current is the

difference between two sampled values taken approximately 17 ms before and after the pulse is applied. The benefit of square-wave polarography, seen in Fig. 3-4 (d), is that the value of τ can be as low as 5 ms, reducing the time required for analysis.

For the redox reaction $O + ne^- \rightleftharpoons R$, if there is no R present at the start, the current after applying the potential can be expressed as $i = K_o([O]_{bulk} - [O]_{x=0})$, as seen in equation (3-18). At the limiting current, as shown in Fig. 3-4 (a) and (16), $i_l = K_o[O]_{bulk}$ since $([O]_{x=0} = 0)$, indicating a linear relationship with the bulk concentration of O. Thus, the equation for the Nernst potential and current can be written as

$$E = E_{\frac{O}{R}}^o - \frac{0.05916}{n} \log_e \frac{[R]_{x=0}}{[O]_{x=0}} \quad (3-19)$$

$$i = i_l - K_o[O]_{x=0} \Rightarrow [O]_{x=0} = \frac{i_l - i}{K_o} \quad (3-20)$$

$$\begin{aligned} i &= K_R([R]_{x=0} - [R]_{bulk}) \Rightarrow i = K_R[R]_{x=0} \Rightarrow [R]_{x=0} = \frac{i}{K_R} \text{ since } [R]_{bulk} \\ &= 0 \end{aligned} \quad (3-21)$$

From equations (3-19), (3-20) and (3-21), the potential equation, equation (3-22), can be deduced.

$$\begin{aligned} E &= E_{\frac{O}{R}}^o - \frac{0.05916}{n} \log_e \frac{K_o}{K_R} - \frac{0.05916}{n} \log_e \frac{i}{i_l - i} \Rightarrow E_{\frac{1}{2}} = E_{\frac{O}{R}}^o - \frac{0.05916}{n} \log_e \frac{K_o}{K_R}; \text{ if } i \\ &= \frac{i_l}{2} \end{aligned} \quad (3-22)$$

Where $E_{1/2}$ is the known half-wave potential. The half-wave potential equals the standard-state potential if K_o and K_R are same, which is exactly the case.

Table 3-3: Differential Pulse Voltametric (DPV) Sensors for Health Monitoring Applications

Type	Electrode Materials	Disease	Bio-Analyte	Normal Range [Physiological]	Linear Range	LOD	Sensitivity	Ref.
Neurotransmitter	GQDs/IL/CPE	Schizophrenia, and Alzheimer's	ACh	0.2 – 1.31 uM	0.2 – 400 uM	0.06 μM	--	[244]
	AChE-ChO/GO-IL/GCE	Schizophrenia, and Alzheimer's	ACh/Ch	0.2 – 1.31 uM	5 – 1000 nM	1.35 nM	--	[245]
	ZnFe ₂ O ₄ /SPE	Schizophrenia, and Alzheimer's	ACh	0.2 – 1.31 uM	0.08 – 500 uM	0.024 μM	0.548 $\mu\text{A } \mu\text{M}^{-1}$	[246]
	Poly (OA)/CNTs/GCE	Schizophrenia, Parkinson's	DA	50 nM	10 – 260 uM	0.12 μM	8.71 $\mu\text{A } \text{mM}^{-1}$	[247]
	OMIMPF-MWCNT	Schizophrenia, Parkinson's	DA	50 nM	1 – 100 uM	0.1 μM	--	[248]
	Pt-Np-MWCNT/GCE	Schizophrenia, Parkinson's	DA	50 nM	0.043 – 62 uM	0.0278 μM	--	[233]
Protein	PANI-MIP/graphene oxide	AMI	cTnT	<0.1 ng/mL	0.02 – 0.09 ng/mL	0.008 ng/mL	--	[249]
	PANI-MIP/PMB/f-MWCNTs/SPCE	AMI	cTnT	<0.1 ng/mL	0.1 – 8.0 pg/mL	0.04 pg/mL	--	[250]
	Binding peptide/DSP	AMI	Myo	30 – 90 ng/mL (serum)	17.8 – 1780 ng/mL	9.8 ng/mL	--	[22]
	PMPC-SH/AuNP	CVDs	CRP	<5 ug/mL	5 – 5000 ng/mL	1.6 ng/mL	--	[251]
	3-APBA/AgNWs	Athletic performance	Lactate	25 uM (sweat)	1 – 10 ⁵ uM	0.22 uM	--	[252]
Glucose	Ferrocene with two boronic acid and hexamethylene Au Nanowire	Diabetes	Glucose	4.9 – 6.9 mM	0.1 – 0.7 mM	--	--	[253]
		Diabetes	Glucose	4.9 – 6.9 mM	0.1 – 20 mM	30 μM	40 $\mu\text{A } \text{mM}^{-1} \text{cm}^{-2}$	[254]
	CoPcTS	Diabetes	Glucose	4.9 – 6.9 mM	0.25 – 20 mM	100 μM	5.695 $\mu\text{A } \text{mM}^{-1}$	[255]
	PtAg/MWCNTs	Diabetes	Glucose	4.9 – 6.9 mM	1 – 25 mM	600 μM	91.4 $\mu\text{A } \text{mM}^{-1} \text{cm}^{-2}$	[256]
	Pt NFs/Au Disk	Diabetes	Glucose	4.9 – 6.9 mM	1 – 16 mM	48 μM	1.87 $\mu\text{A } \text{mM}^{-1} \text{cm}^{-2}$	[257]

Useful Acronym: Graphene quantum dots (**GQDs**); Ionic liquid (**IL**); Carbon paste electrode (**CPE**); Acetylcholine esterase (**AChE**); Choline oxidase (**ChO**); Screen printed electrode (**SPE**); Poly(o-anisidine) (**POA**); 1-octyl-3-methylimidazolium hexafluorophosphate (**OMIMPF₆**); Nanoparticles (**Np**); Polymethylene blue (**PMB**); Acute Myocardial Infarction (**AMI**); Cardiac troponin T (**cTnT**); Screen printed carbon electrode (**SPCE**); Dithiobis(succinimidyl propionate) (**DSP**); Myoglobin (**Myo**); poly(2-methacryloyloxyethyl phosphorylcholine) (**PMPC-SH**); Cardiovascular diseases (**CVDs**); Gold nanoparticles (**AuNPs**); Gold screen printed electrode (**AuSPE**); 3-

aminophenulboronic acid (**3-APBA**); Ag Nanowires (**AgNWs**); cobalt (II) phthalocyanine tetrasulfonate (**CoPcTS**); Multi-Walled Carbon nanotubes Decorated with Platinum and Silver (**PtAg/MWCNTs**); Nanoflowers (**Nfs**).

Differential Pulse Voltametric (DPV) detection of ACh has been reported in both enzymatic [245], and nonenzymatic [244]–[246] sensors. Depending on the linear range, the nonenzymatic ACh sensors showed good compatibility. Beitollahi et al. 2019 showed that ZnFe_2O_4 nonenzymatic sensor had a sensitivity of $0.548 \mu\text{A } \mu\text{M}^{-1}$ [246]. Nonenzymatic detection of DA by Dursun et al. 2010 using DPV showed better performance based on linear range and LOD [233]. Acute myocardial infarction (AMI), also known as a heart attack, is a common life-threatening cardiovascular disease throughout the world, and cardiac troponin T (cTnT), a cardiac regulatory protein, is its specific biomarker.

AMI results in the rapid release of cTnT (37 kDa) from cardiac muscle cells into the bloodstream, which remains elevated up to 14 days after cardiac ischemia, providing the possibility of prognosis of the disease. DPV-based enzymatic sensing of cTnT was recorded in couple of scholarly articles [249]–[250]. The sensor reported by Phonklam et al. 2020 showed a linear range of $0.1 - 8.0 \text{ pg/mL}$ and LOD 0.04 pg/mL . The promising result could be due to the higher surface to volume ratio of f-MWCNTs. A heme-containing protein, cardiac Myo, is one of the markers that increase after AMI onset. Due to its small size of 17.8 kDa, Mb is quickly released into circulation within 1 – 3 h after symptom onset and serves as a valuable screening molecule with high sensitivity and predictivity for AMI detection [22]. The enzyme-based Myo sensing electrode of Lee et al. 2015 showed a linear range of $17.8 - 1780 \text{ ng/mL}$ which is good fit for the serum range of $30 - 90 \text{ ng/mL}$, and LOD of 9.8 ng/mL [22].

DPV has been used for both enzyme-based[253] and enzyme-less[254]·[255]·[256]·[257] detection of glucose in human body. The enzyme-less electrode showed better results compared to enzymatic one. Both the electrodes of Cherevko et al. 2009 and Lin et al. 2015 provided promising results in terms of liner range, LOD, and sensitivity.

Table 3-4: Square Wave Voltametric (SWV) Sensors for Health Monitoring Applications

Type	Electrode Materials	Disease	Bio-Analyte	Normal Range [Physiological]	Linear Range	LOD	Sensitivity	Ref.
Neurotransmitter	f-SWCNTs/GCE	Schizophrenia, Parkinson's	DA	50 nM	5.0 – 100 μ M	0.020 μ M	NI	[258]
	PMoV@GF/GCE	Schizophrenia, Parkinson's	DA	50 nM	2.0 – 300 μ M	0.880 μ M	NI	[259]
	AuNP/GO/ITO	Schizophrenia, and Alzheimer's	ACh	0.2-1.31 μ M	0.1-1000 nM	0.1 nM	0.383 mA/pM	[260]
	Fe ₃ O ₄ @CNT-N/GCE	Schizophrenia, Parkinson's	DA	50 nM	2.5-65 μ M	0.050 μ M	--	[261]
Protein	Aptamer/AuSPE	Chronic inflammation	TNF- α	<75 pg/mL	10 – 100 ng/mL	10 ng/mL	--	[23]
	Poly(o-aminophenol)	MI	Myo	95 – 500 ug/L	> 3.5ug/mL	0.8 ug/mL	--	[262]
	Plastic-antibody/graphite	MI	Myo	95 – 500 ug/L	> 7.4 ug/mL	0.79 ug/mL	--	[263]

Useful Acronym: functionalized single walled carbon nanotubes (**f-SWCNTs**); V-phosphomolybdates (**PMoV**); Graphene flakes (**GFs**); Indium Tin Oxide (**ITO**); Tumor necrosis factor-alpha (**TNF- α**); Myocardial Ischemia (**MI**).

SWV technique has been used to sensing DA in both enzymatic [259] and nonenzymatic [258]·[261]. However, the linear ranges of the above-mentioned DA sensors do not cover the normal physiological range of 50 nM. Tumor necrosis factor-alfa (TNF- α) is naturally produced by activated macrophages and monocytes and has pleiotropic effects on normal and malignant cells. Though it is a key marker of inflammatory diseases, it is involved in a broad range of physiological and pathological responses, such as

atherosclerosis, rheumatoid arthritis, psoriasis, inflammatory bowel disease, Alzheimer's disease, and various pulmonary disorders [23]. Moreover, TNF- α is rapidly upregulated in the brain after injury and is associated with necrosis or apoptosis [23]. Therefore, measuring TNF- α is important for the understanding of inflammation and discovering drugs that alleviate it. Two enzymatic approaches to detect Myo have been reported [262]–[263]. Both electrodes showed good prospect to sensing the normal physiological range of Myo of 95 – 500 $\mu\text{g/mL}$.

Cyclic Voltammetry (CV)

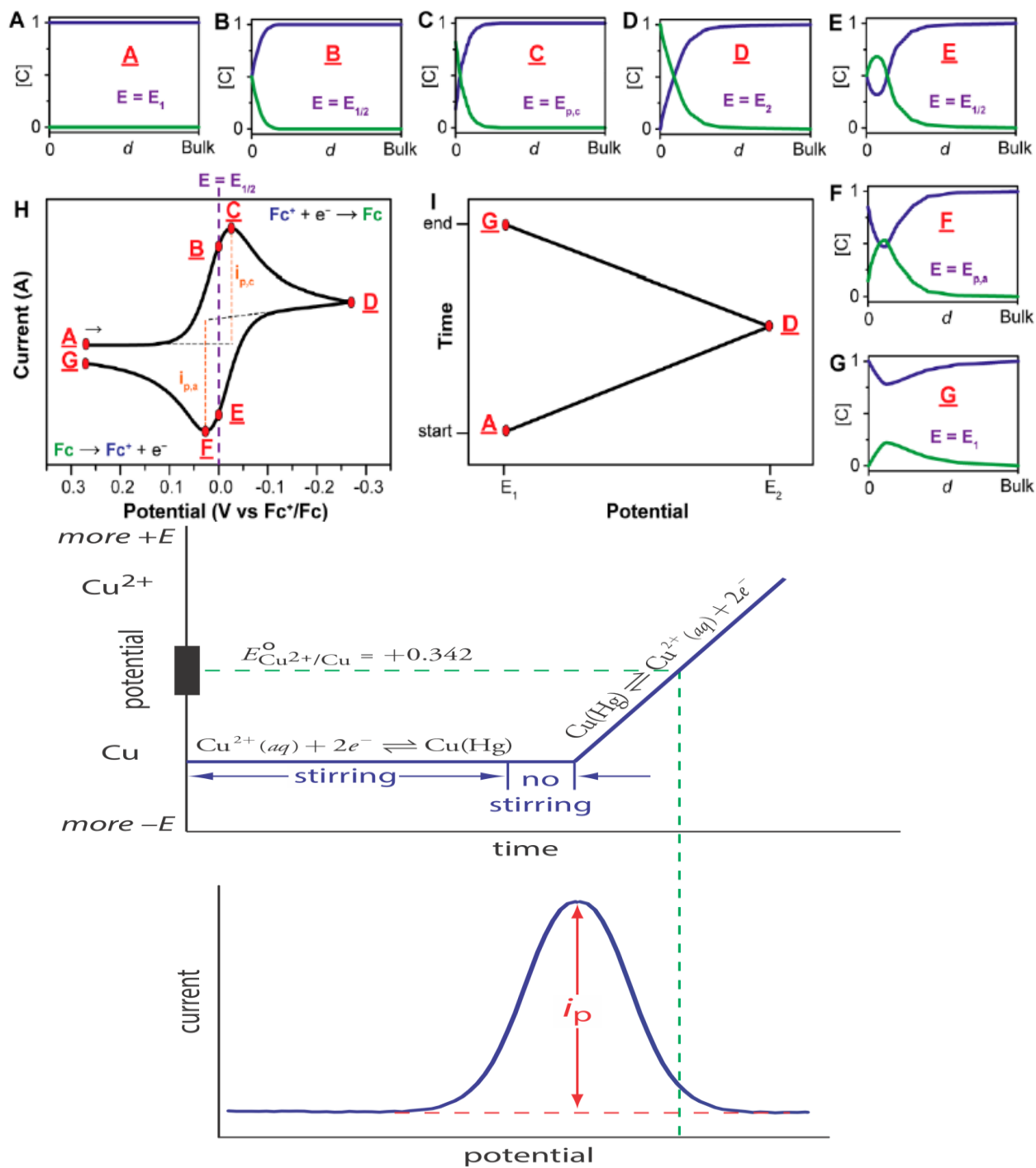
CV is a powerful and popular electrochemical technique commonly employed to investigate the redox processes of molecular species [111] [264]. CV scans the potential in both directions, estimating the standard-state potential from the average potential between points F and C on the cyclic voltammogram (Fig. 3-5(H)). When a solution of ferrocenium $[\text{Fe}(\text{Cp})_2]^+$ (Cp = cyclopentadienyl), abbreviated as Fc^+ , is scanned to negative potentials, Fc^+ is reduced locally to ferrocene $[\text{Fe}(\text{Cp})_2]$, abbreviated as Fc, at the electrode, resulting in a measurement of current and depletion of Fc^+ at the electrode surface [111]–[264], see Fig. 3-5 [I]. Firstly, the negative scan starts from A to D, and during this cathodic scan, $[\text{Fc}^+]$ moves away from the surface after being reduced to Fc. The peak current, at point C, is observed due to extra Fc^+ that has diffused through the interface from the bulk solution. After the peak, the current starts to decrease because of the expansion of the depletion layer that slows down mass transport. The scan is reversed after reaching switching point D, and

the anodic or positive scan begins. Due to the more positive potential, the Fc accumulated at the surface during the negative scan is re-oxidized to Fc^+ .

According to equation (3-19), the redox species are equal at points B and E, as per the Nernst equation ($E = E_{1/2}$). The two peaks are separated due to the diffusion of the analyte to and from the electrode, and the difference between the peaks is 57 mV at 25°C for a chemically and electrochemically reversible process. The width at half-maximum on the forward scan of the peak is 59 mV. The scan rate is another important parameter of CV, which can control the size of the diffusion layer inversely. A high scan rate means a smaller layer width, which increases the flow of electrons through the interface, resulting in a higher current.

$$i_p = 0.446nFAC^o \left(\frac{nFvD_o}{RT} \right)^{1/2} \quad (3 - 23)$$

The *Randles–Sevcik* equation, as shown in equation (3-23), relates the peak current to the scan rate v (V s^{-1}), the electrode surface area A (cm^2), the diffusion coefficient D_o ($\text{cm}^2 \text{s}^{-1}$) of the oxidized analyte, and the bulk concentration C_o (mol cm^{-3}) of the analyte. It is important to note that some analytes undergo oxidation first, in which case the potential would first scan positively [48].



(J)

Fig. 3-5. (A-G): Concentration profiles (mM) for Fc^+ (blue) and Fc (green) as a function of distance from the electrode (0.5 mm) at various points during the voltammogram. (H):

Voltammogram of the reversible reduction of a 1 mM Fc^+ solution to Fc at a scan rate of 100 mV/s. (I): Applied potential as a function of time for a generic cyclic voltammetry experiment, with the initial, switching, and end potentials represented by (A, D, and G, respectively) [111]. Copyright 2017 The American Chemical Society (ACS). Further permissions related to the material excerpted should be directed to the ACS. (J) Applied potential and voltammogram for ASV at a mercury film electrode, with a copper ladder diagram in the upper figure of Fig. 3-5 (J). Typical deposition times are 1-30 minutes, with a lower deposition time for higher analyte concentrations [48]. Reproduced (Adapted) with permission. [137] Copyright 1999-2023, Copyright Holder David Harvey (<https://sites.google.com/depauw.edu/dth/home>), and Libretexts (<https://LibreTexts.org>).

Table 3-5: Cyclic Voltametric (CV) Sensors for Health Monitoring Applications

Type	Electrode Materials	Disease	Bio-Analyte	Normal Range [Physiological]	Linear Range	LOD	Sensitivity	Ref.
Neurotransmitter	ITIES	Schizophrenia, and Alzheimer's	ACh	0.2 – 1.31 μM	0.25 – 6 mM	205 μM	--	[265]
	ITIES	--	5-HT	--	0.15 – 8 mM	77 μM	--	[265]
	ITIES	--	T	--	0.5 – 10 mM	86 μM	--	[265]
protein	Mn-doped TiO_2/Au	AMI	Myo	30 – 90 ng/mL (serum)	0.013 – 15 nM	0.013 nM		[266]
Glucose	α -CD SAM on Au	Diabetes	Glucose	4.9 – 6.9 mM [Blood]	0.1 – 0.8 mM	200 μM	2.91 $\mu\text{A mM}^{-1}$	[267]
	CuNO_x	Diabetes	Glucose	0.05 – 6.9 mM [Sweat & Blood]	0.05 – 7 mM	94.21 μM	603.42 $\mu\text{A mM}^{-1} \text{ cm}^{-2}$	[97]
	Nano Au/Ti	Diabetes	Glucose	4.9 – 6.9 mM	0 – 15 mM	14.80 μM	140 $\mu\text{A mM}^{-1} \text{ cm}^{-2}$	[268]
	Nano Au/Thin Au	Diabetes	Glucose	4.9 – 6.9 mM	0.5 – 8 mM	500 μM	160 $\mu\text{A mM}^{-1} \text{ cm}^{-2}$	[269]
	Nano Au on NH_2 -HSM films	Diabetes	Glucose	4.9 – 6.9 mM	0.2 – 70 mM	100 μM	2.5 $\mu\text{A mM}^{-1} \text{ cm}^{-2}$	[270]
	Chitosan-GNPs/GCE	Diabetes	Glucose	4.9 – 6.9 mM	0.4 – 10.7 mM	370 μM	--	[271]

Nano Au-DHP film/GCE	Diabetes	Glucose	4.9 – 6.9 mM	0.09 – 9.9 mM	10 μ M	--	[272]
Au Nanowire	Diabetes	Glucose	4.9 – 6.9 mM	0.5 – 14 mM	--	960 μ A mM ⁻¹ cm ⁻²	[254]
Ni-BDD	Diabetes	Glucose	4.9 – 6.9 mM	0.25 – 10 mM	2.7 μ M	1 μ A mM ⁻¹ cm ⁻²	[273]
BDND	Diabetes	Glucose	4.9 – 6.9 mM	0.25 – 12 mM	250 μ M	153 μ A mM ⁻¹ cm ⁻²	[274]
Ni/ 1-naphthylamine	Diabetes	Glucose	4.9 – 6.9 mM	0.04 – 1 mM	6 μ M	--	[275]
o-PDA/Au	Diabetes	Glucose	4.9 – 6.9 mM	0.1 – 20 mM	50 μ M	--	[276]
Cu(acac ₂ pn)	Diabetes	Glucose	4.9 – 6.9 mM	0.5 – 10 mM	360 μ M	0.16 μ A mM ⁻¹	[277]
DGNs/GCE	Diabetes	Glucose	4.9 – 6.9 mM	0.1 – 25 mM	50 μ M	190.7 μ A mM ⁻¹ cm ⁻²	[278]
Au MPs/Au/Si	Diabetes	Glucose	4.9 – 6.9 mM	0.5 – 9 mM	60 μ M	13.2 μ A mM ⁻¹ cm ⁻²	[279]
Au NP film/ITO	Diabetes	Glucose	4.9 – 6.9 mM	0.03 – 45 mM	10 μ M	67.2 μ A mM ⁻¹ cm ⁻²	[280]

Useful Acronym: Interface between two immiscible electrolyte solutions (**ITIES**); Serotonin or 5-hydroxytryptamine (**5-HT**); Tryptamine (**T**); Acute myocardial infarction (**AMI**); Myoglobin (**Myo**); α -cyclodextrin (**α -CD**); Amine-functioned hexagonal mesoporous silica (**NH₂-HSM**) films; gold nanoparticles (**GNPs**); dihexadecyl hydrogen phosphate (**DHP**); Boron-doped diamond (**BDD**); Boron-doped nanocrystalline diamond (**BDND**); o-phenylenediamine (**PDA**); N,N'-Bis(acetylacetonato)propylenediimine Copper(II) (**Cu(acac₂pn)**); Dendrite-like gold nanostructures (**DGNs**); Micro-pillars (**MPs**).

It is evident from Table (3-1) to (3-5), CV is one of the most popular electrochemical sensing techniques for detecting glucose in the human body. Among so many articles, the scholarly published works with proper details of linear range (sweat 0.05 – 1 mM; blood 4.9 – 6.9 mM), LOD are presented here in a tabular form. There are enzymatic [267]·[271]·[272]·[275]·[276]·[277] and enzyme-less [97]·[268]·[269]·[270]·[254]·[273]·[274]·[278]·[279]·[280] electrodes given. Depending on the linear range and LOD, the glucose sensing electrodes can be categorized in three groups; for blood [[269]·[270]·[271]·[272]·[273]·[274]·[277]·[278]·[279]], for sweat [275], and for both analyte [[97]·[268]·[276]·[280]]. The glucose sensors fabricated using Au show promising sensing performance of linear range, LOD, and sensitivity, see Table 3-5. Kurniawan et al. 2006 fabricated an electrode to sense glucose using nano/thin Au provides sensitivity of 160 μ A mM⁻¹ cm⁻² [269]. On the other hand, Shu et al. reported a dendrite-

like gold nanostructures (DGNs) electrode of good sensitivity of $190.70 \mu\text{A mM}^{-1} \text{cm}^{-2}$ [278]. Moreover, the electrode of Au nanowires by Cherevko et al. 2009, gives highest sensitivity of glucose sensing of $960 \mu\text{A mM}^{-1} \text{cm}^{-2}$ [254]. The better performances of Au nanowires and dendrite-like nanostructures are due to higher surface to volume ratio at the surface of the electrode. However, Au is an expensive material for an electrode to be suitable for mass production.

Stripping Voltammetry

Among anodic, cathodic, and adsorptive stripping, anodic stripping voltammetry is widely used. The applied potential and response current-potential curve are shown in Fig. 3-5(J). At the start, the working electrode is held at a cathodic potential sufficient for depositing metal ion Cu^{2+} , onto the *Hg* film electrode [48], where copper is amalgamated with mercury. During the process, metal is concentrated from the solution to a small volume on the electrode surface and stirring is used to speed up deposition. Before the end, stirring is stopped to eliminate convection mass transport by allowing the solution to become still. In the sweep step, metal is stripped from the electrode to the solution at a sufficient positive voltage. The peak current in the peak-shaped voltammogram represents metal ion concentration in the solution. The main advantage of this technique is its small detection limits in ppb, due to mass concentration of the analyte. For accurate and precise results, control over experimental conditions is important due to its sensitivity. Key factors include the electrode surface area, deposition time, rest time, stirring rate, and scan rate during the stripping step. The method is mostly useful for metals that form amalgams with mercury [48].

3.2.4 Amperometry

The amperometry technique produces a current versus time curve after applying a controlled potential, rather than a voltammogram. It is also known as chronoamperometry, single step amperometry, or forward step amperometry [58]. Fig. 3-3 (f) shows a step potential function of the technique. When the potential is applied to an electrode submerged in a solution of the electroactive species O (the oxidized form) with a concentration of C_o^* at the electrode's surface, the species are electro-inactive at E1 but become rapidly reduced at a more negative potential E2. This results in a complete depletion of O at the electrode's surface and drives the experiment into a "mass-transfer-limited" region. At $t=0$, O is reduced to the stable anion radical R through the reaction $O + ne^- \rightarrow R$, causing a large instantaneous current that continues until full reduction is achieved at the surface. The depletion of O creates a concentration gradient that diffuses more O towards the electrode, causing a flux of O and a proportional increase in current. The increasing amount of R thickens the zone of O depletion, causing the slope of the concentration profile and current to decline over time, as shown in Fig. 3-3 (g) and (h).

$$i_t = \frac{nFAC_o\sqrt{D_o}}{\sqrt{\pi t}} \quad (3 - 24)$$

The current in chronoamperometry is expressed by the well-known *Cottrell* equation, as shown in equation (3-24), which describes the observed current for a planar electrode at any time following a large forward potential step in a reversible redox reaction as a function of time. The symbols have their usual meaning, which was given previously in [58].

Table 3-6: Amperometric Sensors for Health Monitoring Applications

Type	Electrode Materials	Disease	Bio-Analyte	Normal Range [Physiological]	Linear Range	LOD	Sensitivity	Ref.
Neurotransmitter	TCCF/GCE	Neural functioning	DOPAC	--	6 n – 20 μ M	3 nM	40 μ A mA ⁻¹	[281] [282]
	Ni-NWs	--	MeCHO	--	--	9.35 μ M	0.042 μ A uM ⁻¹ cm ²	[283]
	Ni-NW	--	ACh	0.2 – 1.31 μ M	--	0.84 μ M	1.40 μ A μ M ⁻¹ cm ²	[283]
Protein	Anti-cTnT/CNT/polyethyleneimine	AMI	cTnT	<0.1 ng/mL	0.1 – 10 ng/mL	0.033 ng/mL	--	[284]
	Anti-CRP/COOH-MBs	CVDs	CRP	<5 ug/mL	0.07 – 1000 ng/mL	0.021 ng/mL	--	[285]
	Fe ₃ O ₂ NPs/GO NSs	Prostate cancer	PSA	<10 ng/mL	1.25 – 1000 pg/mL	15 fg/mL	--	[286]
	Fe ₃ O ₂ NPs/GO NSs	Prostate cancer	PSMA	<360 ng/mL	9.7 – 50000 pg/mL	4.8 fg/mL	--	[286]
Glucose	Au Nanowire	Diabetes	Glucose	4.9 – 6.9 mM	1 – 10 mM	50 μ M	310 μ A mM ⁻¹ cm ⁻²	[254]
	Nf-GOx-fMWCNTs-PPy/Pt	Diabetes	Glucose	4.9 – 6.9 mM	0 – 4.1 mM	5 uM	54.2 μ AmM ⁻¹ cm ⁻²	[287]
	Nafion/GOx-CoS-MWCNTs/GCE	Diabetes	Glucose	4.9 – 6.9 mM	8 uM – 1.5 mM	5 uM	15000 μ A M ⁻¹ cm ⁻²	[288]
	CG/C@MWCNTs/PtNPs/GOx/Nafion	Diabetes	Glucose	4.9 – 6.9 mM	0.5 - 13.5 mM	1.3 uM	26.5 μ A mM ⁻¹ cm ⁻²	[289]
	CS/Pd@Pt NC/GOx-GCE	Diabetes	Glucose	4.9 – 6.9 mM	1 – 6 mM	0.2 uM	6.82 μ A cm ⁻² mM ⁻¹	[290]
	Hollow Pt–Ni–graphene	Diabetes	Glucose	4.9 – 6.9 mM	0.5 – 20 mM	2 uM	30.3 μ A cm ⁻² mM ⁻¹	[291]
	CuNPs-LIG	Diabetes	Glucose	4.9 – 6.9 mM	1 μ M - 6.0 mM	0.39 μ M	495 μ A mM ⁻¹ cm ⁻²	[292]
	Ni(TPA)-SWCNT-CS/GCE	Diabetes	Glucose	4.9 – 6.9 mM	20 μ M - 4.4 mM	4.6 μ M	2.44 μ A mM ⁻¹	[293]
	Ni-MOF/CNTs modified GCE	Diabetes	Glucose	4.9 – 6.9 mM	1 μ M– 1.6 mM	0.82 μ M	13850 μ A mM ⁻¹ cm ⁻²	[294]
	PtNCs/Graphene/GCE	Diabetes	Glucose	4.9 – 6.9 mM	1 – 25 mM	30 uM	1.21 μ A mM ⁻¹ cm ⁻²	[295]
	PtNFs/GO/GCE	Diabetes	Glucose	4.9 – 6.9 mM	0.002 – 10.3 mM	2 uM	0.64 μ A mM ⁻¹ cm ⁻²	[296]
	Pt/MCs/GCE	Diabetes	Glucose	4.9 – 6.9 mM	0 – 7.5 mM	3 uM	8.52 μ A mM ⁻¹ cm ⁻²	[297]
	AuNCs from Au@BSA/FTO Glass	Diabetes	Glucose	4.9 – 6.9 mM	0.01 – 10 mM	2 uM	10.65 μ A mM ⁻¹ cm ⁻²	[298]
	AuNP film/ITO Glass	Diabetes	Glucose	4.9 – 6.9 mM	0 – 11 mM	5 uM	23.0 μ A mM ⁻¹ cm ⁻²	[280]
	AuNP/MWCNT-CG/Au disk	Diabetes	Glucose	4.9 – 6.9 mM	0.001 – 1 mM	0.5 uM	27.7 μ A mM ⁻¹ cm ⁻²	[299]
	AuNPs/PANI/CC	Diabetes	Glucose	4.9 – 6.9 mM	0.01 – 10 mM	3.08 uM	150 μ A mM ⁻¹ cm ⁻²	[300]
	Pt-Cd Np/GCE/Nafion	Diabetes	Glucose	4.9 – 6.9 mM	0 – 10 mM	50 uM	146.2 μ A mM ⁻¹ cm ⁻²	[301]
	Pt-Ni NCl MWCNT/GCE/Nafion	Diabetes	Glucose	4.9 – 6.9 mM	0 – 15 mM	0.3 uM	940 μ A mM ⁻¹ cm ⁻²	[302]

NiNPs/SMWNTs/GCE	Diabetes	Glucose	4.9 – 6.9 mM	0.001 – 1 mM	0.5 uM	1438 $\mu\text{A mM}^{-1} \text{cm}^{-2}$	[303]
PC/NiNPs/GCE Nafion	Diabetes	Glucose	4.9 – 6.9 mM	0.015 – 6.45 mM	4.8 uM	207.3 $\mu\text{A mM}^{-1} \text{cm}^{-2}$	[304]
NiO-Pt NP rGO/ GCE	Diabetes	Glucose	4.9 – 6.9 mM	0.001 – 5.66 mM	0.2 uM	668.2 $\mu\text{A mM}^{-1} \text{cm}^{-2}$	[305]
SSCF	Diabetes	Glucose	4.9 – 6.9 mM	0.001 – 4.6 mM	0.03 uM	2149 $\mu\text{A mM}^{-1} \text{cm}^{-2}$	[306]
Cu ₂ O NP/SWCNT/ GCE Nafion	Diabetes	Glucose	4.9 – 6.9 mM	0.0005 – 2.5 mM	0.2 uM	2143 $\mu\text{A mM}^{-1} \text{cm}^{-2}$	[307]
CuO/MWCNTs/Ta foil	Diabetes	Glucose	4.9 – 6.9 mM	0.0004 – 1.2 mM	0.2 uM	2596 $\mu\text{A mM}^{-1} \text{cm}^{-2}$	[308]
CoO _x Thin film/ Np Au film/ Au disk	Diabetes	Glucose	4.9 – 6.9 mM	0.002 – 2 mM	0.094 uM	2025 $\mu\text{A mM}^{-1} \text{cm}^{-2}$	[309]
Co ₃ O ₄ NP bi-C/GCE	Diabetes	Glucose	4.9 – 6.9 mM	0.00005 – 22 mM	0.02 uM	34.23 $\mu\text{A mM}^{-1} \text{cm}^{-2}$	[310]
Co ₃ O ₄ NFs/Ni foam	Diabetes	Glucose	4.9 – 6.9 mM	0.005 – 12 mM	0.08 uM	1440 $\mu\text{A mM}^{-1} \text{cm}^{-2}$	[311]

Useful Acronym: Tyrosinase-chitosan composite film (**TCCF**); 3,4-dihydroxyphenylacetic acid (**DOPAC**); Acetaldehyde (**MeCHO** = Me-methyl); Nafion (**Nf**); Polypyrrole (**PPy**); Glucose oxidase (**GOx**); Prostate specific membrane antigen (**PSMA**); Nanosheets (**NSs**); Cobalt (II) sulfide (**CoS**); Chitosan (**CS**); Palladium (**Pd**); Nanocubes (**NCs**); Laser-induced graphene (**LIG**); Nickel (II)-terephthalic acid (**Ni(TPA)**); Metal-organic framework (**MOF**); Mesoporous carbons (**MCs**); Bovine serum albumin (**BSA**); Indium tin oxide (**ITO**); Fluorine doped tin oxide (**FTO**); Cryogel (**CG**); Carbon cloth (**CC**); Nano porous (**Np**); Nano-clusters (**NCl**s); Straight multi-walled carbon nanotubes (**SMWNTs**); Porous Carbon (**PC**); Sandpaper-supported copper framework (**SSCF**); Bio-inspired pyrolytic carbon (**bi-C**);

DOPAC is a dopamine metabolite found in the cytoplasm of the brain and neurons, as well as in cerebrospinal fluid (CSF). It is absent or undetectable in the blood of healthy human body, although a range of 7—13 nM can be found in the CSF of an adult human body during any neural abnormalities [282]·[312]. An enzymatic amperometric electrode has been fabricated by Liu et al. 2005 [282]. Acetaldehyde, also known as ethanal by IUPAC, is an organic colorless liquid or gas and one of the most important aldehydes. Although it occurs widely in nature in plants, it is also produced by the partial oxidation of ethanol by the liver enzyme alcohol dehydrogenase and is a contributing cause of hangover after alcohol consumption [24]. The International Agency for Research on Cancer (IARC)

has listed acetaldehyde as a Group 1 carcinogen [25]. An enzyme-less sensor has been reported by Blanco et al 2015 which can detect both MeCHO and ACh [283]. An amperometric enzymatic glucose sensor was reported by Li et al. 2020 with excellent sensitivity of $15000 \mu\text{A mM}^{-1} \text{cm}^{-2}$ [288]. The electrode could be used for sensing sweat glucose, since its linear range is 0.008 – 1.5 mM. Additionally, a nonenzymatic glucose sensing electrode fabricated by Zhang et al. 2018 also suitable of sensing sweat glucose which provides $13850 \mu\text{A mM}^{-1} \text{cm}^{-2}$ [294].

In Table 3-6, the amperometric glucose sensors that meet the criteria for linear range (sweat 0.05 – 1 mM; blood 4.9 – 6.9 mM), LOD, sensitivity, reproducibility, stability, and interference analysis are reported. It is evident that the amperometric technique is the most popular electrochemical method for detecting glucose in the human body. This immense popularity is due to the requirement of a single potential, where a range of potentials (mostly -1 to +1 V) is needed to investigate the analyte using CV. The drawbacks (such as required large ranges of sweeping potential from -1 V to +1 V, longer sweeping time, water dissociation after +0.7 V, H_2 evolution at -1V etc.) make CV the second most popular electrochemical technique for sensing glucose in the human body. Among the reported scholarly publications, the nonenzymatic[254]·[291]·[292]·[293]·[294]·[295]·[296]·[297]·[298]·[280]·[299]·[300]·[301]·[302]·[303]·[304]·[305]·[306]·[307]·[308]·[309]·[310]·[311] electrodes show promising prospect over enzymatic[287]·[288]·[289]·[290] ones.

Based on the linear range and LOD, glucose sensing electrodes can be categorized into three groups: for blood [[254]·[289]·[291]·[295]], for sweat

[[287]·[288]·[292]·[293]·[294]·[299]·[303]·[304]·[305]·[306]·[307]·[308]·[309]], and for both analytes [[296]·[297]·[298]·[280]·[300]·[301]·[302]·[310]·[311]]. Among the enzymatic amperometric glucose sensors, the electrode fabricated by Li et al. (2020) using CoS-functionalized MWCNTs with a GOx surface layer exhibits an excellent sensitivity of $15000 \mu\text{A mM}^{-1} \text{cm}^{-2}$ [288]. However, the sensitivity of the electrode may result from two reasons; high surface to volume ratio of MWCNTs and electrons transferring capability of CoS in between GOx and MWCNTs. A nickel metal organic framework supported by carbon nanotubes (Ni-MOF/CNTs) yields a sensitivity of $13850 \mu\text{A mM}^{-1} \text{cm}^{-2}$, which is a non-enzymatic electrode suitable for sweat glucose sensing, fabricated by Zhang et al. (2018) [294].

Furthermore, electrodes that cover the linear ranges of both sweat and blood are primarily based on nanoparticles of noble metals, such as Au, Pt, and Ni. This hinders their mass production [298]·[280]·[300]·[301]·[302]·[311]. In contrast, non-precious transition metal oxide (Cu and Co oxides) electrodes mainly provide a linear range for sweat glucose [306]·[307]·[308]·[309]. Thus, non-noble metal oxides are suitable for sweat glucose monitoring and mass production.

3.3 Research Challenges and Future Perspectives

Electrochemical techniques play a significant role in transitioning health monitoring from expensive, large-scale laboratory apparatus to affordable and easily portable lab-in-a-box solutions [313]. However, some techniques are not as user-friendly, which has led the researcher community to increasingly focus on voltammetry and

amperometry. Junction potential presents a barrier to potentiometric sensing. Furthermore, the requirement for chemical labeling (such as enzyme tags, redox tracers, or nanoparticle labels) poses a significant challenge for specific and direct potentiometric sensing, as the interaction between receptors and bio-analytes typically does not yield a measurable potential signal [234]. Additionally, imprinting bio-analytes is difficult because traditional MIPs are highly cross-linked, making it hard for bio-analytes to access the buried binding sites [234]. On the other hand, coulometry is time-consuming, which renders it unsuitable for rapid sensing. The only coulometric electrochemical sensor listed in Table 3-2, requires about 2 hours of incubation time to achieve a detection limit of 0.4 ng/mL [240]. Although, voltammetry is popular in the academic community, it necessitates scanning the analyte over a range of voltages (mostly - 1 V to + 1 V), a step that is not required in amperometry, a single potential technique.

3.3.1 Sensor Materials and Functionalization

Neurotransmitter

For the enzymatic determination of ACh, various materials have been investigated using potentiometric techniques, such as oxatub[4]arenes (a naphthalene-based macrocycle), a biomimetic-imprinted material (BIM) of multiwalled carbon nanotubes (MWCNTs) and aniline (ANI), a self-assembled platform formed by poly(allylamine) hydrochloride (PAH) and silicon dioxide nanoparticles (SiO₂-Np), and carboxylated single-walled carbon nanotube thin-film (SWCNT-TF) as a pH electrode [7], [8], [231], [232]. In addition, a polymeric structure of polyaniline (PANI) was employed as a physical support

for the composite of multiwalled carbon nanotubes (MWCNTs) and aniline (ANI) [7], [8]. Silicon dioxide nanoparticles ($\text{SiO}_2\text{-Np}$), an insulator, was used to contain the immobilized enzyme acetylcholinesterase (AChE) [231]. Meanwhile, carboxylated single-walled carbon nanotube thin-film (SWCNT-TF) served as an effective pH sensor [232]. A composite of AChE and choline oxidase (ChO) was used as a sensing surface with a good electronic conducting intermediary layer of molecularly bonded graphene oxide (GO) and ionic liquid (IL) of 1-allyl-3-methylimidazoliumbis(trifluoromethylsulfonyl)imide (AMIM TFSI) on a glassy carbon electrode (GCE) for detecting choline (Ch) and ACh, respectively, using differential pulse voltammetry (DPV) [245]. Jahani et al 2020 and Beitollahi et al 2019 have published a few nonenzymatic approaches to detecting ACh using DPV [244][246]. Jahani et al 2020 demonstrated that graphene quantum dots (GQDs) can be used as a nonenzymatic ACh electrode surface [244], while Beitollahi et al. 2019 showed that ZnFe_2O_4 nanoparticles could serve as an excellent nonenzymatic option for sensing ACh [246]. Notably, Blanco et al 2015 used the traditional direct current (DC) amperometric technique to study a nonenzymatic sensor using a nickel nanowire array electrode, which can detect both acetaldehyde (CH_3CHO or MeCHO) and ACh [283].

For enzymatic potentiometric DA sensor, He et al 2021 investigated a conducting polymer poly (3,4-ethylenedioxythiophene) doped with poly (styrenesulfonate) as the solid contact, which was electropolymerized on one end of a gold wire (diameter 0.25 mm) [9]. The conducting polymer was covered with a dopamine-selective membrane containing 12-crown-4-tetraphenylborate as a neutral carrier, 2-nitrophenyloctyl ether as a plasticizer, and poly (vinyl chloride) as the membrane matrix. However, for enzymatic DA detection, the

DPV technique has been applied on a nanocomposite of poly(o-anisidine) and carbon nanotubes (POA/CNTs), along with a gel containing multi-walled carbon nanotubes (MWNTs) and room-temperature ionic liquid of 1-octyl-3-methylimidazolium hexafluorophosphate (OMIMPF(6)) [247]–[248]. Moreover, nonenzymatic detection of DA by Dursun et al. 2010 using DPV showed better performance where the MWCNTs functionalized by electrochemically deposited Pt nanoparticles [233]. The SWV technique has been used to sense DA through both enzymatic[259] and nonenzymatic[258]–[261] approaches. However, in the enzymatic approach, Fernandes et al 2015 prepared hybrid nanocomposites based on the immobilisation of tetrabutylammonium salts of phosphomolybdates (PMo_{12} , PMo_{11} , PMo_{11}V , and $\text{PMo}_{10}\text{V}_2$) on single-walled carbon nanotubes or graphene flakes. The enhancement of the electrochemical properties of polyoxometalates (POMs) was a result of the strong electronic communication between POMs and carbon nanomaterials. Nanocomposites of vanadium–phosphomolybdates exhibited superior V-based electrocatalytic properties for ascorbic acid oxidation compared to free POMs. Moreover, $\text{PMo}_{11}\text{V}@$ graphene shows an outstanding sensing performance for the detection of dopamine [259]. In the realm of nonenzymatic detection, both Fernandes et al 2014, and Li et al 2012 applied SWV to N-doped carbon nanotubes functionalized with Fe_3O_4 nanoparticles ($\text{Fe}_3\text{O}_4@\text{CNT-N}$), and single-walled carbon nanotubes (SWCNTs) fabricated by sodium dodecyl sulfate (SDS) (f-SWCNTs) for detecting DA, respectively [258] [261].

Protein

The electrochemical potentiometric technique is primarily used for the enzymatic detection of important proteins in the human body, such as CRP, trypsin, CEA, and PSA, as shown in Table 3-1. An enzymatic anti-CRP layer was immobilized on ZnO nanotubes, which were grown on Au-coated glass, to sense CRP [11]. To detect trypsin without chemical labels by potentiometric method, a mussel-inspired surface imprinted polymeric membrane was fabricated on ISE [234]. This biomimetic sensing method is based on a blocking mechanism whereby the recognition reaction between the surface imprinted polymer and a biomarker can block the current-induced ion transfer of an indicator ion, thus causing a potential change. A CEA-sensing enzymatic layer of hydroxyl-terminated alkanethiol was created as outlined in [235]. The thiol molecules of the hydroxyl-terminated alkanethiol layer are chemically bonded to a substrate of a gold-coated silicon chip, and template biomolecules are co-adsorbed and later removed to create footprint cavities. The potential changes upon re-adsorption of the CEA biomolecules are measured potentiometrically [235].

On the other hand, potentiometric enzymatic PSA sensor producing protein imprinted materials with charged binding sites (C/PIM) through surface imprinting over graphene layers to which the protein was initially covalently attached [20]. Vinylbenzyl(trimethylammonium chloride) and vinyl benzoate were introduced as charged monomers that labeled the binding site and were allowed to self-organize around the protein. The subsequent polymerization was carried out by the radical polymerization of

vinylbenzene. Neutral PIM (N/PIM) prepared without oriented charges and non-imprinted materials (NIM) obtained without template were used as controls.

DPV-based enzymatic sensing of cTnT has been reported in a couple of studies [249][250]. Phonklam et al. 2020 reported that the molecularly imprinted polymer (MIP) sensor employed an electrodeposited polymethylene blue (PMB) redox probe on multi-walled carbon nanotubes (MWCNTs) modified SPCE, with the electropolymerized polyaniline around the immobilized cTnT templates [250]. However, the biomimetic cavities for targeted cTnT were fabricated by the electro-polymerization of a conductive co-polymer matrix consisting of aniline and carboxylated aniline on the graphene oxide (GO) modified SPE, as described by Karimi et al 2019 [249]. Furthermore, a myoglobin specific binding peptide peptide (Myo-3R7, CPSTLGASC, 838 Da) was covalently immobilized on a gold electrode that was functionalized via a dithiobis(succinimidyl propionate) (DSP) self-assembled monolayer (SAM) to detect myoglobin heme protein [22]. Thiol-terminated poly(2-methacryloyloxyethyl phosphorylcholine) (PMPC-SH) was self-assembled on a gold nanoparticle-modified SPCE for label-free detection of CRP by DPV [251]. In addition, DPA is also used by Zhang et al 2020 for non-invasive monitoring of lactate in the human sweat. This was accomplished by electro-polymerization of 3-aminophenylboronic acid (3-APBA) with the imprinted lactate molecule on the AgNWs-coated working electrode [252].

Some vacant sites were created on the film of poly(o-aminophenol) (PAP) through the electro-polymerization of aminophenol (AP) in the presence of protein Myo, which acted as biomimetic artificial antibodies. Felismina et al 2014 reported the deposition of

this enzymatic polymeric membrane on a gold (Au) screen printed electrode (SPE) to detect Myo using SWV [262]. The authors also fabricated another SWV based enzymatic electrode for detecting Myo, in which the SPE modified with a MIP grafted on a graphite support and incorporated in a matrix composed of poly(vinyl chloride) and the plasticizer o-nitrophenyloctyl ether [263]. The protein-imprinted material (PIM) was produced by growing a reticulated polymer around a protein template, followed by radical polymerization of 4-styrenesulfonic acid, 2-aminoethyl methacrylate hydrochloride, and ethylene glycol dimethacrylate. The polymeric layer was then covalently bound to the graphitic support, and Myo was added during the imprinting stage to act as a template.

Glucose

Potentiometric non-enzymatic electrodes made of polyaniline or polyaniline boronic have been used [225]·[226]. In contrast, enzymatic potentiometric glucose sensors are being mostly investigated using the glucose oxidase (GOx) enzyme [236]·[237]·[238]·[239]. Both enzyme-based [253] and enzyme-less [254]·[255]·[256]·[257] detection of glucose in the human body has been executed using DPV. The enzyme-less electrode delivered superior results compared to the enzymatic one. The sensing material for the enzymatic electrode is ferrocene with two boronic acid and hexamethylene functionalized by AuNWs [253]. Conversely, non-enzymatic electrodes utilize PtAu and PtNPs deposited on MWCNTs and Au disk, respectively.

CV, a prevalent electrochemical sensing techniques for detecting glucose in the human body, has been reported for both enzymatic [267]·[271]·[272]·[275]·[276]·[277] and

non-enzymatic [97][268][269][270][254][273][274][278][279][280] electrodes. Glucose sensing electrodes can be categorized in three groups; for blood [269][270][271][272][273][274][277][278][279], for sweat [275], and for both analytes [97][268][276][280]. The sensing layer of enzymatic glucose electrodes comprises α -CD SAM, chitosan, DHP, 1-naphthylamine, and o-PDA. However, all these sensing layers are functionalized by Au films or nanoparticles, which can be prohibitively expensive for mass production. The sensing surface of non-enzymatic CV-based glucose sensors are Cu-oxides, Au-MPs/NPs/NWs/NFs, DGNs, Ti, and BDD deposited on GCE, ITO, thin Gu etc.

Table 3-6 showcases that nonenzymatic amperometric glucose sensors [254][291][292][293][294][295][296][297][298][280][299][300][301][302][303][304][305][306][307][308][309][310][311] show promising prospects over enzymatic [287][288][289][290] sensors. Among the enzymatic amperometric glucose sensors, the electrode fabricated by Li et al. (2020) using CoS-functionalized MWCNTs with a GOx surface layer exhibits an excellent sensitivity of $15000 \mu\text{A mM}^{-1} \text{cm}^{-2}$ [288]. This sensitivity may arise from the high surface-to-volume ratio of MWCNTs and the electrons transferring capability of CoS between GOx and MWCNTs. Zhang et al. (2018) fabricated a non-enzymatic electrode suitable for sweat glucose sensing, using a nickel metal organic framework supported by carbon nanotubes (Ni-MOF/CNTs), yielding a sensitivity of $13850 \mu\text{A mM}^{-1} \text{cm}^{-2}$ [294]. However, electrodes covering the linear ranges of both sweat and blood primarily rely on nanoparticles of noble metals, such as Au, Pt, and Ni, which impedes their mass production [298][280][300][301][302][311]. In contrast, non-precious transition metal oxide (Cu and Co oxides) electrodes predominantly provide a

linear range for sweat glucose [306][307][308][309], making non-noble metal oxides suitable for sweat glucose monitoring and mass production.

3.3.2 Integrated Sensing Systems & Simultaneous Detection of Biomarkers

Recently, simultaneous analysis of multiple analytes in a single solution using a single electrode or multiple electrodes has been attracting attention from researchers in various fields, from disease diagnosis to food safety and environmental monitoring [314], [315]. This approach offers the most economical, rapid, and complete information on the solution being analyzed [316]. In many cases, the detection of multiple analytes is required to determine an individual's health status of [317]. Zhao et al 2016 demonstrated that an electrochemical sensor for simultaneous detection of ascorbic acid (AA), dopamine (DA), and uric acid (UA) is feasible [317]. Moreover, Fernandes et al (2014) published an article on the simultaneous voltametric determination of ascorbic acid, dopamine and uric acid on N-doped carbon nanotubes functionalized by Fe_3O_4 nanoparticles [261]. Additionally, Dursun et al (2010) presented a simultaneous determination of ascorbic acid, dopamine and uric acid using Pt nanoparticles decorated MWCNTs [233]. However, designing biosensors capable of simultaneously determining two or more analytes in a single measurement, for instance on a single working electrode in single solution, remains a significant challenge [315]. Yáñez-Sedeño et al. reviewed integrated affinity biosensing platforms that couple multiplexed SPESs, utilizing various electrochemical measurement methods, such as amperometry, electrochemical impedance spectroscopy (EIS), and square wave

voltammetry (SWV) for simultaneous detection of biomarkers [318]. Kammarchedu et al demonstrated a machine learning (ML)-powered multimodal analytical device based on a single sensing material made of electrodeposited molybdenum polysulfide (eMoS_x) on laser-induced graphene (LIG) for multiplexed detection of tyrosine (TYR) and uric acid (UA) in sweat and saliva [319]. Park et al proposed an all-in-one electroanalytical device (AED), a miniaturized electronic point-of-care (POC) device integrated with the most used electroanalytical techniques, such as amperometric, voltammetric, potentiometric, conductometric, and impedimetric techniques [320]. In simultaneous sensing, less solution is needed for analysis, enabling the practical use of matrixes that may be difficult to harvest, such as sweat or breath [321], [322]. The potential for sweat or breath to become the matrix of choice for roadside tests and wearable biosensors is increasing, as sensors can detect progressively smaller concentrations of biomarkers [316].

3.3.3 Access to Biofluids

Heikenfeld et al 2019 categorised the development of bio-analyte instruments into three waves: first, in the 20th century, the bio-fluids (Blood, and Urine) were collected and transferred to a separate analytical laboratory. Second, the early 21st century witnessed the widespread use of point-of-care diagnostics by doctors, nurses, first responders and patients. The third wave, which is currently on-going, involves patients carrying wearables devices [323]. However, challenges remain in accessing both invasive (blood, and urine), and non-invasive (saliva, sweat, tears, and breath) bio-fluids.

In modern practices, measuring the presence, concentration, and functionality of analytes in non-invasive biofluids has become increasingly important due to the rapid development of wearables devices. As a result, accessing saliva, sweat, tears, and breath has become highly significant. Saliva is primarily 99% water and is a dilute heterogenous secretion into the oral cavity [323]. The salivary glands receive analyte-rich saliva from capillaries. Due to the difficulties of collecting adequate saliva for conventional tests, there are a scarcity of sensing technologies for saliva. Moreover, sensing in saliva is vital when immediate test feedback is needed for the patient.

Sweat is generated on the skin through eccrine, and apocrine glands and consists of a single tubule [324], [325]. The eccrine sweat glands serve the thermal regulation of most of the body surface and provide a good source of analyte-rich bio-fluids. In contrast, sweat from apocrine glands produces oilier and bacteria-rich composition that can confound analyte measurement. As the use of sweat as a bio-fluid is very cutting-edge technology, more research is needed in this area [326]. However, an integrated sweat stimulation has been demonstrated to ensure prolonged, continuous access to sweat [327], [328].

On the other hand, the use of tears and breaths as bio-fluids is a recent area of investigation. The challenges and prospects of using these bio-fluids are currently being studied.

3.3.4 Standardization of Measured Data by Comparing with Standard Methods like ELISA

Both Engall and Perlmann, and Van Weemen and Schuurs, independently developed the Enzyme-Linked Immunosorbent Assay (ELISA) in 1971 to circumvent

problems associated with radioimmunoassay [329]–[331]. ELISA builds upon the work of Avrameas, who used enzyme-linked antibodies in histochemistry [332], [333]. This method is a commonly used analytical immunochemistry assay that relies on the specific bond between an antigen and an antibody [334]. It is utilized for detecting and quantifying molecules, such as hormones, peptides, antibodies, proteins, and antigens (both native or foreign). Additionally, it helps to determine the intensity and type of immune response immune response, as well as the innate immunity potential [334]. The test is also applicable for determining antibodies to both native and denatured DNA [335], [336], polysaccharide antigens [337]–[339] and phospholipids [340]. As ELISA is widely accepted and used, to evaluate the applicability of neurotransmitter, protein, and glucose biosensors, the experimental data of the sensor must be compared with the standardized results of ELISA for the specific bio-analyte.

3.3.5 Analyzing Large Data using Machine Learning

Given the rise of personalized healthcare monitoring systems equipped with integrated simultaneous electrochemical biosensors, and non-invasive wearable devices with wireless data communications, there is a need handle massive and complex data with sophisticated analytical tools [316], [341]–[345]. These systems can generate a wide range of sensing data using various biofluids, which exceeds the human capacity for processing [341]. This necessitates an analytical technique that can provide an easy, fast, and accurate results of disease conditions, as well as predictions of health conditions. As such, cutting-edge deep learning methods, such as artificial neural networks (ANN), can be combined

with artificial intelligence (AI) via machine learning (ML). This combination can be used to reduce noise, eliminate redundancy, minimize dimensionality, and make decisions about diseases and their future directions [341], [346], [347]. The deep learning process fundamentally equips ANNs with the ability to mimic the human brain which is the essence of AI, through supervised, unsupervised, and reinforcement training algorithms [347]. Individual diseases can be analyzed using AI by evaluating biomarkers and symptoms [348], [349].

Support Vector Machine (SVM)

The support vector machine (SVM), a supervised ML algorithm, has been used to extract features by reducing data dimensionality for heart failure patients with reduced ejection fraction (HFrEF) in the presence of chronic kidney disease (CKD) [350]. Rajliwall et al (2019) used SVM to classify cardiovascular disease (CVD) data from a wearable sensor [351]. Additionally, an electronic nose, ‘Cyrano 320’, was used to collect breath exhale data, which was then analyzed using SVM to differentiate lung cancer patients [352]. SVM has also used as a predictive algorithm for the early prediction of asthma [353], and analyzing normalized glucose concentration data collected from saliva [354]. Furthermore, SVM has been used as a feature selector predictive model for chronic hepatitis-B (HBV) [355] and to classify early liver toxicity based on gene biomarkers [356].

Random Forest

This is a supervised ML algorithm, widely popular for classification and regression tasks. Rajliwall et al (2019) used a random forest classifier to determine the risk for CVD

patients [351]. This model has also been used to extract features from large-scale clinical data for chronic hepatitis-B (HBV) [355].

Artificial Neural Network (ANN)

Combined mixed potential four-electrode electrochemical sensors have been used to detect methane in natural gas, a potential cause of CVD [357]. The ANN was used to analyze the data with 3-layer structure, featuring 3-input nodes and 3-output nodes. ANN has also been used to analyze genetic data of a prostate cancer-specific DNA sequence (PCA3) [358]. Furthermore, the ANN algorithm has been successfully used in identifying triple-negative breast cancer (TNBC), a complex molecule to diagnose [359]. ANN was also used to identify the stage of cancer with a remarkable accuracy of 90% [192]. Additionally, the ANN was used to identify lung cancer using data from an electronic nose [360]. Dorner et al. (2019) used ANN to classify glucose level data from saliva samples [354].

There have also been articles published on unsupervised learning. One such article used unsupervised learning to analyze dementia among Alzheimer's patients [361]. Data was processed using a non-invasive biosensor to identify heart rate variability (HRV).

3.4 Conclusions

In this review, we provide an overview of the fundamental concepts and parameters of analytical chemistry and their applications in various electrochemical sensing methods. The potentiometric technique, while useful, has drawbacks related to temperature and

media dependence, the need for a matrix-dependent formal potential, and junction potential. These limitations, along with factors such as specific analyte dependency and agitation, also apply to other techniques like coulometry, stripping voltammetry, and hydrodynamic voltammetry. Redox reactions, which are key in human physiology, can be analyzed with these techniques in various health contexts, including diabetes, brain diseases, aging, and more. Among these techniques, cyclic voltammetry and amperometry, which requires a single applied potential, are popular in research. Despite drawbacks, recent developments in sensor technology keep the potentiometric technique relevant. However, some techniques like controlled potential coulometry and controlled-current coulometry have significant limitations. Voltametric techniques like cyclic voltammetry are widely used for electrode surface characterization despite their limited voltage range. The amperometric technique emerges as the best fit for lab-in-box health monitoring system due to its simplicity and efficiency. Monitoring systems equipped with ANN capabilities can facilitate the diagnosis and classification of chronic diseases, as well as monitor disease status.

Chapter 4

Nonenzymatic Electrochemical Sensors via Cu Native Oxides (CuNOx) for Sweat Glucose Monitoring

This chapter is our published work ‘M. M. Alam and M. M. R. Howlader, “Nonenzymatic electrochemical sensors via Cu native oxides (CuNOx) for sweat glucose monitoring,” *Sens Biosensing Res*, vol. 34, p. 100453, Dec. 2021, doi: 10.1016/J.SBSR.2021.100453.’

Diabetes is a chronic disease, which is the seventh leading cause of death worldwide. The increased risk to the health of diabetic patients, with comorbidities in harsh situations like COVID-19 pandemics, necessitates real-time monitoring of blood glucose. Monitoring of blood glucose is invasive, hence, sweat glucose monitoring can be an alternative approach to address the invasive issue in blood glucose monitoring. This work reports a facile, low-cost, high-performance nonenzymatic copper (Cu) native oxide (CuNOx)-based electrochemical sensor for sweat glucose sensing. We utilized a very thin Cu native oxide of ~10 nm on Cu thin film for the sensing because of the excellent catalytic oxidation behavior of cuprous oxide (Cu₂O) to glucose. The anodic sweep of cyclic voltammetry of glucose showed that the hydroxyl ions from sodium hydroxide convert the electrode surface into different oxides [Cu(I), Cu(II) Cu(III)], which electro-oxidize glucose to gluconolactone, then eventually to gluconic acid resulting in oxidation current. The CuNOx sensors exhibited a sensitivity of 603.42 $\mu\text{A mM}^{-1} \text{cm}^{-2}$, a linear range beyond the desired limit of 7.00 mM with excellent linearity, and a low limit of detection of 94.21 μM . Excellent repeatability and stability (stable >1 year) with relative standard deviation

(RSD) of 2.67%, and 2.70%, respectively were achieved for 1 mM glucose. The selectivity with common interferants of glucose in human sweat and blood showed an RSD of 3.56%. We believe the electrocatalytic efficacy of the CuNO_x sensors for glucose sensing can open a new prospect in the fabrication of wearable sweat glucose sensors.

4.1 Background

Diabetes is a chronic disorder, which is caused by uncontrolled blood sugar, and it is the result of ineffective use or the deficiency of insulin in the body. Diabetes causes blindness, kidney failure, heart attack, stroke, and serious damage to the nerves and blood vessels. It is the seventh leading cause of death worldwide. According to the World Health Organization, diabetes directly caused an estimated 1.6 million deaths in 2019 [28]. It has been reported that illnesses associated with metabolic syndrome including diabetes act as comorbidities by putting excess strain on the organ systems affected by COVID-19 [30]–[32]. Therefore, early detection of diabetes through real-time monitoring of glucose is critical to prevent complications caused by low blood glucose and can save lives.

Blood is the gold standard of glucose biomarkers. Extraction of blood is invasive and hence, regular blood harvesting can infect patients. In contrast, sweat glucose sensing is non-invasive. [362]. It is well-known that there is a metabolic correlation between sweat and blood glucose levels [363][7]. Therefore, sweat glucose sensors, especially electrochemical sensors, become attractive for wearable applications. Some key advantages of these sensors include rapid collection, sampling, and storage of sweat (fluid handling) under various environmental conditions (humidity, temperature, and wet settings) with

adequate power and memory capacity for continuous operation (energy requirements) [364]. Electrochemical sensors exist mainly in two kinds: enzymatic and nonenzymatic. Enzymatic sensors offer high sensitivity. They are expensive, less stable, and have a shorter shelf-life compared with nonenzymatic sensors [83]. The latter also offers outstanding sensitivity, ultra-low limit of detection, and prompt response [83], [316], [345].

For nonenzymatic glucose sensors, metal oxides including copper oxides, possess excellent electrochemical and electrocatalytic activity on the oxidation of glucose, enhancing electron-transfer kinetics [365]. Copper oxides can easily be synthesized, and they are bio-compatible, and chemically stable [366]. Moreover, while elementary copper is unstable, copper oxide nanomaterials are relatively stable for electroanalysis, hence, appealing for nonenzymatic glucose sensors [367]. Depending on the valence state of copper, there are two copper oxides: cuprous oxide (Cu_2O) and cupric oxide (CuO). Both copper oxides are p-type semiconductors because of copper vacancies in the lattice [368]. The Cu_2O has direct band gaps between 2.0 and 2.17 eV with the highest hole mobility of $100 \text{ cm}^2\text{V}^{-1}\text{s}^{-1}$ at room temperature, 25 °C [369], and the CuO has an indirect bandgap of 1.2 to 1.9 eV [370]. Since the reduction-oxidation (Redox) potentials of Cu oxides (Cu_xO) lie within their bandgap energies [371]–[373], these semiconductors are excellent catalysts in wet air [374], electrochemical, and photoelectrochemical oxidations [55].

Understanding the electrochemical properties of Cu_xO enables fabrication of sensors towards sweat glucose sensing. There are many viable structures for glucose sensing related to Cu and its oxides, including Cu pillars [375], Cu micropillars [376], Cu nanorods [377], Cu_2O porous microcubes [378], Cu_2O hollow nanocubes [379], Cu_2O hollow nanospheres

[380], CuO porous films [381], CuO micro/nanostructures [382], [383], CuO microneedles [384], CuO microflowers [384], CuO nanoparticles [385], CuO nanorods [386], CuO nanowires [387]–[390], CuO nanofibers [391], CuO nanospheres [392], Cu/Cu₂O microstructures [393], Cu/Cu₂O hollow microspheres [394], Cu₂O nanosheets on Cu nanowires [395], Cu/Cu₂O hybrid nanocomposites [396], Cu/Cu₂O porous nanoparticles [397], and Cu/CuO nanoflowers [398]. The roles of the semiconducting nature of Cu oxides in glucose sensing, however, are not yet clarified.

Existing technologies for fabricating sensors require various chemicals and complicated processes like a deposition in high-vacuum pressure and high temperature. These processes could change the chemical state of the investigated copper or copper oxide layers of the thin films. In addition, these processes are expensive. In contrast, native oxide of Cu-thin film-based glucose sensors are easy to fabricate using a low-cost fabrication technique [399]. However, there is no reported research work on structural and performance analysis of naturally grown native oxide Cu-based glucose sensors to the best of our knowledge. While the native oxides of Cu are stable, materials analyses and insights into their electrochemical efficacy, including sensitivity, stability, and selectivity will be imperative for glucose sensing.

In the present work, we report Cu native oxide (CuNO_x)-based low-cost, high-performance nonenzymatic glucose sensors. First, we investigated chemical compositions and electronic bonding states, then performed structural analysis of the CuNO_x electrode using an X-ray photoelectron spectroscope (XPS) and a high-resolution transmission electron microscope (HRTEM). Finally, we developed a simple, facile, and robust

fabrication process for the glucose sensors using the CuNO_x grown on commercially available Cu thin foils at ambient. The CuNO_x sensing electrodes showed excellent performance in the presence of some interferants in sweat, covered a linear range of sweat glucose and beyond (0.05-7.00 mM), and offered the best trade-off between sensitivity and fabrication process in comparison to other Cu/Cu₂O/CuO based glucose sensors.

4.2 Experimental Procedure

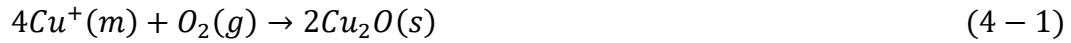
4.2.1 Chemical & Reagents

D-(+)-glucose (Dextrose, C₆H₁₂O₆, ≥ 99.5%), Sodium Hydroxide (NaOH, ≥ 98%), Acetaminophen (APAP, CH₃CONHC₆H₄OH, ≥ 99%), Dopamine Hydrochloride (DA, (HO)₂C₆H₃CH₂CH₂NH₂·HCl), L-Ascorbic Acid (AA, C₆H₈O₆, ≥ 99.0%), Uric Acid (UA, C₅H₄N₄O₃, ≥ 99%), L-Cysteine (Cyst., HSCH₂CH(NH₂)CO₂H, ≥ 97%), Sodium Chloride (NaCl, ≥ 99.5%), Potassium Chloride (KCl, ≥ 99%), were purchased from Sigma-Aldrich. The 35 μm thick Cu foil was also purchased from Sigma-Aldrich. All the chemical reagents used in our research are of analytical grade and used without further purification. All solutions were prepared with 18.2 MΩ.cm deionized (DI) water which prepared by deionized water of resistivity 18.2 MΩ.cm from a purifier ELGAPurelab Ultra Water Purifier at 25 ± 2 °C.

4.2.2 Formation of Native Oxide of Copper

We prepared a thin layer of oxides on the surface of Cu thin foil under room temperature and pressure. This composite is known as Cu native oxide. Here, we briefly deciphered the

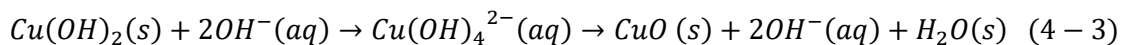
formation of native oxide of Cu. It is a continuous and very slow process of oxidation of the Cu surface [400]. Generally, the Cu oxide layers may form through three distinct but simultaneous steps. Firstly, the Cu metal surface starts to convert into the Cu_2O as soon as it is exposed to air by an induced electric field, which can be described as the following reaction, given in equation (4-1) [401], [402].



The process is influenced by an electric field induced between Cu metal and adsorbed oxygen layer due to Cu cations at metal-oxide interface and oxygen anions at the oxide-air interface [403], [404]. Initially, the oxidation of the Cu surface is accelerated by the field-enhanced ionic transport in between the Cu metal and oxygen layer interface, which depends, basically, on the concentration of adsorbed oxygen. The effect of the induced electric field becomes less as the thickness of the oxide layer increases. As a result, the oxygen concentration dependency becomes negligible, and the growth rate attenuates. Secondly, the metastable formation of $\text{Cu}(\text{OH})_2$ as a wetting layer on Cu_2O is the function of hydroxyl ion (OH^-) concentration on the surface of Cu_2O . The hydroxyl ion interacts with the Cu ions that migrate to oxide-oxygen layer and can be represented as reaction shown in equation (4-2) [401].



Finally, the $\text{Cu}(\text{OH})_2$ layer is converted to a stable CuO layer. The conversion is fast at ambient conditions with higher humidity. The process can be expressed as equation (4-3) where $\text{Cu}(\text{OH})_4^{2-}$ is known as tetrahydroxocuprate anions [401].



4.2.3 Preparation of Working Electrode

We prepared the sensing electrode by using the Cu native oxides, as discussed in 2.2. These oxide layers can easily be reacted with glucose in the presence of 0.1 NaOH. We used commercially available 35 μm thick Cu thin foils.

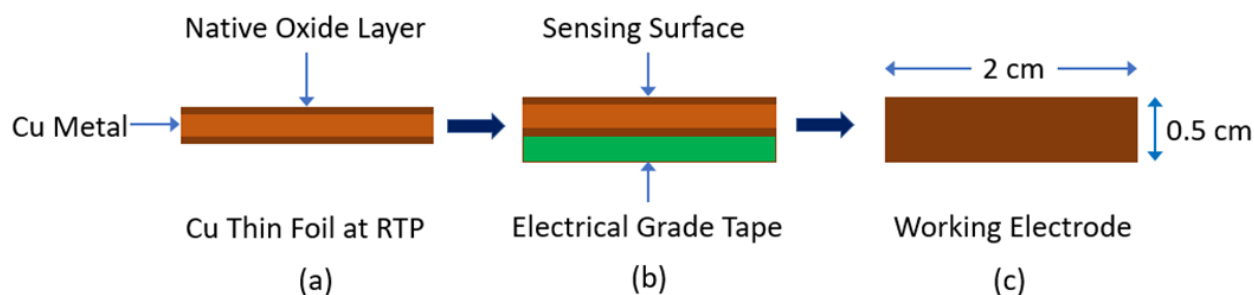


Fig. 4-1. Schematic representation of working electrode preparation. Cross-sectional view of (a) The thin Cu foil at room temperature and pressure (RTP); (b) the foil after attaching with electrical grade scotch tape that covered the oxide layer of one side as well as works as substrate. (c) The dimension of the sensing surface of the electrode for electro-oxidation of glucose using Cyclic Voltammetry. Note: Working electrode and sensing electrode are interchangeably used.

The foils were kept in a dry environment of 25°C (room temperature) and normal pressure, and humidity. The storage time of the foil is more than 2 years which is enough to be stable for the growth of the oxide layers. Previously, the thicknesses and the stability of the grown Cu native oxide layers were investigated. In the case of thin film, the thickness of Cu_2O can be grown to 5.70 nm within 66 days from the first exposure to air and becomes stable [401]. Finally, the CuO layer started to grow at around 24 hours and continued to increase in thickness with the increase of exposure time, reaching about 1.0 nm after 112

days and becomes stable [401]. The overall thickness of the composite oxide grew between 2.5 and 6.70 nm after exposure to air [401], [405]. In this research, the native oxide layers have been grown on thin Cu foils kept at ambient conditions for more than 2 years. We chose the time to make sure that the full-grown oxide layers are fully stable.

If both sides of the foil have the same exposure to ambient conditions, the thickness of the oxide layer might be the same on both surfaces of the foil. Moreover, the raw thin foil is not suitable to be handled due to its tractability, high ductility, and low tensile strength. So, electrical-grade scotch tape is used as substrate attaching on one of the surfaces of Cu thin foil (Fig. 4-1(b)). The technique is very simple as well as more suitable than a substrate, which needs a physical and/or chemical process for the fabrication of the sensing electrode. The tape offers wearability, protects the sensing electrode from oxidation, and controls the sensing area.

4.2.4 Electrochemical Sensing Method

Electrochemical measurements, including cyclic voltammetry (CV), were performed using a three-electrode PalmSens EmStat 3 potentiostat with PSTrace 4.8 software. All experiments were done at room temperature (25 ± 2 °C) using a platinum (Pt) wire as a counter electrode and a silver (Ag) wire coated with silver chloride (AgCl), widely known as Ag/AgCl electrode as a reference electrode. Both counter and reference electrodes were purchased from CH Instruments Inc. USA. The working electrode of length 2 cm and width 0.5 cm (sensing surface area of 1 cm^2) was prepared for electrochemical measurements of glucose oxidation. The working electrode was evaluated as a glucose sensor in an aqueous of 0.1 NaOH solution. There was not any special procedure done before each

electrochemical measurement such as cleaning and stirring. Each experiment was done simply by dipping the working electrode in the glucose aqueous solution with sodium hydroxide (NaOH) alkaline solution.

4.3 Results and Discussion

4.3.1 Chemical Elemental Characterization

We investigated the chemical elemental species of the Cu native oxide electrode using an XPS to explore the compositions and the role of the electronic bonding states of the electrode. Fig. 4-2. (a) shows the representative wide scan XPS survey spectra of the electrode surface of the metallic and their oxides phases in the binding energy range of 0—1000 eV. The survey confirms the Cu core level doublet peaks of $\text{Cu}_{2p1/2}$ and $\text{Cu}_{2p3/2}$ at 952.0 and 932.0 eV, respectively, with a spin-orbit splitting of 20 eV, Cu_{3s} at 122.0 eV, Cu_{3p} at 75.0 eV, and Cu_{3d} at 3.0 eV along with peaks of oxygen, O_{1s} , at 532.0 eV and carbon, C_{1s} , at 285.0 eV. This is in good agreement with the values reported in the literature [406]–[408]. The strong oxygen and carbon peaks in Fig. 4-2. (a) are adventitious oxygen and carbon peaks that occur due to the reaction of copper with atmospheric oxygen and contamination from air-formed film on the surface [409], [410]. The wide scan survey also represents that the existence of Cu^{2+} ions through the satellite peaks on the high binding energy side of the main peaks which connects with an open $3d^9$ shell of Cu [411].

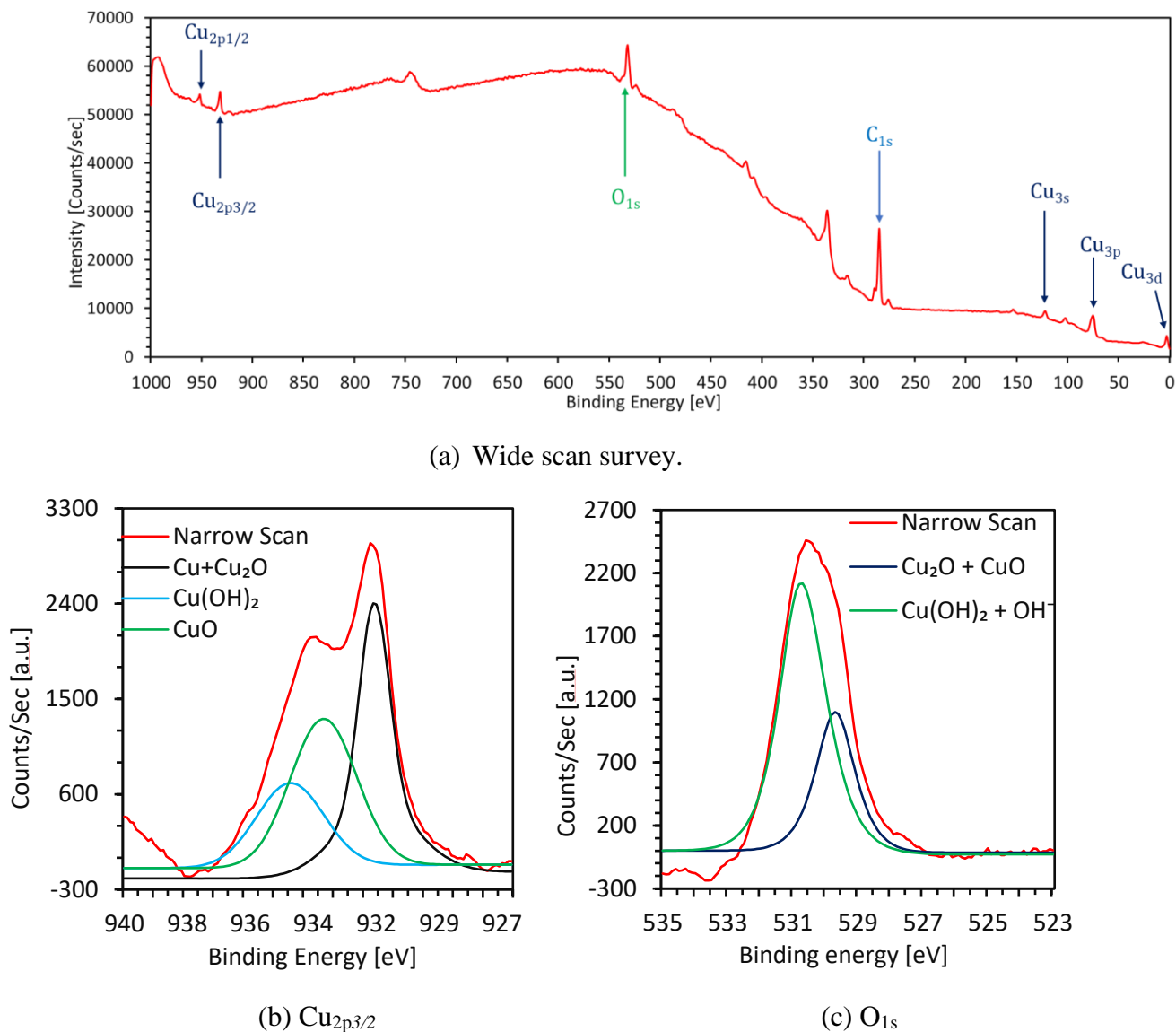


Fig. 4-2. (a) Wide scan XPS spectrum, and deconvolved high-resolution narrow scan for (b) $\text{Cu}_{2p_{3/2}}$, and (c) O_{1s} spectra of the naturally grown Cu native oxide surface of the electrode.

We further investigated high-resolution narrow scan of $\text{Cu}_{2p_{3/2}}$ and O_{1s} for more detailed qualitative and quantitative information about the oxide layers of the electrode surface. The high-resolution spectra of $\text{Cu}_{2p_{3/2}}$ and O_{1s} with curve-fitting components are presented in

Fig. 4-2. (b), and Fig. 4-2. (c), respectively, where the deconvolved components were achieved using Gauss-Lorentz (70–30%) method [412]. As in Fig. 4-2. (b), the different chemical states of the electrode are metallic Cu at 931.58 eV, Cu₂O at 931.45 eV, CuO at 933.27 eV, and Cu(OH)₂ at 934.38 eV. The binding energies are consistent with the values reported in the literature [401], [413], [414]. Since the relative shift of Cu and Cu₂O peaks in binding energy is tiny, 0.13 eV only, both grouped together [401], [415], [416]. The full width at half maximum (FWHM) values of Cu+Cu₂O, CuO, and Cu(OH)₂ are 1.20, 1.30, and 1.33 eV, respectively.

The deconvolved O_{1s} spectra provide three chemical bonding states of Cu oxides: Cu_xO (Cu₂O & CuO), hydroxides radicals, (OH⁻ & Cu(OH)₂) and water (H₂O) [401]. In Fig. 4-2. (c), there are two deconvolved peaks at 529.60 eV and 530.61 eV. The first peak has FWHM and intensity of 1.40 eV and 1192.50, respectively. The second peak has FWHM and intensity of 1.60 eV and 2117.55, respectively. The first and second peaks are mostly attributed to the chemical bonding of the lattice O²⁻ and surface (adsorbed O⁻ and/or OH⁻) oxygen species, respectively [413]. The peaks at 529.60 and 530.61 eV correspond to Cu_xO and Cu(OH)₂+OH⁻, respectively. In addition, we observed an extremely low-intensity peak of the H₂O and neglected it. The controlled ambience of a cleanroom (10000-class) can contribute to achieving water-free Cu oxides. In contrast, in Ref [401], the peak intensity of H₂O was significantly high, which attributes to the wetting layer due to the high relative humidity at ambient conditions [401].

4.3.2 Morphological and Structural Characterization

We analyzed the Cu oxide thin films using an HRTEM to get more insights into the morphology and structural features of the sensing electrodes. Fig. 4-3. (a) shows the oxide growth is not uniformly distributed on the Cu metal surface. This inhomogeneous formation of the oxide layers is opposite to the previous findings [403], [404], [417]–[420]. Also, the growth of the oxide layer depends on the lattice defects, the microstructure, and the surface morphology of the Cu films [405]. Fig. 4-3. (b) shows a typical surface morphology of Cu film with inhomogeneous oxide, which may be due to high surface roughness, small grains, and low purity of the thin film. It is clear from Fig. 4-3. (a), and Fig. 4-3. (b) that the native oxide layers can grow higher than 10 nm, which was about 6.7 nm in Ref [421] after keeping the foil 112 days in ambient. This behavior is suitable for a high oxidation rate of Cu, which magnifies the electric field and affects the number of ion lattice vacancies [422]–[424]. The contact potential difference between metal and oxide layer creates Cu ion vacancies in the metal lattice driving Cu ions and electrons to the oxide-air interface to form more Cu₂O absorbing O₂ molecules without much help from temperature [425], [426]. The grains on rough surfaces cause higher surface energy at the grain boundaries that increase the concentration of OH⁻ on the thin film, which is a crucial part of converting Cu₂O to the final layer CuO [401].

Fig. 4-3. (c)—(f) show the energy dispersive X-ray spectroscopy (EDS) mapping of the native Cu oxide surface at ambient conditions. The surface possesses Cu and O, with a small amount of adventitious carbon. The EDS and XPS results are complementary and support the other studies [409], [410]. Fig. 4-3. (g) is the Fast Fourier transform (FFT) of

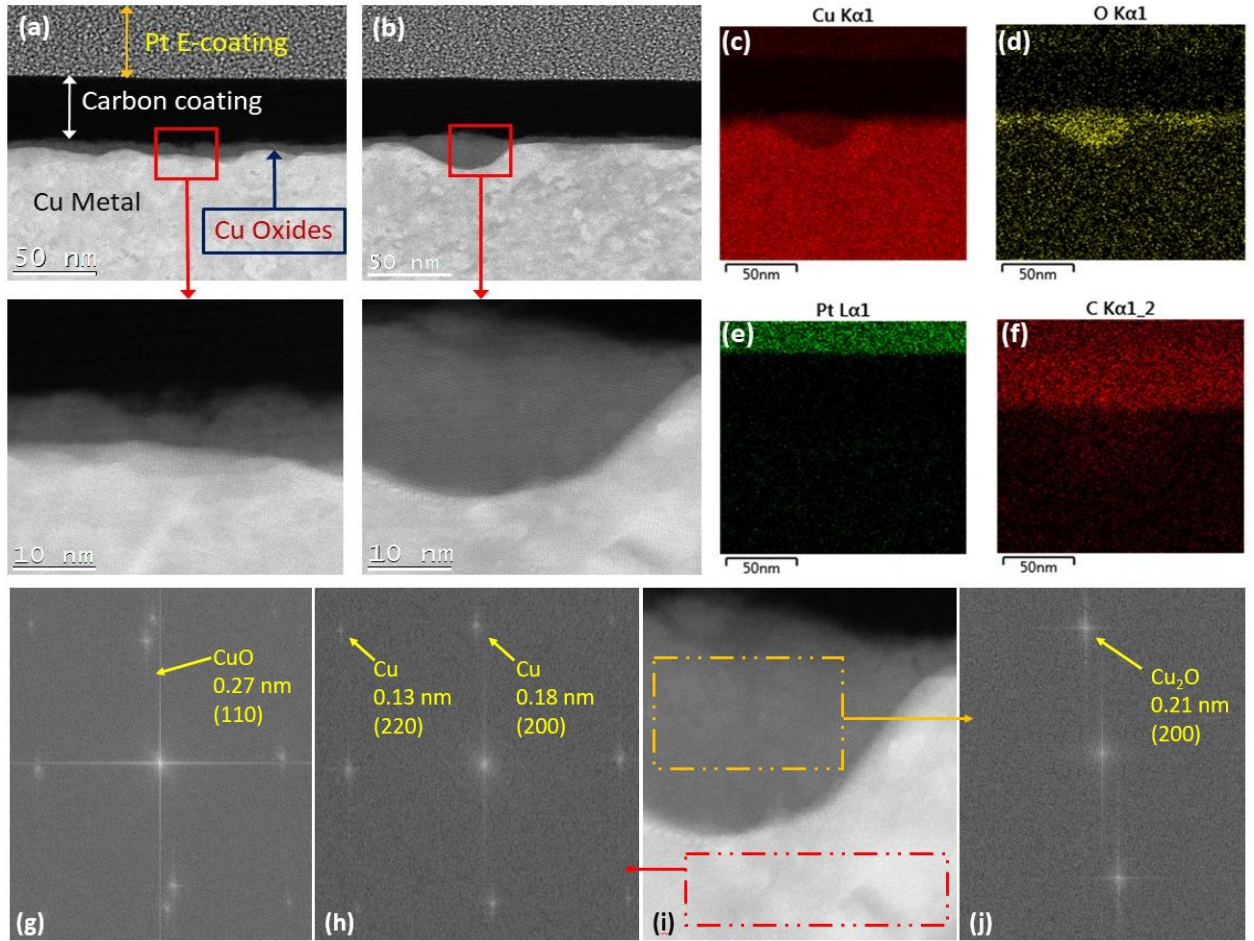


Fig. 4-3. HRTEM image shows (a) the growth of Cu oxides is not uniform, (b) the surface morphology affects the growth of the oxide hugely. (c)—(f) EDS images of (b) shows distribution of Cu, O, Pt and C. (g) FFT image of (i), (h) FFT image of Cu metal, red dotted box of (i), and (j) FFT image of Cu₂O, yellow dotted box of (i).

Fig. 4-3. (i), which shows the presence of twin crystalline Cu metal, single crystal Cu₂O, and single crystal CuO in the HRTEM image of the electrode. Moreover, the Cu and Cu₂O FFT are processed using a yellow dotted box and a red dotted box of Fig. 4-3. (i), respectively. The technique has been used to separate FFT data of Cu metal from Fig. 4-3. (g). So, the thin Cu foil's lattice spacings are 0.13 and 0.18 nm of the plane (220) and (200),

respectively. However, the inter-planar spacing of Cu_2O is 0.21 nm of the plane (200), as shown in Fig. 4-3. (j), which is in good agreement with previous results [427]. The d spacing of CuO is 0.27 nm, which corresponds to (110) plane [428]–[430]. The intensity difference between Cu_2O and CuO FFT data clearly shows that the CuO width is very thin compared to Cu_2O , which greatly matches other investigational data [401], [405].

4.3.3 Cyclic Voltammetry of Glucose

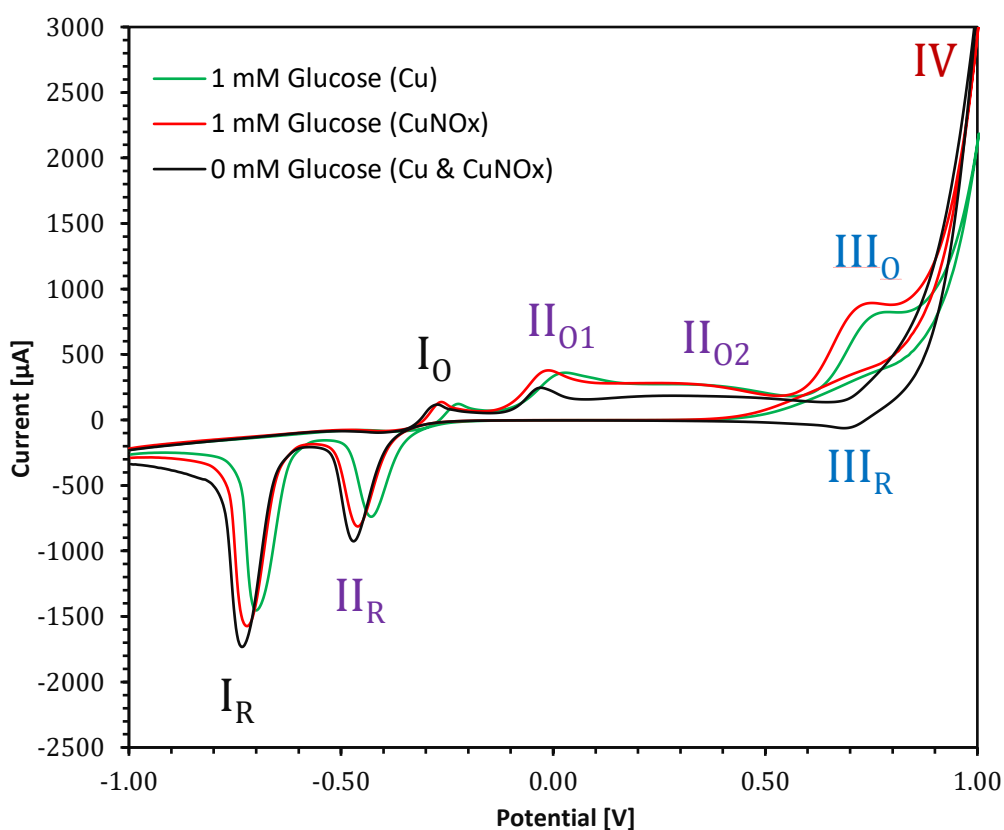


Fig. 4-4. Cyclic Voltammograms of Cu and Cu native oxide (CuNO_x) electrodes with and without glucose at 30 mVs^{-1} scan rate in 0.1 M NaOH solution.

In this section, we systematically investigated the electrochemical behavior of the Cu native oxide (CuNO_x) thin film-based electrode for the sensing of glucose. The various accessible oxidation states, $\text{Cu}(0)$, $\text{Cu}(\text{I})$, $\text{Cu}(\text{II})$, and $\text{Cu}(\text{III})$, make Cu an excellent electrocatalytic transition metal through a reaction via both one- and two-electron pathways

[431]. The electrode was characterized electrochemically for glucose electro-oxidation in 0.1 M NaOH alkaline solution to get a higher peak current at a lower potential, and lower background noise of glucose electro-oxidation [432].

Electro-Oxidation Mechanism

Fig. 4-4 shows the electrocatalytic behavior of the Cu and Cu oxide electrodes in 1 mM concentration of glucose with 0.1 M NaOH solution at scan rate of 30 mVs⁻¹. The voltammograms show eight peaks (I_O, II_{O1}, II_{O2}, III_O, IV, III_R, II_R, and I_R) in the anodic and cathodic sweeps of the CV, where I_R and I_O are reduction-oxidation (redox) pairs. Seven of them are significant peaks. There are three redox pairs peaks and the IV represents the water breakdown peak. These peaks are compared with the literature data of the voltammograms of Cu and Cu oxide electrodes, as shown in Table 4-1. Ref [433] reported two distinguishable peaks of oxidation peak of the I_O. Most of the other works, including this work, demonstrated two separate peaks of the second oxidation peak, II_O. Among all reported research results, shown in Table 4-1, the CuNO_x electrode provides the lowest oxidation current in NaOH solution without glucose (blank solution) (see Fig. 4-4). This indicates that the CuNO_x sensor generates the lowest background noises.

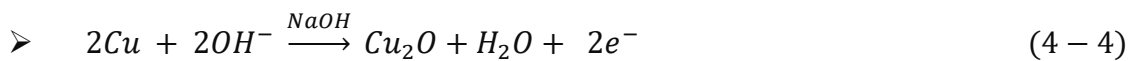
Table 4-1: Summary of voltammogram data of Cu, and Cu oxides-based nonenzymatic sensors in presence and absence of glucose from Fig. 4-4 in comparison with that of literature.

CV Sweep		Anodic					Cathodic			Ref.	Electrodes	
Glucose	Peaks	I _O		II _O		III Glucose	IV (H ₂ O Split)	III _R	II _R			I _R
		I _{O1}	I _{O2}	II _{O1}	II _{O2}							
Potential [V]	0 mM	-0.75		-0.35		Nil	0.30	0.17	-0.92	-1.27	[376]	Cu Micropillars
	1 mM	-0.75		-0.55	-0.20	0.10	0.30	0.17	-0.92	-1.25		
	0 mM	-0.40		-0.10	0.10	Nil	0.80	0.55	-0.63	-0.95	[306]	Cu Frameworks
	1 mM	-0.40		-0.15	0.13	0.44	0.80	0.55	-0.60	-0.90		
	0 mM	-0.35		-0.08	1.50	Nil	0.80	0.65	-0.42	-0.78	[434]	Nafion/Cu Nanowares
	2 mM	-0.35		-0.10		0.47	0.80	Nil	-0.42	-0.72		
	0 mM	-0.62	-0.48	-1.92	0.98	Nil	0.80	0.58	-0.63	-0.82	[433]	Cu
	1 mM	-0.62	-0.48	-1.98	1.98	0.48	0.80	0.58	-0.63	-0.82		
	0 mM	-0.24		0.00	0.30	Nil	1.00	0.70	-0.46	-0.72	This Work	CuNO _x (@RTP)
	1 mM	-0.27		-0.02	0.31	0.73	1.00	0.77	-0.45	-0.71		

Now, we provide the chemical reactions for the conversion of Cu(0) to Cu (I), Cu(II), and Cu(III) and discuss the three oxidation peaks: I_o, II_o, and III_o. The first oxidation peak, I_o, recorded around -0.25 V, both with and without glucose, may be related to the oxidation of Cu(0) to Cu(I), where metallic Cu atom is ionized and then converted to Cu₂O in the presence of the supporting aqueous solution of 0.1 M NaOH, as the equation (4-4) shown in below [435]–[438].

□ I_o

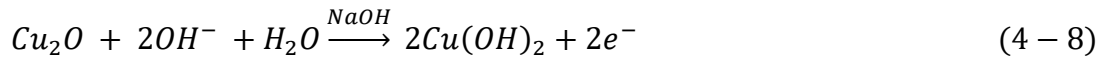
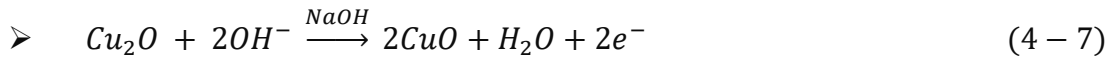
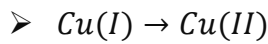
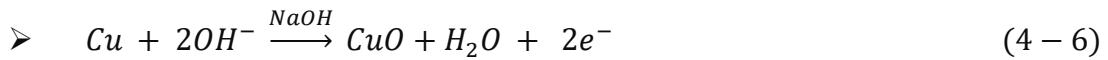
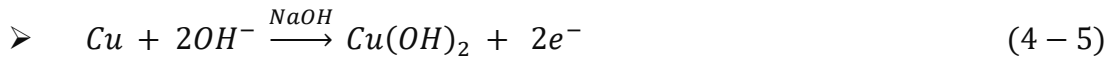
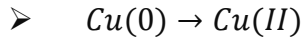
➤ Cu(0) → Cu(I)



The prior one of the second oxidation peaks, II_{o1}, around 0 V may be due to the oxidization of Cu(I) to Cu(II) and subsequent formation of CuO and cupric hydroxide, Cu(OH)₂. The last one of the second oxidation peaks, II_{o2}, at 0.30 V may be attributed to the further

oxidation of Cu(0) to Cu(II) and can be represented by specific equation (4-5), (4-6), (4-7), and (4-8) as follows [433], [434], [436], [439]–[441].

□ II_{01} & II_{02}

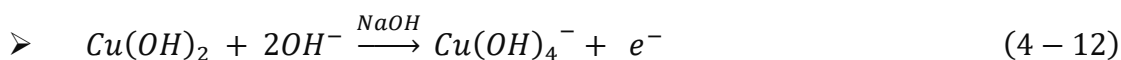
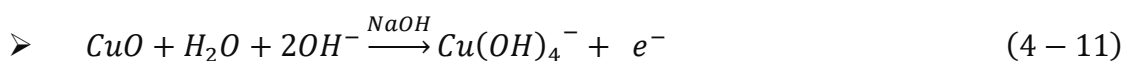
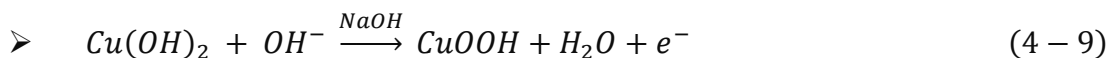


The electrodes reported in [306], [376], [433], [434], [442], mostly, generate one peak II_O , in absence of glucose and produce higher current than any amount of glucose produces. This is basically the background current. In contrast, our sensor produces lower background current with two distinguishable peaks of II_{O1} and II_{O2} .

The oxidation peak III_O at 0.73 V indicates the glucose concentration. At this peak, all the reactions convert Cu(II) to Cu(III) in the form of cumene hydroperoxide (CuOOH), hydroxyl radicals Cu(III) tetrahydroxide anion, $Cu(OH)_4^-$. The Cu(II) plays a vital role as the active substance at low potentials and donates an electron to form Cu(III). The reactions may be represented by the equations given in (4-9), (4-10), (4-11), and (4-12) below [376], [439], [443]–[446].

□ III_0

➤ $Cu(II) \rightarrow Cu(III)$



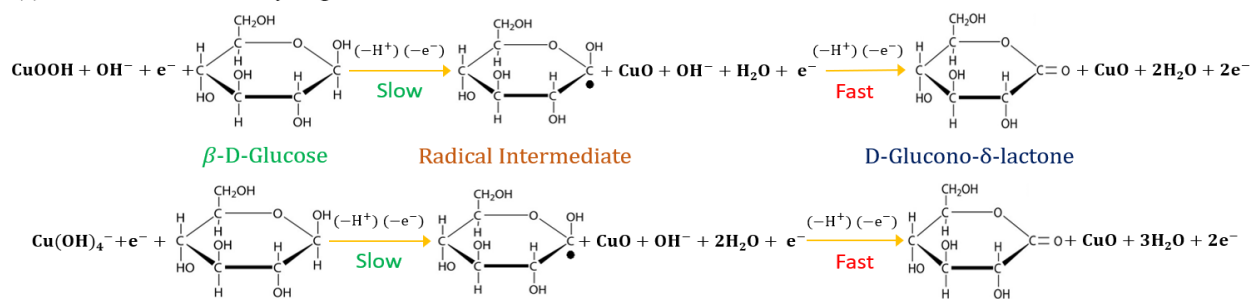
As potential increases, the adsorbed glucose molecules on the electrode surface are stripped off, due to the agitation of a strong electric field, which makes the path of interactions of hydroxyl ions converting Cu(II) to Cu(III) [447]. It is worth noting that the electro-oxidation of glucose can be attributed to the transformation of Cu(II) to Cu(III) in alkaline solution [433]. Briefly, the electrocatalytic oxidation of glucose depends on the electrons released during the electrochemical oxidation process of Cu(II) to Cu(III) [448].

After receiving the required electrons, the glucose oxidized to gluconolactone ($C_6H_{10}O_6$) is further oxidized to gluconic acid ($C_6H_{12}O_7$) as described in scheme 1, which is an irreversible reaction process [83][444], [449]. The cyclic form of glucose has been used in the reactions because, at equilibrium, it is most stable in water at room temperature [450]. The D-glucose and L-glucose are two stereoisomers of the glucose and do not mutarotate spontaneously. The D-glucose is the only naturally generating form of glucose, where L-glucose very rarely occurs. Moreover, α - and β -glucose have opposite stereochemical configurations. The human body cells consume β -glucose in the blood for

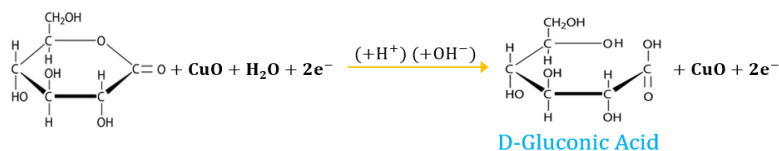
further use in glycolysis [451]. β -glucose is the preferred orientation for faster oxidation on metal-based electrode's surface, because it is four times better for electro-catalyzation [450], [452]. So, the β -D-glucose is being used for electrochemical detection and analysis.

In summary, the conversion of Cu(II) to Cu(III) and electro-oxidation of glucose occurred with the presence of OH^- and related to the amount of Cu(III), which is consistent with other research results [432]. Also, the generated Cu(II) as CuO in the scheme (a) and (b) releases an electron to the electrode surface and converted into Cu(III) as described in equation (4-10) and (4-11), resulting in significant increase of the anodic current signal [453].

(a) Glucose Oxidation & Hydrogen Abstraction



(b) Gluconic Acid Formation & Hydrolyzation



Scheme 1: Electrocatalytic oxidation of glucose; (a) Firstly, intermediate radical has been formed when glucose reacts with highly catalyst Cu(III) molecules/anions releasing one hydrogen ion (H^+) and electron (e^-); secondly, D-Glucono- δ -lactone has been formed when intermediate radical further oxidized releasing one more hydrogen ion (H^+) and electron (e^-)

); (b) Final product of glucose oxidation is D-Gluconic acid that generated when D-Glucono- δ -lactone goes through hydrolyzation process.

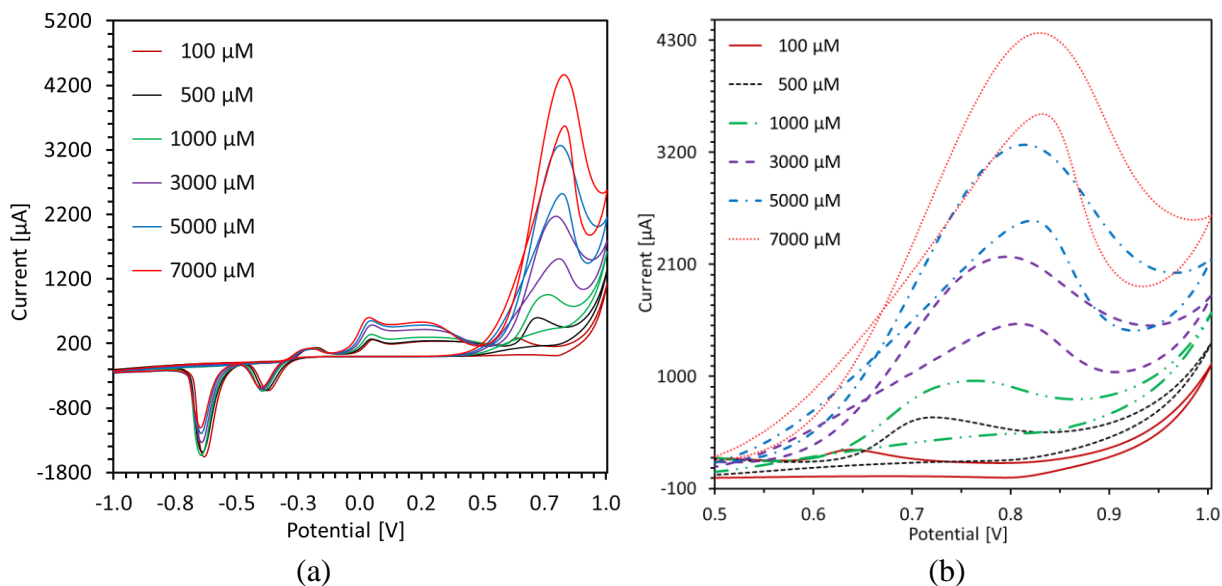


Fig. 4-5. (a) Cyclic Voltammograms of 0.1—7 mM glucose at 30 mVs^{-1} scan rate in 0.1 M NaOH solution using Cu native oxide electrode, and (b) Magnified version of (a) for the electro-oxidation peak of glucose.

Fig. 4-5. (a), and Fig. 4-5. (b) represent the voltammograms of 0.1—7 mM glucose, where more glucose electrocatalytic oxidation occurred with the increase of concentration, and C(III) could be transformed into Cu(II), simultaneously [432]. The abrupt change of current, peak (IV), can be attributed to water breakdown [383], [454], [455]. From Table 4-1 and Fig. 4-4, and Fig. 4-5, we may conclude that the water splitting peak potential depends on the maximum value of the anodic sweep of an applied CV potential.

In the cathodic voltammetric sweep, the peak III_R (see Fig. 4-4) is a broad reduction peak around 0.7 V that shows the conversion of Cu(III) to Cu(II), and it corresponds to

remaining CuOOH and $\text{Cu}(\text{OH})_4^-$. The cathodic sweep peaks for different glucose concentrations are summarized in Table 4-1.

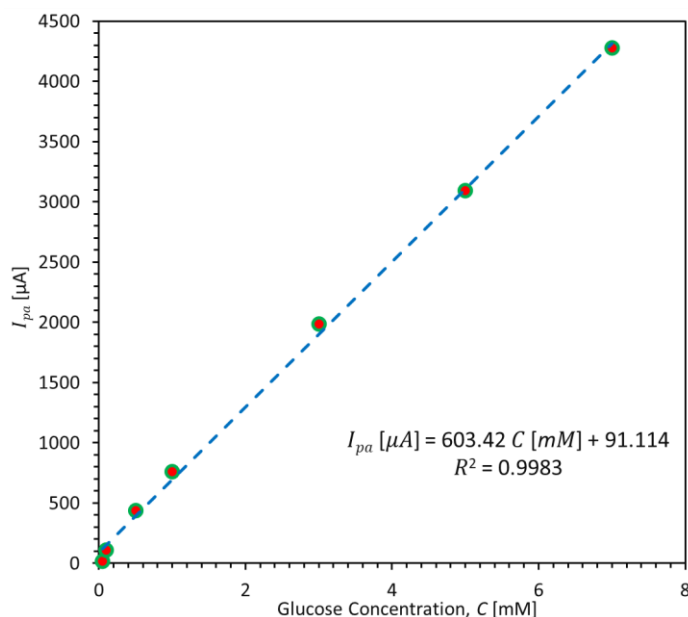


Fig. 4-6. Calibration curve illustrates the linear relationship between glucose concentration and peak oxidation current (current density) for native oxide (at RTP) electrode with correlation coefficient $R^2 = 0.9983$, at 30 mV/s^{-1} scan rate.

When considering the cathodic sweep peaks (see Fig. 4-5), it can be observed that at lower concentration of glucose, the potentials for the peak, III_R , shift towards higher potential values (see Fig. 4-4, and Fig. 4-5. (a)), and the peaks disappear at higher concentration of glucose (Table 4-1 and Fig. 4-5). This may indicate that most of the $\text{Cu}(\text{III})$ molecules are consumed by electrocatalytic oxidation of glucose [433]. The reduction peak II_R , associated with the oxidation peak II_O , at -0.45 V is the partially converted CuO to Cu_2O . It is known that the conductivity of Cu_2O film is poor, which limits the full reduction of CuO into Cu_2O at -0.45 V . Hence, the remaining CuO is further reduced to Cu at -0.7 V which is the last reduction peak. In addition, all the Cu_2O are reduced to Cu at the peak I_R

[456]. Therefore, the reduction peak I_R at -0.7 is larger than the corresponding oxidation peak I_O at -0.25 V.

Sensitivity and LOD

Fig. 4-6 shows the cyclic voltammetric calibration curve of the Cu native oxide electrode for glucose sensing. A linear relationship between the glucose concentration and the peak oxidation current in the range of 0.050—7.00 mM can be observed. This range covers the sweat glucose concentration of healthy and diabetic patients between 0.05 and 1 mM [457], and the range of blood glucose concentration of healthy persons in between 4.90 and 6.90 mM [95]. So, for the first time, we demonstrate that the CuNOx sensors detect glucose concentration ranging from 0.050 mM to 7.00 mM, as sweat glucose and beyond. The linear regression has been done and can be represented as follows:

$$I_{pa}(\mu A) = 603.42 C(mM) + 91.114 \quad [R^2 = 0.998] \quad (4 - 13)$$

From equation (4-13), the estimated sensitivity of the electrode is $603.42 \mu A \text{ mM}^{-1} \text{ cm}^{-2}$ ($0.60342 \mu A \mu M^{-1} \text{ cm}^{-2}$). The regression coefficient is 0.998. The limit of detection was estimated using the equation (4-14), where s is the standard deviation of the blank solution, m is the slope of the calibration curve, and k (=3) is the multiplying factor [458].

$$LoD = \frac{ks}{m} = \frac{3s}{m} \quad (4 - 14)$$

Based on the standard deviation of the blank solution ($18.95 \mu A$), the slope of the calibration curve ($0.60342 \mu A \mu M^{-1}$), and signal-to-noise ratio ($S/N = 3$), the estimated LoD is $94.21 \mu M$. The sensitivity and LOD of CuNOx sensors are compared with literature data shown below in Table 4-2.

Exponential and Logarithmic Characteristics

Fig. 4-7. (a) shows the peak electro-oxidation current of glucose for 0.1—7 mM concentrations. The peak current is exponentially related to the applied potential, as shown in equation (4-15). Fig. 4-7. (b) represents that the potential at the peak oxidation current is logarithmically related with glucose concentrations, presents in equation (4-16).

$$I_{pa}[\mu A] = 0.0004e^{19.428E_{pa}[V]} \quad [R^2 = 0.9844] \quad (4 - 15)$$

$$E_{pa}[V] = 0.0434 \log_e C[\mu M] + 0.4485 \quad [R^2 = 0.9838] \quad (4 - 16)$$

This is the first time we have observed these two phenomena, the exponential relations of peak current with potential, and the logarithmic relations of potential with glucose concentration. The phenomena may be explained as follows. As we know, the diffusion layer, meaning the interface width, between the electrode surface and bulk solution, is the function of the concentrations of the analyte means glucose [459]. The width decreases as the concentration of glucose molecules increases. The smaller width of the interface allows a higher rate of reactions between Cu native oxide layers and glucose molecules. Moreover, the reaction rate determines the amount of current [459]. Consequently, the higher electro-oxidation current of glucose produces a higher rate of reactions.

When the anodic sweep potential increases, the rate of oxidation of glucose molecules at the electrode surface increases. So, the anodic electro-oxidation current of glucose increases and gluconic acid is produced on the surface of the CuNO_x electrode. The gluconic acid diffuses to the bulk solution. However, the electro-oxidation current of glucose is kept increasing with potential, because higher potential diffuses more glucose

molecules from bulk solution [111]. After reaching a point, peak, the current slows down due to the wider width of the depletion region created by gluconic acid that reduces the mass transport, which is known as the ‘mass-transfer-limited’ region [111], [459]. If the glucose concentration increases, the required potential to reach the ‘mass-transfer-limited’ region also increases. Therefore, the diffusion layer width may get smaller logarithmically with the increase of concentration of glucose molecules, which is why the potential at peak oxidation is increasing logarithmically. Since the peak current is linear with the glucose concentration, as shown in Fig. 4-6, the peak current increases exponentially with the increase of the potential (see Fig. 4-7. (a)). This is why the electro-oxidation current of glucose on Cu and Cu oxides-based electrode normally covers a very wide potential region, as shown in Fig. 4-7. (a).

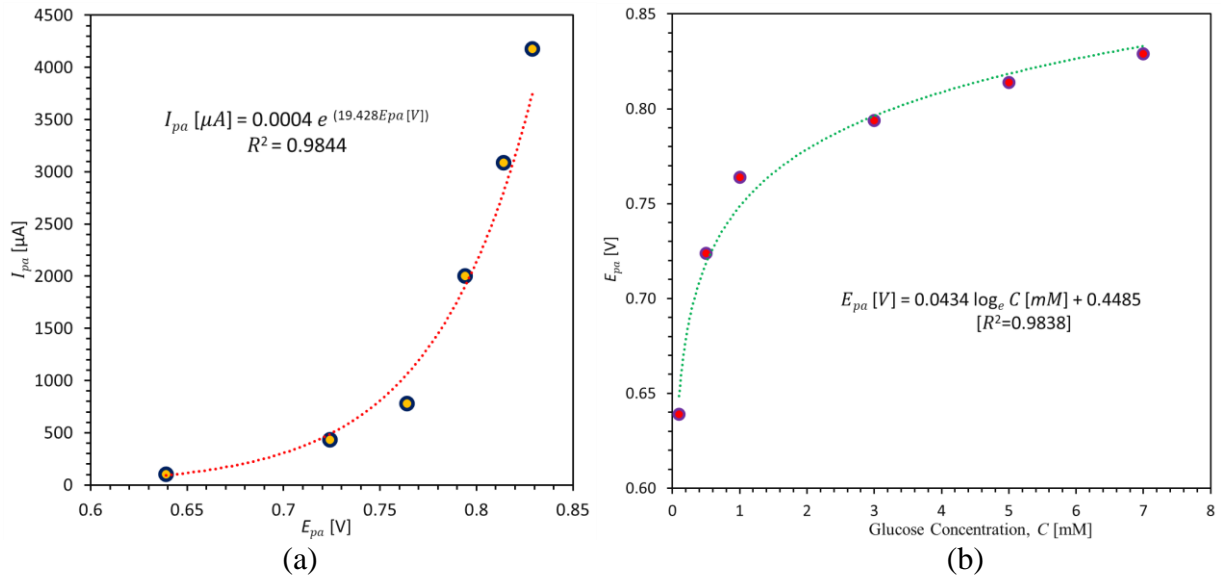


Fig. 4-7. The curve illustrates that (a) Both the peak oxidation current of glucose and associated potential are increasing with the increase of glucose concentrations, and they are exponentially related. (b) The potential at peak oxidation current of glucose is increasing

logarithmically with increase of glucose concentrations. The data has been collected from Fig. 4-5. (a).

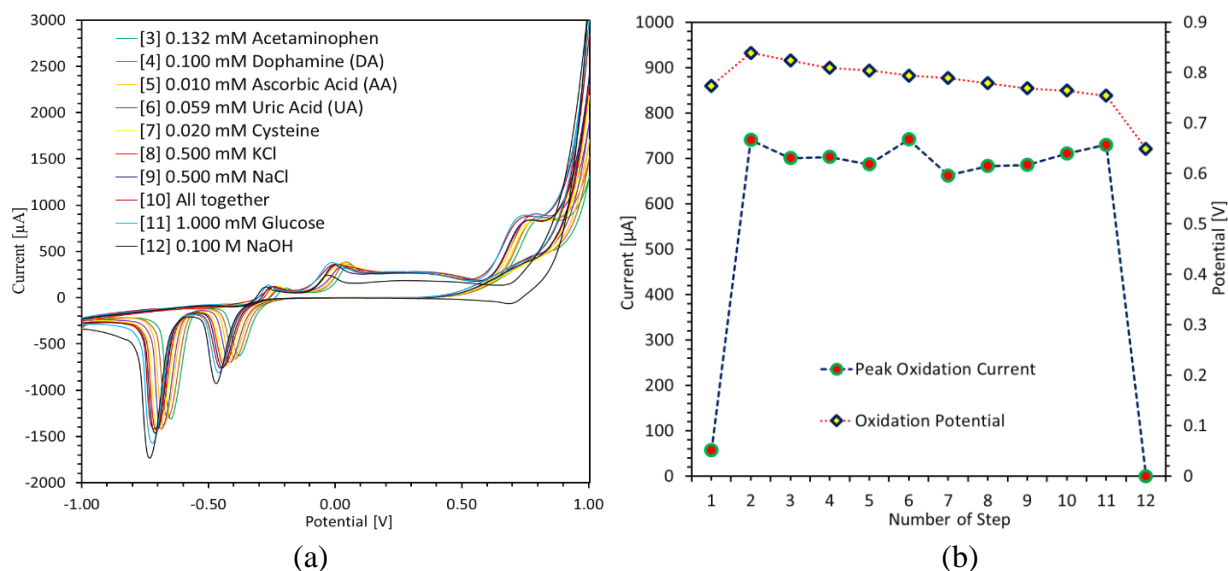
4.3.4 Interference Analysis

The CuNOx sensor should be a highly selective, rejecting interference elements, towards glucose molecules under common biomolecules. The common interferants that usually co-exist with glucose in human sweat and blood, are (a) easily oxidizable species like ascorbic acid (AA) and uric acid (UA); (b) a pain reliever, acetaminophen; (c) a neurotransmitter, dopamine (DA) and an amino acid, cysteine; as well as (d) common salts, sodium chloride (NaCl) and potassium chloride (KCl) [448], [457]. The interferent concentrations, see legends of Fig. 4-8. (a), are chosen as those generally found in blood and sweat [448], [457]. The anti-interference capability of a glucose sensor is crucial, because the interferants have higher electron transfer rates than the glucose, which can easily deviate the actual glucose oxidation currents [389].

The selectivity of the CuNOx sensor was investigated using a freshly made electrode. The electrode was used to get 12 distinct CV results, see Fig. 4-8. (a) without first and second CV results. The chronological list of peak currents, I_{III_0} in Fig. 4-4, of glucose oxidation and associated potential, see Table 4-1, of the 12 CVs are depicted in Fig. 4-8. (b), where 1st step represents, the values using 0.1 M NaOH only (blank solution). The values at 2nd step are after adding 1 mM glucose with 0.1 M NaOH. From step 3rd to 10th, the specific interferent, see legends of Fig. 4-8. (a), is added with 1 mM glucose and 0.1 M NaOH.

While there are reports that UA and AA interferents with concentrations of 0.059 mM and 0.01 mM can be easily oxidized [460], adding such concentrations with glucose does not show a significant change in the oxidation current, as shown in steps 5 and 6. The 11th step is the repetition of the 2nd step by adding 0.5 mM KCl (step 8), and 0.5 mM NaCl (step 9) with glucose to the chloride poisoning effect (that degrades redox activity) on the CuNOx electrode [389]. No change in the oxidation current, at step 11, was observed, indicating no poisoning effect. Moreover, the resultant relative standard deviation (RSD) of the peak oxidation current was 3.56% (see Fig. 4-8. (b)), which represents an excellent performance of the CuNOx sensors against all the interferents.

In summary, the addition of interferents with 1 mM glucose and 0.1 M NaOH, does not show significant variation in the increase of the peak oxidation current. This finding demonstrates that the CuNOx sensing electrode possesses an excellent anti-interference capability and favorable selectivity for the nonenzymatic detection of glucose.



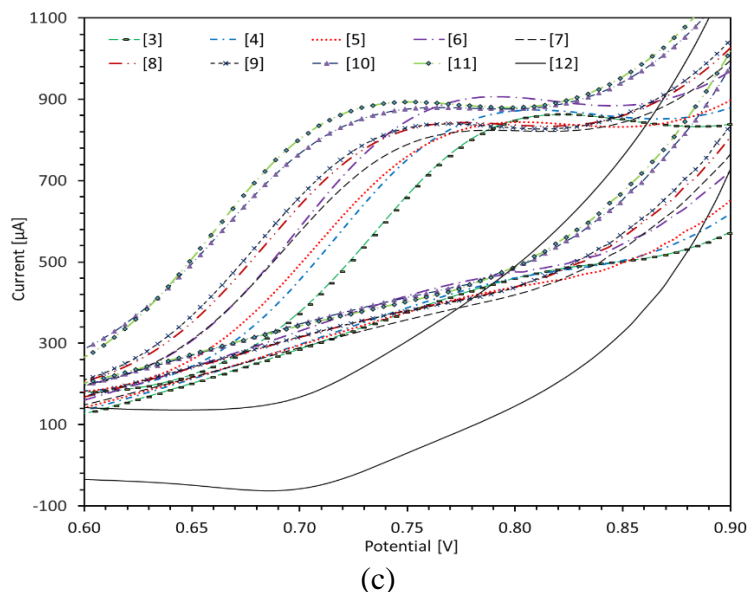


Fig. 4-8. (a) Cyclic voltammograms of 1 mM glucose with 0.1 M NaOH after adding different interferences presence in human sweat. Here, Step 1: Blank solution's signal in presence of 0.1 M NaOH. Step 12: Same as in step 1 after taking CV results in presence of all above-mentioned interferants. Step 2 and 11: Response to 1 mM glucose in presence of 0.1 M NaOH. The experiment results in Steps 1 and 2 were discarded from Fig. 4-8(a) to eliminate redundancy. Step 3: Response to 0.132 mM acetaminophen with 1 mM glucose and 0.1 M NaOH. Steps 4 and 7: Responses to 0.1 mM dopamine and 0.02 mM cysteine, respectively. (b) The peak oxidation current and the associated oxidation potential vs. the step order, shown in legends of Fig. 4-8. (a), and Fig. 4-8. (c) Magnified version of Fig. 4-8. (a).

4.3.5 Reproducibility & Reusability

The reproducibility of the CuNO_x glucose sensing electrode was evaluated by utilizing 4 freshly prepared electrodes in the same circumstances. The CV responses were performed

in 0.1 M NaOH solution containing 0.1-, 1-, 4-, and 6-mM glucose at a scan rate of 30 mVs⁻¹. Moreover, each glucose concentration was investigated using 4 electrodes for 7 distinct trials. The peak oxidation current of glucose is presented in Fig. 4-9, with a standard deviation. The resultant relative standard deviation (RSD) of the peak oxidation current were 5.99%, 2.67%, 2.22%, and 1.8% for 0.1, 1.0, 4.0, and 6.0 mM, respectively. The RSD demonstrated excellent reproducibility and reusability of the Cu native oxides electrode that represents the reliability of the CuNOx sensors.

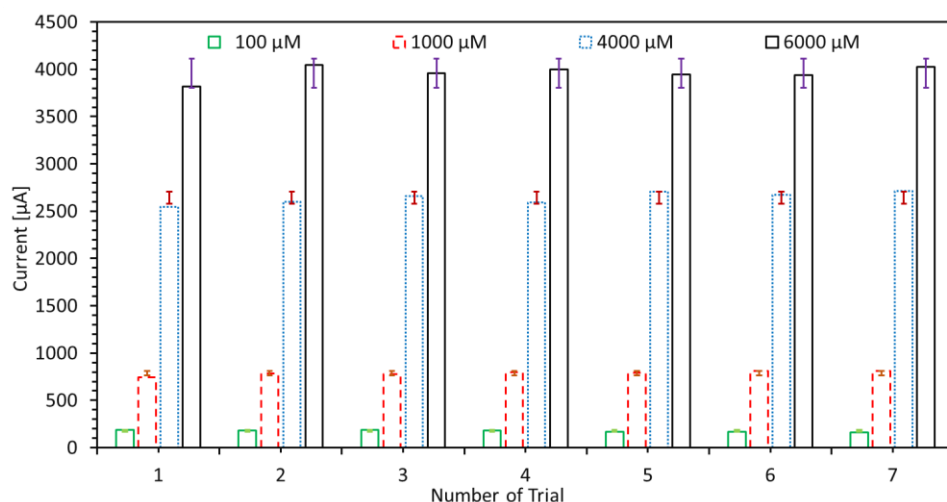


Fig. 4-9. Repeatability test of the CuNOx in 0.1 M NaOH alkaline solution with 0.1-, 1.0-, 4.0-, and 6.0-mM glucose concentrations. An electrode was used for each concentration in the same solution and the solution was shaken before applying the next CV.

4.3.6 Stability

Stability is the ageing behavior of the sensors, indicating drifting in the sensitivity. The stability of the CuNOx sensing electrode was investigated in 0.1 M NaOH with 1.0 mM glucose at 30 mVs⁻¹ scan rate. The peak oxidation current of glucose with a relative standard

deviation for 55 days is shown in Fig. 4-10. (a). The CV was performed for sensitivity measurement every 5 days while keeping the sensor in ambient conditions without any special treatment. The RSD is 2.70% which shows high stability of the electrode. After 12 times of usage, the native Cu oxides glucose sensor retains 96.91% of its original response, suggesting excellent stability and long-term (8 weeks) storage capability of the sensing electrode. The results demonstrated that the sensor was not poisoned by the oxidation product and is useful for long-term glucose monitoring.

Fig. 4-10. (b) represents voltammograms of a CuNO_x electrode against several Ag/AgCl reference electrodes. The results show that the redox potential differs for different reference electrodes but the peak current for glucose oxidation is almost the same as shown in Fig. 4-10. (d). These differences in the redox potentials of CuNO_x electrodes could be interpreted as the thickness of AgCl coating on Ag metal rod, which may differ due to manufacturing process as well as ageing of the electrode. Fig. 4-10. (c) represents the CV results of 3 CuNO_x electrodes, where one is freshly prepared, and others are 1 year old and used. It is worth noting that we have not observed any significant difference between the CV behavior of the freshly prepared CuNO_x electrode and the one-year-old used electrode. This may be indicative of the essence of this sensor for practical applications in long shelf-life. However, the long-term stability, reproducibility, and reusability of the sensor suggested that the Cu native oxide layers are chemically stable, prevent any Cu-based materials conglomeration, and are free from the interference of oxygen in the air [391].

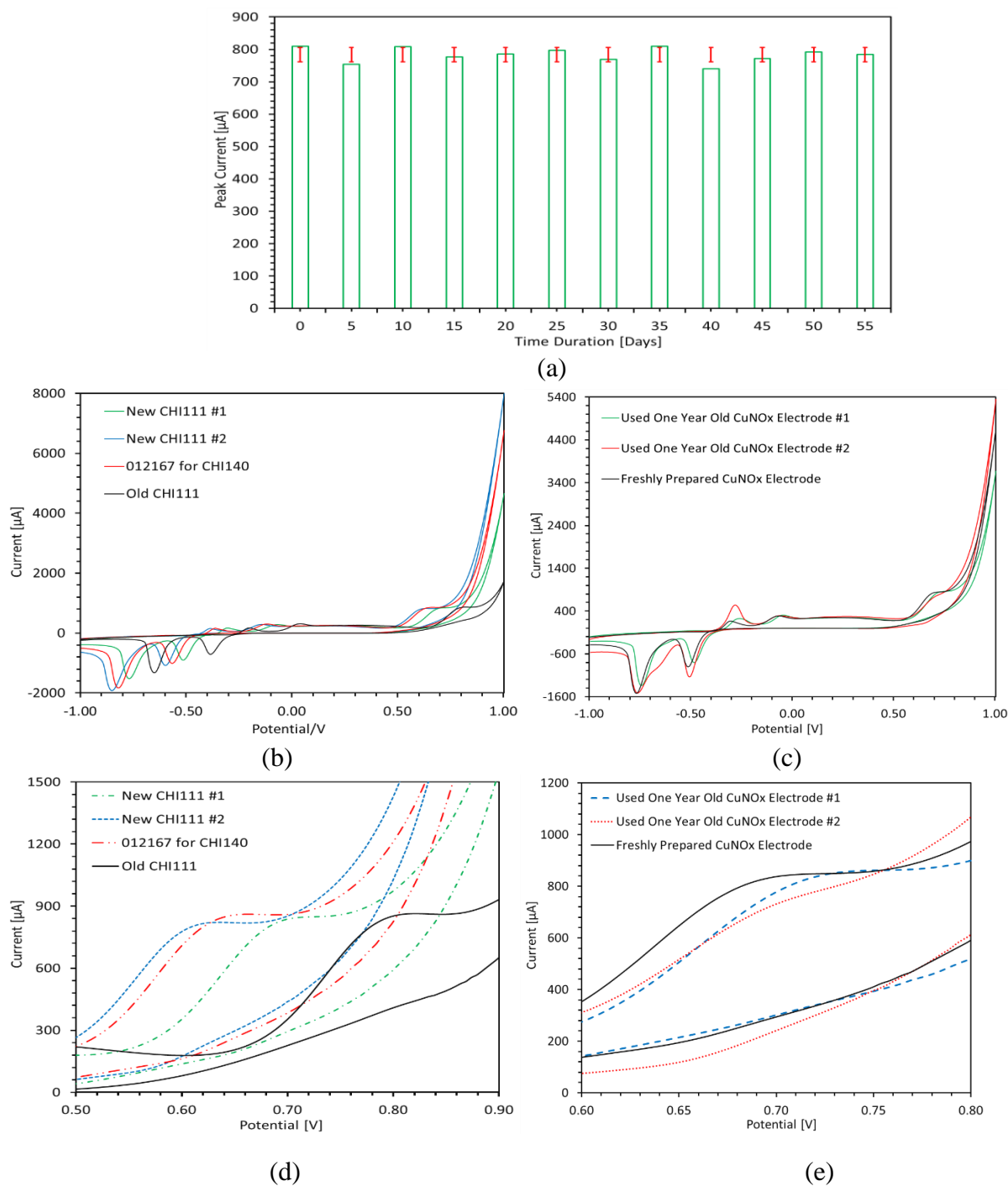


Fig. 4-10. Stability test of the CuNOx electrode in 0.1 M NaOH alkaline solution with 1.0 mM glucose concentration, (a) the peak oxidation current of glucose vs. days for 12 times with 5 days gap, (b) the CV readings were recorded for a single CuNOx electrode using

different Ag/AgCl reference electrodes, (c) the voltammograms of different working electrodes using same Ag/AgCl reference electrode, (d) Magnified version of (b), and (e) Magnified version of (c).

4.3.7 CuNO_x Sensing Parameters with Others

Table 4-2 compares the limit of detection (LoD), sensitivity, and linear range of the native Cu oxide sensors of this study with that of the previously reported Cu and Cu oxides based nonenzymatic electrochemical glucose sensors. The data presented in Table 4-2 shows that while some sensors provide a lower limit of detection with a higher sensitivity in a smaller linear range, others provide a higher limit of detection with lower sensitivity in the larger linear range. Therefore, there is a trade-off in the sensing performance among limit of detection, concentration range, selectivity, and stability of the sensors. These tradeoffs are influenced by the fabrication processes of the sensors. The CuNO_x sensors are comparable to the sensors reported in [376], [384], [398], [461]. Typically, the sweat glucose levels for diabetic patients have been measured between 0.050—1.0 mM. While existing sensors are only suitable for sweat glucose sensing in the range of 0.050—1.0 mM, CuNO_x sensors offer a range of glucose sensing of 0.050—7.0 mM. Both the sensitivity and the range of detection of CuNO_x sensors are considerably higher than that of the sensor in Ref [390]. The stability of CuNO_x sensors (55 days) was higher than that of the sensors in Ref [376]. The storage time for the sensors in Ref [376] was 4 weeks; for the fabrication of these sensors, a wet-chemical process using 1 M sulfuric acid (H₂SO₄) was used.

Table 4-2: Comparison of CuNO_x sensors with other Cu, and Cu oxides-based nonenzymatic glucose sensors. While the sensors reported in this work are characterized by cyclic voltammetry, the other sensors are characterized by amperometry.

Electrode	Fabrication Method	LoD (μM)	Stability (Days)(% of IR)	Sensitivity (μA mM ⁻¹ cm ⁻²)	Linear Range (μM — mM)	Ref.
Cu pillars	DC Electrodepositions	00.500	60 (85.00%)	699.449	001.00—00.500	[375]
Cu micropillar array	AC Electrodepositions	00.190	28 (85.33%)	2432.000	000.50—04.710	[376]
Cu nanorods	Hydrothermal Reactions	00.008	14 (90.00%)	1490.000	000.10—00.800	[377]
Cu ₂ O porous microcubes	Sonochemical Reactions	00.800	21 (88.60%)	-70.000	001.50—00.500	[378]
Cu ₂ O hollow nanospheres	Chemical Reactions	00.410		2038.200	001.25—00.038	[379]
CuO microflowers	Hydrothermal Reactions	00.500		1322.000	001.00—04.000	[384]
CuO nanorods	Hydrothermal Reactions	01.200		450.000	000.00—00.100	[386]
CuO nanowires	Chemical Reactions	00.020	12 (94.10%)	32330.000	000.10—00.500	[387]
CuO nanowires	Chemical Reactions	00.045	28 (94.30%)	64.100	000.50—00.488	[390]
CuO nanofibers	Electrospinning	00.800	60 (92.60%)	431.300	006.00—02.500	[391]
CuO nanosheets	Chemical Reactions	00.800	15 (96.77%)	2792.640	000.80—02.200	[461]
Cu ₂ O/Cu microstructures	DC Electrodepositions	37.000	07 (98.15%)	62.290	050.00—06.750	[462]
Cu ₂ O/Cu hollow μ-spheres	Hydrothermal Reactions	00.050	28 (93.40%)	33.630	220.00—10.890	[394]
CuO/Cu nanoflowers	Hydrothermal Reactions	01.200		5368.000	005.00—01.600	[398]
CuNO _x thin films	Surface Oxidations @RTP	94.210	>55 (96.91%)	603.420	050.00—07.000	This work

RTP = Room Temperature & Pressure; IR = Initial Response

Furthermore, the sensors reported in [376],[384],[398], and [461] used complex fabrication processes with chemical, and mechanical polishing, ultrasound cleaning, and complicated series of chemical treatments. In contrast, for CuNO_x sensors, we grew large-scale Cu native oxide in ambient conditions without the use of any of the above-complicated processes and treatments. The CuNO_x sensor fabrication method is a simple approach that more easily creates sweat sensors suitable for mass production. In terms of reproducibility, CuNO_x sensors RSD of the peak oxidation current is 5.99% for 0.1 mM glucose, whereas 7.50%, 4.22%, and 5.13% are figures for sensors reported in Ref [391], Ref [376], and Ref [461], respectively. Moreover, the RSD is 3.50% for the sensors in Ref [398] for 1 mM glucose which is 2.67% for our sensors. The excellent reproducibility and long-term stability of CuNO_x sensors could be endorsed to the chemical stability of Cu native oxide layers in the alkaline solution [392] and used in long storage times for routine applications.

4.3.8 CuNO_x Towards Wearable Applications

The sensor is applicable for sensing human sweat glucose beyond the range of 0.05 to 7 mM. The sweat could be collected from subjects during ergometer-based cycling exercise and then used in an alkaline solution to apply CV [463] for the glucose reading. For real-time monitoring of sweat glucose, a wearable sweat glucose sensor platform with microfluidic components such as reservoirs and channels, and electrochemical sensing electrodes can be developed. In this platform, microfluidic channels and reservoirs route spatially split and deliver sweat samples to the sensing electrode [464]–[466]. The sweat can be generated by applying current to the sweat extraction electrode, which is widely

known as iontophoresis [467]. Biocompatible elastomers such as PDMS with defined orifices with an iontophoretic component for sweat collection to deliver sweat to an inlet of the microfluidic reservoir can be fabricated. The reservoir can be separated by a valve from that of the CuNO_x sensing electrode with 0.1 M NaOH solution. The passive valve will allow one-directional sweat flow towards the reservoir so that the human skin will be protected from an alkaline environment. Electronic control circuits can be integrated into the system to implement an effective sweat glucose monitoring system.

4.4 Conclusion

This paper reports the electrochemical sensing behavior of naturally grown Cu native oxide (CuNO_x)-based sensing electrodes for high-performance nonenzymatic sweat glucose sensors. To grow stable Cu native oxide layers, we kept commercially available 35 µm thick Cu foils in ambient conditions of a 10000-class clean room for more than two years. We investigated the chemical bonding states using XPS to identify the stability of the oxide layers. The peak-fitting of high-resolution XPS spectra of the Cu-oxides for O_{1s}, see Fig. 4-2. (c), showed almost zero intensity for water, H₂O, bonding states meaning the stable Cu-oxide layers are not prone to further growth of oxide layers. To gain further insights into the structural integrity of the Cu-oxides, we investigated them by using an HRTEM. This is the first time we observed that the oxide layer can be grown to 10 nm (in [401], 6.7 nm for 112 days) or more without any external energy like heat. The growth of the oxides is not uniform, and structural defects of the foil can accelerate the growth of the

oxides. The HRTEM FFT data also shows that the growth of CuO is ultra-thin compared to Cu₂O layers.

We developed a facile and low-cost fabrication method to fabricate the sensing electrode, which does not need any chemical and mechanical pre-and post-processing. In this method, the Cu thin film with native oxides was attached with electrical grade tape. For analyzing the electrochemical sensing performances of the CuNO_x sensors for glucose sensing, we have compiled a complete (possible) set of reduction-oxidation (Redox) reactions of Cu oxides with supporting electrolyte (NaOH, basically OH⁻ ions). Moreover, the electro-oxidation reactions of glucose on the surface of the CuNO_x electrode are given explicitly in Scheme 1. This has happened for the first time in the history of nonenzymatic electrochemical glucose sensors. Then, we discovered two phenomena: (1) the peak oxidation currents of different glucose concentrations and the associated oxidation potentials are exponentially related, and (2) the applied potential at which the peak oxidation current of glucose occurred is growing logarithmically with the concentrations of the glucose (see Fig. 4-7. (a), and Fig. 4-7. (b)). We explained the possible reasons for the phenomena with details from the basics of the electrochemical cell properties; the interface, the depletion region, and the diffusion-driven as well as the "mass-transfer-limited" species movement.

For the first time, we presented that naturally grown Cu native oxides layer is better as a glucose sensor in some respects for the sweat glucose and beyond range, 0.05 to 7 mM. The CuNO_x sensors exhibited a sensitivity of 603.42 $\mu\text{A mM}^{-1} \text{cm}^{-2}$. The straightforward sensor fabrication makes it a better sensor among the nonenzymatic electrochemical

glucose sensors based on the Cu/Cu₂O/CuO materials than ever reported in the literature. Also, the CuNO_x sensors showed outstanding stability of more than one year of self-life, kept in ambient conditions without any special treatment and precautions. Moreover, the sensors demonstrated excellent reproducibility and reusability, while exhibiting negligible interference effects in the presence of acetaminophen, dopamine, ascorbic acid, uric acid, cysteine, KCl, and NaCl. The CuNO_x sensors are suitable for further miniaturization for flexible packaging for wearable applications. The overall characteristics show that the CuNO_x sensors may be an excellent choice for an extremely inexpensive and truly simple way of fabricating for sensing sweat glucose beyond the 0.05—7 mM range. In this paper, we focused on the development of CuNO_x-based nonenzymatic glucose sensors; future research will test these sensors in real world applications with human sweat.

Chapter 5

High Performance Nonenzymatic Electrochemical Sensors via Thermally Grown Cu Native Oxides (CuNOx) Towards Sweat Glucose Monitoring

This chapter is part of our work submitted for consideration for publication as ‘M Maksud Alam, and Matiar M. R. Howlader,” High performance nonenzymatic electrochemical sensors via thermally grown Cu native oxides (CuNOx) towards sweat glucose monitoring.” Analyst (September 2023), DOI: 10.1039/D3AN01153D.’

Diabetes, the seventh leading cause of death globally, requires real-time blood glucose monitoring, which is often an invasive process. An alternative is sweat glucose monitoring, typically using transition metals and their oxides as sensors. Despite their excellent surface-to-volume ratio, these metals present issues such as poor conductivity, structural collapse, and aggregation. Therefore, the choice of highly electroconductive materials and optimization of nanostructures are critical. In this work, we have developed a high-performance, low-cost, nonenzymatic sensor for sweat glucose detection, using the thermally grown native oxide of copper (CuNOx). By heating Cu foil at 160, 250, and 280 °C, we grew a native oxide layer of approximately 140 nm cupric oxide (CuO), which is excellent for glucose electrocatalysis. Using cyclic voltammetry, we found that our CuNOx sensors prepared at 280 °C exhibited a sensitivity of $1795 \mu\text{A mM}^{-1} \text{cm}^{-2}$, a linear range up to the desired limit of 1.00 mM for sweat glucose with excellent linearity ($R^2 = 0.9844$),

and a lower limit of detection of 135.39 μM . In glucose sensing, the redox couple Cu(II)/Cu(III) oxidizes glucose to gluconolactone, then eventually to gluconic acid, resulting in an oxidation current in an alkaline environment. We achieved excellent repeatability and stability (stable for over 1 year) with a relative standard deviation (RSD) of 2.48% and 4.17%, respectively, for 1 mM glucose. The selectivity with common interferants found in human sweat and blood showed an RSD of 4.32%. We believe that the electrocatalytic efficacy of thermally grown CuNO_x sensors for glucose sensing can open up new prospects in the fabrication of sweat glucose sensors.

5.1 Background

Diabetes is a chronic disorder caused by uncontrolled blood sugar, which results from either ineffective use or deficiency of insulin in the body. This disease can lead to blindness, kidney failure, heart attacks, strokes, and severe damage to the nerves and blood vessels, making it the seventh leading cause of death worldwide. According to the World Health Organization, diabetes directly caused an estimated 1.6 million deaths in 2016 [28]. It has been reported that illnesses associated with metabolic syndrome, including diabetes, act as comorbidities, putting additional strain on the organ systems affected by COVID-19 [30][31][32]. Therefore, early detection of diabetes through glucose monitoring is crucial to prevent complications caused by low blood glucose and can save lives. Although blood is the gold-standard glucose biomarker, its extraction is invasive, and regular blood harvesting can lead to infections. In contrast, sweat has gained growing interest in glucose sensing due to the non-invasive nature of its extraction processes [362].

Various noble metals (Au, Pt), non-noble metals (Co, Cu, Fe, Mn, Ni, Pd, V, Zn), metal oxides (Ag_2O , CoO , Co_2O_3 , Co_3O_4 , CuO , Cu_2O , Fe_3O_4 , MnO_2 , M_3O_4 , NiO , RuO_2 , ZnO), metal hydroxides, sulfides, phosphides, alloys, and complexes have been studied extensively for use as electrocatalysts in non-enzymatic electrochemical glucose biosensors [468][469]. Noble metal sensing electrodes are expensive and susceptible to chloride poisoning [83]. Ni and its compounds are promising due to their excellent electrocatalytic activities, but they have stability issues in changing pH environments and poor electroconductivity [468] due to the formation of oxides and hydroxides [83]. However, new substrates, such as CNTs [470]–[473], graphene[474], other and carbon substances [475]–[478] can enhance their electron transfer capabilities. Co-based catalysts are efficient and economical. Their reversible or quasi-reversible redox properties make them suitable for glucose electrocatalysis [468], but bulk Co and its oxides suffer from poor performance and lack of active electrocatalysis sites [362]. Co-based nanostructures also have a problem with structural collapse. Conductive supports like CNTs [479], [480], graphene[481]–[484], carbon matrices[485], conducting polymers [486], and high-conductivity metals [487] have been investigated to enhance their properties.

Another commonly used metal oxide is $\beta\text{-MnO}_2$, which has excellent chemical stability among α -, β -, γ -, ϵ -, and λ - MnO_2 . It can receive electrons from glucose and catalyze their electro-oxidation, but its low electronic conductivity and the tendency for nanostructures to aggregate pose challenges [468]. Techniques such as nitrogen doped graphene (NG) [488], modified graphene nanofibers [489] have been explored to improve conductivity and prevent aggregation [488]. While metallic Fe is unstable in air, Fe-oxides such as FeO ,

Fe_2O_3 , and Fe_3O_4 are effective electron mediators due to the reversible redox pair of Fe(III)/Fe(II) with good performance in neutral pH conditions [468]. Fe_3O_4 nanostructures can directly electro-catalyze glucose oxidation, providing direct channels for electron transfer and reversible aggregation [468]. ZnO , despite its excellent properties and ease of synthesis [448], is rarely used for non-enzymatic glucose catalysis due to its poor electronic conductivity [362] and the need for a high operational potential [362], which can interfere with interferents, such as ascorbic acid (AA) and uric acid (UA), in output signals [490]. Transition metals and their oxides used for glucose sensing often suffer from poor electronic conductivity, structural collapse, and aggregation during synthesis.

Copper oxide nanomaterials are attractive for nonenzymatic glucose sensors due to their relatively stable electroanalysis and excellent catalyst behavior [6]. Previous investigations have replicated the similar redox reaction pattern of Ni for Cu-based electrode surfaces, exhibiting Cu(II)/Cu(III) transitions during glucose electro-oxidation in an alkaline environment [8], [39]. Two types of copper oxides exist: cuprous oxide (Cu_2O) and cupric oxide (CuO), both of which are p-type semiconductors due to copper vacancies in their lattice [40]. Several methods have been investigated to boost the electroconductivity of copper oxide nanomaterials in glucose electrodes, including the use of diverse structures like porous films, nanowires, hybrid nanocomposites, and nanoflowers to increase the active surface area for glucose electro-oxidation [39]. However, these structures present electron transport challenges due to high lattice mismatch [48]. Improving the interface contact between the highly electrocatalytic material and the current collector is vital for enhancing electrode conductivity and taking full advantage of electroactive substances [6].

An effective method to improve conductivity is to use native copper oxides (Cu_xO) as the active catalytic electrode surface and copper thin films under Cu_xO as the current collector. This concurrently provides good conductivity for electron transport during glucose biosensing, as shown in previous work [39]. However, to achieve a stable copper oxide layer, the native oxide layers must be grown on thin Cu foils kept at ambient conditions for over two years, which presents a significant challenge in using native stable Cu_xO as glucose sensors.

In this work, we have developed a simple, facile, and robust fabrication process for glucose sensors. This process involves thermally growing CuNO_x on commercially available Cu thin foils at temperatures of 160, 230, and 280 °C. This approach offers several advantages over earlier methods, including a significant reduction in the time required to establish a stable copper oxide layer (from two years to less than eight hours). It also results in a 14-fold increase in the thickness of the layer (from roughly 10 nm to 140 nm) and transforms the surface into a highly stable and efficient glucose catalyst CuO with larger crystal structures. The thermally grown CuNO_x sensing electrodes demonstrated excellent performance in the presence of some interferants in sweat (0.05 – 1.00 mM) and blood (1.00 – 7.00 mM) with twin calibration curves. They offer the best trade-off between sensitivity and the fabrication process compared to other Cu/ Cu_2O /CuO-based glucose sensors.

5.2 Experimental Procedure

5.2.1 Chemical & Reagents

D-(+)-glucose (Dextrose, $C_6H_{12}O_6$, $\geq 99.5\%$), Sodium Hydroxide (NaOH, $\geq 98\%$), Acetaminophen (APAP, $CH_3CONHC_6H_4OH$, $\geq 99\%$), Dopamine Hydrochloride (DA, $(HO)_2C_6H_3CH_2CH_2NH_2 \cdot HCl$), L-Ascorbic Acid (AA, $C_6H_8O_6$, $\geq 99.0\%$), Uric Acid (UA, $C_5H_4N_4O_3$, $\geq 99\%$), L-Cysteine (Cyst., $HSCH_2CH(NH_2)CO_2H$, $\geq 97\%$), Sodium Chloride (NaCl, $\geq 99.5\%$), and Potassium Chloride (KCl, $\geq 99\%$) were purchased from Sigma-Aldrich. A 35 μm thick Cu foil was also purchased from Sigma-Aldrich. All the chemical reagents used in our research are of analytical grade and were used without further purification. All solutions were prepared with 18.2 M Ω .cm deionized (DI) water, which was prepared by deionized water of resistivity 18.2 M Ω .cm from an ELGAPurelab Ultra Water Purifier, at 25 ± 2 °C.

5.2.2 Formation of Thermally grown Native Oxide of Copper & Electrode Preparation

Under ambient conditions (dry, room temperature, normal pressure, and humidity), a storage time of 2 years is required to grow a stable Cu_2O layer of approximately 10 nm on the Cu thin foil [97]. In this research work, one of our main intentions was to reduce the excessively required time to obtain native oxide layers. Moreover, various studies have shown that the deposition of copper oxide thin films at room temperature results in the Cu_2O phase; however, subsequent annealing process transform them to the CuO phase at higher substrate temperatures [491], [492].

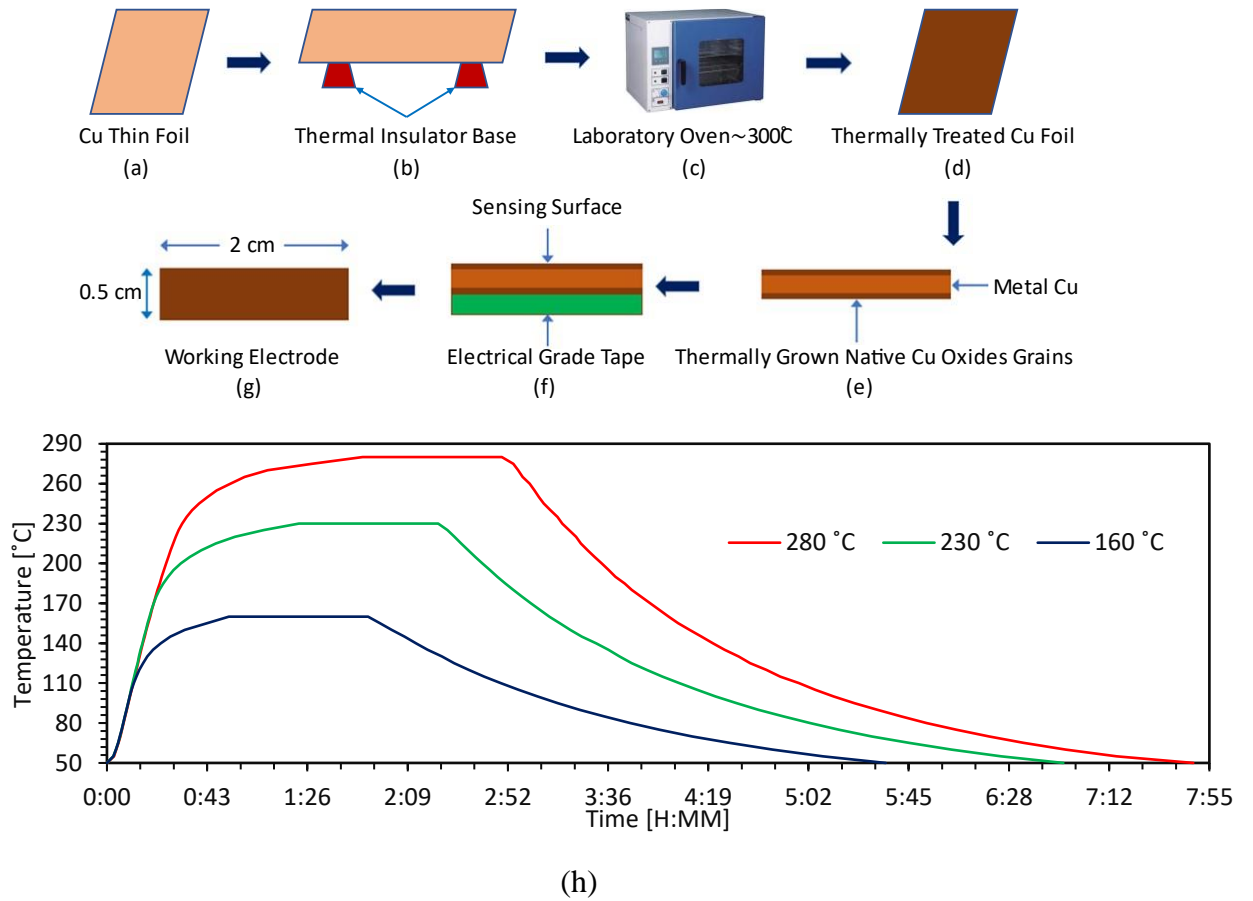


Fig. 5-1. Schematic representation of the working electrode preparation. (a) The as-received thin Cu foil at room temperature and pressure (RTP); (b) The foil supported by a thermal insulator to protect it from metal contact in the oven; (c) The laboratory oven, which can be used up to 300°C; (d) The Cu thin foil after annealing at 160, 230, and 280°C. The electrode preparation steps (e), (f), and (g) are the same as shown in our previous work [97]; (h) The temperature profile for annealing the Cu thin foil.

Previous investigations have shown that Cu-oxide films deposited by chemical vapor deposition on a 300°C heated substrate contain mixed phases of Cu_2O and CuO [493]. In contrast, Cu-oxide films deposited by ion beam sputtering on a 200°C heated substrate consist of only the CuO phase [494]. Moreover, the formation of the CuO phase in the as-

deposited film is a stable phase for temperatures below 300°C, regardless of the partial pressure of oxygen [495]. From thermodynamic considerations, the Gibbs free energy for the oxidation of Cu₂O to CuO at a temperature of 200 °C is -3.73 kcal/mol. Therefore, the formation of CuO phase in the as-deposited copper oxide thin film is reasonable, and no Cu₂O phase is observed in this film, as thermodynamically expected [496].

We prepared the sensing electrode using the thermally grown CuO on the as-received Cu thin foil. This CuO layer is highly electrocatalytic to glucose electro-oxidation in the presence of 0.1 NaOH. We used commercially available 35 µm thick Cu thin foils and annealed them at different temperatures, such as 160, 230, and 280°C. The CuO phase, once formed, is insensitive to higher temperature ranges, specifically between 300 - 600°C [495]. Annealing above 300°C affects only the crystal quality, altering size and microstrain [495]. The largest crystallite size was observed at an annealing temperature of 600°C [495]. This can be attributed to the thermal energy produced by annealing, which results in the formation of larger crystallites [495]. It is clear that the crystallite size can be simply controlled by varying the post-deposition annealing temperature [495]. Hence, we utilized an exponentially increasing and decreasing temperature profile, as depicted in Fig. 5-1(h), primarily to amplify the thermal energy while ensuring that the peak temperature doesn't exceed 280°C. The rationale behind this specific profile lies in its ability to offer enhanced thermal energy - effectively, the thermal energy corresponds to the area under this profile curve. Furthermore, the gradual rise and fall in temperature in this profile are believed to favorably influence the growth of the oxide layer and its crystallite structure, thus leading to a more consistent and well-defined oxide formation. It's essential to highlight that the

varying time for different temperature intervals isn't an arbitrary choice but stems from the built-in function of the laboratory oven, as illustrated in Fig. 5-1(c). In mathematical terms, the oven requires a longer duration to achieve higher temperatures when following an exponential profile, and the same is true when the temperature is gradually decreasing.

5.2.3 Electrochemical Sensing Method

Electrochemical measurements, including cyclic voltammetry (CV), were performed using a three-electrode PalmSens EmStat 3 potentiostat with PSTrace 4.8 software. All experiments were conducted at room temperature (25 ± 2 °C) using a platinum (Pt) wire as a counter electrode and a silver (Ag) wire coated with silver chloride (AgCl), widely known as Ag/AgCl electrode, as a reference electrode. Both counter and reference electrodes were purchased from CH Instruments Inc. USA. The working electrode, with a length of 2 cm and width of 0.5 cm (sensing surface area of 1 cm^2), was prepared for electrochemical measurements of glucose oxidation. The working electrode was evaluated as a glucose sensor in an aqueous of 0.1 NaOH solution. No special procedure, such as cleaning or stirring was performed before each electrochemical measurement. Each experiment was simply conducted by immersing the working electrode in the glucose aqueous solution, combined with the NaOH alkaline solution. The glucose analyte was prepared by adding a specific amount of glucose to deionized (DI) water. This base aqueous glucose solution was then used to prepare a 50 mL analyte by adding 0.1 M NaOH solution and solutions of each interferent at specific concentrations. Our next focus will be on actual sweat.

5.3 Results and Discussion

5.3.1 Chemical Elemental Characterization

We investigated the chemical elemental species of thermally grown Cu native oxide electrodes using XPS to examine the compositions and the role of the electronic bonding states of the electrodes at the as received (25°C), and at 230°C, and 280°C. Figure 5-2(a) shows the representative wide scan XPS survey spectra of the electrode surfaces, including the metallic and oxide phases, in the binding energy range of 0—1000 eV. The wide scan XPS survey spectra of the electrodes at as-received (25°C), 230°C, and 280°C are virtually identical to each other. The survey confirms the Cu core level doublet peaks of $\text{Cu}_{2p_{1/2}}$ and $\text{Cu}_{2p_{3/2}}$ around 952.0 and 932.0 eV, respectively, with a spin-orbit splitting of 20 eV. In addition, the copper core level peaks of Cu_{3s} at 122.0 eV, Cu_{3p} at 75.0 eV, and Cu_{3d} at 3.0 eV, as well as the peak of oxygen, O_{1s} , at 532.0 eV, are found to be in better agreement with previously published scholarly work. Contaminants, such as carbon (C_{1s}), argon (Ar_{2s}), and palladium (Pd_{3d} , and Pd_{4d5}) are also observed on the surfaces of the electrodes around 285, 316, 337, and 415 eV, respectively. This is in good agreement with the values reported in the literature [97], [407], [495], [497]. The strong oxygen and carbon peaks in Fig. 5-3(a) and (b) are adventitious oxygen and carbon peaks that occur due to the reaction of copper with atmospheric oxygen and contamination from air-formed film on the surface [409], [410]. The wide scan survey also indicates the existence of Cu^{2+} ions through the satellite peaks on the high binding energy side of the main peaks, which correlate with the open $3d^9$ shell of Cu [411].

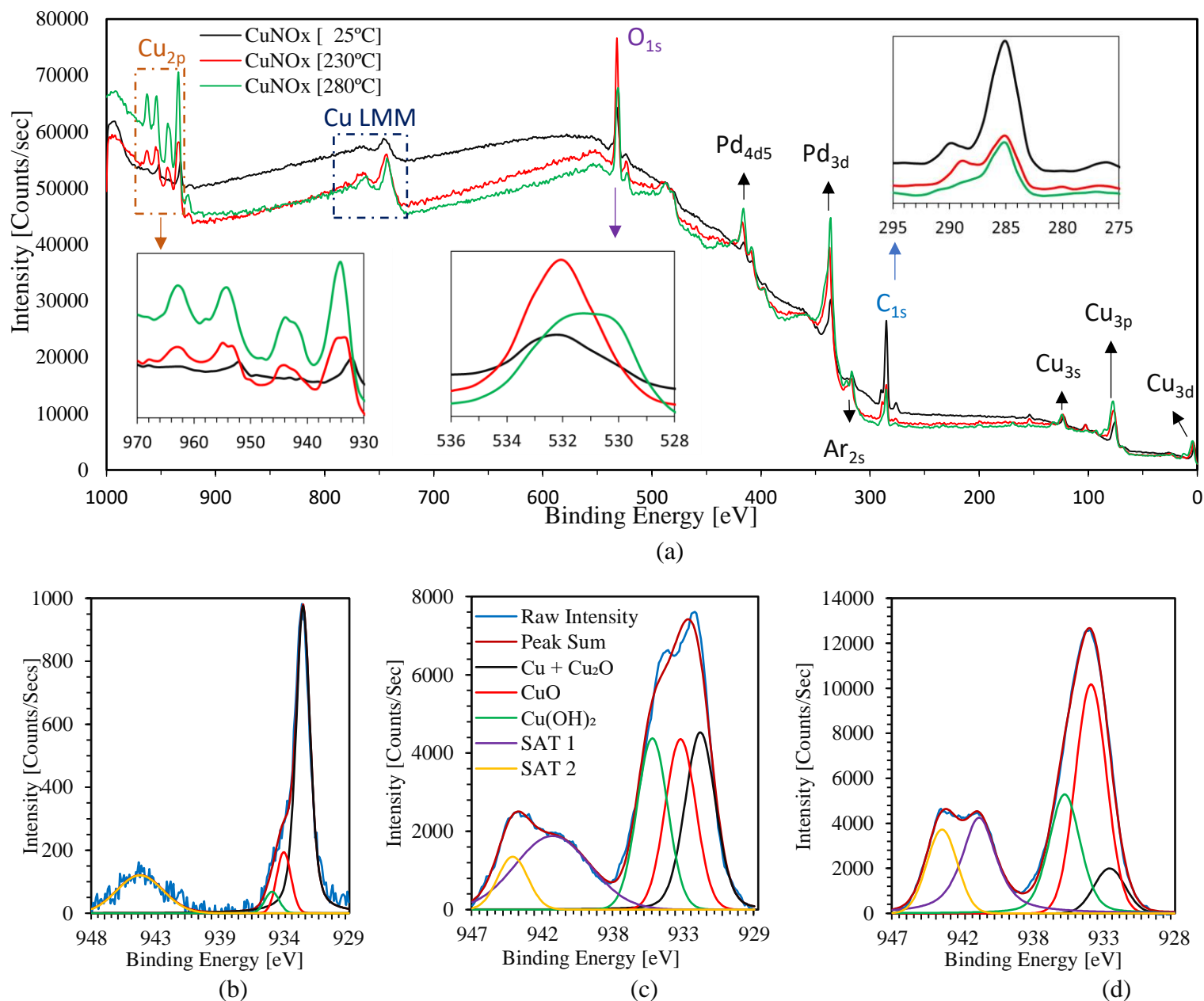


Fig. 5-2. (a) Wide scan XPS spectrum, along with the deconvoluted high-resolution narrow scan for $\text{Cu}_{2p_{3/2}}$ of (b) as received copper oxide thin films (at 25°C), (c) those annealed at 230°C , and (d) those annealed at 280°C , utilizing the temperature profile shown in Fig. 1(h).

The high-resolution spectra of $\text{Cu}_{2p_{3/2}}$ and associated shake-up satellites, located about 8 eV and 10 eV binding energies higher than the main Cu_{2p} peak, are presented in Fig. 5-

2(a), (b), and (c). These figures show the electrodes with curve-fitting components for the as received (25°C), and for annealed copper oxide thin films at 230°C, and 280°C, respectively. The deconvolved components were achieved using the Gauss-Lorentz (70–30%) method [412] and XPSPEAK41 software. Since the relative shift of Cu and Cu₂O peaks in binding energy is minuscule, only 0.13 eV, both grouped together at 932.44 eV [401], [415], [416]. As shown in Fig. 5-2(b), (c), and (d), the different chemical states of the electrode are deconvolved as Cu + Cu₂O at 932.44 eV, CuO at 933.7 eV, and Cu(OH)₂ at 935.5 eV, respectively [495].

Table 5-I: Peak fitting parameters and percentage relative concentrations for copper oxide thin films in their as received state (25°C), and after annealing at 230°C and 280°C, using the temperature profile shown in Fig. 5-1(h).

Peak Fitting Parameters	As-received 25°C			Annealed at 230°C			Annealed at 280°C		
	Cu+Cu ₂ O	CuO	Cu(OH) ₂	Cu+Cu ₂ O	CuO	Cu(OH) ₂	Cu+Cu ₂ O	CuO	Cu(OH) ₂
Binding Energy (eV)	932.44	933.7	935.5	932.44	933.7	935.5	932.44	933.7	935.5
FWHM (eV)	1.25	1.25	1.25	2.3	2.3	2.3	2.5	2.5	2.5
Relative Concentration (%)	64.35	31.92	3.73	25.02	52.5	22.48	7.13	71.67	21.2

The peak deconvolved data of Cu_{2p3/2}, as shown in Fig. 5-2. (b), (c), and (d), are presented in Table 5-I. The percentage relative concentrations for Cu + Cu₂O, CuO, and Cu(OH)₂ are calculated using equations (5-1), (5-2), and (5-3), respectively [495]. Here, $A_{[Cu+Cu_2O]}$ represents the area under the curve of Cu + Cu₂O, and so on.

$$\therefore \%[Cu + Cu_2O] = \frac{A_{[Cu+Cu_2O]}}{A_{[Cu+Cu_2O]} + A_{[CuO]} + A_{[Cu(OH)_2]} + A_{[SAT1]} + A_{[SAT2]}} \times 100\% \quad (5-1)$$

$$\therefore \%[CuO] = \frac{A_{[CuO]} + A_{[SAT1]} + A_{[SAT2]}}{A_{[Cu+Cu_2O]} + A_{[CuO]} + A_{[Cu(OH)_2]} + A_{[SAT1]} + A_{[SAT2]}} \times 100\% \quad (5-2)$$

$$\therefore \%[Cu(OH)_2] = \frac{A_{[Cu(OH)_2]}}{A_{[Cu+Cu_2O]} + A_{[CuO]} + A_{[Cu(OH)_2]} + A_{[SAT1]} + A_{[SAT2]}} \times 100\% \quad (5 - 3)$$

However, the satellite peaks are due to the partially filled d^9 shell configuration of CuO, while such peaks are absent for Cu₂O due to its fully filled d^{10} shell [498]. The electronic structure of Cu₂O and CuO is further explained in [47]. As the satellite peaks are known to be characteristics of CuO phase, the area under these peaks is used to calculate the percentage of CuO [495]. The ratio of relative concentration of Cu⁺ (Cu₂O) to Cu²⁺ (CuO) on the surface of the as-received electrode is 2.02, which suggests the simultaneous formation of Cu₂O, and CuO [495]. This growth of these oxides at ambient conditions over time is well supported by published scholarly articles [39]. Moreover, the surface of the Cu thin films at ambient conditions is predominantly rich in Cu₂O. Therefore, this spontaneous formation of native Cu₂O at ambient conditions on the Cu thin films implies that the change in Gibbs' free energy, ΔG , as shown in equation (5-4), is negative for Cu₂O formation. Here, ΔH is the change in enthalpy, ΔS is the change in entropy, and T is the absolute temperature [495].

$$\Delta G = \Delta H - T(\Delta S) \quad (5 - 4)$$

The oxidation process of Cu thin films to native Cu₂O at ambient conditions is governed by the diffusion kinetics of O₂ through the surface oxide layer, known as the reaction-limited growth regime [495]. At ambient conditions, the change in Gibbs' free energy, ΔG , is positive, implying the absence of sufficient chemical activation energy to facilitate Cu₂O growth. However, as annealing temperature ascends, enhanced diffusion kinetics, attributable to thermal energy, initiate the oxidation process. As a result, the change in

Gibb's free energy turns negative around 160°C, paving the way for further growth of Cu oxide layers.

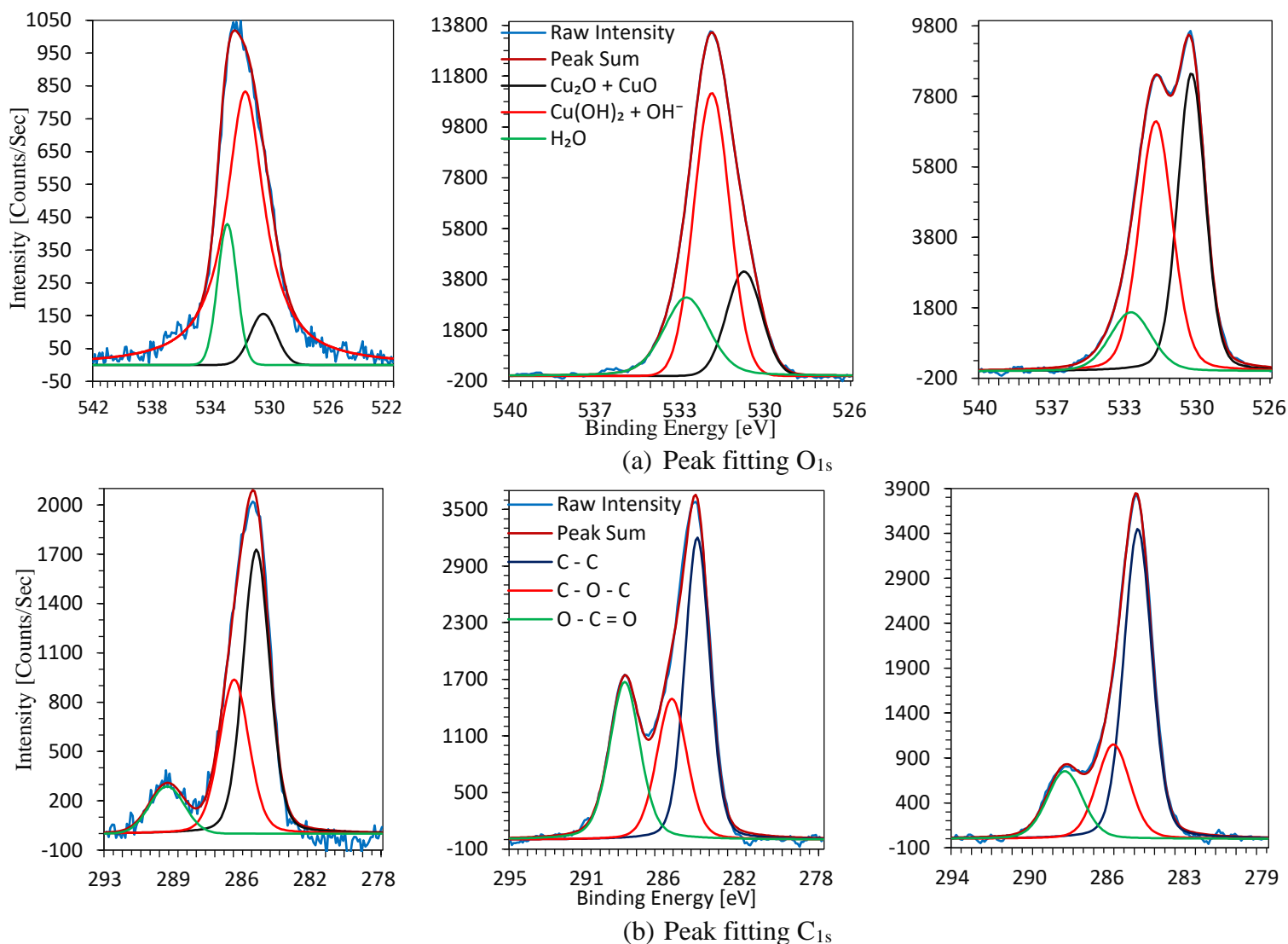


Fig. 5-3. Peak fitting of (a) O_{1s}, and (b) C_{1s} of the electrodes of as-received (25°C), annealed at 230°C, and 280°C (from left to right).

As evident from Fig. 5-2(c), 5-2(d) and Table 5-I, the ratios of relative concentration of Cu⁺ (Cu₂O) to Cu²⁺ (CuO) on the electrode surfaces at 230°C, and 280°C, relative to the as-received electrode, stand at 0.48, and 0.01, respectively. Thus, at temperatures like

230°C and 280°C, CuO formation skyrockets. Furthermore, at the 280°C annealing temperature, a negligible amount of Cu+Cu₂O is present on the surface of the electrode, indicating a lack of coexistence between metallic Cu and CuO. Therefore, it is clear that oxide growth at higher temperatures is purely dominated by the oxidation temperature, rather than the growth kinetics [495].

The prominent peaks of the O_{1s} spectrum, shown in Fig. 5-3(a), correspond to Cu₂O+CuO, Cu(OH)₂+OH⁻, and H₂O, with binding energies of 530.60, 531.80, and 533.00 eV, respectively. This is in good alignment with the findings of Platzman et al. [401]. The first peak, which represents Cu₂O+CuO for all cases, shows an increasing trend, aligning with the data from the oxides of Cu_{2p3/2} peaks. The second peak can be attributed to Cu(OH)₂+OH⁻ groups, which form a wetting layer due to the high relative humidity at room temperature conditions and are observed in the Cu_{2p3/2} spectra [401]. The area of the Cu(OH)₂+OH⁻ peak increases on the electrode surface at 230°C, as illustrated in Fig. 5-3(a), but diminishes at 280°C. This phenomenon could be the result of the formation of a thicker oxide layer at 280°C. A similar effect is observed for the low-intensity peak of the H₂O wetting layer.

The deconvolved C_{1s} spectra, shown in Fig. 5-3(b), reveal three chemical bonding states on the Cu oxides surface: C – C, C – O – C, and O – C = O with binding energies of 284.80, 286.00, and 288.58 eV, respectively [499]. The areas of the C – C state at 25°C, 230°C, and 280°C are 3421.89, 6004.88, and 6511.35, respectively. On the other hand, the areas under the curve of the C – O – C state at 25°C, 230°C, and 280°C are 2062.61,

3406.13, and 2347.57, respectively. Additionally, the peak fitting graph indicates that the areas under the $O - C = O$ state at 25°C, 230°C, and 280°C are 678.71, 4002.92, and 1807.05, respectively. At 230°C, the area of all the three components of carbon bonding states increases, which could be due to the carbon available in the air in the oven interacting with the O_2 rich wetting surface of the electrode. Interestingly, at 280°C, only the area of $C - C$ increases, while for other two components decrease. Most likely, as the temperature further increases towards 280°C, the bonds between carbon and oxygen in $C - O - C$ and $O - C = O$ break. Consequently, O_2 diffuses deeper to create oxides, leaving only the $C - C$ state on the surface, as illustrated in Fig. 5-3(b).

5.3.2 Morphological and Structural Characterization

High-resolution transmission electron microscopy (HRTEM) has been used to examine the Cu oxide thin films annealed at 280°C, offering further insight into the morphology and structural features of the sensing electrodes. Fig. 5-4(a) shows the oxide growth is almost uniformly distributed on the Cu metal surface. This homogeneous formation of the oxide layers is opposite to the previous findings of thin films stored under ambient conditions [97], [401]. The growth of the oxide layer on Cu thin films in ambient conditions, however, is contingent upon lattice defects, microstructure, and surface morphology of the Cu films [401], [405]. Fig. 5-4(b) shows a typical surface morphology of a Cu thin film annealed at 280°C with a homogeneous oxide layer. This may be attributable to the considerable diffusion kinetics of O_2 , driven by high thermal energy from the annealing temperature profile shown in Fig. 5-1(h) at 280°C. In the case of Cu thin films kept under ambient

conditions, the native oxide layers can grow to exceed 6.7 nm and 10 nm over 112, and 730 days, respectively[97], [401]. On the other hand, it is feasible to grow a 137 nm oxide layer in under 8 hours utilizing the temperature profile shown in Fig. 5-1(h).

Fig. 5-4(c), and (d) present the energy dispersive X-ray spectroscopy (EDS) mapping of the native Cu oxide surface under ambient conditions. Fig. 5-4(c) reveals that the oxides layer contains quantity of O₂, while the presence of metallic Cu is lesser. The EDS and XPS results corroborate each other, in line with previous studies [97]. Fig. 5-4(h), and (i) depict the Fast Fourier transform (FFT) of the dotted portion in Fig. 5-4(g), and (k), respectively, illustrating the existence of crystal Cu metal, single crystal Cu₂O, and twin crystalline CuO in the HRTEM image of the electrode. Furthermore, it is evident that CuO heavily dominates the created crystalline structure due to high thermal energy. Therefore, the thin Cu lattice spacing measures 0.17 nm along the (200) plane. The inter-planar spacing of Cu₂O, however, measures 0.21 nm along the (200) plane, as shown in Fig. 5-4(h), and (i), which aligns well with prior results [97], [427]. The d spacings of CuO are 0.27 nm and 0.29 nm, which correspond to the (110) plane [429], [430]. The intensity difference between Cu₂O and CuO FFT data clearly indicates that the CuO width is significantly thinner than Cu₂O, a finding that aligns closely with other experimental data [401], [405].

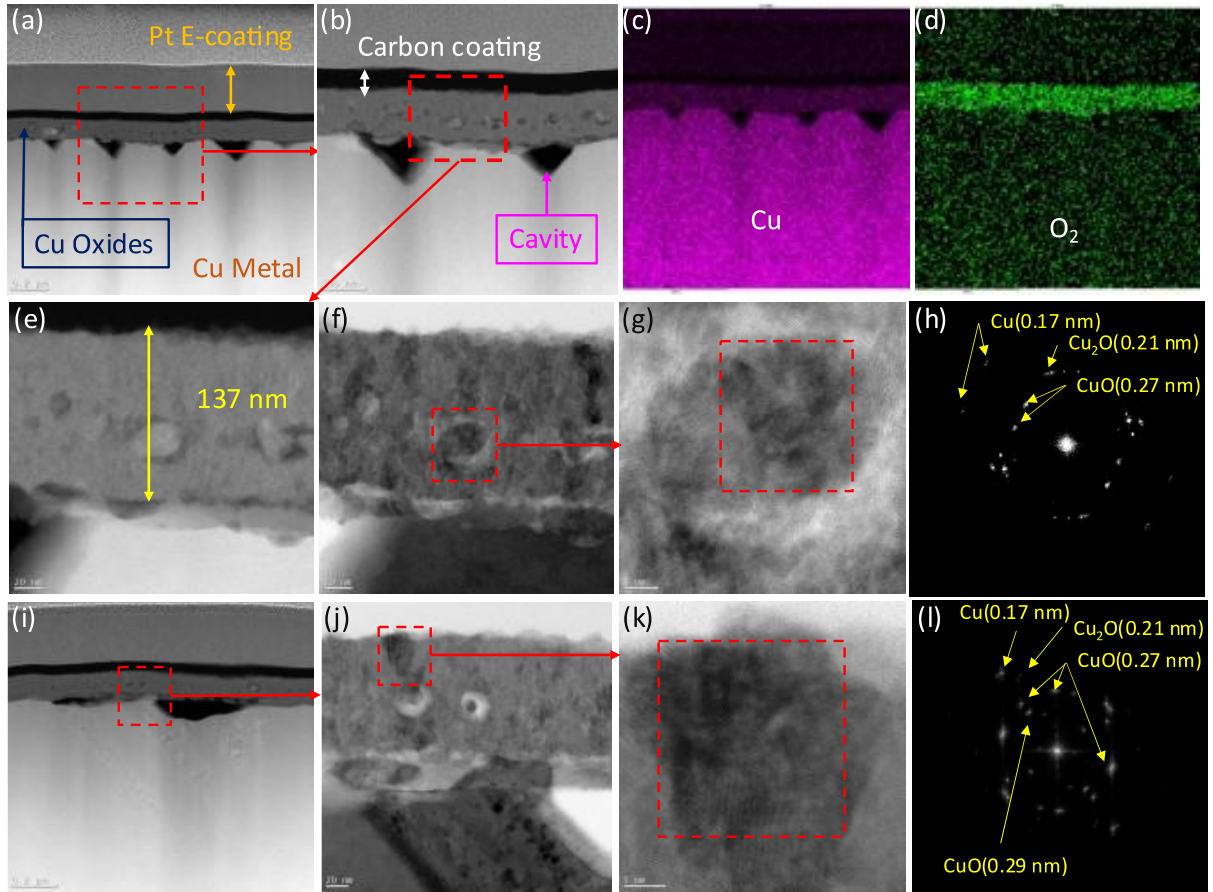
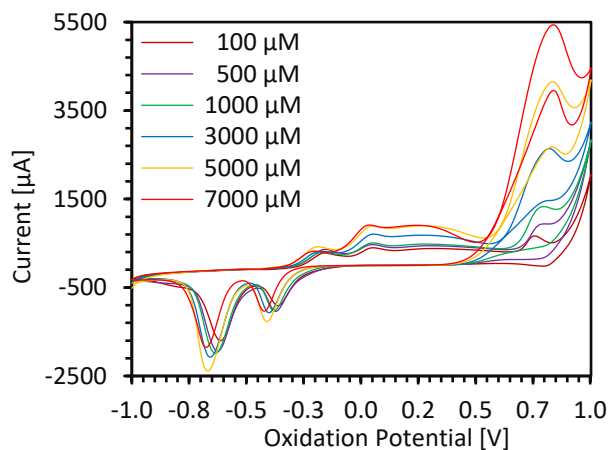


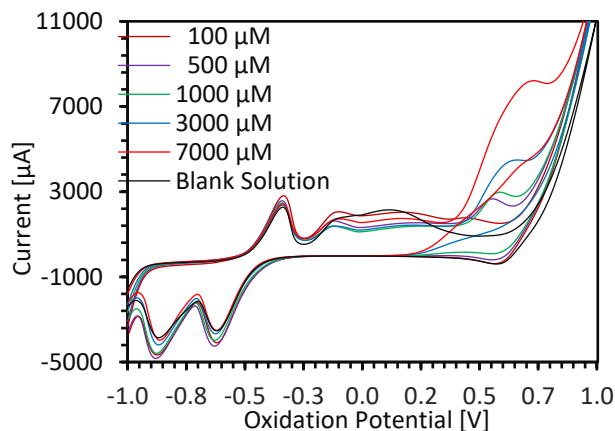
Fig. 5-4. HRTEM image of the electrode annealed at 280°C presents (a) nearly uniform growth of Cu oxides, (b) an enlarged version of the dotted portion in (a), (c) EDS image of (a) showing Cu distribution, (d) EDS image of (a) showing O distribution, (e) an enlarged version of the dotted portion in (b), (f) the annular bright-field (ABF) image of (e), (g) an enlarged version of the dotted portion in (f), (h) FFT image of the dotted portion in (g), (i) an image of the oxides layer from a different part of the thin film, (j) an enlarged version of the dotted portion in (i), (k) an enlarged version of the dotted portion in (j), and (l) FFT image of the dotted portion in (k).

5.4 Cyclic Voltammograms and calibration curves

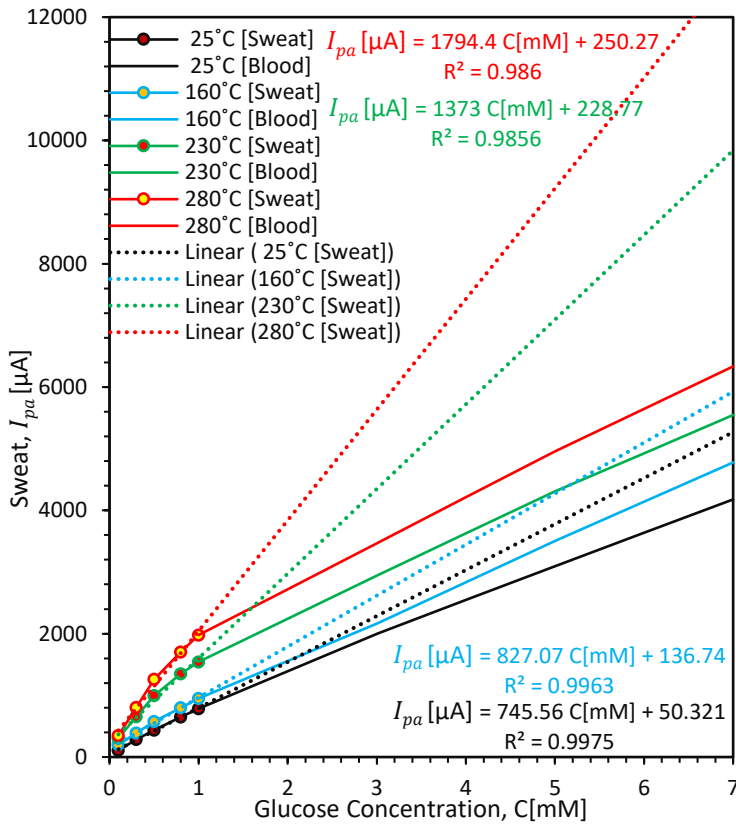
The electrochemical behavior of the thermally grown Cu native oxide (CuNO_x) electrodes has been systematically investigated for glucose sensing. The various accessible oxidation states of Cu, namely Cu(0), Cu(I), Cu(II), and Cu(III), make it an outstanding electrocatalytic transition metal, capable of facilitating reactions through both one- and two-electron pathways [82]. The electrode was electrochemically characterized for glucose electro-oxidation in 0.1 M NaOH alkaline solution with the aim of achieving a higher peak current at a lower potential, as well as reducing the background noise of glucose electro-oxidation [83]. Details of the electrocatalytic reactions and explanations for associated peaks have been provided in our previous work, referenced in [97].



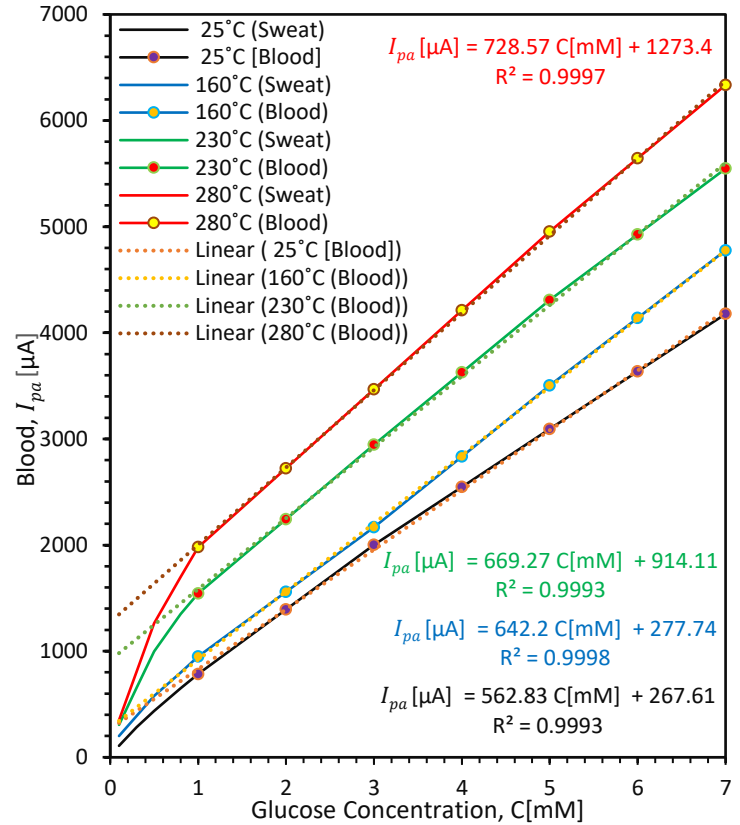
(a)



(b)



(c)



(d)

Fig. 5-5. Cyclic voltammograms of the CuNOx electrode after annealing at (a) 160 °C and (b) 280 °C captured at a 30 mVs⁻¹ scan rate. Calibration curves (C) Sweat, and (D) Blood glucose concentrations using the CuNOx electrodes annealed at 25, 160, 230, and 280°C.

5.4.1 Sensitivity and LOD

Fig. 5-5(c) shows the cyclic voltammetric calibration curves of the CuNOx electrodes prepared at 25, 160, 230, and 280°C for glucose sensing. While the calibration curves for 25°C, and 160°C exhibit a single linear region, dual linear regions appear for the electrodes prepared by annealing at 230°C, and 280°C. Given that the sensitivities of the CuNOx electrode at 280°C for both regions are higher, further study is conducted on the calibration

curve of this CuNOx electrode. The calibration curve for the CuNOx sensors annealed at 280°C for sweat and blood glucose sensing exhibits two linear regions in the ranges of 0.05—1.00 mM and 1.00—7.00 mM, respectively [500]. This span encompasses the sweat glucose concentration for healthy and diabetic individuals between 0.277 and 1.11 mM [94], [98], as well as the range of blood glucose concentration for healthy individuals, which is between 4.90 and 6.90 mM [97]. Hence, for the first time, we have defined the glucose concentration range from 0.050 mM to 7.00 mM as pertaining to sweat glucose and beyond. In Fig. 5-5(d), linear regressions have been performed for both the sweat and blood glucose ranges, and can be represented as follows:

$$\text{For Sweat:} \quad I_{pa}(\mu A) = 1795 C(mM) + 239.57 \quad [R^2 = 0.9824] \quad (5 - 5)$$

$$\text{For Blood:} \quad I_{pa}(\mu A) = 727.8 C(mM) + 1272.8 \quad [R^2 = 0.9997] \quad (5 - 6)$$

From equation (5-5), the estimated sensitivity of the CuNOx electrode annealed at 280°C is 1795 $\mu A \text{ mM}^{-1} \text{ cm}^{-2}$ (or 1.795 $\mu A \text{ }\mu\text{M}^{-1} \text{ cm}^{-2}$). The sensitivity of the CuNOx electrode for sweat glucose sensing is 603.42 $\mu A \text{ mM}^{-1} \text{ cm}^{-2}$ at 25°C, and 1795 $\mu A \text{ mM}^{-1} \text{ cm}^{-2}$ at 280°C. Hence, the sensitivity increases nearly three-fold (approximately 2.97) with a regression coefficient of 0.9824. On the other hand, equation (5-6) estimates the sensitivity for blood glucose sensing to be 727.8 $\mu A \text{ mM}^{-1} \text{ cm}^{-2}$, with a regression coefficient of 0.9997. The limit of detection (LOD) was estimated using equation (5-7), where s is the standard deviation of the blank solution, m is the slope of the calibration curve, and k ($=3$) is the multiplying factor [112]. As sweat glucose detection is the primary concern, the parameters from equation (5-5) are employed.

$$LOD = \frac{ks}{m} = \frac{3s}{m} \quad (5 - 7)$$

The measured standard deviation of the blank solution is 81.01 μA , and the signal-to-noise ratio is $S/N = 3$. The estimated LODs for sweat and blood glucose detection are 135.39, and 333.92 μM , respectively.

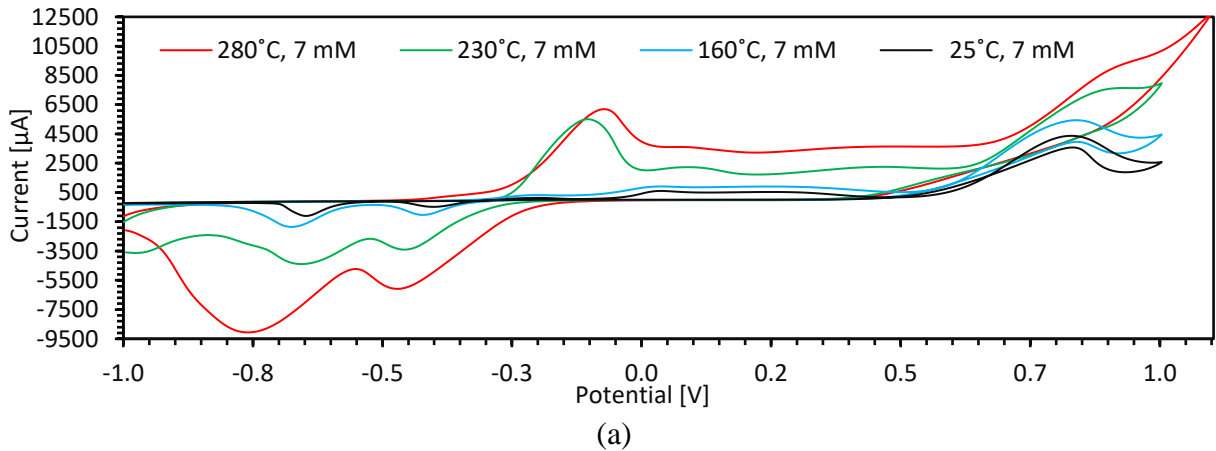
5.4.2 Effect of Annealing Temperature on Peak oxidation Current & Potential

Fig. 5-6(a) shows the cyclic voltammograms of sensing 7.00 mM glucose in a 0.1 M NaOH alkaline environment at a 30 mVs^{-1} scan rate, using the CuNO_x electrodes annealed at 25, 160, 230, and 280°C, following the temperature profile shown in Fig. 5-1(h). In Fig. 5-6(a), it is noteworthy to observe the electro-oxidation currents beyond -0.3 V . There is not much difference between voltammograms of the CuNO_x at 25 and 160°C. This may be since up to the 160°C annealing temperature, the surface oxide layer is dominated by the Cu₂O phase [97]. Since the surface oxide layer for CuNO_x at both 230 °C and 280°C is dominated by CuO, as confirmed by XPS and HRTEM data, the electro-oxidation currents increase significantly.

Moreover, the initial peak for the oxidation current for the 25 °C and 160°C-treated electrodes is around +0.03 V, whereas the potential is around -0.1 V for the 230 °C and 280°C electrodes. This can be explained by the electronic properties of CuO and Cu₂O. Cu₂O has direct band gaps between 2.0 and 2.17 eV at room temperature, 25 °C, while CuO has an indirect bandgap of 1.2 eV to 1.9 eV [97], [369], [370]. The lower bandgap energy makes CuO more electro-conductive than Cu₂O. On the other hand, the difference in oxidation current between the 230°C and 280°C-treated electrodes could be due to the larger

crystalline structure and grain size of CuO on the surface of 280°C annealed electrode, a fact also supported by other studies [495], [501].

Fig 5-6 (b) depicts the relationship between the peak electro-oxidation currents of 7.00 mM glucose oxidations and the associated oxidation potentials, as shown in Fig. 5-6(a), with the annealing temperatures of the electrodes. The electro-oxidation currents and associated potentials increase with the annealing temperatures of the electrodes. Furthermore, Fig. 5-6(c) determines the precise relationship between the peak electro-oxidation currents of 7.00 mM glucose and the associated oxidation potentials. Fig. 5-6(c) reveals that the peak electro-oxidation currents and their potentials are linearly related to the square root of the temperature, \sqrt{T} . Therefore, if a higher electro-oxidation current is needed, the electrode must be annealed at a higher temperature.



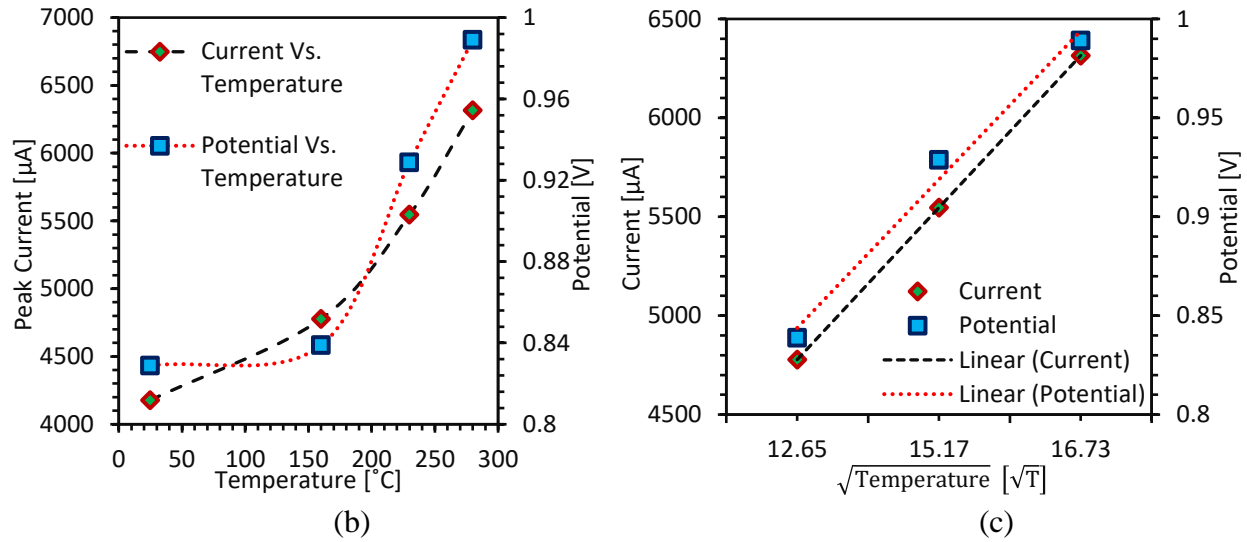


Fig. 5-6. (a) Voltammograms of 7.00 mM glucose detection using CuNO_x electrodes annealed 25, 160, 230, and 280°C at a 30 mVs⁻¹ scan rate in a 0.1 M NaOH alkaline environment. (b) The graphs show the relationship between the peak current of glucose oxidation and the oxidation potential at peak current, as shown in Fig. (a), plotted against temperature. (c) The curve fitting of data shown in Fig. (b), excluding 25°C, illustrates that peak electro-oxidation currents and their potentials are linearly related to \sqrt{T} .

It is evident from Fig. 5-6 that a higher peak electro-oxidation current of glucose can be achieved if the Cu thin films are annealed at higher temperatures. However, the potential associated with the peak electro-oxidation currents also increases, as seen in Fig. 5-6. Fig. 5-7(a) shows the peak electro-oxidation current of glucose for concentrations ranging from 0.1—7 mM, plotted against the associated oxidation potential. The peak current is exponentially related to the applied potential, as shown in Eq. (8) for the electrode at 25°C [97].

$$I_{pa}[\mu A] = 0.0004e^{19.428E_{pa}[V]} \quad [R^2 = 0.9844] \quad (8)$$

$$E_{pa}[V] = 0.0434 \log_e C[\mu M] + 0.4485 \quad [R^2 = 0.9838] \quad (9)$$

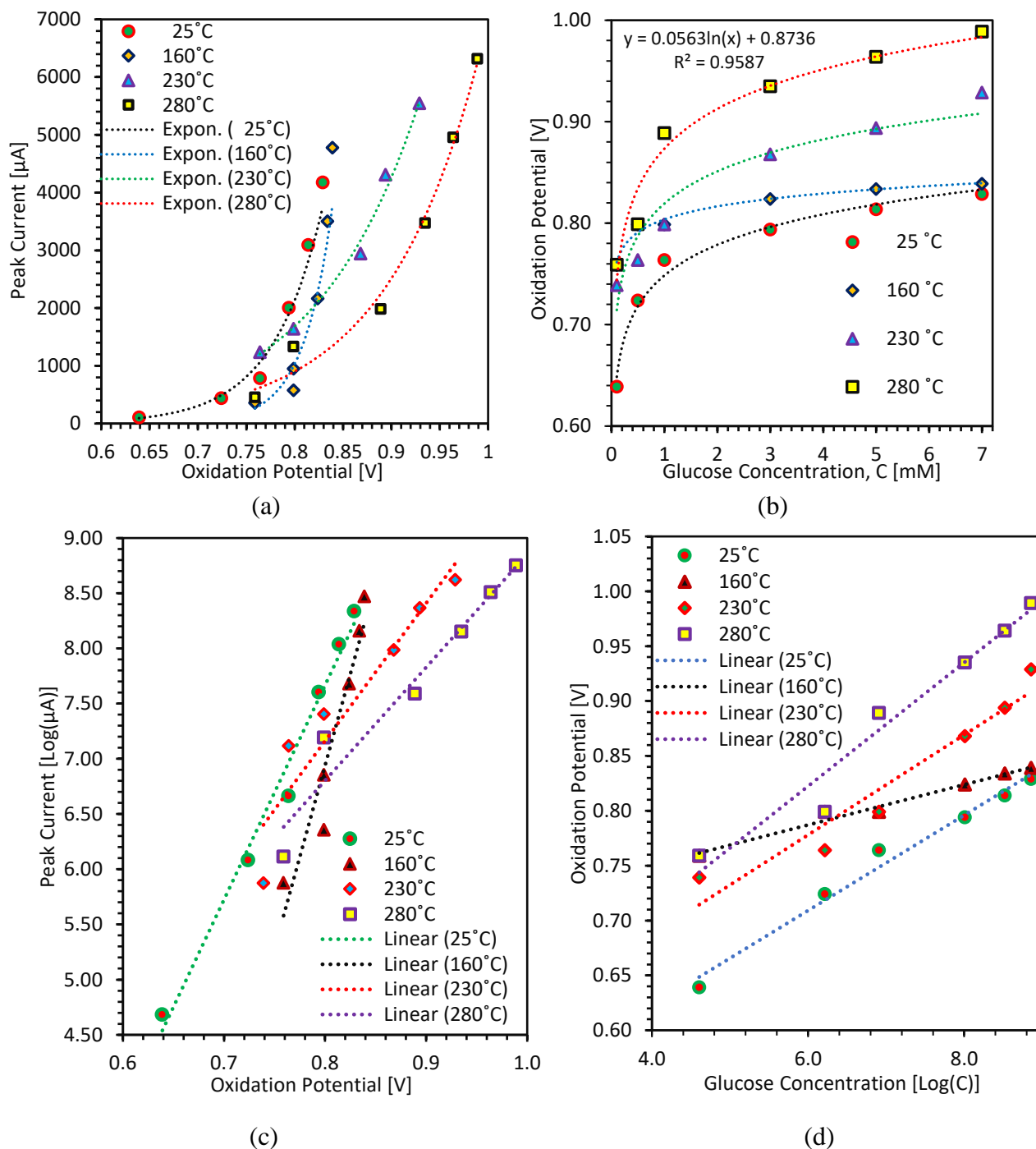


Fig. 5-7. The curve illustrates the following: (a) Both the peak oxidation current of glucose and the associated potential increase with the increasing glucose concentrations, showing an exponential relationship. (b) The potential at the peak oxidation current of glucose

increases logarithmically with the increase of glucose concentrations. (c) and (d) Semi log graphs of figure (a), and (b), respectively.

The same equation set for the electrode at 280°C can be determined from Fig. 5-7(a) and (b), as given below in equations (5-10) and (5-11).

$$I_{pa}[\mu A] = 0.247e^{10.252E_{pa}[V]} \quad [R^2 = 0.9876] \quad (5 - 10)$$

$$E_{pa}[V] = 0.0563 \log_e C[\mu M] + 0.8736 \quad [R^2 = 0.9587] \quad (5 - 11)$$

Some parameters have changed between these sets of equations. These sets can be used to decrease the oxidation potential, thereby ensuring that the maximum potential does not reach the point of water dissociation. This phenomenon may be explained as follows. As we know, the diffusion layer, which is the interface width between the electrode surface and bulk solution, is determined by the concentration of the analyte, in this case, glucose [459]. The width decreases as the concentration of glucose molecules increases. This smaller interface width allows a higher rate of reactions between the Cu native oxide layers and glucose molecules. Furthermore, the reaction rate determines the current amount [459]. Therefore, a higher electro-oxidation current of glucose results in a higher reaction rate.

When the anodic sweep potential increases, the oxidation rate of glucose molecules at the electrode surface also increases. Consequently, the anodic electro-oxidation current of glucose increases, leading to the production of gluconic acid. This gluconic acid then moves towards the bulk solution after being converted from glucose. However, the electro-oxidation current of glucose continues to increase with potential, as a higher potential diffuses more glucose molecules from the bulk solution [111], [459]. After reaching a certain point, or peak, the current slows down due to the larger width of the depletion region

created by gluconic acid, which reduces mass transport. This is known as the ‘mass-transfer-limited’ region [111], [459]. If the glucose concentration increases, the required potential to reach the ‘mass-transfer-limited’ region also increases. Therefore, the diffusion layer width may decrease logarithmically with the increase in glucose molecule concentration, which is why the potential at peak oxidation increases logarithmically. Since the peak current is linear with glucose concentration, as shown in Figure 5-(6), the peak current increases exponentially with the increase in potential (Fig 5-7(a)). This is why the electro-oxidation current of glucose on Cu and Cu oxides-based electrodes usually covers a very wide potential region, as shown in Figure 5-7(a).

5.4.3 Interference Analysis

The CuNO_x sensor prepared at 25°C has demonstrated high selectivity towards glucose molecules, rejecting interference from common biomolecules [97]. The usual interferants, which typically coexist with glucose in human sweat and blood, include (a) easily oxidizable species such as ascorbic acid (AA) and uric acid (UA); (b) a pain reliever, acetaminophen; (c) a neurotransmitter, dopamine (DA) and an amino acid, cysteine; as well as (d) common salts, sodium chloride (NaCl) and potassium chloride (KCl) [448], [457]. The interferent concentrations, as mentioned in the legends of Fig. 5-8(a), are chosen to generally match those found in blood and sweat [448], [457]. The anti-interference capability of a glucose sensor is crucial, as the interferants have higher electron transfer rates than glucose, which can easily deviate the actual glucose oxidation currents [389]. However, there is a well-known and widely accepted method of evaluating the performance of an electrode under various interferents for amperometric sensors. In contrast, the

evaluation process is absent in voltametric sensing systems. Moreover, it is challenging to obtain important information about the effects of different interferents on an electrode using the CV technique, as seen in Fig. 5-8(a).

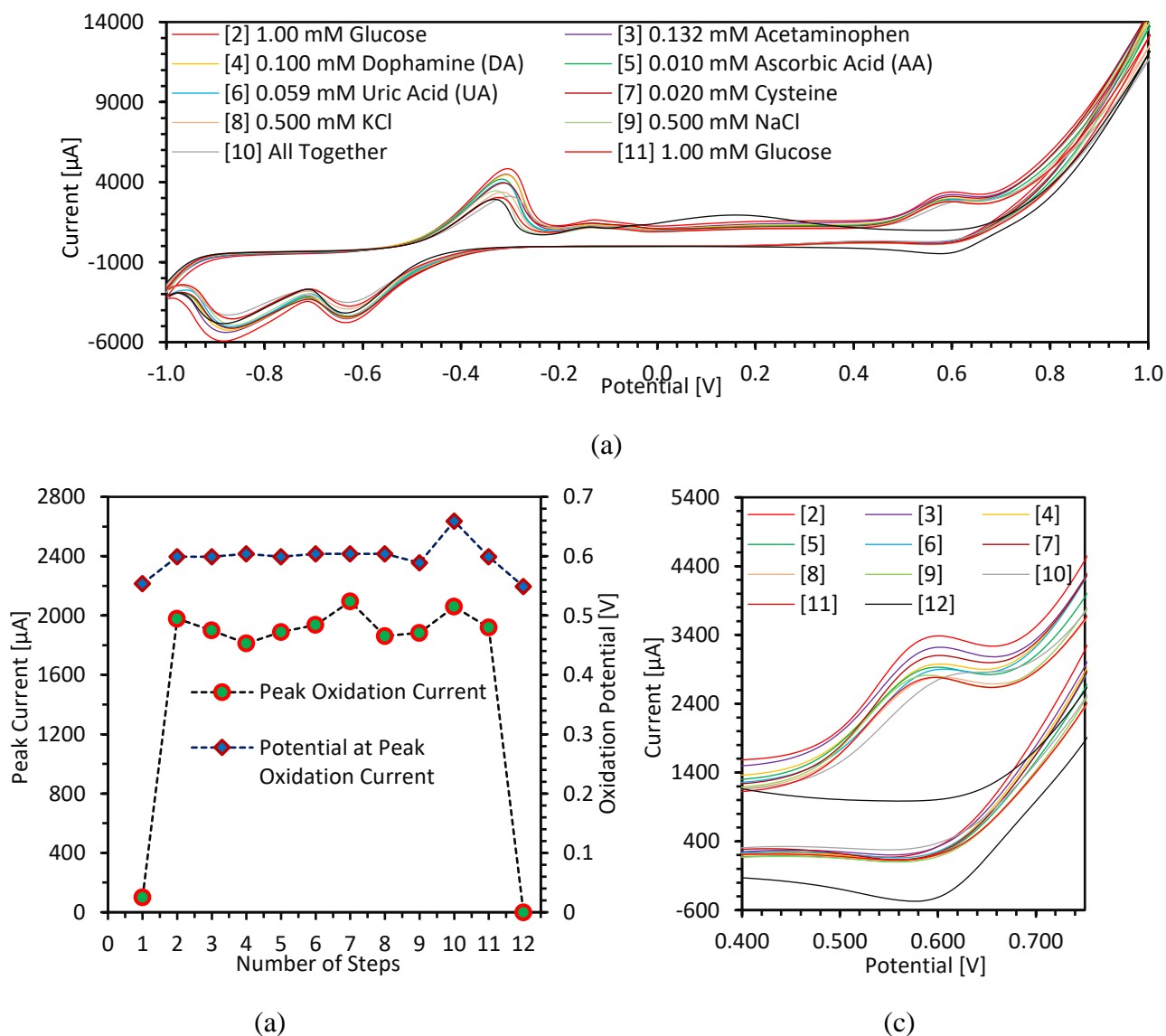


Fig. 5 – 8. (a) Cyclic voltammograms of 1 mM glucose with 0.1 M NaOH after adding different interferents present in human sweat. Here, Step 1: Signal of a blank solution in the presence of 0.1 M NaOH, which is omitted from Fig.5- 8(a) since the CV results of

steps 1 and 12 are the same. Step 12: Identical to step 1, after recording all CV results up to step 11 in the presence of all interferants. Step 2 and 11: Response to 1 mM glucose in the presence of 0.1 M NaOH. Step 3, 5, 7, and 9: Response to 0.132 mM acetaminophen; to 0.01 mM ascorbic acid; to 0.02 mM cysteine and 0.5 mM NaCl, respectively, in the presence of 1 mM glucose and 0.1 M NaOH. (b) The peak oxidation current and the associated oxidation potential vs. the step order, as shown in the legends of Figure 5-8(a), and (c) Magnified version of Fig. 5-8(a).

For the first time, we propose an evaluation method of the effects of the interferents on the electrode for the CV technique, as illustrated in Fig. 5-8(b). It is evident from the Fig. 5-8(b) that not only qualitative information, as in the case of amperometric technique, but also quantitative information — meaning the actual variations in oxidation current between different interferents — can be achieved using this evaluation method.

The selectivity of the CuNOx annealed at 280°C sensor was investigated using a freshly prepared electrode. The electrode was used to obtain 12 distinct CV results, as shown in Fig. 5-8(a), excluding the first and second CV results. The chronological list of peak electro-oxidation currents of glucose and associated potential of the 12 CVs are depicted in Fig. 5-8(b), where 1st step represents, the values using only 0.1 M NaOH (blank solution). The value at the 2nd step is for 1.00 mM glucose with 0.1 M NaOH. From the step 3rd to the 10th, a specific interferent, as noted in the legends of Fig. 5-8(a), is added along with 1 mM glucose and 0.1 M NaOH.

While there are reports that UA and AA interferents with concentrations of 0.059 mM and 0.01 mM can be easily oxidized [460], the addition of such concentrations with glucose

does not significantly change the oxidation current, as shown in steps 5 and 6. In step 8 and 9, 0.5 mM KCl and 0.5 mM NaCl, respectively, were used to run CV results. According to previous studies, Cu electrodes suffer from the chloride poisoning effect which degrades redox activity [389]. However, as there is no change in the peak electro-oxidation current in step 11, it can be concluded that the CuNO_x at 280°C electrode doesn't suffer from the chloride poisoning effect. Moreover, the resultant relative standard deviation (RSD) of the peak oxidation current was 4.32%, as shown in Fig. 5-8. (b), representing an excellent performance of the CuNO_x electrode annealed at 280°C against all the interferents. In summary, the addition of interferents to a solution of 1 mM glucose and 0.1 M NaOH does not significantly alter the increase in the peak oxidation current. This finding demonstrates that the CuNO_x sensing electrode possesses excellent anti-interference capacity and favorable selectivity for the nonenzymatic detection of glucose.

5.4.4 Reproducibility & Reusability

The reproducibility of the glucose sensing of CuNO_x electrode annealed at 280°C was evaluated by utilizing 4 freshly prepared electrodes under the same conditions. The CV responses were performed in a 0.1 M NaOH solution containing 0.5-, 1-, 3-, and 7-mM glucose at a scan-rate of 30 mVs⁻¹. Furthermore, each glucose concentration was investigated using 4 electrodes for seven distinct trials. The peak oxidation current of glucose is presented in Fig. 5-9, along with the standard deviation. The resultant RSDs of the peak oxidation current were 2.16%, 2.32%, 2.42%, and 2.48% for 0.5, 1.0, 3.0, and 7.0 mM, respectively. The RSD demonstrates the excellent reproducibility and reusability of

the Cu native oxides electrode, showcasing the reliability of the CuNOx sensors annealed at 280°C.

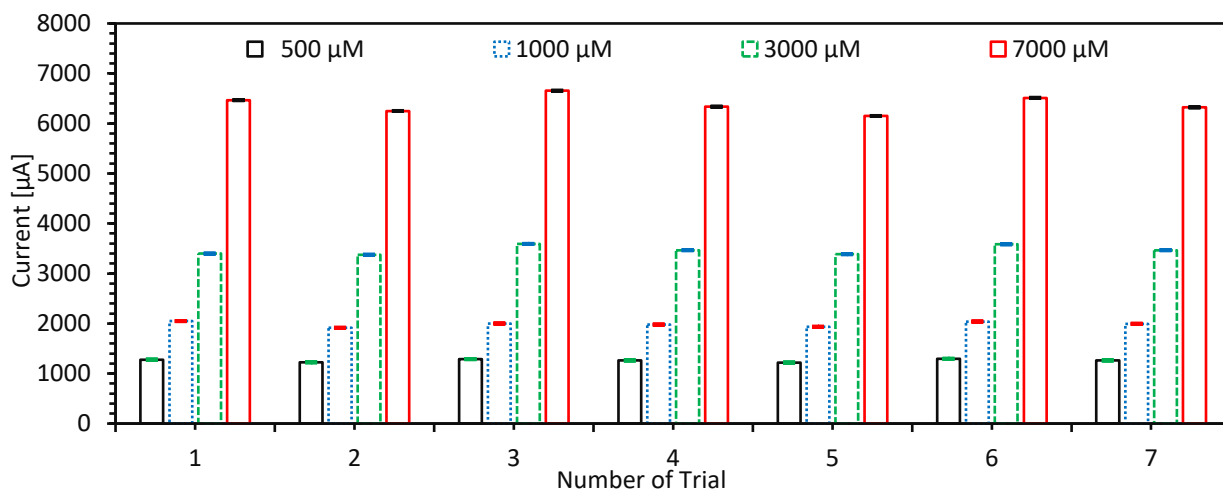


Fig. 5-9. Repeatability test of the CuNOx electrode annealed at 280°C in a 0.1 M NaOH alkaline solution with glucose concentrations of 0.5-, 1.0-, 3.0-, and 7.0-mM. A distinct electrode was used for each concentration in the same solution. The solution was shaken before each subsequent CV measurement.

5.4.5 Stability

Stability refers to the sensor's ageing behavior, indicating the electrode's robustness against sensitivity drift. The stability of the CuNOx sensing electrode was examined in 0.1 M NaOH with 1.0 mM glucose at a scan-rate of 30 mVs^{-1} . Fig. 5-10. displays the peak oxidation current of glucose along with its RSD for 65 days. The CV was conducted every 5 days to measure sensitivity while the sensor was stored under ambient conditions without any special treatment. The RSD values are 4.17% and 2.32% for 50 days and 65 days, respectively, illustrating the high stability of the electrode. After 12 usages, the native Cu oxides glucose sensor retains 96.91% of its original response, indicating excellent stability

and long-term (8 weeks) storage capability of the sensing electrode. The results demonstrated that the sensor was not poisoned by the oxidation product, proving its usefulness for long-term glucose monitoring.

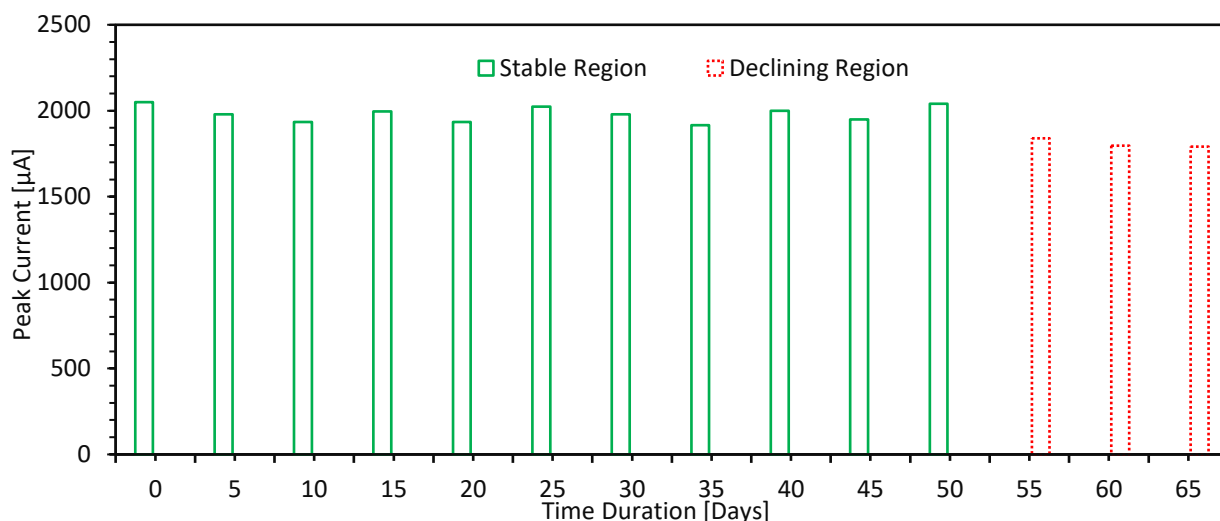


Fig. 5-10. Stability test of the CuNOx electrode annealed at 280°C, conducted in a 0.1 M NaOH alkaline solution with a glucose concentration of 1.0 mM.

5.4.6 CuNOx annealed at 280°C Sensing Parameters with Others

Table 5-II compares the linear range, LOD, sensitivity, selectivity, stability, repeatability, and reusability of the CuNOx at 280°C sweat glucose sensor of this study with that of the previously reported non-enzymatic electrochemical glucose sensors. The sensing performance of this Cu-roll based CuNOx sensor demonstrates significant advantages in comparison to other sensors.

Table 5-II: Comparison of CuNOx @280°C sensors with other non-enzymatic glucose sensors.

Electrode	Method	Linear Range (mM)	LOD (μM)	Sensitivity ($\mu\text{A mM}^{-1}\text{cm}^{-2}$)	Selectivity	Stability	Repeatability & Reusability	Ref.
CuNOx @ 280°C	CV	0.05 – 1.00	135.39	1795.00	4.32% (AA, UA, AP, DA, NaCl, KCl, Cys)	96.91% (50 Days)	2.32% (n = 7)	This work
CuNOx @ 25°C	CV	0.05 – 7.00	94.21	603.42	3.56% (AA, UA, AP, DA, NaCl, KCl, Cys)	96.91% (55 Days)	2.67% (n = 7)	[97]
Pt-NFw/GO/GCE	Amp	0.002 – 10.30	2.00	0.64	- (AA, UA, NaCl)	73.4% (14 Days)	6.30% (n = 5)	[296]
AuNCs film/FTO Glass	Amp	0.01 – 10.00	2.00	10.65	- (AA, AP, UA, NaCl)	98% (30 Days)	5.00% (n = 5)	[298]
AuNPs film/ITO	CV	0.03 – 45.00	10.00	67.20	- (AA, NaCl, KCl)	-	-	[280]
Pt-Ni-NCs/MWCNT/GCE	Amp	0.00 – 15.00	0.30	940.00	- (AA, AP, UA, Urea, Fru, Gal, Lac)	99% (2 Days)	10% (n = 5)	[302]
Cu@Cu ₂ O-NSs/rGO/GCE	Amp	0.005 – 7.00	0.50	145.20	- (AA, UA, Fru, Lac)	95% (14 Days)	2.10% (n = 7)	[502]

Useful Acronym: CuNOx @280°C– Cu Native Oxide annealed at 280°C, AP – Acetaminophen, NaCl – Sodium Chloride, KCl – Potassium Chloride, Cys – Cysteine, AS – Acidum Salicylicum, Ch – Cholesterol, Ep – Ephedrine, EtOH – Ethanol, Fru – Fructose, Gal – Galactose, Lac – Lactose, Tyr – tyrosine, Xyl – Xylose, Pt-NFw – Platinum Nano Flower, GO – Graphene Oxide, GCE – Glassy Carbon Electrode, Amp – Amperometric, AuNCs – Gold Nano Clusters, FTO - Fluorine doped Tin Oxide, AuNPs – Gold Nano Particles, ITO - Indium Tin Oxide, Ni – Nickle, MWCNT – Multi-Walled Carbon Nanotube, NSs – Nano Sheets, rGO – Reduced Graphene Oxide.

5.5 Challenges & Opportunities

The main disadvantage of a Cu electrode is its inability to function in low or neutral pH environments because hydroxyl anions, OH⁻, are required to produce CuOOH catalysis, which is necessary for glucose oxidation [468]. Consequently, an OH⁻ rich alkaline environment is created with 0.1 M NaOH, but this is unsuitable for direct sensing of sweat glucose on human skin[503]–[506]. Hence, technology needs to be developed to allow us to utilize a CuNOx electrode as a wearable sweat monitoring sensor. We envision a dual-

chamber system to circumvent this challenge. Specifically, we propose an initial chamber containing 0.1 M NaOH. This chamber will remain sealed until a predefined potential or current is applied, serving as an electrically activated gate. Upon activation, this chamber will release its contents and subsequently interface with a larger, secondary chamber designated for sweat collection. Once the requisite amount of sweat is accumulated, the secondary chamber will be sealed off, ensuring no direct contact of the skin with the alkaline 0.1 M NaOH. This design is intended to not only facilitate the sensor's function in the desired environment but also prioritize user safety by preventing any potential skin-alkali interactions.

While nanostructures offer a high surface-to-volume ratio, effective electron transfer, and physiochemical features promising for sensing applications, a significant challenge lies in the attachment between nanoparticles and the substrate [448]. A CuNO_x electrode prepared at 280°C heat treatment could potentially overcome these issues, including the aggregation phenomenon of the nanoparticles.

Although the reaction mechanisms of Cu materials are not clear, they are thought to be like those of Ni. The electro-oxidation peak of Cu(II) and glucose involves high background currents, causing the glucose oxidation peak to be nearly indiscernible in some cases. Competitive reactions, such as the oxygen evolution reaction, can disrupt the anodic signal from glucose oxidation, leading to complications in quantitative glucose analysis [365]. However, the information from Fig. 5-7(a), and (b) may be useful in mitigating these effects.

Based on these results, bonding these Cu rolls, which have CuNO_x electrodes, to flexible polymer substrates at low temperatures [68] can lead to the development of robust, low-cost, miniaturized integrated sensors for wearable applications. In addition, these CuNO_x electrodes can be fabricated using the Cu/LCP method explained by Redhwan et al. 2023 [507]. The bonded Cu/LCP curled after heating, indicating flexibility. This flexible integrated bond system did not lose its bond strength observed by peel test [508], [509].

5.6 Conclusions

In conclusion, the innovative fabrication of three CuNO_x electrodes via a unique annealing temperature profile has yielded an affordable and efficient process to produce precise, reproducible electrodes onto Cu rolls with a thickness of 35 µm. The thermally grown Cu oxides layers show a distinct increase from 10 nm at 25°C to 140 nm at 280°C. This facile fabrication technique paves the way for an inexpensive process in the production line of precise and reproducible sensing electrodes. Advanced characterization techniques, X-ray photoelectron spectroscopy (XPS) and high-resolution transmission electron microscopy (HRTEM) were utilized for the characterization of the bare electrodes. XPS analysis reveals distinct chemical states of the electrode at different temperatures, along with the spontaneous formation of native Cu₂O and CuO on the surface, with Cu₂O being more predominant due to a negative Gibbs' free energy change. As the temperature increased, oxidation overcame diffusion barriers, leading to a significant increase in CuO formation, peaking at 280°C, suggesting that the oxidation temperature primarily drove oxide growth. This increased CuO growth, driven by higher thermal energy, enhances the

surface-to-volume ratio and ultimately increases the electro-oxidation current of glucose, thereby boosting sensitivity. Moreover, HRTEM investigations reveal that the crystallization of CuO increases on the surface and within the Cu oxide layer. However, the surface CuO crystals were abundant in different CuO planes, which improves glucose detection. The fabricated electrodes onto Cu rolls could be bonded to flexible substrates to create simple, robust sensors, capable of withstanding a strong alkaline environment over an extended period.

The thermally grown CuNO_x electrodes were analyzed using CV, demonstrating their high performance as electrocatalysts for glucose detection. All three types of electrodes exhibited excellent electrocatalytic activity towards glucose. In terms of sensitivity, the electrodes exhibited a sensitivity of 1794.4 $\mu\text{A mM}^{-1} \text{cm}^{-2}$ at 280°C, while sensitivities of 1373 and 827.07 $\mu\text{A mM}^{-1} \text{cm}^{-2}$ were observed at 230°C, and 160°C annealing temperatures respectively, for sweat glucose sensing. These sensitivity results are commendable among nonenzymatic glucose sensors (Table 5-II). Furthermore, the thermally grown CuNO_x electrodes at 280°C showed strong resistance to the poisoning effects of chloride ions, while also exhibiting excellent reproducibility and reusability, and negligible interference effects in the presence of various interferents. This work also highlights the promising advantages of native oxides grains electrodes in terms of stability, as compared to Cu nanomaterials. The fabricated sensors can be conveniently miniaturized for point-of-care packaging devices.

Chapter 6

Conclusions and recommendations

6.1 Conclusions

Electrochemical enzymatic electrodes dominate the world market of blood glucose monitoring devices for controlling and reducing the detrimental effects of diabetes. However, the enzymatic electrodes exhibit constraints, restricting their reliance on the enzyme's activity which can be influenced by external environmental factors such as temperature, pH, and humidity. Moreover, the larger thickness of the enzyme hinders the performance of the glucose biosensors, resulting in signal dampening or loss. In addition, the selectivity of the electrodes is affected by the interferences present in blood. On the other hand, the invasive nature of the electrodes is another major problem. Hence, recent research activities demonstrated that the electrochemical non-enzymatic electrodes are inexpensive and highly sensitive towards glucose, which is promising for glucose biosensing devices, yet these electrochemical nonenzymatic electrodes are non-invasive in nature. Therefore, the purpose of this research was to fabricate facile and flexible electrochemical non-enzymatic electrodes for sweat glucose monitoring devices.

This thesis focuses on the design, fabrication, and characterization of electrochemical non-enzymatic non-invasive biosensors for glucose monitoring systems. For sweat glucose sensing, a very simple low-cost fabrication technique has been shown to make the facile, flexible, and inexpensive electrodes to detect sugar in sweat bio-analyte

for a non-invasive glucose monitoring system using the native stable Cu oxides (CuNO_x), Cu₂O, layers grown on 35 μm thin Cu foils keeping under ambient conditions (25°C- and 760-mm Hg) for more than 2 years so that the oxide layers are fully grown, and stable. Moreover, the foils also annealed at various temperatures such as 160, 230, and 280°C with new temperature profile for reducing the required time of growing stable oxides and producing oxides with larger crystallized structures, and grains with higher surface – to – volume ratio. The X-ray photoelectron spectroscopy (XPS) and high-resolution transmission electron microscopy (HRTEM) results supported that at 280°C annealing temperature the surface, mostly, transformed into highly electrocatalytic CuO with larger grain sizes, crystallized structures, and the uniform layer of ~ 140 nm. The electrochemical characterization, and sensing performance of the electrodes have been done by cyclic voltammetry (CV), one of the excellent and well accepted electrochemical methods, with the 3 – electrode configuration of the potentiostat. The CuNO_x sensors of having ~10 nm layer of stable Cu₂O exhibited a sensitivity of 603.42 μA mM⁻¹ cm⁻², a linear range beyond the desired limit of 7.00 mM with excellent linearity ($R^2 = 0.9983$) and a low limit of detection of 94.21 μM. In contrast, the new annealing profile has. the CuNO_x sensors annealed at 280 °C using new temperature profile provided twin calibration curves of linear ranges of 0.05 – 1.00 mM and 1.00 – 7.00 mM, that applicable for sweat and blood glucose sensing, respectively, and exhibited a sensitivity of 1795 μA mM⁻¹ cm⁻², a linear range up to the desired limit of 1.00 mM for sweat glucose sensing with excellent linearity ($R^2 = 0.9844$), and a lower limit of detection of 135.39 μM.

The fabrication technique proved to be very cost effective due to its simple procedure and easy to use substrate without using any rigorous processes such as ultrasonic processing, chemical synthesis, and electrochemical modification. Moreover, the facile fabrication technique shows the robustness of the electrical grade scotch tape as a substrate of the electrodes over the expensive substrate fabrication processes under cleanroom environment, high-temperature/pressure conditions, and/or high-vacuum equipment. Hence, the CuNO_x electrodes are facile, flexible, and ultra-low-cost glucose biosensors.

In Chapter 1, the necessity of human health, and glucose monitoring was presented, followed by a comprehensive overview of the electrochemical enzymatic and non-enzymatic glucose biosensors. Then, the motivation of developing facile, flexible, inexpensive, and high-performance electrodes for sweat glucose monitoring systems was presented. By comparing different types of sensing materials, the potentiostat configurations, and electrochemical sensing techniques, we choose to use Cu native oxides (Cu₂O, CuO), the three – electrode potentiostat configuration, and the cyclic voltametric (CV) method, respectively. Finally, a summary of the main contributions of this research and the structure of this thesis are described.

In Chapter 2, we analyzed the crucial topics of chemical reactions in the electrochemical sensing environments and sensor-electrode interactions considering their applications in the healthcare section. First, we discussed the dynamics of chemical energy, the roles of acidic and alkaline fluids, chemical reaction tendencies, thermodynamic equilibria, Gibbs free energy, water dissociation, and the pH scale. Since, the sensing materials and/or biomarkers undergo oxidation and reduction reactions in electrochemical

sensing platform, we also presented the effects of oxygen-derived radicals and nonradical reactive species on human health, the impact of oxidation reduction reactions on human psychology, the pattern of redox reactions in hemoglobin, the redox environments in human serum albumin and cells/tissues, and the thermodynamics of biological redox reactions. Moreover, the significance of oxygen-derived radicals and nonradical reactive species in biochemical reactions, cellular responses, and clinical outcomes have been discussed in context of the impact of oxidation reduction reactions on human psychology, redox reactions in hemoglobin, redox environments in human serum albumin and cells/tissues, and thermodynamics of biological redox reactions.

In Chapter 3, we summarized advanced knowledge of the fundamental principles of various electrochemical techniques for healthcare applications. Emphasize has been given to the crucial topics necessary to understand chemical reactions in an electrochemical cell environment. We provided a detailed explanation of the methods, the formulation and the solution of mathematical equations related to the techniques with present limitations, and future research perspectives for health applications.

In Chapter 4, we reported a facile, low-cost, high-performance nonenzymatic copper (Cu) native oxide (CuNO_x)-based electrochemical sensor for sweat glucose sensing. We utilized a very thin Cu native oxide of ~10 nm layer on Cu thin films for the glucose sensing because of the excellent catalytic oxidation behavior of cuprous oxide (Cu₂O) to glucose. The anodic sweep of cyclic voltammetry of glucose showed that the hydroxyl ions from sodium hydroxide convert the electrode surface into different oxides [Cu(I), Cu (II) Cu(III)], which electro-oxidize glucose to gluconolactone, then eventually

to gluconic acid resulting in oxidation current. Advanced characterization techniques, X-ray photoelectron spectroscopy (XPS) and high-resolution transmission electron microscopy (HRTEM) were utilized for the characterization of the bare electrodes. The CuNOx sensors exhibited a sensitivity of $603.42 \mu\text{A mM}^{-1} \text{cm}^{-2}$, a linear range beyond the desired limit of 7.00 mM with excellent linearity, and a low limit of detection of 94.21 μM . Excellent repeatability and stability (stable >1 year) with relative standard deviation (RSD) of 2.67%, and 2.70%, respectively were achieved for 1 mM glucose. The selectivity with common interferants of glucose in human sweat and blood showed an RSD of 3.56%. We believed the electrocatalytic efficacy of the CuNOx sensors for glucose sensing can open a new prospect in the fabrication of wearable sweat glucose sensors.

In Chapter 5, we fabricated three CuNOx electrodes via a unique annealing temperature profile yielded an affordable and efficient process to produce precise, reproducible electrodes onto Cu rolls with a thickness of 35 μm using 160, 230, and 280°C. The thermally grown Cu oxides layers show a distinct increase from 10 nm at 25°C to 140 nm at 280°C. This facile fabrication technique paves the way for an inexpensive process in the production line of precise and reproducible sensing electrodes. Advanced characterization techniques, X-ray photoelectron spectroscopy (XPS) and high-resolution transmission electron microscopy (HRTEM) were utilized for the characterization of the bare electrodes. XPS analysis reveals distinct chemical states of the electrode at different temperatures, along with the spontaneous formation of native Cu₂O and CuO on the surface, with Cu₂O being more predominant till 160°C due to a negative Gibbs' free energy change. As the temperature increased, oxidation overcame diffusion barriers, leading to a

significant increase in CuO formation, peaking at 280°C, suggesting that the oxidation temperature primarily drove oxide growth. This increased CuO growth, driven by higher thermal energy, enhances the surface-to-volume ratio and ultimately increases the electro-oxidation current of glucose, thereby boosting sensitivity. Moreover, HRTEM investigations reveal that the crystallization of CuO increases on the surface and within the Cu oxide layer. However, the surface CuO crystals were abundant in different CuO planes, which improves glucose detection. The fabricated electrodes onto Cu rolls could be bonded to flexible substrates to create simple, robust sensors, capable of withstanding a strong alkaline environment over an extended period. The thermally grown CuNO_x electrodes were analyzed using CV, demonstrating their high performance as electrocatalysts for glucose detection. All three types of electrodes exhibited excellent electrocatalytic activity towards glucose. In terms of sensitivity, the electrodes exhibited a sensitivity of 1794.4 $\mu\text{A mM}^{-1} \text{cm}^{-2}$ at 280°C, while sensitivities of 1373 and 827.07 $\mu\text{A mM}^{-1} \text{cm}^{-2}$ were observed at 230°C, and 160°C annealing temperatures respectively, for sweat glucose sensing.

6.2 Recommendations

This research work focused on fabricating facile, flexible, and inexpensive electrochemical non-enzymatic electrodes for sweat glucose monitoring devices. The sweat glucose monitoring system, we have envisioned, is shown in figure 7 – 1 as follows.

However, a few steps needed to be taken to integrate the sensors in a sweat glucose monitoring device.

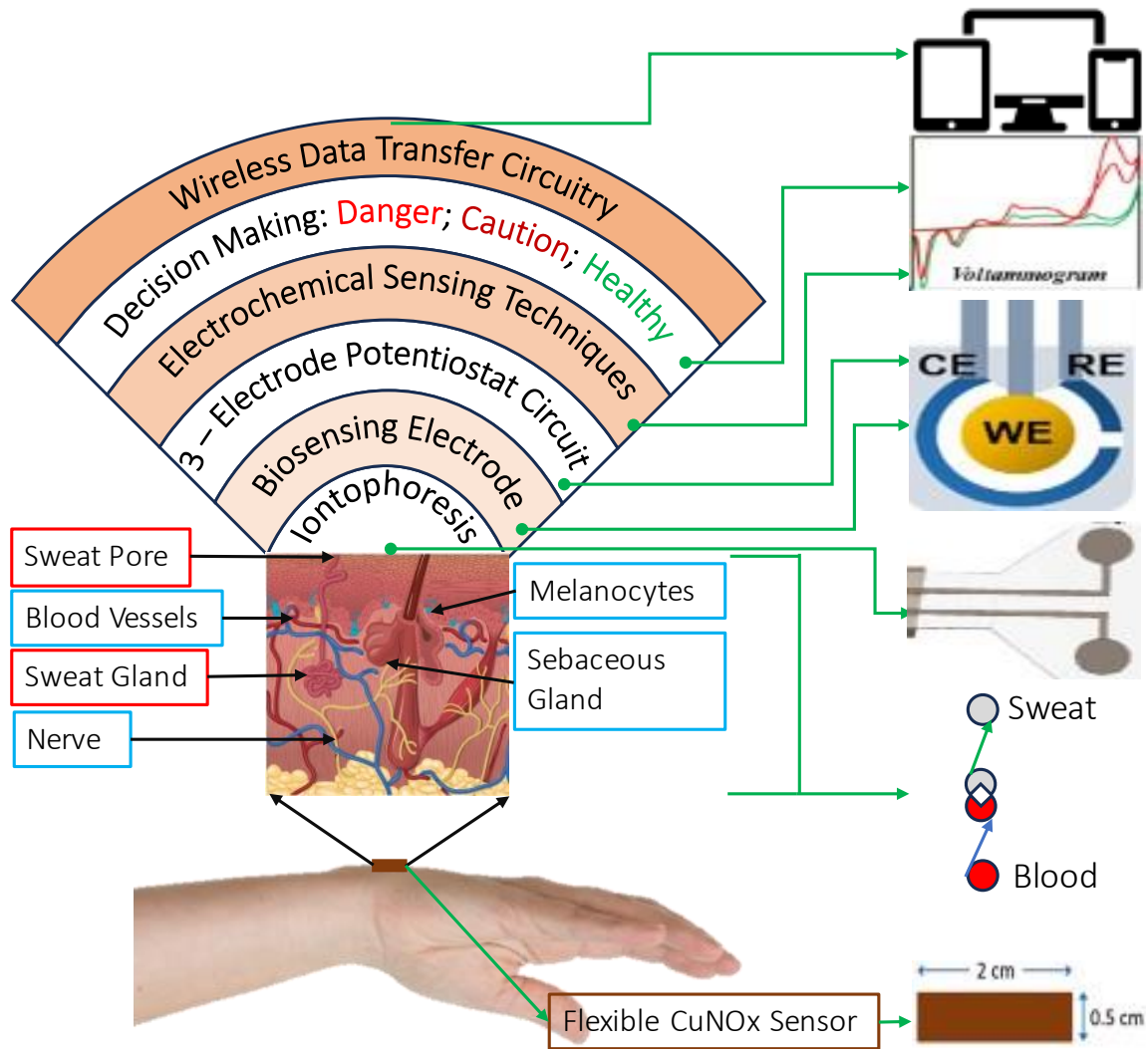


Fig. 6 – 1: Schematic diagram of sweat glucose monitoring systems.

- *Evaluation of the sensors using artificial as well as real sweat*

The immediate step is to evaluate the performance of the electrodes using the sweat serum as well as real sweat. Moreover, the bare electrodes primarily cannot be used directly on the skin because the non-enzymatic glucose sensors require high pH alkaline environments.

Although, the sensor can be used in an electrochemical cell separate from human skin, that would not serve the full potential of the sensor.

- *Development of a Mechanism to Attach a Chamber for NaOH*

The main disadvantage of a Cu electrode is its inability to function in low or neutral pH environments because hydroxyl anions, OH^- , are required to produce CuOOH catalysis, which is necessary for glucose oxidation. Consequently, an OH^- rich alkaline environment is created with 0.1 M NaOH, but this is unsuitable for direct sensing of sweat glucose on human skin. Hence, technology needs to be developed to allow us to utilize a CuNOx electrode as a wearable sweat monitoring sensor. We envision a dual-chamber system to circumvent this challenge. Specifically, we propose an initial chamber containing 0.1 M NaOH. This chamber will remain sealed until a predefined potential or current is applied, serving as an electrically activated gate. Upon activation, this chamber will release its contents and subsequently interface with a larger, secondary chamber designated for sweat collection. Once the requisite amount of sweat is accumulated, the secondary chamber will be sealed off, ensuring no direct contact of the skin with the alkaline 0.1 M NaOH. This design is intended to not only facilitate the sensor's function in the desired environment but also prioritize user safety by preventing any potential skin-alkali interactions.

- *Evaluation of The Sensor Attaching on Human Skin*

The major impediment towards sweat glucose sensing is the low concentrations of glucose in sweat which is 0.277–1.11 mM. To evaluate the real potential of the electrodes, the sensor needs to be attached to human skin for sensing real time sugar variation.

The target of this research was to fabricate a facile, flexible, and inexpensive electrode for a sweat glucose monitoring device. It is demonstrated that thin films based thermally grown native Cu oxide electrode, CuNO_x, could be a noble candidate to integrate in a system of sweat glucose monitoring device. This research provides the feasibility, challenges, and potential solutions to develop non-invasive glucose monitoring systems for practical applications.

References

- [1] “WHO Coronavirus (COVID-19) Dashboard | WHO Coronavirus (COVID-19) Dashboard With Vaccination Data.” Accessed: Jul. 08, 2023. [Online]. Available: <https://covid19.who.int/>
- [2] N. Chauhan, S. Soni, P. Agrawal, Y. P. S. Balhara, and U. Jain, “Recent advancement in nanosensors for neurotransmitters detection: Present and future perspective,” *Process Biochemistry*, vol. 91, pp. 241–259, Apr. 2020, doi: 10.1016/J.PROCBIO.2019.12.016.
- [3] Z. Tavakolian-Ardakani, O. Hosu, C. Cristea, M. Mazloun-Ardakani, and G. Marrazza, “Latest Trends in Electrochemical Sensors for Neurotransmitters: A Review,” *Sensors 2019, Vol. 19, Page 2037*, vol. 19, no. 9, p. 2037, Apr. 2019, doi: 10.3390/S19092037.
- [4] G. Slaughter, M. Robinson, J. Tyson, and C. J. Zhang, “Neuroelectronic device process development and challenge,” <https://doi.org/10.1117/12.2256297>, vol. 10147, pp. 264–271, Mar. 2017, doi: 10.1117/12.2256297.
- [5] L. Wu, L. Feng, J. Ren, and X. Qu, “Electrochemical detection of dopamine using porphyrin-functionalized graphene,” *Biosens Bioelectron*, vol. 34, no. 1, pp. 57–62, Apr. 2012, doi: 10.1016/J.BIOS.2012.01.007.
- [6] G. C.-I. J. of Zoology and undefined 1950, “Elenco delle Cocciniglie osservate in Sicilia: (Hemiptera - Homoptera, Fam. Goccidae),” *Taylor & Francis*, vol. 17, no. 1–3, pp. 1–24, 2009, doi: 10.1080/11250005009439097.
- [7] A. S. Sacramento, F. T. C. Moreira, J. L. Guerreiro, A. P. Tavares, and M. G. F. Sales, “Novel biomimetic composite material for potentiometric screening of acetylcholine, a neurotransmitter in Alzheimer’s disease,” *Materials Science and Engineering: C*, vol. 79, pp. 541–549, Oct. 2017, doi: 10.1016/J.MSEC.2017.05.098.
- [8] Q. Chen, L. P. Yang, D. H. Li, J. Zhai, W. Jiang, and X. Xie, “Potentiometric determination of the neurotransmitter acetylcholine with ion-selective electrodes containing oxatub[4]arenes as the ionophore,” *Sens Actuators B Chem*, vol. 326, Jan. 2021, doi: 10.1016/J.SNB.2020.128836.
- [9] C. He, G. Li, Y. Wang, and W. Zhou, “A miniature potentiometric sensor for dopamine determination in vitro,” *Meas Sci Technol*, vol. 32, no. 6, Jun. 2021, doi: 10.1088/1361-6501/ABBFED.

- [10] M. Vestergaard, K. Kerman, and E. Tamiya, “An Overview of Label-free Electrochemical Protein Sensors,” *Sensors 2007, Vol. 7, Pages 3442-3458*, vol. 7, no. 12, pp. 3442–3458, Dec. 2007, doi: 10.3390/S7123442.
- [11] Z. H. Ibupoto, N. Jamal, K. Khun, and M. Willander, “Development of a disposable potentiometric antibody immobilized ZnO nanotubes based sensor for the detection of C-reactive protein,” *Sens Actuators B Chem*, vol. 166–167, pp. 809–814, May 2012, doi: 10.1016/J.SNB.2012.03.083.
- [12] J. Kaur and P. K. Singh, “Trypsin Detection Strategies: A Review,” <https://doi.org/10.1080/10408347.2020.1846490>, vol. 52, no. 5, pp. 949–967, 2020, doi: 10.1080/10408347.2020.1846490.
- [13] M. Hirota, M. Ohmuraya, and H. Baba, “The role of trypsin, trypsin inhibitor, and trypsin receptor in the onset and aggravation of pancreatitis,” *J Gastroenterol*, vol. 41, no. 9, pp. 832–836, Sep. 2006, doi: 10.1007/S00535-006-1874-2.
- [14] P. Dandona, M. Hodson, J. Bell, L. Ramdial, I. Beldon, and J. C. Batten, “Serum immunoreactive trypsin in cystic fibrosis,” *Thorax*, vol. 36, no. 1, pp. 60–62, 1981, doi: 10.1136/THX.36.1.60.
- [15] V. Fonseca *et al.*, “Serum immunoreactive trypsin and pancreatic lipase in primary biliary cirrhosis,” *J Clin Pathol*, vol. 39, no. 6, pp. 638–640, 1986, doi: 10.1136/JCP.39.6.638.
- [16] A. De La Escosura-Muñiz and A. Merkoçi, “Electrochemical detection of proteins using nanoparticles: applications to diagnostics,” <http://dx.doi.org/10.1517/17530050903386661>, vol. 4, no. 1, pp. 21–37, Jan. 2009, doi: 10.1517/17530050903386661.
- [17] Z. Mujagić, H. Mujagic, and B. Prnjavorac, “The relationship between circulating carcinoembryonic antigen (CEA) levels and parameters of primary tumor and metastases in breast cancer patients,” *Med Arh*, vol. 58, no. 1, pp. 23–26, Jan. 2004, Accessed: Jul. 15, 2023. [Online]. Available: <https://europepmc.org/article/med/15017899>
- [18] B. V. Chikkaveeraiah, A. A. Bhirde, N. Y. Morgan, H. S. Eden, and X. Chen, “Electrochemical immunosensors for detection of cancer protein biomarkers,” *ACS Nano*, vol. 6, no. 8, pp. 6546–6561, Aug. 2012, doi: 10.1021/NN3023969/ASSET/IMAGES/LARGE/NN-2012-023969_0010.JPEG.
- [19] T. J. Polascik, J. E. Oesterling, and A. W. Partin, “PROSTATE SPECIFIC ANTIGEN: A DECADE OF DISCOVERY-WHAT WE HAVE LEARNED AND WHERE WE ARE GOING,” *J Urol*, vol. 162, no. 2, pp. 293–306, Aug. 1999, doi: 10.1016/S0022-5347(05)68543-6.

- [20] T. S. C. R. Rebelo, C. Santos, J. Costa-Rodrigues, M. H. Fernandes, J. P. Noronha, and M. G. F. Sales, “Novel Prostate Specific Antigen plastic antibody designed with charged binding sites for an improved protein binding and its application in a biosensor of potentiometric transduction,” *Electrochim Acta*, vol. 132, pp. 142–150, Jun. 2014, doi: 10.1016/J.ELECTACTA.2014.03.108.
- [21] J. E. Tamis-Holland *et al.*, “Contemporary Diagnosis and Management of Patients With Myocardial Infarction in the Absence of Obstructive Coronary Artery Disease: A Scientific Statement From the American Heart Association,” *Circulation*, vol. 139, no. 18, pp. E891–E908, Apr. 2019, doi: 10.1161/CIR.0000000000000670.
- [22] H. Y. Lee, J. S. Choi, P. Guruprasath, B. H. Lee, and Y. W. Cho, “An electrochemical biosensor based on a myoglobin-specific binding peptide for early diagnosis of acute myocardial infarction,” *Analytical Sciences*, vol. 31, no. 7, pp. 699–704, 2015, doi: 10.2116/ANALSCI.31.699.
- [23] Y. Liu, Q. Zhou, and A. Revzin, “An aptasensor for electrochemical detection of tumor necrosis factor in human blood,” *Analyst*, vol. 138, no. 15, pp. 4321–4326, Aug. 2013, doi: 10.1039/C3AN00818E.
- [24] D. W. Lachenmeier and M. Uebelacker, “Quantitative Determination of Acetaldehyde in Foods Using Automated Digestion with Simulated Gastric Fluid Followed by Headspace Gas Chromatography,” *J Autom Methods Manag Chem*, vol. 2011, p. 13, 2011, doi: 10.1155/2011/907317.
- [25] “List of Classifications – IARC Monographs on the Identification of Carcinogenic Hazards to Humans.” Accessed: Feb. 17, 2023. [Online]. Available: <https://monographs.iarc.who.int/list-of-classifications>
- [26] J. D. Newman and A. P. F. Turner, “Home blood glucose biosensors: A commercial perspective,” *Biosensors and Bioelectronics*, vol. 20, no. 12. Elsevier Ltd, pp. 2435–2453, Jun. 15, 2005. doi: 10.1016/j.bios.2004.11.012.
- [27] “What is diabetes? | CDC.” Accessed: Jul. 21, 2023. [Online]. Available: <https://www.cdc.gov/diabetes/basics/diabetes.html>
- [28] “World Health Organization (WHO),” Diabetes Fact Sheet. Accessed: Aug. 27, 2021. [Online]. Available: <https://www.who.int/news-room/fact-sheets/detail/diabetes>
- [29] “Global Burden of Disease Collaborative Network. Global Burden of Disease Study 2019. Results. Institute for Health Metrics and Evaluation. 2020.” Accessed: Jul. 19, 2023. [Online]. Available: <https://vizhub.healthdata.org/gbd-results/>

- [30] F. F. Costa, W. R. Rosário, A. C. Ribeiro Farias, R. G. de Souza, R. S. Duarte Gondim, and W. A. Barroso, “Metabolic syndrome and COVID-19: An update on the associated comorbidities and proposed therapies,” *Diabetes & Metabolic Syndrome: Clinical Research & Reviews*, vol. 14, no. 5, pp. 809–814, Sep. 2020, doi: 10.1016/J.DSX.2020.06.016.
- [31] R. M. Torrente-Rodríguez, H. Lukas, J. Tu, C. Xu, H. B. Rossiter, and W. Gao, “SARS-CoV-2 RapidPlex: A Graphene-Based Multiplexed Telemedicine Platform for Rapid and Low-Cost COVID-19 Diagnosis and Monitoring,” 2020, doi: 10.1016/j.matt.2020.09.027.
- [32] S. Kotru *et al.*, “Electrochemical sensing: A prognostic tool in the fight against COVID-19,” 2021, doi: 10.1016/j.trac.2021.116198.
- [33] “Diabetes and Vascular Disease — Vascular Cures.” Accessed: Jul. 21, 2023. [Online]. Available: <https://www.vascularcures.org/diabetes-and-vascular-disease>
- [34] “2. Classification and Diagnosis of Diabetes: Standards of Medical Care in Diabetes—2022,” *Diabetes Care*, vol. 45, pp. S17–S38, Jan. 2022, doi: 10.2337/DC22-S002.
- [35] “Kids & type 1 - Diabetes Canada.” Accessed: Jul. 21, 2023. [Online]. Available: <https://www.diabetes.ca/managing-my-diabetes/kids,-teens---diabetes/kids---type-1>
- [36] N. Chukwuemeka, “Diabetes mellitus: a complete ancient and modern historical perspective,” *Webmedcentral*, vol. 6, no. 2, 2015.
- [37] M. H. Hassan, C. Vyas, B. Grieve, and P. Bartolo, “Recent advances in enzymatic and non-enzymatic electrochemical glucose sensing,” *Sensors*, vol. 21, no. 14, MDPI AG, Jul. 02, 2021. doi: 10.3390/s21144672.
- [38] D. Bruen, C. Delaney, L. Florea, and D. Diamond, “Glucose sensing for diabetes monitoring: Recent developments,” *Sensors (Switzerland)*, vol. 17, no. 8, 2017, doi: 10.3390/s17081866.
- [39] J. Ju *et al.*, “Surface Enhanced Raman Spectroscopy Based Biosensor with a Microneedle Array for Minimally Invasive In Vivo Glucose Measurements,” *ACS Sens*, vol. 5, no. 6, pp. 1777–1785, Jun. 2020, doi: 10.1021/ACSSENSORS.0C00444.
- [40] L. R. Bornhoeft, A. Biswas, and M. J. McShane, “Composite Hydrogels with Engineered Microdomains for Optical Glucose Sensing at Low Oxygen Conditions,” *Biosensors 2017, Vol. 7, Page 8*, vol. 7, no. 1, p. 8, Jan. 2017, doi: 10.3390/BIOS7010008.

- [41] Z. Vafapour, “Polarization-Independent Perfect Optical Metamaterial Absorber as a Glucose Sensor in Food Industry Applications,” *IEEE Trans Nanobioscience*, vol. 18, no. 4, pp. 622–627, Oct. 2019, doi: 10.1109/TNB.2019.2929802.
- [42] M. Shehab, S. Ebrahim, and M. Soliman, “Graphene quantum dots prepared from glucose as optical sensor for glucose,” *J Lumin*, vol. 184, pp. 110–116, Apr. 2017, doi: 10.1016/J.JLUMIN.2016.12.006.
- [43] I. L. Jernelv, K. Milenko, S. S. Fuglerud, D. R. Hjelme, R. Ellingsen, and A. Aksnes, “A review of optical methods for continuous glucose monitoring,” <https://doi.org/10.1080/05704928.2018.1486324>, vol. 54, no. 7, pp. 543–572, Aug. 2018, doi: 10.1080/05704928.2018.1486324.
- [44] V. P. Rachim and W. Y. Chung, “Wearable-band type visible-near infrared optical biosensor for non-invasive blood glucose monitoring,” *Sens Actuators B Chem*, vol. 286, pp. 173–180, May 2019, doi: 10.1016/J.SNB.2019.01.121.
- [45] V. Garzón, D. G. Pinacho, R. H. Bustos, G. Garzón, and S. Bustamante, “Optical Biosensors for Therapeutic Drug Monitoring,” *Biosensors (Basel)*, vol. 9, no. 4, 2019, doi: 10.3390/BIOS9040132.
- [46] M. E. Bosch, A. J. R. Sánchez, F. S. Rojas, and C. B. Ojeda, “Recent Development in Optical Fiber Biosensors,” *Sensors 2007, Vol. 7, Pages 797-859*, vol. 7, no. 6, pp. 797–859, Jun. 2007, doi: 10.3390/S7060797.
- [47] A. S. M. Z. Kausar, A. W. Reza, T. A. Latef, M. H. Ullah, and M. E. Karim, “Optical Nano Antennas: State of the Art, Scope and Challenges as a Biosensor Along with Human Exposure to Nano-Toxicology,” *Sensors 2015, Vol. 15, Pages 8787-8831*, vol. 15, no. 4, pp. 8787–8831, Apr. 2015, doi: 10.3390/S150408787.
- [48] D. Harvey, *Modern analytical chemistry*. McGraw-Hill, 2000.
- [49] N. Paniel, J. Baudart, A. Hayat, and L. Barthelmebs, “Aptasensor and genosensor methods for detection of microbes in real world samples,” *Methods*, vol. 64, no. 3, pp. 229–240, Dec. 15, 2013. doi: 10.1016/j.ymeth.2013.07.001.
- [50] J. Kirsch, C. Siltanen, Q. Zhou, A. Revzin, and A. Simonian, “Biosensor technology: recent advances in threat agent detection and medicine,” *Chem Soc Rev*, vol. 42, no. 22, pp. 8733–8768, Oct. 2013, doi: 10.1039/C3CS60141B.
- [51] A. Chen and B. Shah, “Electrochemical sensing and biosensing based on square wave voltammetry,” *Analytical Methods*, vol. 5, no. 9. The Royal Society of Chemistry, pp. 2158–2173, May 07, 2013. doi: 10.1039/c3ay40155c.
- [52] V. Urbanova, M. Magro, A. Gedanken, D. Baratella, F. Vianello, and R. Zboril, “Nanocrystalline iron oxides, composites, and related materials as a platform for

- electrochemical, magnetic, and chemical biosensors,” *Chemistry of Materials*, vol. 26, no. 23, pp. 6653–6673, Dec. 2014, doi: 10.1021/cm500364x.
- [53] M. M. Alam, V. Mitea, M. M. R. Howlader, P. R. Selvaganapathy, and M. J. Deen, “Analyzing Electrochemical Sensing Fundamentals for Health Applications,” *Advanced Sensor Research*, vol. Submitted, 2023.
- [54] C. Zhu, G. Yang, H. Li, D. Du, and Y. Lin, “Electrochemical sensors and biosensors based on nanomaterials and nanostructures,” *Anal Chem*, vol. 87, no. 1, pp. 230–249, Jan. 2015, doi: 10.1021/AC5039863/ASSET/IMAGES/LARGE/AC-2014-039863_0006.JPEG.
- [55] D. Giziński, A. Brudzisz, J. S. Santos, F. Trivinho-Strixino, W. J. Stępniewski, and T. Czujko, “Nanostructured anodic copper oxides as catalysts in electrochemical and photoelectrochemical reactions,” *Catalysts*, vol. 10, no. 11, pp. 1–38, 2020, doi: 10.3390/catal10111338.
- [56] E. Bakker and M. Telting-Diaz, “Electrochemical Sensors,” *Anal Chem*, vol. 74, no. 12, pp. 2781–2800, Jun. 2002, doi: 10.1021/AC0202278.
- [57] N. R. Stradiotto, H. Yamanaka, and M. V. B. Zanoni, “Electrochemical sensors: a powerful tool in analytical chemistry,” *J Braz Chem Soc*, vol. 14, no. 2, pp. 159–173, Apr. 2003, doi: 10.1590/S0103-50532003000200003.
- [58] A. J. Bard and L. R. Faulkner, *Electrochemical methods: fundamentals and applications*. Wiley, 2001.
- [59] M. Gutiérrez-Capitán, A. Baldi, Á. Merlos, and C. Fernández-Sánchez, “Array of individually addressable two-electrode electrochemical cells sharing a single counter/reference electrode for multiplexed enzyme activity measurements,” *Biosens Bioelectron*, vol. 201, p. 113952, Apr. 2022, doi: 10.1016/J.BIOS.2021.113952.
- [60] P. Makaram, D. Owens, and J. Aceros, “Trends in Nanomaterial-Based Non-Invasive Diabetes Sensing Technologies,” *Diagnostics*, vol. 4, no. 2, pp. 27–46, Apr. 2014, doi: 10.3390/diagnostics4020027.
- [61] L. C. Clark and C. Lyons, “Electrode Systems For Continuous Monitoring In Cardiovascular Surgery,” *Ann N Y Acad Sci*, vol. 102, no. 1, pp. 29–45, Oct. 1962, doi: 10.1111/J.1749-6632.1962.TB13623.X.
- [62] “Meddevicetracker: Diabetes Management: Blood Glucose Monitoring Devices Market,” London, 2017. Accessed: Jul. 29, 2023. [Online]. Available: <https://www.meddevicetracker.com/ReportDetail.cfm?ReportID=463>

- [63] “Diabetes Care Devices Market Forecast to 2028 - COVID-19 Impact and Global Analysis By Type and End User,” May 2022. Accessed: Jul. 29, 2023. [Online]. Available: https://www.researchandmarkets.com/reports/4769863/diabetes-care-devices-market-forecast-to-2028?gclid=EAIaIQobChMIw4qwwNi2gAMV-SWtBh1DHQXjEAAAYAAEgIOk_D_BwE
- [64] S. J. Updike and G. P. Hicks, “The enzyme electrode,” *Nature*, vol. 214, no. 5092, pp. 986–988, 1967, doi: 10.1038/214986A0.
- [65] G. G. Guilbault and G. J. Lubrano, “An enzyme electrode for the amperometric determination of glucose,” *Anal Chim Acta*, vol. 64, no. 3, pp. 439–455, 1973, doi: 10.1016/S0003-2670(01)82476-4.
- [66] C. Chen *et al.*, “Recent advances in electrochemical glucose biosensors: a review,” *RSC Adv*, vol. 3, no. 14, pp. 4473–4491, Mar. 2013, doi: 10.1039/C2RA22351A.
- [67] A. A. Karyakin, O. V. Gitelmacher, and E. E. Karyakina, “Prussian Blue-Based First-Generation Biosensor. A Sensitive Amperometric Electrode for Glucose,” *Anal Chem*, vol. 67, no. 14, pp. 2419–2423, Jul. 1995, doi: 10.1021/AC00110A016.
- [68] C. Kaçar, B. Dalkiran, P. E. Erden, and E. Kiliç, “An amperometric hydrogen peroxide biosensor based on Co₃O₄ nanoparticles and multiwalled carbon nanotube modified glassy carbon electrode,” *Appl Surf Sci*, vol. 311, pp. 139–146, Aug. 2014, doi: 10.1016/J.APSUSC.2014.05.028.
- [69] J. Wang, “Electrochemical glucose biosensors,” *Chem Rev*, vol. 108, no. 2, pp. 814–825, Feb. 2008, doi: 10.1021/CR068123A.
- [70] N. G. Poulos, J. R. Hall, and M. C. Leopold, “Functional layer-by-layer design of xerogel-based first-generation amperometric glucose biosensors,” *Langmuir*, vol. 31, no. 4, pp. 1547–1555, Feb. 2015, doi: 10.1021/LA504358T/SUPPL_FILE/LA504358T_SI_001.PDF.
- [71] G. Reach and S. W. George, “Can Continuous Glucose Monitoring Be Used for the Treatment of Diabetes ?,” *Anal Chem*, vol. 64, no. 6, 1992, doi: 10.1021/AC00030A001.
- [72] A. N. Sekretaryova, D. V. Vokhmyanina, T. O. Chulanova, E. E. Karyakina, and A. A. Karyakin, “Reagentless biosensor based on glucose oxidase wired by the mediator freely diffusing in enzyme containing membrane,” *Anal Chem*, vol. 84, no. 3, pp. 1220–1223, Feb. 2012, doi: 10.1021/AC203056M.

- [73] D. A. Gough, J. Y. Lucisano, and P. H. S. Tse, “Two-Dimensional Enzyme Electrode Sensor for Glucose,” *Anal Chem*, vol. 57, no. 12, pp. 2351–2357, Oct. 1985, doi: 10.1021/AC00289A042.
- [74] S. Kashyap and F. Lu, “Oxygen-rich oxidase enzyme electrodes for operation in oxygen-free solutions,” *J Am Chem Soc*, vol. 120, no. 5, pp. 1048–1050, Feb. 1998, doi: 10.1021/JA972759P/ASSET/IMAGES/LARGE/JA972759PF00003.JPEG.
- [75] J. Wang, J. W. Mo, S. Li, and J. Porter, “Comparison of oxygen-rich and mediator-based glucose-oxidase carbon-paste electrodes,” *Anal Chim Acta*, vol. 441, no. 2, pp. 183–189, Aug. 2001, doi: 10.1016/S0003-2670(01)01116-3.
- [76] I. Jeerapan, J. R. Sempionatto, J. M. You, and J. Wang, “Enzymatic glucose/oxygen biofuel cells: Use of oxygen-rich cathodes for operation under severe oxygen-deficit conditions,” *Biosens Bioelectron*, vol. 122, pp. 284–289, Dec. 2018, doi: 10.1016/J.BIOS.2018.09.063.
- [77] R. Kontani, S. Tsujimura, and K. Kano, “Air diffusion biocathode with CueO as electrocatalyst adsorbed on carbon particle-modified electrodes,” *Bioelectrochemistry*, vol. 76, no. 1–2, pp. 10–13, Sep. 2009, doi: 10.1016/J.BIOELECTCHEM.2009.02.009.
- [78] H. Teymourian *et al.*, “Microneedle-Based Detection of Ketone Bodies along with Glucose and Lactate: Toward Real-Time Continuous Interstitial Fluid Monitoring of Diabetic Ketosis and Ketoacidosis,” *Anal Chem*, vol. 92, no. 2, pp. 2291–2300, Jan. 2020, doi: 10.1021/ACS.ANALCHEM.9B05109/ASSET/IMAGES/MEDIUM/AC9B05109_0004.GIF.
- [79] W. Schuhmann, H. L. Schmidt, T. J. Ohara, and A. Heller, “Electron Transfer between Glucose Oxidase and Electrodes via Redox Mediators Bound with Flexible Chains to the Enzyme Surface,” *J Am Chem Soc*, vol. 113, no. 4, pp. 1394–1397, 1991, doi: 10.1021/JA00004A048/ASSET/JA00004A048.FP.PNG_V03.
- [80] K. I. Ozoemena and T. Nyokong, “Novel amperometric glucose biosensor based on an ether-linked cobalt(II) phthalocyanine–cobalt(II) tetraphenylporphyrin pentamer as a redox mediator,” *Electrochim Acta*, vol. 51, no. 24, pp. 5131–5136, Jul. 2006, doi: 10.1016/J.ELECTACTA.2006.03.055.
- [81] M. Dervisevic, E. Çevik, and M. Şenel, “Development of glucose biosensor based on reconstitution of glucose oxidase onto polymeric redox mediator coated pencil

- graphite electrodes,” *Enzyme Microb Technol*, vol. 68, pp. 69–76, Jan. 2015, doi: 10.1016/J.ENZMICTEC.2014.09.007.
- [82] H. Al-Sagur, S. Komathi, M. A. Khan, A. G. Gurek, and A. Hassan, “A novel glucose sensor using lutetium phthalocyanine as redox mediator in reduced graphene oxide conducting polymer multifunctional hydrogel,” *Biosens Bioelectron*, vol. 92, pp. 638–645, Jun. 2017, doi: 10.1016/J.BIOS.2016.10.038.
- [83] K. E. Toghill and R. G. Compton, “Electrochemical non-enzymatic glucose sensors: A perspective and an evaluation,” *Int J Electrochem Sci*, vol. 5, no. 9, pp. 1246–1301, 2010.
- [84] E. Mehmeti, D. M. Stanković, S. Chaiyo, J. Zavasnik, K. Žagar, and K. Kalcher, “Wiring of glucose oxidase with graphene nanoribbons: an electrochemical third generation glucose biosensor,” *Microchimica Acta*, vol. 184, no. 4, pp. 1127–1134, Apr. 2017, doi: 10.1007/S00604-017-2115-5/TABLES/2.
- [85] P. Rafighi, M. Tavahodi, and B. Haghighi, “Fabrication of a third-generation glucose biosensor using graphene-polyethyleneimine-gold nanoparticles hybrid,” *Sens Actuators B Chem*, vol. 232, pp. 454–461, Sep. 2016, doi: 10.1016/J.SNB.2016.03.147.
- [86] Y. Degani and A. Heller, “Electrical Communication between Redox Centers of Glucose Oxidase and Electrodes via Electrostatically and Covalently Bound Redox Polymers,” *J Am Chem Soc*, vol. 111, no. 6, pp. 2357–2358, 1989, doi: 10.1021/JA00188A091/ASSET/JA00188A091.FP.PNG_V03.
- [87] Y. Wang and F. Caruso, “Enzyme encapsulation in nanoporous silica spheres,” *Chemical Communications*, vol. 4, no. 13, pp. 1528–1529, Jun. 2004, doi: 10.1039/B403871A.
- [88] S. Wu, H. Ju, and Y. Liu, “Conductive Mesocellular Silica–Carbon Nanocomposite Foams for Immobilization, Direct Electrochemistry, and Biosensing of Proteins,” *Adv Funct Mater*, vol. 17, no. 4, pp. 585–592, Mar. 2007, doi: 10.1002/ADFM.200600491.
- [89] Z. Zhu, L. Garcia-Gancedo, A. J. Flewitt, H. Xie, F. Moussy, and W. I. Milne, “A Critical Review of Glucose Biosensors Based on Carbon Nanomaterials: Carbon Nanotubes and Graphene,” *Sensors 2012, Vol. 12, Pages 5996-6022*, vol. 12, no. 5, pp. 5996–6022, May 2012, doi: 10.3390/S120505996.
- [90] M. M. Rahman, A. J. S. Ahammad, J. H. Jin, S. J. Ahn, and J. J. Lee, “A Comprehensive Review of Glucose Biosensors Based on Nanostructured Metal-Oxides,” *Sensors 2010, Vol. 10, Pages 4855-4886*, vol. 10, no. 5, pp. 4855–4886, May 2010, doi: 10.3390/S100504855.

- [91] P. Bollella and L. Gorton, “Enzyme based amperometric biosensors,” *Curr Opin Electrochem*, vol. 10, pp. 157–173, Aug. 2018, doi: 10.1016/J.COEELEC.2018.06.003.
- [92] N. Gupta, V. Renugopalakrishnan, D. Liepmann, R. Paulmurugan, and B. D. Malhotra, “Cell-based biosensors: Recent trends, challenges and future perspectives,” *Biosens Bioelectron*, vol. 141, p. 111435, Sep. 2019, doi: 10.1016/J.BIOS.2019.111435.
- [93] D. A. Gough, J. Y. Lucisano, and P. H. S. Tse, “Two-Dimensional Enzyme Electrode Sensor for Glucose,” *Anal Chem*, vol. 57, no. 12, pp. 2351–2357, Oct. 1985, doi: 10.1021/AC00289A042.
- [94] P. Makaram, D. Owens, and J. Aceros, “Trends in Nanomaterial-Based Non-Invasive Diabetes Sensing Technologies,” *Diagnostics 2014, Vol. 4, Pages 27-46*, vol. 4, no. 2, pp. 27–46, Apr. 2014, doi: 10.3390/DIAGNOSTICS4020027.
- [95] C. E. Ferrante do Amaral and B. Wolf, “Current development in non-invasive glucose monitoring,” *Medical Engineering and Physics*, vol. 30, no. 5. Elsevier, pp. 541–549, Jun. 01, 2008. doi: 10.1016/j.medengphy.2007.06.003.
- [96] E. H. Yoo and S. Y. Lee, “Glucose Biosensors: An Overview of Use in Clinical Practice,” *Sensors 2010, Vol. 10, Pages 4558-4576*, vol. 10, no. 5, pp. 4558–4576, May 2010, doi: 10.3390/S100504558.
- [97] M. M. Alam and M. M. R. Howlader, “Nonenzymatic electrochemical sensors via Cu native oxides (CuNOx) for sweat glucose monitoring,” *Sens Biosensing Res*, vol. 34, p. 100453, Dec. 2021, doi: 10.1016/J.SBSR.2021.100453.
- [98] J. Moyer, D. Wilson, I. Finkelshtein, B. Wong, and R. Potts, “Correlation Between Sweat Glucose and Blood Glucose in Subjects with Diabetes,” <https://home.liebertpub.com/dia>, vol. 14, no. 5, pp. 398–402, May 2012, doi: 10.1089/DIA.2011.0262.
- [99] M. D. Ryan and J. Q. Chambers, “Dynamic Electrochemistry: Methodology and Applications,” *Analytical Chemistry*, vol. 64, pp. 79R-116R, 1992.
- [100] M. D. Ryan, E. F. Bowden, and J. Q. Chambers, “Dynamic Electrochemistry: Methodology and Application,” *Anal Chem*, vol. 66, no. 12, pp. 360–427, Jun. 1994, doi: 10.1021/AC00084A015.
- [101] J. L. Anderson, E. F. Bowden, and P. G. Pickup, “Dynamic electrochemistry: Methodology and application,” *Anal Chem*, vol. 68, no. 12, Jun. 1996, doi: 10.1021/A1960015Y/ASSET/A1960015Y.FP.PNG_V03.

- [102] J. L. Anderson, L. A. Coury, and J. Leddy, “Dynamic Electrochemistry: Methodology and Application,” *Anal Chem*, vol. 70, no. 12, Jun. 1998, doi: 10.1021/A19800186.
- [103] J. L. Anderson, J. A. Coury, and J. Leddy, “Dynamic electrochemistry: Methodology and application,” *Anal Chem*, vol. 72, no. 18, pp. 4497–4520, Sep. 2000, doi: 10.1021/AC0007837/ASSET/AC0007837.FP.PNG_V03.
- [104] J. R. Stetter, W. R. Penrose, and S. Yao, “Sensors, Chemical Sensors, Electrochemical Sensors, and ECS,” *J Electrochem Soc*, vol. 150, no. 2, p. S11, 2003, doi: 10.1149/1.1539051/PDF.
- [105] O. A. Farghaly, R. S. A. Hameed, and A.-A. H. Abu-Nawwas, “Analytical Application Using Modern Electrochemical Techniques,” 2014. [Online]. Available: www.electrochemsci.org
- [106] M. M. Rahman, A. J. S. Ahammad, J. H. Jin, S. J. Ahn, and J. J. Lee, “A comprehensive review of glucose biosensors based on nanostructured metal-oxides,” *Sensors*, vol. 10, no. 5, 2010, doi: 10.3390/s100504855.
- [107] J. Monzó, I. Insua, F. Fernandez-Trillo, and P. Rodriguez, “Fundamentals, achievements and challenges in the electrochemical sensing of pathogens,” *Analyst*, vol. 140, no. 21, pp. 7116–7128, 2015, doi: 10.1039/C5AN01330E.
- [108] D. Grieshaber, R. Mackenzie, J. Vörös, and E. Reimhult, “Electrochemical Biosensors-Sensor Principles and Architectures,” *Sensors*, vol. 8, pp. 1400–1458, 2008, [Online]. Available: www.mdpi.org/sensors
- [109] J. Baranwal, B. Barse, G. Gatto, G. Broncova, and A. Kumar, “Electrochemical Sensors and Their Applications: A Review,” *Chemosensors*, vol. 10, no. 9. MDPI, Sep. 01, 2022. doi: 10.3390/chemosensors10090363.
- [110] S. Banerjee, S. Mccracken, F. Hossain, and G. Slaughter, “Electrochemical Detection of Neurotransmitters”, doi: 10.3390/bios10080101.
- [111] N. Elgrishi, K. J. Rountree, B. D. McCarthy, E. S. Rountree, T. T. Eisenhart, and J. L. Dempsey, “A Practical Beginner’s Guide to Cyclic Voltammetry,” *J Chem Educ*, vol. 95, no. 2, pp. 197–206, 2018, doi: 10.1021/acs.jchemed.7b00361.
- [112] J. QUÍLEZ, “A Historical Approach to The Development of Chemical Equilibrium Through the Evolution of the Affinity Concept: Some Educational Suggestions,” *Chem. Educ. Res. Pract.*, vol. 5, no. 1, pp. 69–87, Feb. 2004, doi: 10.1039/b3rp90031b.
- [113] C. C. Gillispie, “Scientific Aspects of the French Egyptian Expedition 1798-1801,” in *Proceedings of the American Philosophical Society*, 1989, pp. 447–474.

- [114] P. H. Rogers, K. D. Benkstein, and S. Semancik, “Machine learning applied to chemical analysis: Sensing multiple biomarkers in simulated breath using a temperature-pulsed electronic-nose,” *Anal Chem*, vol. 84, no. 22, pp. 9774–9781, Nov. 2012, doi: 10.1021/AC301687J/SUPPL_FILE/AC301687J_SI_001.PDF.
- [115] J. Wallerstein *et al.*, “Entropy-Entropy Compensation between the Protein, Ligand, and Solvent Degrees of Freedom Fine-Tunes Affinity in Ligand Binding to Galectin-3C,” *J Am Chem Soc*, vol. 1, no. 4, pp. 484–500, Apr. 2021, doi: 10.1021/JACSAU.0C00094/ASSET/IMAGES/LARGE/AU0C00094_0011.JPEG.
- [116] A. Münster, *Classical thermodynamics*. Wiley-Interscience, 1970.
- [117] D. J. Evans, D. J. Searles, and E. Mittag, “Fluctuation theorem for Hamiltonian Systems: Le Chatelier’s principle,” *Phys Rev E Stat Phys Plasmas Fluids Relat Interdiscip Topics*, vol. 63, no. 5, p. 051105, Apr. 2001, doi: 10.1103/PhysRevE.63.051105.
- [118] R. Zhang *et al.*, “Label-Free Electrochemical Sensor for CD44 by Ligand-Protein Interaction,” 2019, doi: 10.1021/acs.analchem.8b05966.
- [119] F. T. Liu and G. A. Rabinovich, “Galectins: Regulators of acute and chronic inflammation,” *Ann N Y Acad Sci*, vol. 1183, pp. 158–182, Jan. 2010, doi: 10.1111/J.1749-6632.2009.05131.X/PDF.
- [120] F. T. Liu and G. A. Rabinovich, “Galectins as modulators of tumour progression,” *Nat Rev Cancer*, vol. 5, no. 1, pp. 29–41, Jan. 2005, doi: 10.1038/NRC1527.
- [121] T. Delaine *et al.*, “Galectin-3-Binding Glycomimetics that Strongly Reduce Bleomycin-Induced Lung Fibrosis and Modulate Intracellular Glycan Recognition,” *Chembiochem*, vol. 17, no. 18, pp. 1759–1770, Sep. 2016, doi: 10.1002/CBIC.201600285.
- [122] M. B. Lerner *et al.*, “Hybrids of a genetically engineered antibody and a carbon nanotube transistor for detection of prostate cancer biomarkers,” *ACS Nano*, vol. 6, no. 6, pp. 5143–5149, Jun. 2012, doi: 10.1021/NN300819S/SUPPL_FILE/NN300819S_SI_001.PDF.
- [123] A. Plumer *et al.*, “Development of fragment-specific osteopontin antibodies and ELISA for quantification in human metastatic breast cancer,” *BMC Cancer*, vol. 8, Jan. 2008, doi: 10.1186/1471-2407-8-38.
- [124] Hill A, “The possible effects of the aggregation of the molecules of haemoglobin on its oxygen dissociation curve,” *J Physiol*, vol. 40, pp. 4–7, 1910.
- [125] N. R. Syme, C. Dennis, A. Bronowska, G. C. Paesen, and S. W. Homans, “Comparison of entropic contributions to binding in a ‘ hydrophilic’ versus

- ‘hydrophobic’ ligand-protein interaction,” *J Am Chem Soc*, vol. 132, no. 25, pp. 8682–8689, Jun. 2010, doi: 10.1021/JA101362U.
- [126] G. W. Gibbs, *Collected works of J. Willard Gibbs, Thermodynamics*, vol. 1. Longmans, 1928.
- [127] C. A. Brautigam, H. Zhao, C. Vargas, S. Keller, and P. Schuck, “Integration and global analysis of isothermal titration calorimetry data for studying macromolecular interactions,” *Nat Protoc*, vol. 11, no. 5, pp. 882–894, May 2016, doi: 10.1038/NPROT.2016.044.
- [128] L. Freiburger, K. Auclair, and A. Mittermaier, “Global ITC fitting methods in studies of protein allostery,” *Methods*, vol. 76, pp. 149–161, Apr. 2015, doi: 10.1016/J.YMETH.2014.12.018.
- [129] V. Vodyanoy, “Thermodynamic evaluation of vesicles shed by erythrocytes at elevated temperatures,” *Colloids Surf B Biointerfaces*, vol. 133, pp. 231–238, Sep. 2015, doi: 10.1016/J.COLSURFB.2015.06.013.
- [130] G. Brecher and M. Bessis, “Present Status of Spiculed Red Cells and Their Relationship to the Discocyte-Echinocyte Transformation: A Critical Review,” *Blood*, vol. 40, no. 3, pp. 333–344, Sep. 1972, doi: 10.1182/BLOOD.V40.3.333.333.
- [131] D. Vittori, D. Vota, A. Nesse, D. Vittori, D. Vota, and A. Nesse, “Erythrocyte: Programmed Cell Death,” *Anemia*, Feb. 2012, doi: 10.5772/30238.
- [132] W. Good, “A Biological Example of the Compensation Law,” *Nature* 1967 214:5094, vol. 214, no. 5094, pp. 1250–1252, 1967, doi: 10.1038/2141250a0.
- [133] T. Moore *et al.*, “Microscopic evaluation of vesicles shed by erythrocytes at elevated temperatures,” *Microsc Res Tech*, vol. 76, no. 11, pp. 1163–1170, Nov. 2013, doi: 10.1002/JEMT.22280.
- [134] T. Moore, I. Sorokulova, O. Pustovyy, L. Globa, and V. Vodyanoy, “Microscopic evaluation of vesicles shed by rat erythrocytes at elevated temperatures,” *J Therm Biol*, vol. 38, no. 8, pp. 487–492, Dec. 2013, doi: 10.1016/J.JTHERBIO.2013.08.001.
- [135] F. L. A. Willekens *et al.*, “Liver Kupffer cells rapidly remove red blood cell–derived vesicles from the circulation by scavenger receptors,” *Blood*, vol. 105, no. 5, pp. 2141–2145, Mar. 2005, doi: 10.1182/BLOOD-2004-04-1578.
- [136] F. L. A. Willekens *et al.*, “Liver Kupffer cells rapidly remove red blood cell–derived vesicles from the circulation by scavenger receptors,” *Blood*, vol. 105, no. 5, pp. 2141–2145, Mar. 2005, doi: 10.1182/BLOOD-2004-04-1578.

- [137] K. D. Bauer and K. J. Henle, “Arrhenius analysis of heat survival curves from normal and thermotolerant CHO cells,” *Radiat Res*, vol. 78, no. 2, pp. 251–263, 1979, doi: 10.2307/3575042.
- [138] I. Segel, *Biochemical calculations: how to solve mathematical problems in general biochemistry*. 1991. Accessed: Mar. 26, 2023. [Online]. Available: <https://books.google.com/books?hl=en&lr=&id=XxeUEAAQBAJ&oi=fnd&pg=PR8&ots=K8k3Fy6WGf&sig=sQ1a-6vBhMfaZvSAfL-Mej5ltBs>
- [139] G. L. Hofacker, “Henry Eyring, S. H. Lin, S. M. Lin: Basic Chemical Kinetics. John Wiley & Sons, New York, Chichester, Brisbane, Toronto 1980. 493 Seiten, Preis: £ 20. -,” *Berichte der Bunsengesellschaft für physikalische Chemie*, vol. 85, no. 7, pp. 618–619, Jul. 1981, doi: 10.1002/BBPC.19810850721.
- [140] E. A. Chernitskiĭ, E. I. Slobozhanina, I. E. Fedorovich, and G. P. Novitskaia, “Vesiculation of erythrocytes during storage and connection of it with other processes in the cell,” *Biofizika*, vol. 39, no. 2, pp. 357–361, Mar. 1994, Accessed: Mar. 29, 2023. [Online]. Available: <https://europepmc.org/article/med/8193198>
- [141] A. I. Dragan, J. Klass, C. Read, M. E. A. Churchill, C. Crane-Robinson, and P. L. Privalov, “DNA Binding of a Non-sequence-specific HMG-D Protein is Entropy Driven with a Substantial Non-electrostatic Contribution,” *J Mol Biol*, vol. 331, no. 4, pp. 795–813, Aug. 2003, doi: 10.1016/S0022-2836(03)00785-X.
- [142] J. S. Beck, “Echinocyte formation: A test case for mechanisms of cell shape changes,” *J Theor Biol*, vol. 71, no. 4, pp. 515–524, Apr. 1978, doi: 10.1016/0022-5193(78)90322-3.
- [143] E. Tomlinson, “Enthalpy-entropy compensation analysis of pharmaceutical, biochemical and biological systems,” *Int J Pharm*, vol. 13, no. 2, pp. 115–144, Jan. 1983, doi: 10.1016/0378-5173(83)90001-7.
- [144] J. E. Leffler, “The enthalpy-entropy relationship and its implications for organic chemistry,” *Journal of Organic Chemistry*, vol. 20, no. 9, pp. 1202–1231, 1955, doi: 10.1021/JO01126A009/ASSET/JO01126A009.FP.PNG_V03.
- [145] V. Lafont, A. A. Armstrong, H. Ohtaka, Y. Kiso, L. Mario Amzel, and E. Freire, “Compensating Enthalpic and Entropic Changes Hinder Binding Affinity Optimization,” *Chem Biol Drug Des*, vol. 69, no. 6, pp. 413–422, Jun. 2007, doi: 10.1111/J.1747-0285.2007.00519.X.
- [146] A. Cooper, “Heat capacity effects in protein folding and ligand binding: a re-evaluation of the role of water in biomolecular thermodynamics,” *Biophys Chem*, vol. 115, no. 2–3, pp. 89–97, Apr. 2005, doi: 10.1016/J.BPC.2004.12.011.

- [147] J. C. Kotz, Paul. Treichel, and G. C. Weaver, *Chemistry & chemical reactivity*, 6th ed. Thomson Brooks/Cole, 2006.
- [148] “14.2: pH and pOH - Chemistry LibreTexts.” Accessed: Aug. 14, 2022. [Online]. Available: [https://chem.libretexts.org/Bookshelves/General_Chemistry/Chemistry_\(OpenSTAX\)/14%3A_Acid-Base_Equilibria/14.2%3A_pH_and_pOH](https://chem.libretexts.org/Bookshelves/General_Chemistry/Chemistry_(OpenSTAX)/14%3A_Acid-Base_Equilibria/14.2%3A_pH_and_pOH)
- [149] “pH and Water | U.S. Geological Survey.” Accessed: Aug. 14, 2022. [Online]. Available: https://www.usgs.gov/special-topics/water-science-school/science/ph-and-water?qt-science_center_objects=0#qt-science_center_objects
- [150] J. Li *et al.*, “Effects of pH, Temperature, Suspended Solids, and Biological Activity on Transformation of Illicit Drug and Pharmaceutical Biomarkers in Sewers,” *Environ Sci Technol*, vol. 55, no. 13, pp. 8771–8782, Jul. 2021, doi: 10.1021/ACS.EST.1C01516.
- [151] E. Zuccato *et al.*, “Cocaine in surface waters: a new evidence-based tool to monitor community drug abuse,” *Environmental Health*, vol. 4, p. 14, Aug. 2005, doi: 10.1186/1476-069X-4-14.
- [152] I. González-Mariño *et al.*, “Spatio-temporal assessment of illicit drug use at large scale: evidence from 7 years of international wastewater monitoring,” *Addiction (Abingdon, England)*, vol. 115, no. 1, pp. 109–120, Jan. 2020, doi: 10.1111/ADD.14767.
- [153] Z. Li, A. Sobek, and M. Radke, “Flume experiments to investigate the environmental fate of pharmaceuticals and their transformation products in streams,” *Environ Sci Technol*, vol. 49, no. 10, pp. 6009–6017, May 2015, doi: 10.1021/ACS.EST.5B00273.
- [154] B. G. Plósz, M. J. Reid, M. Borup, K. H. Langford, and K. V. Thomas, “Biotransformation kinetics and sorption of cocaine and its metabolites and the factors influencing their estimation in wastewater,” *Water Res*, vol. 47, no. 7, pp. 2129–2140, May 2013, doi: 10.1016/J.WATRES.2012.12.034.
- [155] J. Li *et al.*, “Stability of Illicit Drugs as Biomarkers in Sewers: From Lab to Reality,” *Environ Sci Technol*, vol. 52, no. 3, pp. 1561–1570, Feb. 2018, doi: 10.1021/ACS.EST.7B05109.
- [156] A. K. McCall *et al.*, “Influence of Different Sewer Biofilms on Transformation Rates of Drugs,” *Environ Sci Technol*, vol. 50, no. 24, pp. 13351–13360, Dec. 2016, doi: 10.1021/ACS.EST.6B04200.

- [157] I. Senta, I. Krizman, M. Ahel, and S. Terzic, “Assessment of stability of drug biomarkers in municipal wastewater as a factor influencing the estimation of drug consumption using sewage epidemiology,” *Sci Total Environ*, vol. 487, no. 1, pp. 659–665, Jul. 2014, doi: 10.1016/J.SCITOTENV.2013.12.054.
- [158] M. Hörsing *et al.*, “Determination of sorption of seventy-five pharmaceuticals in sewage sludge,” *Water Res*, vol. 45, no. 15, pp. 4470–4482, 2011, doi: 10.1016/J.WATRES.2011.05.033.
- [159] T. Urase and T. Kikuta, “Separate estimation of adsorption and degradation of pharmaceutical substances and estrogens in the activated sludge process,” *Water Res*, vol. 39, no. 7, pp. 1289–1300, 2005, doi: 10.1016/J.WATRES.2005.01.015.
- [160] J. Dobor, M. Varga, and G. Záray, “Biofilm controlled sorption of selected acidic drugs on river sediments characterized by different organic carbon content,” *Chemosphere*, vol. 87, no. 2, pp. 105–110, 2012, doi: 10.1016/J.CHEMOSPHERE.2011.11.067.
- [161] F. Liu, A. H. Nielsen, and J. Vollertsen, “Sorption and Degradation Potential of Pharmaceuticals in Sediments from a Stormwater Retention Pond,” *Water 2019*, Vol. 11, Page 526, vol. 11, no. 3, p. 526, Mar. 2019, doi: 10.3390/W11030526.
- [162] R. Gulde, D. E. Helbling, A. Scheidegger, and K. Fenner, “PH-dependent biotransformation of ionizable organic micropollutants in activated sludge,” *Environ Sci Technol*, vol. 48, no. 23, pp. 13760–13768, Dec. 2014, doi: 10.1021/ES5037139.
- [163] J. Li and H. Zhang, “Adsorption-desorption of oxytetracycline on marine sediments: Kinetics and influencing factors,” *Chemosphere*, vol. 164, pp. 156–163, Dec. 2016, doi: 10.1016/J.CHEMOSPHERE.2016.08.100.
- [164] B. Halliwell and J. M. C. Gutteridge, *Free Radicals in Biology and Medicine*, Third Edition. 2015.
- [165] B. N. Ames, M. K. Shigenaga, and T. M. Hagen, “Oxidants, antioxidants, and the degenerative diseases of aging,” *Proc Natl Acad Sci U S A*, vol. 90, no. 17, pp. 7915–7922, 1993, doi: 10.1073/PNAS.90.17.7915.
- [166] B. T. Ashok and R. Ali, “The aging paradox: free radical theory of aging,” *Exp Gerontol*, vol. 34, no. 3, pp. 293–303, 1999, doi: 10.1016/S0531-5565(99)00005-4.
- [167] T. Finkel, “Reactive oxygen species and signal transduction,” *IUBMB Life*, vol. 52, no. 1–2, pp. 3–6, 2001, doi: 10.1080/15216540252774694.

- [168] T. Finkel and N. J. Holbrook, “Oxidants, oxidative stress and the biology of ageing,” *Nature*, vol. 408, no. 6809, pp. 239–247, Nov. 2000, doi: 10.1038/35041687.
- [169] R. W. Gracy, J. M. Talent, Y. Kong, and C. C. Conrad, “Reactive oxygen species: the unavoidable environmental insult?,” *Mutat Res*, vol. 428, no. 1–2, pp. 17–22, Jul. 1999, doi: 10.1016/S1383-5742(99)00027-7.
- [170] R. L. Prior and G. Cao, “In vivo total antioxidant capacity: comparison of different analytical methods,” *Free Radic Biol Med*, vol. 27, no. 11–12, pp. 1173–1181, 1999, doi: 10.1016/S0891-5849(99)00203-8.
- [171] J. M. McCord and I. Fridovich, “Superoxide Dismutase: An Enzymic Function For Erythrocyte (Hemocuprein),” *Journal of Biological Chemistry*, vol. 244, no. 22, pp. 6049–6055, Nov. 1969, doi: 10.1016/S0021-9258(18)63504-5.
- [172] I. Fridovich, “Superoxide radical and superoxide dismutases,” *Annu Rev Biochem*, vol. 64, pp. 97–112, 1995, doi: 10.1146/ANNUREV.BI.64.070195.000525.
- [173] G. Cao and R. L. Prior, “Comparison of different analytical methods for assessing total antioxidant capacity of human serum,” *Clin Chem*, vol. 44, no. 6, pp. 1309–1315, Jun. 1998, doi: 10.1093/CLINCHEM/44.6.1309.
- [174] R. Kohen and A. Nyska, “Oxidation of biological systems: Oxidative stress phenomena, antioxidants, redox reactions, and methods for their quantification,” *Toxicol Pathol*, vol. 30, no. 6, pp. 620–650, Nov. 2002, doi: 10.1080/01926230290166724.
- [175] “Biological redox activity: Its importance, methods for its quantification and implication for health and disease - Hrbac - 2000 - Drug Development Research - Wiley Online Library.” Accessed: Apr. 13, 2023. [Online]. Available: [https://onlinelibrary.wiley.com/doi/pdf/10.1002/1098-2299\(200007/08\)50:3/4%3C516::AID-DDR35%3E3.0.CO;2-B](https://onlinelibrary.wiley.com/doi/pdf/10.1002/1098-2299(200007/08)50:3/4%3C516::AID-DDR35%3E3.0.CO;2-B)
- [176] H. M. Shapiro, “Redox balance in the body: An approach to quantitation,” *Journal of Surgical Research*, vol. 13, no. 3, pp. 138–152, 1972, doi: 10.1016/0022-4804(72)90057-1.
- [177] H. J. H. Fenton, “LXXIII. - Oxidation of tartaric acid in presence of iron,” *Journal of the Chemical Society, Transactions*, vol. 65, pp. 899–910, 1894, doi: 10.1039/CT8946500899.
- [178] “The catalytic decomposition of hydrogen peroxide by iron salts,” *Proc R Soc Lond A Math Phys Sci*, vol. 147, no. 861, pp. 332–351, Nov. 1934, doi: 10.1098/RSPA.1934.0221.

- [179] D. T. Sawyer and J. S. Valentine, “How Super Is Superoxide?,” *Acc Chem Res*, vol. 14, no. 12, pp. 393–400, 1981, doi: 10.1021/AR00072A005.
- [180] B. Halliwell and J. M. C. Gutteridge, “Biologically relevant metal ion-dependent hydroxyl radical generation An update,” *FEBS Lett*, vol. 307, no. 1, pp. 108–112, Jul. 1992, doi: 10.1016/0014-5793(92)80911-Y.
- [181] H. C. Sutton and C. C. Winterbourn, “On the participation of higher oxidation states of iron and copper in fenton reactions,” *Free Radic Biol Med*, vol. 6, no. 1, pp. 53–60, Jan. 1989, doi: 10.1016/0891-5849(89)90160-3.
- [182] W. H. Koppenol, “Free Radical Damage and its Control,” *New Comprehensive Biochemistry*, vol. 28, pp. 3–24, 1994, Accessed: Apr. 13, 2023. [Online]. Available: <http://www.sciencedirect.com/science/article/pii/S0167730608604378>
- [183] C. Walling, R. E. Partch, and T. Weil, “Kinetics of the decomposition of hydrogen peroxide catalyzed by ferric ethylenediaminetetraacetate complex,” *Proc Natl Acad Sci U S A*, vol. 72, no. 1, pp. 140–142, Jan. 1975, doi: 10.1073/PNAS.72.1.140.
- [184] N. Lu, C. Chen, Y. He, R. Tian, Q. Xiao, and Y. Y. Peng, “The dual effects of nitrite on hemoglobin-dependent redox reactions,” *Nitric Oxide*, vol. 40, pp. 1–9, Aug. 2014, doi: 10.1016/J.NIOX.2014.04.010.
- [185] A. S. Tsiftoglou, A. I. Tsamadou, and L. C. Papadopoulou, “Heme as key regulator of major mammalian cellular functions: Molecular, cellular, and pharmacological aspects,” *Pharmacol Ther*, vol. 111, no. 2, pp. 327–345, Aug. 2006, doi: 10.1016/J.PHARMTHERA.2005.10.017.
- [186] B. R. Van Dyke and P. Saltman, “Hemoglobin: A mechanism for the generation of hydroxyl radicals,” *Free Radic Biol Med*, vol. 20, no. 7, pp. 985–989, Jan. 1996, doi: 10.1016/0891-5849(95)02186-8.
- [187] R. L. Aft and G. C. Mueller, “Hemin-mediated oxidative degradation of proteins.,” *Journal of Biological Chemistry*, vol. 259, no. 1, pp. 301–305, Jan. 1984, doi: 10.1016/S0021-9258(17)43657-X.
- [188] A. I. Alayash, R. P. Patel, and R. E. Cashion, “Redox Reactions of Hemoglobin and Myoglobin: Biological and Toxicological Implications,” *https://home.liebertpub.com/ars*, vol. 3, no. 2, pp. 313–327, Jul. 2004, doi: 10.1089/152308601300185250.
- [189] B. J. Reeder, D. A. Svistunenko, C. E. Cooper, and M. T. Wilson, “The radical and redox chemistry of myoglobin and hemoglobin: From in vitro studies to human

- pathology,” *Antioxid Redox Signal*, vol. 6, no. 6, pp. 954–966, Dec. 2004, doi: 10.1089/ARS.2004.6.954.
- [190] C. Yuan *et al.*, “Amyloid beta-heme peroxidase promoted protein nitrotyrosination: Relevance to widespread protein nitration in Alzheimer’s disease,” *Journal of Biological Inorganic Chemistry*, vol. 17, no. 2, pp. 197–207, Feb. 2012, doi: 10.1007/S00775-011-0842-3/FIGURES/6.
- [191] N. Lu, Y. Zhang, H. Li, and Z. Gao, “Oxidative and nitrative modifications of α -enolase in cardiac proteins from diabetic rats,” *Free Radic Biol Med*, vol. 48, no. 7, pp. 873–881, Apr. 2010, doi: 10.1016/J.FREERADBIOMED.2010.01.010.
- [192] N. Lu, X. Li, J. Li, W. Xu, H. Li, and Z. Gao, “Nitrative and oxidative modifications of enolase are associated with iron in iron-overload rats and in vitro,” *Journal of Biological Inorganic Chemistry*, vol. 16, no. 3, pp. 481–490, Mar. 2011, doi: 10.1007/S00775-010-0747-6/FIGURES/9.
- [193] P. Kleinbongard *et al.*, “Plasma nitrite concentrations reflect the degree of endothelial dysfunction in humans,” *Free Radic Biol Med*, vol. 40, no. 2, pp. 295–302, Jan. 2006, doi: 10.1016/J.FREERADBIOMED.2005.08.025.
- [194] P. Pacher, J. S. Beckman, and L. Liaudet, “Nitric oxide and peroxynitrite in health and disease,” *Physiol Rev*, vol. 87, no. 1, pp. 315–424, Jan. 2007, doi: 10.1152/PHYSREV.00029.2006/ASSET/IMAGES/LARGE/Z9J0010724240018.JPEG.
- [195] N. S. Bryan, J. W. Calvert, J. W. Elrod, S. Gundewar, Y. J. Sang, and D. J. Lefer, “Dietary nitrite supplementation protects against myocardial ischemia-reperfusion injury,” *Proc Natl Acad Sci U S A*, vol. 104, no. 48, pp. 19144–19149, Nov. 2007, doi: 10.1073/PNAS.0706579104/ASSET/78C88B24-24B4-480D-96B5-C01D9D81ED41/ASSETS/GRAPHIC/ZPQ0460783410005.JPEG.
- [196] C. G. Kevil, G. K. Kolluru, C. B. Pattillo, and T. Giordano, “Inorganic nitrite therapy: historical perspective and future directions,” *Free Radic Biol Med*, vol. 51, no. 3, pp. 576–593, Aug. 2011, doi: 10.1016/J.FREERADBIOMED.2011.04.042.
- [197] L. Turell, R. Radi, and B. Alvarez, “The thiol pool in human plasma: The central contribution of albumin to redox processes,” *Free Radic Biol Med*, vol. 65, pp. 244–253, 2013, doi: 10.1016/j.freeradbiomed.2013.05.050.
- [198] T. Jr. Peters, *All about Albumin: Biochemistry, Genetics, and Medical Applications*, 1st ed., vol. 1. San Diego: Academic Press, 1995.

- [199] A. Bocedi, G. Cattani, L. Stella, R. Massoud, G. Ricci, and G. Ricci, “Thiol disulfide exchange reactions in human serum albumin: the apparent paradox of the redox transitions of Cys 34”, doi: 10.1111/febs.14609.
- [200] A. Bocedi *et al.*, “Erythrocyte glutathione transferase in kidney transplantation: a probe for kidney detoxification efficiency,” *Cell Death & Disease* 2018 9:3, vol. 9, no. 3, pp. 1–11, Feb. 2018, doi: 10.1038/s41419-018-0289-3.
- [201] H. Watanabe, T. Imafuku, M. Otagiri, and T. Maruyama, “Clinical Implications Associated With the Posttranslational Modification–Induced Functional Impairment of Albumin in Oxidative Stress–Related Diseases,” *J Pharm Sci*, vol. 106, no. 9, pp. 2195–2203, Sep. 2017, doi: 10.1016/J.XPHS.2017.03.002.
- [202] H. Terawaki *et al.*, “Dialyzable Uremic Solutes Contribute to Enhanced Oxidation of Serum Albumin in Regular Hemodialysis Patients,” *Blood Purif*, vol. 25, no. 3, pp. 274–279, Jul. 2007, doi: 10.1159/000101986.
- [203] H. Terawaki *et al.*, “Oxidative stress is enhanced in correlation with renal dysfunction: Examination with the redox state of albumin,” *Kidney Int*, vol. 66, no. 5, pp. 1988–1993, Nov. 2004, doi: 10.1111/J.1523-1755.2004.00969.X.
- [204] K. Nagumo *et al.*, “Cys34-cysteinylated human serum albumin is a sensitive plasma marker in oxidative stress-related chronic diseases,” *PLoS One*, vol. 9, no. 1, Jan. 2014, doi: 10.1371/JOURNAL.PONE.0085216.
- [205] K. Mera, M. Anraku, K. Kitamura, K. Nakajou, T. Maruyama, and M. Otagiri, “The structure and function of oxidized albumin in hemodialysis patients: Its role in elevated oxidative stress via neutrophil burst,” *Biochem Biophys Res Commun*, vol. 334, no. 4, pp. 1322–1328, Sep. 2005, doi: 10.1016/J.BBRC.2005.07.035.
- [206] J. Himmelfarb and E. McMonagle, “Albumin is the major plasma protein target of oxidant stress in uremia,” *Kidney Int*, vol. 60, no. 1, pp. 358–363, Jul. 2001, doi: 10.1046/J.1523-1755.2001.00807.X.
- [207] K. Oettl and G. Marsche, “Redox State of Human Serum Albumin in Terms of Cysteine-34 in Health and Disease,” *Methods Enzymol*, vol. 474, pp. 181–195, Jan. 2010, doi: 10.1016/S0076-6879(10)74011-8.
- [208] Y. Spanidis *et al.*, “Oxidation of human serum albumin exhibits inter-individual variability after an ultra-marathon mountain race,” *Exp Ther Med*, vol. 13, no. 5, pp. 2382–2390, May 2017, doi: 10.3892/ETM.2017.4268/HTML.
- [209] F. Q. Schafer and G. R. Buettner, “Redox environment of the cell as viewed through the redox state of the glutathione disulfide/glutathione couple,” *Free Radic*

- Biol Med*, vol. 30, no. 11, pp. 1191–1212, Jun. 2001, doi: 10.1016/S0891-5849(01)00480-4.
- [210] Th. Bücher and M. Klingenberg, “Wege des Wasserstoffs in der lebendigen Organisation,” *Angewandte Chemie*, vol. 70, no. 17–18, pp. 552–570, Sep. 1958, doi: 10.1002/ANGE.19580701707.
- [211] F. Q. Schafer and G. R. Buettner, “Redox environment of the cell as viewed through the redox state of the glutathione disulfide/glutathione couple,” *Free Radic Biol Med*, vol. 30, no. 11, pp. 1191–1212, Jun. 2001, doi: 10.1016/S0891-5849(01)00480-4.
- [212] I. F. F. Benzie and J. J. Strain, “Ferric reducing/antioxidant power assay: Direct measure of total antioxidant activity of biological fluids and modified version for simultaneous measurement of total antioxidant power and ascorbic acid concentration,” *Methods Enzymol*, vol. 299, pp. 15–27, Jan. 1999, doi: 10.1016/S0076-6879(99)99005-5.
- [213] D. A. Skoog, “Fundamentals of Analytical Chemistry (Saunders Golden Sunburst Series),” p. 928, 1995, Accessed: May 04, 2023. [Online]. Available: <http://www.amazon.co.uk/Fundamentals-Analytical-Chemistry-Saunders-Sunburst/dp/0030059380>
- [214] R. Kohen, O. Tirosh, and R. Gorodetsky, “The biological reductive capacity of tissues is decreased following exposure to oxidative stress: A cyclic voltammetry study of irradiated rats,” *Free Radic Res*, vol. 17, no. 4, pp. 239–248, 1992, doi: 10.3109/10715769209079516.
- [215] A. Ornoy, V. Zaken, and A. R. Kohen, “Role of Reactive Oxygen Species (ROS) in the Diabetes-Induced Anomalies in Rat Embryos In Vitro: Reduction in Antioxidant Enzymes and Low-Molecular-Weight Antioxidants (LMWA) May Be the Causative Factor for Increased Anomalies,” *Teratology*, vol. 60, pp. 376–386, 1999, doi: 10.1002/(SICI)1096-9926(199912)60:6.
- [216] R. N. DuBois *et al.*, “Cyclooxygenase in biology and disease,” *The FASEB Journal*, vol. 12, no. 12, pp. 1063–1073, Sep. 1998, doi: 10.1096/FASEBJ.12.12.1063.
- [217] R. Kohen, E. Beit-Yannai, E. M. Berry, and O. Tirosh, “Overall low molecular weight antioxidant activity of biological fluids and tissues by cyclic voltammetry,” *Methods Enzymol*, vol. 300, pp. 285–296, Jan. 1999, doi: 10.1016/S0076-6879(99)00135-4.
- [218] S. Blau, R. Kohen, P. Bass, and A. Rubinstein, “Relation between colonic inflammation severity and total low-molecular- weight antioxidant profiles in

- experimental colitis,” *Dig Dis Sci*, vol. 45, no. 6, pp. 1180–1187, 2000, doi: 10.1023/A:1005510321278/METRICS.
- [219] R. Kohen, D. Fanberstein, and O. Tirosh, “Reducing equivalents in the aging process,” *Arch Gerontol Geriatr*, vol. 24, no. 2, pp. 103–123, Mar. 1997, doi: 10.1016/S0167-4943(96)00744-3.
- [220] R. Kohen, D. Fanberstein, A. Zelkowicz, O. Tirosh, and S. Farfour, “Noninvasive in vivo evaluation of skin antioxidant activity and oxidation status,” *Methods Enzymol*, vol. 300, pp. 428–437, 1999, doi: 10.1016/S0076-6879(99)00148-2.
- [221] R. EZRA, S. BENITA, I. GINSBURG, and R. KOHEN, “Prevention of oxidative damage in fibroblast cell cultures and rat skin by positively-charged submicron emulsion of α -tocopherol,” *European journal of pharmaceuticals and biopharmaceuticals*, vol. 42, no. 4, pp. 291–298, 1996.
- [222] R. Kohen and I. Gati, “Skin low molecular weight antioxidants and their role in aging and in oxidative stress,” *Toxicology*, vol. 148, no. 2–3, pp. 149–157, Aug. 2000, doi: 10.1016/S0300-483X(00)00206-7.
- [223] F. L. Bookstein, P. D. Sampson, A. P. Streissguth, and P. D. Connor, “Vitamins C and E improve rat embryonic antioxidant defense mechanism in diabetic culture medium,” *Teratology*, vol. 64, no. 1, pp. 33–44, Jul. 2001, doi: 10.1002/TERA.1045.
- [224] M. Battino, M. S. Ferreiro, I. Gallardo, H. N. Newman, and P. Bullon, “The antioxidant capacity of saliva,” *J Clin Periodontol*, vol. 29, no. 3, pp. 189–194, Mar. 2002, doi: 10.1034/J.1600-051X.2002.290301X.X.
- [225] E. Shoji and M. S. Freund, “Potentiometric sensors based on the inductive effect on the pKa of poly(aniline): A nonenzymatic glucose sensor [3],” *Journal of the American Chemical Society*, vol. 123, no. 14, pp. 3383–3384, 2001. doi: 10.1021/ja005906j.
- [226] E. Shoji and M. S. Freund, “Potentiometric saccharide detection based on the pKa changes of poly(aniline boronic acid),” *J Am Chem Soc*, vol. 124, no. 42, pp. 12486–12493, Oct. 2002, doi: 10.1021/ja0267371.
- [227] S. Park, H. Boo, and T. D. Chung, “Electrochemical non-enzymatic glucose sensors,” *Analytica Chimica Acta*, vol. 556, no. 1, pp. 46–57, Jan. 18, 2006. doi: 10.1016/j.aca.2005.05.080.
- [228] R. S. Kingsbury, S. Flotron, S. Zhu, D. F. Call, and O. Coronell, “Junction Potentials Bias Measurements of Ion Exchange Membrane Permselectivity,”

- Environ Sci Technol*, vol. 52, no. 8, pp. 4929–4936, Apr. 2018, doi: 10.1021/ACS.EST.7B05317/SUPPL_FILE/ES7B05317_SI_001.PDF.
- [229] D. Hervey, *Analytical Chemistry 2.1—an open-access digital textbook. Analytical and bioanalytical chemistry*, 1st ed., vol. 2. LibreTexts, 2011. Accessed: Oct. 24, 2023. [Online]. Available: [https://chem.libretexts.org/Bookshelves/Analytical_Chemistry/Analytical_Chemistry_2.1_\(Harvey\)](https://chem.libretexts.org/Bookshelves/Analytical_Chemistry/Analytical_Chemistry_2.1_(Harvey))
- [230] M. Watanabe, A. Kimura, K. Akasaka, and S. Hayashi, “Determination of acetylcholine in human blood,” *Biochem Med Metab Biol*, vol. 36, no. 3, pp. 355–362, 1986, doi: 10.1016/0885-4505(86)90147-7.
- [231] I. G. Arruda, F. E. G. Guimarães, R. J. Ramos, and N. C. S. Vieira, “Self-assembly of SiO₂nanoparticles for the potentiometric detection of neurotransmitter acetylcholine and its inhibitor,” *J Nanosci Nanotechnol*, vol. 14, no. 9, pp. 6658–6661, Sep. 2014, doi: 10.1166/JNN.2014.9351.
- [232] D. Lee and T. Cui, “Carbon nanotube thin film pH electrode for potentiometric enzymatic acetylcholine biosensing,” *Microelectron Eng*, vol. 93, pp. 39–42, May 2012, doi: 10.1016/J.MEE.2011.10.017.
- [233] Z. Dursun and B. Gelmez, “Simultaneous determination of ascorbic acid, dopamine and uric acid at pt nanoparticles decorated multiwall carbon nanotubes modified GCE,” *Electroanalysis*, vol. 22, no. 10, pp. 1106–1114, May 2010, doi: 10.1002/ELAN.200900525.
- [234] R. Liang, J. Ding, S. Gao, and W. Qin, “Mussel-Inspired Surface-Imprinted Sensors for Potentiometric Label-Free Detection of Biological Species,” *Angewandte Chemie International Edition*, vol. 56, no. 24, pp. 6833–6837, Jun. 2017, doi: 10.1002/ANIE.201701892.
- [235] Y. Wang *et al.*, “Potentiometric sensors based on surface molecular imprinting: Detection of cancer biomarkers and viruses,” *Sens Actuators B Chem*, vol. 146, no. 1, pp. 381–387, Apr. 2010, doi: 10.1016/J.SNB.2010.02.032.
- [236] S. Muhammad, U. Ali, O. Nur, M. Willander, and B. Danielsson, “Glucose Detection With a Commercial MOSFET Using a ZnO Nanowires Extended Gate,” *IEEE Trans Nanotechnol*, vol. 8, no. 6, 2009, doi: 10.1109/TNANO.2009.2019958.
- [237] A. Seki, S. I. Ikeda, I. Kubo, and I. Karube, “Biosensors based on light-addressable potentiometric sensors for urea, penicillin and glucose,” *Anal Chim Acta*, vol. 373, no. 1, pp. 9–13, Nov. 1998, doi: 10.1016/S0003-2670(98)00364-X.

- [238] X. L. Luo, J. J. Xu, W. Zhao, and H. Y. Chen, “Glucose biosensor based on ENFET doped with SiO₂ nanoparticles,” *Sens Actuators B Chem*, vol. 97, no. 2–3, pp. 249–255, Feb. 2004, doi: 10.1016/J.SNB.2003.08.024.
- [239] A. S. Poghossian, “Method of fabrication of ISFET-based biosensors on an Si-SiO₂-Si structure,” *Sens Actuators B Chem*, vol. 44, no. 1–3, pp. 361–364, 1997, doi: 10.1016/S0925-4005(97)00202-5.
- [240] I. Anshori and H. Suzuki, “Microfluidic device for high-sensitivity coulometric detection of proteins,” *Sens Actuators B Chem*, vol. 256, pp. 835–838, Mar. 2018, doi: 10.1016/J.SNB.2017.10.017.
- [241] J. T. Maloy, “Factors affecting the shape of current-potential curves,” *J Chem Educ*, vol. 60, no. 4, pp. 285–289, 1983, doi: 10.1021/ED060P285.
- [242] P. M. Biesheuvel, S. Porada, and J. E. Dykstra, “The difference between Faradaic and non-Faradaic electrode processes,” Sep. 2018, Accessed: Dec. 06, 2022. [Online]. Available: <http://arxiv.org/abs/1809.02930>
- [243] Kissinger PT and Bott AW, “Electrochemistry for the non-electrochemist,” *Current Separations*.
- [244] P. M. Jahani, M. Jafari, V. K. Gupta, and S. Agarwal, “Graphene quantum dots/ionic liquid-modified carbon paste electrode-based sensor for simultaneous voltammetric determination of norepinephrine and acetylcholine,” *Int J Electrochem Sci*, vol. 15, no. 1, pp. 947–958, Jan. 2020, doi: 10.20964/2020.01.45.
- [245] H. M. Albishri and D. Abd El-Hady, “Hyphenation of enzyme/graphene oxide-ionic liquid/glassy carbon biosensors with anodic differential pulse stripping voltammetry for reliable determination of choline and acetylcholine in human serum,” *Talanta*, vol. 200, pp. 107–114, Aug. 2019, doi: 10.1016/J.TALANTA.2019.03.028.
- [246] H. Beitollahi, M. Safaei, and S. Tajik, “Screen-printed Electrode Modified with ZnFe₂O₄ Nanoparticles for Detection of Acetylcholine,” *Electroanalysis*, vol. 31, no. 6, pp. 1135–1140, Jun. 2019, doi: 10.1002/ELAN.201900116.
- [247] D. Sangamithirai, S. Munusamy, V. Narayanan, and A. Stephen, “Fabrication of neurotransmitter dopamine electrochemical sensor based on poly(o-anisidine)/CNTs nanocomposite,” *Surfaces and Interfaces*, vol. 4, pp. 27–34, Oct. 2016, doi: 10.1016/J.SURFIN.2016.09.003.
- [248] Y. Zhao *et al.*, “Selective detection of dopamine in the presence of ascorbic acid and uric acid by a carbon nanotubes-ionic liquid gel modified electrode,” *Talanta*, vol. 66, no. 1, pp. 51–57, Mar. 2005, doi: 10.1016/J.TALANTA.2004.09.019.

- [249] M. Karimi, M. Rabiee, M. Tahriri, R. Salarian, and L. Tayebi, “A graphene based–biomimetic molecularly imprinted polyaniline sensor for ultrasensitive detection of human cardiac troponin T (cTnT),” *Synth Met*, vol. 256, Oct. 2019, doi: 10.1016/J.SYNTHMET.2019.116136.
- [250] K. Phonklam, R. Wannapob, W. Sriwimol, P. Thavarungkul, and T. Phairatana, “A novel molecularly imprinted polymer PMB/MWCNTs sensor for highly-sensitive cardiac troponin T detection,” *Sens Actuators B Chem*, vol. 308, Apr. 2020, doi: 10.1016/J.SNB.2019.127630.
- [251] C. Pinyorospatham *et al.*, “Disposable paper-based electrochemical sensor using thiol-terminated poly(2-methacryloyloxyethyl phosphorylcholine) for the label-free detection of C-reactive protein,” *Microchimica Acta*, vol. 186, no. 7, Jul. 2019, doi: 10.1007/S00604-019-3559-6.
- [252] Q. Zhang *et al.*, “Wearable electrochemical biosensor based on molecularly imprinted Ag nanowires for noninvasive monitoring lactate in human sweat,” *Sens Actuators B Chem*, vol. 320, Oct. 2020, doi: 10.1016/J.SNB.2020.128325.
- [253] S. Arimori, S. Ushiroda, L. M. Peter, A. T. A. Jenkins, and T. D. James, “A modular electrochemical sensor for saccharides,” *Chemical Communications*, vol. 2, no. 20, pp. 2368–2369, Oct. 2002, doi: 10.1039/B207643H.
- [254] S. Cherevko and C. H. Chung, “Gold nanowire array electrode for non-enzymatic voltammetric and amperometric glucose detection,” *Sens Actuators B Chem*, vol. 142, no. 1, pp. 216–223, Oct. 2009, doi: 10.1016/J.SNB.2009.07.023.
- [255] L. Özcan, Y. Şahin, and H. Türk, “Non-enzymatic glucose biosensor based on overoxidized polypyrrole nanofiber electrode modified with cobalt(II) phthalocyanine tetrasulfonate,” *Biosens Bioelectron*, vol. 24, no. 4, pp. 512–517, Dec. 2008, doi: 10.1016/J.BIOS.2008.05.004.
- [256] K.-C. Lin, C.-Y. Yang, and S.-M. Chen, “Fabrication of a Nonenzymatic Glucose Sensor Based on Multi-Walled Carbon Nanotubes Decorated with Platinum and Silver Hybrid Composite,” 2015. [Online]. Available: www.electrochemsci.org
- [257] M. Q. Guo, H. S. Hong, X. N. Tang, H. D. Fang, and X. H. Xu, “Ultrasonic electrodeposition of platinum nanoflowers and their application in nonenzymatic glucose sensors,” *Electrochim Acta*, vol. 63, pp. 1–8, Feb. 2012, doi: 10.1016/J.ELECTACTA.2011.11.114.
- [258] Y. Li, J. Du, J. Yang, D. Liu, and X. Lu, “Electrocatalytic detection of dopamine in the presence of ascorbic acid and uric acid using single-walled carbon nanotubes modified electrode,” *Colloids Surf B Biointerfaces*, vol. 97, pp. 32–36, Sep. 2012, doi: 10.1016/J.COLSURFB.2012.03.029.

- [259] D. M. Fernandes and C. Freire, “Carbon Nanomaterial-Phosphomolybdate Composites for Oxidative Electrocatalysis,” *ChemElectroChem*, vol. 2, no. 2, pp. 269–279, Feb. 2015, doi: 10.1002/CELC.201402271.
- [260] C. Tyagi, N. Chauhan, A. Tripathi, U. Jain, and D. K. Avasthi, “Voltammetric measurements of neurotransmitter-acetylcholine through metallic nanoparticles embedded 2-D material,” *Int J Biol Macromol*, vol. 140, pp. 415–422, Nov. 2019, doi: 10.1016/J.IJBIOMAC.2019.08.102.
- [261] D. M. Fernandes *et al.*, “Novel electrochemical sensor based on N-doped carbon nanotubes and Fe₃O₄ nanoparticles: Simultaneous voltammetric determination of ascorbic acid, dopamine and uric acid,” *J Colloid Interface Sci*, vol. 432, pp. 207–213, Oct. 2014, doi: 10.1016/J.JCIS.2014.06.050.
- [262] F. T. C. Moreira, S. Sharma, R. A. F. Dutra, J. P. C. Noronha, A. E. G. Cass, and M. G. F. Sales, “Protein-responsive polymers for point-of-care detection of cardiac biomarker,” *Sens Actuators B Chem*, vol. 196, pp. 123–132, Jun. 2014, doi: 10.1016/J.SNB.2014.01.038.
- [263] F. T. C. Moreira, S. Sharma, R. A. F. Dutra, J. P. C. Noronha, A. E. G. Cass, and M. G. F. Sales, “Detection of cardiac biomarker proteins using a disposable based on a molecularly imprinted polymer grafted onto graphite,” *Microchimica Acta*, vol. 182, no. 5–6, pp. 975–983, Apr. 2015, doi: 10.1007/S00604-014-1409-0.
- [264] N. Elgrishi, K. J. Rountree, B. D. McCarthy, E. S. Rountree, T. T. Eisenhart, and J. L. Dempsey, “A Practical Beginner’s Guide to Cyclic Voltammetry,” *J Chem Educ*, vol. 95, no. 2, pp. 197–206, Feb. 2018, doi: 10.1021/ACS.JCHEMED.7B00361/ASSET/IMAGES/LARGE/ED-2017-00361M_0002.JPEG.
- [265] M. L. Colombo, J. v. Sweedler, and M. Shen, “Nanopipet-based liquid-liquid interface probes for the electrochemical detection of acetylcholine, tryptamine, and serotonin via ionic transfer,” *Anal Chem*, vol. 87, no. 10, pp. 5095–5100, May 2015, doi: 10.1021/AC504151E.
- [266] A. al Fatease *et al.*, “Label-free electrochemical sensor based on manganese doped titanium dioxide nanoparticles for myoglobin detection: Biomarker for acute myocardial infarction,” *Molecules*, vol. 26, no. 14, Jul. 2021, doi: 10.3390/MOLECULES26144252.
- [267] S. J. Choi, B. G. Choi, and S. M. Park, “Electrochemical sensor for electrochemically inactive β -D(+)-glucose using α -cyclodextrin template molecules,” *Anal Chem*, vol. 74, no. 9, pp. 1998–2002, May 2002, doi: 10.1021/AC0107913.

- [268] Q. Yi and W. Yu, “Electrocatalytic activity of a novel titanium-supported nanoporous gold catalyst for glucose oxidation,” *Microchimica Acta*, vol. 165, no. 3–4, pp. 381–386, Jun. 2009, doi: 10.1007/S00604-009-0148-0.
- [269] F. Kurniawan, V. Tsakova, and V. M. Mirsky, “Gold nanoparticles in nonenzymatic electrochemical detection of sugars,” *Electroanalysis*, vol. 18, no. 19–20, pp. 1937–1942, Oct. 2006, doi: 10.1002/ELAN.200603607.
- [270] J. J. Yu, S. Lu, J. W. Li, F. Q. Zhao, and B. Z. Zeng, “Characterization of gold nanoparticles electrochemically deposited on amine-functioned mesoporous silica films and electrocatalytic oxidation of glucose,” *Journal of Solid State Electrochemistry*, vol. 11, no. 9, pp. 1211–1219, Sep. 2007, doi: 10.1007/S10008-007-0272-X/FIGURES/10.
- [271] D. Feng, F. Wang, and Z. Chen, “Electrochemical glucose sensor based on one-step construction of gold nanoparticle–chitosan composite film,” *Sens Actuators B Chem*, vol. 138, no. 2, pp. 539–544, May 2009, doi: 10.1016/J.SNB.2009.02.048.
- [272] J. Zhao, J. Yu, F. Wang, and S. Hu, “Fabrication of gold nanoparticle-dihexadecyl hydrogen phosphate film on a glassy carbon electrode, and its application to glucose sensing,” *Microchimica Acta*, vol. 156, no. 3–4, pp. 277–282, Dec. 2006, doi: 10.1007/S00604-006-0631-9.
- [273] K. E. Toghill, L. Xiao, M. A. Phillips, and R. G. Compton, “The non-enzymatic determination of glucose using an electrolytically fabricated nickel microparticle modified boron-doped diamond electrode or nickel foil electrode,” *Sens Actuators B Chem*, vol. 147, no. 2, pp. 642–652, Jun. 2010, doi: 10.1016/J.SNB.2010.03.091.
- [274] J. Zhao, D. Wu, and J. Zhi, “A direct electrochemical method for diabetes diagnosis based on as-prepared boron-doped nanocrystalline diamond thin film electrodes,” *Journal of Electroanalytical Chemistry*, vol. 626, no. 1–2, pp. 98–102, Feb. 2009, doi: 10.1016/J.JELECHEM.2008.11.007.
- [275] R. Ojani, J. B. Raoof, and P. Salmany-Afagh, “Electrocatalytic oxidation of some carbohydrates by poly(1-naphthylamine)/nickel modified carbon paste electrode,” *Journal of Electroanalytical Chemistry*, vol. 571, no. 1, pp. 1–8, Sep. 2004, doi: 10.1016/J.JELECHEM.2004.03.032.
- [276] Z. Cheng, E. Wang, and X. Yang, “Capacitive detection of glucose using molecularly imprinted polymers,” *Biosens Bioelectron*, vol. 16, no. 3, pp. 179–185, May 2001, doi: 10.1016/S0956-5663(01)00137-3.
- [277] D. S. Perušković, N. R. Stevanović, G. N. Kovačević, D. M. Stanković, A. Lolić, and R. M. Baošić, “Application of N,N’-Bis(acetylacetonato)propylenediimine

- Copper(II) Complex as Mediator for Glucose Biosensor,” *ChemistrySelect*, vol. 5, no. 5, pp. 1671–1675, Feb. 2020, doi: 10.1002/SLCT.201904873.
- [278] H. Shu, L. Cao, G. Chang, H. He, Y. Zhang, and Y. He, “Direct Electrodeposition of Gold Nanostructures onto Glassy Carbon Electrodes for Non-enzymatic Detection of Glucose,” *Electrochim Acta*, vol. 132, pp. 524–532, Jun. 2014, doi: 10.1016/J.ELECTACTA.2014.04.031.
- [279] X. Gong *et al.*, “High-performance non-enzymatic glucose sensors based on CoNiCu alloy nanotubes arrays prepared by electrodeposition,” *Front Mater*, vol. 6, Jan. 2019, doi: 10.3389/FMATS.2019.00003/FULL.
- [280] J. Wang, X. Cao, X. Wang, S. Yang, and R. Wang, “Electrochemical Oxidation and Determination of Glucose in Alkaline Media Based on Au (111)-Like Nanoparticle Array on Indium Tin Oxide Electrode,” *Electrochim Acta*, vol. 138, pp. 174–186, Aug. 2014, doi: 10.1016/J.ELECTACTA.2014.06.116.
- [281] M. L. Colombo, J. v. Sweedler, and M. Shen, “Nanopipet-Based Liquid–Liquid Interface Probes for the Electrochemical Detection of Acetylcholine, Tryptamine, and Serotonin via Ionic Transfer,” *Anal Chem*, vol. 87, no. 10, p. 5095, May 2015, doi: 10.1021/AC504151E.
- [282] A. Liu, I. Honma, and H. Zhou, “Amperometric biosensor based on tyrosinase-conjugated polysaccharide hybrid film: selective determination of nanomolar neurotransmitters metabolite of 3,4-dihydroxyphenylacetic acid (DOPAC) in biological fluid,” *Biosens Bioelectron*, vol. 21, no. 5, pp. 809–816, Nov. 2005, doi: 10.1016/J.BIOS.2005.03.005.
- [283] S. Blanco, R. Vargas, J. Mostany, C. Borrás, and B. R. Scharifker, “A novel nickel nanowire amperometric sensor: Direct current vs. alternating current strategies for ethanol, acetaldehyde and acetylcholine detection,” *Journal of Electroanalytical Chemistry*, vol. 740, pp. 61–67, Mar. 2015, doi: 10.1016/J.JELECHEM.2014.12.028.
- [284] S. L. R. Gomes-Filho, A. C. M. S. Dias, M. M. S. Silva, B. V. M. Silva, and R. F. Dutra, “A carbon nanotube-based electrochemical immunosensor for cardiac troponin T,” *Microchemical Journal*, vol. 109, pp. 10–15, Jul. 2013, doi: 10.1016/j.microc.2012.05.033.
- [285] B. Esteban-Fernández De Ávila *et al.*, “Ultrasensitive amperometric magnetoimmunosensor for human C-reactive protein quantification in serum,” *Sens Actuators B Chem*, vol. 188, pp. 212–220, 2013, doi: 10.1016/J.SNB.2013.07.026.

- [286] M. Sharafeldin, G. W. Bishop, S. Bhakta, A. El-Sawy, S. L. Suib, and J. F. Rusling, “Fe₃O₄ nanoparticles on graphene oxide sheets for isolation and ultrasensitive amperometric detection of cancer biomarker proteins,” *Biosens Bioelectron*, vol. 91, pp. 359–366, May 2017, doi: 10.1016/J.BIOS.2016.12.052.
- [287] B. K. Shrestha, R. Ahmad, S. Shrestha, C. H. Park, and C. S. Kim, “Globular Shaped Polypyrrole Doped Well-Dispersed Functionalized Multiwall Carbon Nanotubes/Nafion Composite for Enzymatic Glucose Biosensor Application,” *Scientific Reports 2017 7:1*, vol. 7, no. 1, pp. 1–13, Nov. 2017, doi: 10.1038/s41598-017-16541-9.
- [288] J. Li *et al.*, “Multiwalled carbon nanotubes coated with cobalt(II) sulfide nanoparticles for electrochemical sensing of glucose via direct electron transfer to glucose oxidase,” *Microchimica Acta*, vol. 187, no. 1, pp. 1–9, Jan. 2020, doi: 10.1007/S00604-019-4047-8/FIGURES/6.
- [289] M. F. Hossain and G. Slaughter, “PtNPs decorated chemically derived graphene and carbon nanotubes for sensitive and selective glucose biosensing,” *Journal of Electroanalytical Chemistry*, vol. 861, p. 113990, Mar. 2020, doi: 10.1016/J.JELECHEM.2020.113990.
- [290] S. K. Krishnan, E. Prokhorov, D. Bahena, R. Esparza, and M. Meyyappan, “Chitosan-Covered Pd@Pt Core-Shell Nanocubes for Direct Electron Transfer in Electrochemical Enzymatic Glucose Biosensor,” *ACS Omega*, vol. 2, no. 5, pp. 1896–1904, May 2017, doi: 10.1021/ACSOMEGA.7B00060.
- [291] Y. Hu, F. He, A. Ben, and C. Chen, “Synthesis of hollow Pt–Ni–graphene nanostructures for nonenzymatic glucose detection,” *Journal of Electroanalytical Chemistry*, vol. 726, pp. 55–61, Jul. 2014, doi: 10.1016/J.JELECHEM.2014.05.012.
- [292] Y. Zhang *et al.*, “A flexible non-enzymatic glucose sensor based on copper nanoparticles anchored on laser-induced graphene,” *Carbon N Y*, vol. 156, pp. 506–513, Jan. 2020, doi: 10.1016/J.CARBON.2019.10.006.
- [293] F. Wang, X. Chen, L. Chen, J. Yang, and Q. Wang, “High-performance non-enzymatic glucose sensor by hierarchical flower-like nickel(II)-based MOF/carbon nanotubes composite,” *Materials Science and Engineering: C*, vol. 96, pp. 41–50, Mar. 2019, doi: 10.1016/J.MSEC.2018.11.004.
- [294] X. Zhang, Y. Xu, and B. Ye, “An efficient electrochemical glucose sensor based on porous nickel-based metal organic framework/carbon nanotubes composite (Ni-MOF/CNTs),” *J Alloys Compd*, vol. 767, pp. 651–656, Oct. 2018, doi: 10.1016/J.JALLCOM.2018.07.175.

- [295] G. Chang *et al.*, “Synthesis of highly dispersed Pt nanoclusters anchored graphene composites and their application for non-enzymatic glucose sensing,” *Electrochim Acta*, vol. 157, pp. 149–157, Mar. 2015, doi: 10.1016/J.ELECTACTA.2015.01.085.
- [296] G. H. Wu, X. H. Song, Y. F. Wu, X. M. Chen, F. Luo, and X. Chen, “Non-enzymatic electrochemical glucose sensor based on platinum nanoflowers supported on graphene oxide,” *Talanta*, vol. 105, pp. 379–385, Feb. 2013, doi: 10.1016/J.TALANTA.2012.10.066.
- [297] C. Su, C. Zhang, G. Lu, and C. Ma, “Nonenzymatic Electrochemical Glucose Sensor Based on Pt Nanoparticles/Mesoporous Carbon Matrix,” *Electroanalysis*, vol. 22, no. 16, pp. 1901–1905, Aug. 2010, doi: 10.1002/ELAN.200900633.
- [298] L. Han, S. Zhang, L. Han, D. P. Yang, C. Hou, and A. Liu, “Porous gold cluster film prepared from Au@BSA microspheres for electrochemical nonenzymatic glucose sensor,” *Electrochim Acta*, vol. 138, pp. 109–114, Aug. 2014, doi: 10.1016/J.ELECTACTA.2014.06.095.
- [299] T. Kangkamano, A. Numnuam, W. Limbut, P. Kanatharana, and P. Thavarungkul, “Chitosan cryogel with embedded gold nanoparticles decorated multiwalled carbon nanotubes modified electrode for highly sensitive flow based non-enzymatic glucose sensor,” *Sens Actuators B Chem*, vol. 246, pp. 854–863, Jul. 2017, doi: 10.1016/J.SNB.2017.02.105.
- [300] M. Xu *et al.*, “A novel flexible electrochemical glucose sensor based on gold nanoparticles/polyaniline arrays/carbon cloth electrode,” *Sens Actuators B Chem*, vol. 252, pp. 1187–1193, Nov. 2017, doi: 10.1016/J.SNB.2017.07.147.
- [301] A. Ahmadalinezhad, S. Chatterjee, and A. Chen, “Synthesis and electrochemical study of nanoporous palladium–cadmium networks for non-enzymatic glucose detection,” *Electrochim Acta*, vol. 112, pp. 927–932, Dec. 2013, doi: 10.1016/J.ELECTACTA.2013.05.143.
- [302] Y. Zhao *et al.*, “Nonenzymatic detection of glucose using three-dimensional PtNi nanoclusters electrodeposited on the multiwalled carbon nanotubes,” *Sens Actuators B Chem*, vol. 231, pp. 800–810, Aug. 2016, doi: 10.1016/J.SNB.2016.03.115.
- [303] H. Nie, Z. Yao, X. Zhou, Z. Yang, and S. Huang, “Nonenzymatic electrochemical detection of glucose using well-distributed nickel nanoparticles on straight multi-walled carbon nanotubes,” *Biosens Bioelectron*, vol. 30, no. 1, pp. 28–34, Dec. 2011, doi: 10.1016/J.BIOS.2011.08.022.

- [304] L. Wang *et al.*, “A green and simple strategy to prepare graphene foam-like three-dimensional porous carbon/Ni nanoparticles for glucose sensing,” *Sens Actuators B Chem*, vol. 239, pp. 172–179, Feb. 2017, doi: 10.1016/J.SNB.2016.06.173.
- [305] M. Li, X. Bo, Z. Mu, Y. Zhang, and L. Guo, “Electrodeposition of nickel oxide and platinum nanoparticles on electrochemically reduced graphene oxide film as a nonenzymatic glucose sensor,” *Sens Actuators B Chem*, vol. 192, pp. 261–268, Mar. 2014, doi: 10.1016/J.SNB.2013.10.140.
- [306] L. Hou, H. Zhao, S. Bi, Y. Xu, and Y. Lu, “Ultrasensitive and highly selective sandpaper-supported copper framework for non-enzymatic glucose sensor,” *Electrochim Acta*, vol. 248, pp. 281–291, 2017, doi: 10.1016/j.electacta.2017.07.142.
- [307] X. Zhou, H. Nie, Z. Yao, Y. Dong, Z. Yang, and S. Huang, “Facile synthesis of nanospindle-like Cu₂O/straight multi-walled carbon nanotube hybrid nanostructures and their application in enzyme-free glucose sensing,” *Sens Actuators B Chem*, vol. 168, pp. 1–7, Jun. 2012, doi: 10.1016/j.snb.2011.12.012.
- [308] L. C. Jiang and W. De Zhang, “A highly sensitive nonenzymatic glucose sensor based on CuO nanoparticles-modified carbon nanotube electrode,” *Biosens Bioelectron*, vol. 25, no. 6, pp. 1402–1407, Feb. 2010, doi: 10.1016/J.BIOS.2009.10.038.
- [309] C. Zhou *et al.*, “Electrochemical Fabrication of Cobalt Oxides/Nanoporous Gold Composite Electrode and its Nonenzymatic Glucose Sensing Performance,” *Electroanalysis*, vol. 28, no. 9, pp. 2149–2157, Sep. 2016, doi: 10.1002/ELAN.201501177.
- [310] R. Madhu, V. Veeramani, S. M. Chen, A. Manikandan, A. Y. Lo, and Y. L. Chueh, “Honeycomb-like Porous Carbon-Cobalt Oxide Nanocomposite for High-Performance Enzymeless Glucose Sensor and Supercapacitor Applications,” *ACS Appl Mater Interfaces*, vol. 7, no. 29, pp. 15812–15820, Jul. 2015, doi: 10.1021/ACSAMI.5B04132/SUPPL_FILE/AM5B04132_SI_001.PDF.
- [311] C. Guo, X. Zhang, H. Huo, C. Xu, and X. Han, “Co₃O₄ microspheres with free-standing nanofibers for high performance non-enzymatic glucose sensor,” *Analyst*, vol. 138, no. 22, pp. 6727–6731, Nov. 2013, doi: 10.1039/c3an01403g.
- [312] J. Kalita, S. Kumar, K. Vijaykumar, G. Palit, and U. K. Misra, “A study of CSF catecholamine and its metabolites in acute and convalescent period of encephalitis,” *J Neurol Sci*, vol. 252, no. 1, pp. 62–66, Jan. 2007, doi: 10.1016/J.JNS.2006.10.010.

- [313] J. F. Hernándezhernández-Rodríguez, D. Rojas, and A. Escarpa, “Electrochemical Sensing Directions for Next-Generation Healthcare: Trends, Challenges, and Frontiers,” *Cite This: Anal. Chem.*, vol. 93, pp. 167–183, 2021, doi: 10.1021/acs.analchem.0c04378.
- [314] P. S. Pakchin, S. A. Nakhjavani, R. Saber, H. Ghanbari, and Y. Omid, “Recent advances in simultaneous electrochemical multi-analyte sensing platforms,” *TrAC Trends in Analytical Chemistry*, vol. 92, pp. 32–41, Jul. 2017, doi: 10.1016/J.TRAC.2017.04.010.
- [315] I. Grabowska, M. Hepel, and K. Kurzątkowska-Adaszyńska, “Advances in design strategies of multiplex electrochemical aptasensors,” *Sensors*, vol. 22, no. 1, Jan. 2022, doi: 10.3390/S22010161.
- [316] M. Klimuntowski, M. M. Alam, G. Singh, and M. M. R. Howlader, “Electrochemical Sensing of Cannabinoids in Biofluids: A Noninvasive Tool for Drug Detection,” *ACS Sens*, vol. 5, no. 3, pp. 620–636, 2020, doi: 10.1021/acssensors.9b02390.
- [317] D. Zhao, G. Yu, K. Tian, and C. Xu, “A highly sensitive and stable electrochemical sensor for simultaneous detection towards ascorbic acid, dopamine, and uric acid based on the hierarchical nanoporous PtTi alloy,” *Biosens Bioelectron*, vol. 82, pp. 119–126, Aug. 2016, doi: 10.1016/J.BIOS.2016.03.074.
- [318] P. Yáñez-Sedeño, S. Campuzano, and J. M. Pingarrón, “Integrated Affinity Biosensing Platforms on Screen-Printed Electrodes Electrografted with Diazonium Salts,” *Sensors 2018, Vol. 18, Page 675*, vol. 18, no. 2, p. 675, Feb. 2018, doi: 10.3390/S18020675.
- [319] V. Kammarchedu, D. Butler, and A. Ebrahimi, “A machine learning-based multimodal electrochemical analytical device based on eMoSx-LIG for multiplexed detection of tyrosine and uric acid in sweat and saliva,” *Anal Chim Acta*, vol. 1232, Nov. 2022, doi: 10.1016/j.aca.2022.340447.
- [320] H. Park *et al.*, “Portable All-in-One Electroanalytical Device for Point of Care,” *IEEE Access*, vol. 10, pp. 68700–68710, 2022, doi: 10.1109/ACCESS.2022.3186678.
- [321] A. J. Bandonkar and J. Wang, “Non-invasive wearable electrochemical sensors: a review,” *Trends Biotechnol*, vol. 32, no. 7, pp. 363–371, Jul. 2014, doi: 10.1016/J.TIBTECH.2014.04.005.
- [322] N. Jadon, R. Jain, S. Sharma, and K. Singh, “Recent trends in electrochemical sensors for multianalyte detection – A review,” *Talanta*, vol. 161, pp. 894–916, Dec. 2016, doi: 10.1016/J.TALANTA.2016.08.084.

- [323] J. Heikenfeld *et al.*, “Accessing analytes in biofluids for peripheral biochemical monitoring,” *Nature Biotechnology* 2019 37:4, vol. 37, no. 4, pp. 407–419, Feb. 2019, doi: 10.1038/s41587-019-0040-3.
- [324] T. C. Boysen, S. Yanagawa, F. Sato, and K. Sato, “A modified anaerobic method of sweat collection,” *J Appl Physiol Respir Environ Exerc Physiol*, vol. 56, no. 5, pp. 1302–1307, 1984, doi: 10.1152/JAPPL.1984.56.5.1302.
- [325] Z. Sonner *et al.*, “The microfluidics of the eccrine sweat gland, including biomarker partitioning, transport, and biosensing implications,” *Biomicrofluidics*, vol. 9, no. 3, May 2015, doi: 10.1063/1.4921039.
- [326] J. Heikenfeld, “Non-invasive Analyte Access and Sensing through Eccrine Sweat: Challenges and Outlook circa 2016,” *Electroanalysis*, vol. 28, no. 6, pp. 1242–1249, Jun. 2016, doi: 10.1002/ELAN.201600018.
- [327] P. Simmers, S. K. Li, G. Kasting, and J. Heikenfeld, “Prolonged and localized sweat stimulation by iontophoretic delivery of the slowly-metabolized cholinergic agent carbachol,” *J Dermatol Sci*, vol. 89, no. 1, pp. 40–51, Jan. 2018, doi: 10.1016/J.JDERMSCI.2017.10.013.
- [328] Z. Sonner, E. Wilder, T. Gaillard, G. Kasting, and J. Heikenfeld, “Integrated sudomotor axon reflex sweat stimulation for continuous sweat analyte analysis with individuals at rest,” *Lab Chip*, vol. 17, no. 15, pp. 2550–2560, Jul. 2017, doi: 10.1039/C7LC00364A.
- [329] K. Miura, A. C. Orcutt, O. V. Muratova, L. H. Miller, A. Saul, and C. A. Long, “Development and Characterization of a Standardized ELISA Including a Reference Serum on Each Plate to Detect Antibodies Induced by Experimental Malaria Vaccines,” *Vaccine*, vol. 26, no. 2, p. 193, Jan. 2008, doi: 10.1016/J.VACCINE.2007.10.064.
- [330] B. K. Van Weemen and A. H. W. M. Schuurs, “Immunoassay using antigen—enzyme conjugates,” *FEBS Lett*, vol. 15, no. 3, pp. 232–236, Jun. 1971, doi: 10.1016/0014-5793(71)80319-8.
- [331] E. Engvall and P. Perlmann, “Enzyme-linked immunosorbent assay (ELISA) quantitative assay of immunoglobulin G,” *Immunochemistry*, vol. 8, no. 9, pp. 871–874, Sep. 1971, doi: 10.1016/0019-2791(71)90454-X.
- [332] S. Avrameas, “Coupling of enzymes to proteins with glutaraldehyde. Use of the conjugates for the detection of antigens and antibodies,” *Immunochemistry*, vol. 6, no. 1, 1969, doi: 10.1016/0019-2791(69)90177-3.

- [333] S. Avrameas, “Immunoenzyme techniques: enzymes as markers for the localization of antigens and antibodies,” *Int Rev Cytol*, vol. 27, no. C, pp. 349–385, Jan. 1970, doi: 10.1016/S0074-7696(08)61250-4.
- [334] R. Minic, I. Zivkovic, R. Minic, and I. Zivkovic, “Optimization, Validation and Standardization of ELISA,” *Norovirus*, Dec. 2020, doi: 10.5772/INTECHOPEN.94338.
- [335] J. L. Klotz, R. M. Minami, and R. L. Teplitz, “An enzyme-linked immunosorbent assay for antibodies to native and denatured DNA,” *J Immunol Methods*, vol. 29, no. 2, pp. 155–165, Aug. 1979, doi: 10.1016/0022-1759(79)90065-6.
- [336] L. A. Dimitrijević *et al.*, “Human monoclonal IgM DJ binds to ssDNA and human commensal bacteria,” *Hum Antibodies*, vol. 9, no. 1, pp. 37–45, 1999, doi: 10.3233/hab-1999-9104.
- [337] V. Petrušić *et al.*, “Autoantibody response and pregnancy-related pathology induced by combined LPS and tetanus toxoid hyperimmunization in BALB/c and C57BL/6 mice,” *Autoimmunity*, vol. 48, no. 2, pp. 87–99, Mar. 2015, doi: 10.3109/08916934.2014.961061.
- [338] P. Chiani, C. Bromuro, A. Cassone, and A. Torosantucci, “Anti-beta-glucan antibodies in healthy human subjects,” *Vaccine*, vol. 27, no. 4, pp. 513–519, Jan. 2009, doi: 10.1016/J.VACCINE.2008.11.030.
- [339] A. Yoneda and T. Kurokawa, “A sensitive sandwich ELISA to measure (1→3)- β -d-glucan levels in blood,” *J Immunol Methods*, vol. 365, no. 1–2, pp. 158–165, Feb. 2011, doi: 10.1016/J.JIM.2010.12.011.
- [340] I. P. Zivkovic, M. M. Stojanovic, V. Z. Petrusic, A. B. Inic-Kanada, M. V. Micic, and L. A. Dimitrijevic, “Network connectivity is shown to change in C57BL/6 mice during a continuing immune response subsequent to tetanus toxoid hyperimmunization,” *Biol Res*, vol. 43, no. 4, pp. 393–402, 2010, doi: 10.4067/S0716-97602010000400003.
- [341] K. Sinha, Z. Uddin, H. I. Kawsar, S. Islam, M. J. Deen, and M. M. R. Howlader, “Analyzing chronic disease biomarkers using electrochemical sensors and artificial neural networks,” *TrAC Trends in Analytical Chemistry*, vol. 158, p. 116861, Jan. 2023, doi: 10.1016/J.TRAC.2022.116861.
- [342] P. C. Ferreira *et al.*, “Wearable electrochemical sensors for forensic and clinical applications,” *TrAC Trends in Analytical Chemistry*, vol. 119, p. 115622, Oct. 2019, doi: 10.1016/J.TRAC.2019.115622.

- [343] J. R. Sempionatto, I. Jeerapan, S. Krishnan, and J. Wang, “Wearable Chemical Sensors: Emerging Systems for On-Body Analytical Chemistry,” *Anal Chem*, 2019, doi: 10.1021/ACS.ANALCHEM.9B04668/ASSET/IMAGES/LARGE/AC9B04668_0006.JPEG.
- [344] Y. Song, J. Min, and W. Gao, “Wearable and Implantable Electronics: Moving toward Precision Therapy,” *ACS Nano*, vol. 13, no. 11, pp. 12280–12286, Nov. 2019, doi: 10.1021/ACSNANO.9B08323/ASSET/IMAGES/LARGE/NN9B08323_0003.JPG.
- [345] J. Schultz, Z. Uddin, G. Singh, and M. M. R. Howlader, “Glutamate sensing in biofluids: recent advances and research challenges of electrochemical sensors,” *Analyst*, vol. 145, no. 2, pp. 321–347, Jan. 2020, doi: 10.1039/C9AN01609K.
- [346] O. Boursalie, R. Samavi, and T. E. Doyle, “M4CVD: Mobile Machine Learning Model for Monitoring Cardiovascular Disease,” *Procedia Comput Sci*, vol. 63, pp. 384–391, Jan. 2015, doi: 10.1016/J.PROCS.2015.08.357.
- [347] P. D. S. Grewal, “A Critical Conceptual Analysis of Definitions of Artificial Intelligence as Applicable to Computer Engineering,” *IOSR J Comput Eng*, vol. 16, no. 2, pp. 09–13, 2014, doi: 10.9790/0661-16210913.
- [348] T. Pekkala *et al.*, “Development of a Late-Life Dementia Prediction Index with Supervised Machine Learning in the Population-Based CAIDE Study,” *Journal of Alzheimer’s Disease*, vol. 55, no. 3, pp. 1055–1067, Jan. 2017, doi: 10.3233/JAD-160560.
- [349] H. Haick and N. Tang, “Artificial Intelligence in Medical Sensors for Clinical Decisions,” *ACS Nano*, vol. 15, no. 3, pp. 3557–3567, Mar. 2021, doi: 10.1021/ACSNANO.1C00085/ASSET/IMAGES/LARGE/NN1C00085_0006.JPG.
- [350] D. Farmakis *et al.*, “Urine proteome analysis in heart failure with reduced ejection fraction complicated by chronic kidney disease: feasibility, and clinical and pathogenetic correlates,” *Eur J Heart Fail*, vol. 18, no. 7, pp. 822–829, Jul. 2016, doi: 10.1002/EJHF.544.
- [351] N. S. Rajliwall, R. Davey, and G. Chetty, “Machine learning based models for cardiovascular risk prediction,” *Proceedings - International Conference on Machine Learning and Data Engineering, iCMLDE 2018*, pp. 149–153, Jan. 2019, doi: 10.1109/ICMLDE.2018.00034.

- [352] M. Tirzite, M. Bukovskis, G. Strazda, N. Jurka, and I. Taivans, “Detection of lung cancer in exhaled breath with an electronic nose using support vector machine analysis,” *J Breath Res*, vol. 11, no. 3, p. 036009, Aug. 2017, doi: 10.1088/1752-7163/AA7799.
- [353] J. Finkelstein and I. cheol Jeong, “Machine learning approaches to personalize early prediction of asthma exacerbations,” *Ann N Y Acad Sci*, vol. 1387, no. 1, pp. 153–165, Jan. 2017, doi: 10.1111/NYAS.13218.
- [354] T. Dörner and R. Furie, “Novel paradigms in systemic lupus erythematosus,” *The Lancet*, vol. 393, no. 10188, pp. 2344–2358, Jun. 2019, doi: 10.1016/S0140-6736(19)30546-X.
- [355] W. Zhou *et al.*, “Predictive model for inflammation grades of chronic hepatitis B: Large-scale analysis of clinical parameters and gene expressions,” *Liver International*, vol. 37, no. 11, pp. 1632–1641, Nov. 2017, doi: 10.1111/LIV.13427.
- [356] B. P. Smith *et al.*, “Identification of early liver toxicity gene biomarkers using comparative supervised machine learning,” *Scientific Reports 2020 10:1*, vol. 10, no. 1, pp. 1–27, Nov. 2020, doi: 10.1038/s41598-020-76129-8.
- [357] S. Martin *et al.*, “Combined Mixed Potential Electrochemical Sensors and Artificial Neural Networks for the Quantification and Identification of Methane in Natural Gas Emissions Monitoring,” *J Electrochem Soc*, vol. 168, no. 9, p. 097506, Sep. 2021, doi: 10.1149/1945-7111/AC2465.
- [358] V. C. Rodrigues *et al.*, “Electrochemical and optical detection and machine learning applied to images of genosensors for diagnosis of prostate cancer with the biomarker PCA3,” *Talanta*, vol. 222, p. 121444, Jan. 2021, doi: 10.1016/J.TALANTA.2020.121444.
- [359] M. Alafeef, I. Srivastava, and D. Pan, “Machine Learning for Precision Breast Cancer Diagnosis and Prediction of the Nanoparticle Cellular Internalization,” *ACS Sens*, vol. 5, no. 6, pp. 1689–1698, Jun. 2020, doi: 10.1021/ACSSENSORS.0C00329/ASSET/IMAGES/LARGE/SE0C00329_0006.JPEG.
- [360] Q. Chen, Z. Chen, D. Liu, Z. He, and J. Wu, “Constructing an E-Nose Using Metal-Ion-Induced Assembly of Graphene Oxide for Diagnosis of Lung Cancer via Exhaled Breath,” *ACS Appl Mater Interfaces*, vol. 12, no. 15, pp. 17713–17724, Apr. 2020, doi: 10.1021/ACSAMI.0C00720/ASSET/IMAGES/LARGE/AM0C00720_0010.JPEG.

- [361] S. H. Kuo *et al.*, “Climbing fiber-Purkinje cell synaptic pathology in tremor and cerebellar degenerative diseases,” *Acta Neuropathol*, vol. 133, no. 1, pp. 121–138, Jan. 2017, doi: 10.1007/S00401-016-1626-1/TABLES/5.
- [362] H. Zhu, L. Li, W. Zhou, Z. Shao, and X. Chen, “Advances in non-enzymatic glucose sensors based on metal oxides,” *J Mater Chem B*, vol. 4, no. 46, pp. 7333–7349, 2016, doi: 10.1039/C6TB02037B.
- [363] M. S. Talary, F. Dewarrat, D. Huber, and A. Caduff, “In vivo life sign application of dielectric spectroscopy and non-invasive glucose monitoring,” *J Non Cryst Solids*, vol. 353, no. 47–51, pp. 4515–4517, 2007, doi: 10.1016/j.jnoncrysol.2007.03.038.
- [364] R. Ghaffari, J. A. Rogers, and T. R. Ray, “Recent progress, challenges, and opportunities for wearable biochemical sensors for sweat analysis,” *Sens Actuators B Chem*, vol. 332, no. October 2020, p. 129447, 2021, doi: 10.1016/j.snb.2021.129447.
- [365] D. W. Hwang, S. Lee, M. Seo, and T. D. Chung, “Recent advances in electrochemical non-enzymatic glucose sensors – A review,” *Anal Chim Acta*, vol. 1033, pp. 1–34, 2018, doi: 10.1016/j.aca.2018.05.051.
- [366] G. Wang *et al.*, “Non-enzymatic electrochemical sensing of glucose,” *Microchimica Acta*, vol. 180, no. 3–4, pp. 161–186, 2013. doi: 10.1007/s00604-012-0923-1.
- [367] X. Niu, X. Li, J. Pan, Y. He, F. Qiu, and Y. Yan, “Recent advances in non-enzymatic electrochemical glucose sensors based on non-precious transition metal materials: Opportunities and challenges,” *RSC Adv*, vol. 6, no. 88, pp. 84893–84905, 2016, doi: 10.1039/c6ra12506a.
- [368] B. K. Meyer *et al.*, “Binary copper oxide semiconductors: From materials towards devices,” *Phys Status Solidi B Basic Res*, vol. 249, no. 8, pp. 1487–1509, 2012, doi: 10.1002/PSSB.201248128.
- [369] D. Nunes *et al.*, “Structural, optical, and electronic properties of metal oxide nanostructures,” in *Metal oxide nanostructures: Synthesis, properties and applications*, 1st ed., G. Korotcenkov, Ed., Elsevier, 2018, pp. 59–102. doi: 10.1016/C2016-0-01647-9.
- [370] I. M. Tiginyanu, O. Lupan, V. V. Ursaki, L. Chow, and M. Enachi, “Nanostructures of Metal Oxides,” in *Comprehensive Semiconductor Science and Technology*, 1st ed., vol. 1–6, Pallab Bhattacharya, Roberto Fornari, and K. Hiroshi, Eds., Elsevier, 2011, pp. 396–479. doi: 10.1016/B978-0-44-453153-7.00105-X.

- [371] J. M. Thornton and D. Raftery, “Photocatalysts for Solar Hydrogen Conversion,” in *New and Future Developments in Catalysis: Solar Photocatalysis*, 1st ed., S. L. Suib, Ed., Elsevier, 2013, pp. 191–217. doi: 10.1016/B978-0-444-53872-7.00009-1.
- [372] M. J. Dignam and D. B. Gibbs, “Anodic oxidation of copper in alkaline solution,” *Can J Chem*, vol. 48, no. 8, pp. 1242–1250, 1970, doi: 10.1139/v70-205.
- [373] Y. Wan, Y. Zhang, X. Wang, and Q. Wang, “Electrochemical formation and reduction of copper oxide nanostructures in alkaline media,” *Electrochem commun*, vol. 36, pp. 99–102, 2013, doi: 10.1016/j.elecom.2013.09.026.
- [374] J. Ramírez-Ortiz *et al.*, “A catalytic application of Cu₂O and CuO films deposited over fiberglass,” *Appl Surf Sci*, vol. 174, no. 3–4, pp. 177–184, 2001, doi: 10.1016/S0169-4332(00)00822-9.
- [375] F. Sun, L. Li, P. Liu, and Y. Lian, “Nonenzymatic Electrochemical Glucose Sensor Based on Novel Copper Film,” *Electroanalysis*, vol. 23, no. 2, pp. 395–401, 2011, doi: 10.1002/elan.201000391.
- [376] M. M. Guo, Y. Xia, W. Huang, and Z. Li, “Electrochemical fabrication of stalactite-like copper micropillar arrays via surface rebuilding for ultrasensitive nonenzymatic sensing of glucose,” *Electrochim Acta*, vol. 151, pp. 340–346, 2015, doi: 10.1016/j.electacta.2014.11.041.
- [377] X. Liu, W. Yang, L. Chen, and J. Jia, “Synthesis of copper nanorods for non-enzymatic amperometric sensing of glucose,” *Microchimica Acta*, vol. 183, no. 8, pp. 2369–2375, 2016, doi: 10.1007/s00604-016-1878-4.
- [378] L. Zhang, H. Li, Y. Ni, J. Li, K. Liao, and G. Zhao, “Porous cuprous oxide microcubes for non-enzymatic amperometric hydrogen peroxide and glucose sensing,” *Electrochem commun*, vol. 11, no. 4, pp. 812–815, 2009, doi: 10.1016/j.elecom.2009.01.041.
- [379] Z. Gao *et al.*, “Mesocrystalline Cu₂O hollow nanocubes: Synthesis and application in non-enzymatic amperometric detection of hydrogen peroxide and glucose,” *CrystEngComm*, vol. 14, no. 20, pp. 6639–6646, 2012, doi: 10.1039/c2ce25498k.
- [380] H. Cao *et al.*, “A non-enzymatic glucose sensing based on hollow cuprous oxide nanospheres in a Nafion matrix,” *Sensors and Actuators B*, vol. 214, pp. 169–173, 2015, doi: 10.1016/j.snb.2015.03.026.
- [381] S. Cherevko and C. H. Chung, “The porous CuO electrode fabricated by hydrogen bubble evolution and its application to highly sensitive non-enzymatic glucose

- detection,” *Talanta*, vol. 80, no. 3, pp. 1371–1377, 2010, doi: 10.1016/j.talanta.2009.09.038.
- [382] M. U. Anu Prathap, B. Kaur, and R. Srivastava, “Hydrothermal synthesis of CuO micro-/nanostructures and their applications in the oxidative degradation of methylene blue and non-enzymatic sensing of glucose/H₂O₂,” *J Colloid Interface Sci*, vol. 370, no. 1, pp. 144–154, 2012, doi: 10.1016/j.jcis.2011.12.074.
- [383] X. Wang, C. Hu, H. Liu, G. Du, X. He, and Y. Xi, “Synthesis of CuO nanostructures and their application for nonenzymatic glucose sensing,” *Sens Actuators B Chem*, vol. 1, no. 144, pp. 220–225, Jan. 2010, doi: 10.1016/J.SNB.2009.09.067.
- [384] X. Ma, Q. Zhao, H. Wang, and S. Ji, “Controlled synthesis of CuO from needle to flower-like particle morphologies for highly sensitive glucose detection,” *Int J Electrochem Sci*, vol. 12, no. 9, pp. 8217–8226, 2017, doi: 10.20964/2017.09.37.
- [385] S. Liu *et al.*, “A simple route for preparation of highly stable CuO nanoparticles for nonenzymatic glucose detection,” *Catal Sci Technol*, vol. 2, no. 4, pp. 813–817, 2012, doi: 10.1039/c2cy00453d.
- [386] C. Batchelor-McAuley, Y. Du, G. G. Wildgoose, and R. G. Compton, “The use of copper(II) oxide nanorod bundles for the non-enzymatic voltammetric sensing of carbohydrates and hydrogen peroxide,” *Sens Actuators B Chem*, vol. 135, no. 1, pp. 230–235, 2008, doi: 10.1016/j.snb.2008.08.006.
- [387] X. Liu, W. Yang, L. Chen, and J. Jia, “Three-Dimensional Copper Foam Supported CuO Nanowire Arrays: An Efficient Non-enzymatic Glucose Sensor,” *Electrochim Acta*, vol. 235, pp. 519–526, 2017, doi: 10.1016/j.electacta.2017.03.150.
- [388] Y. Zhang *et al.*, “CuO nanowires based sensitive and selective non-enzymatic glucose detection,” *Sens Actuators B Chem*, vol. 191, pp. 86–93, 2014, doi: 10.1016/j.snb.2013.08.096.
- [389] Z. Zhuang, X. Su, H. Yuan, Q. Sun, D. Xiao, and M. M. F. Choi, “An improved sensitivity non-enzymatic glucose sensor based on a CuO nanowire modified Cu electrode,” *Analyst*, vol. 133, no. 1, pp. 126–132, 2008, doi: 10.1039/b712970j.
- [390] P. Zhang, L. Zhang, G. Zhao, and F. Feng, “A highly sensitive nonenzymatic glucose sensor based on CuO nanowires,” *Microchimica Acta*, vol. 176, no. 3–4, pp. 411–417, 2012, doi: 10.1007/s00604-011-0733-x.
- [391] W. Wang, L. Zhang, S. Tong, X. Li, and W. Song, “Three-dimensional network films of electrospun copper oxide nanofibers for glucose determination,” *Biosens Bioelectron*, vol. 25, no. 4, pp. 708–714, 2009, doi: 10.1016/j.bios.2009.08.013.

- [392] E. Reitz, W. Jia, M. Gentile, Y. Wang, and Y. Lei, “CuO nanospheres based nonenzymatic glucose sensor,” *Electroanalysis*, vol. 20, no. 22, pp. 2482–2486, 2008, doi: 10.1002/elan.200804327.
- [393] L. Wang, J. Fu, and Y. Song, “A facile strategy to prepare Cu₂O/Cu electrode as a sensitive enzyme-free glucose sensor,” *Int J Electrochem Sci*, vol. 7, no. 12, pp. 12587–12600, 2012.
- [394] A. J. Wang, J. J. Feng, Z. H. Li, Q. C. Liao, Z. Z. Wang, and J. R. Chen, “Solvothetmal synthesis of Cu/Cu₂O hollow microspheres for non-enzymatic amperometric glucose sensing,” *CrystEngComm*, vol. 14, no. 4, pp. 1289–1295, 2012, doi: 10.1039/c1ce05869j.
- [395] Y. Zhao *et al.*, “Hyper-Branched Cu@Cu₂O Coaxial Nanowires Mesh Electrode for Ultra-Sensitive Glucose Detection,” 2015, doi: 10.1021/acsami.5b04614.
- [396] X. Cheng, J. Zhang, H. Chang, L. Luo, F. Nie, and X. Feng, “High performance Cu/Cu₂O nanohybrid electrocatalyst for nonenzymatic glucose detection,” *J Mater Chem B*, vol. 4, no. 27, pp. 4652–4656, 2016, doi: 10.1039/c6tb01158f.
- [397] Y. Zhao, Y. Li, Z. He, and Z. Yan, “Facile preparation of Cu–Cu₂O nanoporous nanoparticles as a potential catalyst for non-enzymatic glucose sensing,” *RSC Adv*, vol. 3, no. 7, pp. 2178–2181, Jan. 2013, doi: 10.1039/C2RA22654E.
- [398] K. Li, G. Fan, L. Yang, and F. Li, “Novel ultrasensitive non-enzymatic glucose sensors based on controlled flower-like CuO hierarchical films,” *Sens Actuators B Chem*, vol. 199, pp. 175–182, 2014, doi: 10.1016/j.snb.2014.03.095.
- [399] T. Z. Redhwan, A. U. Alam, Y. M. Haddara, and M. M. R. Howlader, “Copper and liquid crystal polymer bonding towards lead sensing,” *Jpn J Appl Phys*, vol. 57, no. 2, 2018, doi: 10.7567/JJAP.57.02BB03.
- [400] S. Suzuki, Y. Ishikawa, M. Isshiki, and Y. Waseda, “Native oxide layers formed on the surface of ultra high-purity iron and copper investigated by angle resolved XPS,” *Materials Transactions, JIM*, vol. 38, no. 11, pp. 1004–1009, 1997, doi: 10.2320/matertrans1989.38.1004.
- [401] I. Platzman, R. Brener, H. Haick, and R. Tannenbaum, “Oxidation of polycrystalline copper thin films at ambient conditions,” *Journal of Physical Chemistry C*, vol. 112, no. 4, pp. 1101–1108, 2008, doi: 10.1021/jp076981k.
- [402] J. E. Boggio, “The room temperature oxidation of Cu (111): Pressure effects,” *J Chem Phys*, vol. 70, no. 11, pp. 5054–5058, 1979, doi: 10.1063/1.437347.

- [403] N. Cabrera and N. F. Mott, “Theory of the oxidation of metals,” *Reports on Progress in Physics*, vol. 12, no. 1, pp. 163–184, 1949, doi: 10.1088/0034-4885/12/1/308.
- [404] N. F. Mott, “A theory of the formation of protective oxide films on metals,” *Transactions of the Faraday Society*, vol. 35, no. 0, pp. 1175–1177, Jan. 1939, doi: 10.1039/TF9393501175.
- [405] J. Iijima, J. W. Lim, S. H. Hong, S. Suzuki, K. Mimura, and M. Isshiki, “Native oxidation of ultra high purity Cu bulk and thin films,” *Appl Surf Sci*, vol. 253, no. 5, pp. 2825–2829, 2006, doi: 10.1016/j.apsusc.2006.05.063.
- [406] F. A. Akgul, G. Akgul, N. Yildirim, H. E. Unalan, and R. Turan, “Influence of thermal annealing on microstructural, morphological, optical properties and surface electronic structure of copper oxide thin films,” *Mater Chem Phys*, vol. 147, no. 3, pp. 987–995, 2014, doi: 10.1016/j.matchemphys.2014.06.047.
- [407] D. Tahir and S. Tougaard, “Electronic and optical properties of Cu, CuO and Cu₂O studied by electron spectroscopy,” *Journal of Physics Condensed Matter*, vol. 24, no. 17, 2012, doi: 10.1088/0953-8984/24/17/175002.
- [408] D. Barreca, A. Gasparotto, and E. Tondello, “CVD Cu₂O and CuO Nanosystems Characterized by XPS,” *Surface Science Spectra*, vol. 14, no. 1, pp. 41–51, 2007, doi: 10.1116/11.20080701.
- [409] T. L. Barr and S. Seal, “Nature of the use of adventitious carbon as a binding energy standard,” *Journal of Vacuum Science & Technology A: Vacuum, Surfaces, and Films*, vol. 13, no. 3, pp. 1239–1246, 1995, doi: 10.1116/1.579868.
- [410] C. D. Wagner *et al.*, “Auger and photoelectron line energy relationships in aluminum–oxygen and silicon–oxygen compounds,” *Journal of Vacuum Science and Technology*, vol. 21, no. 4, pp. 933–944, 1982.
- [411] M. Brandhorst *et al.*, “Cobalt-, copper- and iron-containing monolithic aluminosilicate-supported preparations for selective catalytic reduction of NO with NH₃ at low temperatures,” *Appl Catal B*, vol. 55, no. 4, pp. 267–276, 2005, doi: 10.1016/j.apcatb.2004.09.004.
- [412] J. F. Moulder, W. F. Stickle, P. E. Sobol, and K. D. Bomben, *Handbook of X-ray photoelectron spectroscopy: a reference book of standard spectra for identification and interpretation of XPS data*. Perkin-Elmer Corporation, USA, 1992. Accessed: Aug. 28, 2021. [Online]. Available: <https://www.cnyn.unam.mx/~wencel/XPS/MANXPS.pdf>

- [413] A. Amri *et al.*, “Surface structural features and optical analysis of nanostructured Cu-oxide thin film coatings coated via the sol-gel dip coating method,” *Ceram Int*, vol. 45, no. 10, pp. 12888–12894, 2019, doi: 10.1016/j.ceramint.2019.03.213.
- [414] S. Choudhary *et al.*, “Oxidation mechanism of thin Cu films: A gateway towards the formation of single oxide phase,” *AIP Adv*, vol. 8, no. 5, 2018, doi: 10.1063/1.5028407.
- [415] S. Poulston, P. M. Parlett, P. Stone, and M. Bowker, “Surface oxidation and reduction of CuO and Cu₂O studied using XPS and XAES,” *Surface and Interface Analysis: An International Journal devoted to the development and application of techniques for the analysis of surfaces, interfaces and thin films*, vol. 24, no. 12, pp. 811–820, 1996.
- [416] J. P. Tobin, W. Hirschwald, and J. Cunningham, “XPS and XAES studies of transient enhancement of Cu1 at CuO surfaces during vacuum outgassing,” *Applications of surface science*, vol. 16, no. 3–4, pp. 441–452, 1983.
- [417] F. M. Leibsle, “STM studies of oxygen-induced structures and nitrogen coadsorption on the Cu (100) surface: evidence for a one-dimensional oxygen reconstruction and reconstructive interactions,” *Surf Sci*, vol. 337, no. 1–2, pp. 51–66, 1995.
- [418] K. ichi Tanaka, Y. Matsumoto, T. Fujita, and Y. Okawa, “Nano-scale patterning of metal surfaces by adsorption and reaction,” *Appl Surf Sci*, vol. 130–132, pp. 475–483, 1998, doi: 10.1016/S0169-4332(98)00104-4.
- [419] M. Lampimäki, K. Lahtonen, M. Hirsimäki, and M. Valden, “Nanoscale oxidation of Cu(100): Oxide morphology and surface reactivity,” *Journal of Chemical Physics*, vol. 126, no. 3, p. 034703, Jan. 2007, doi: 10.1063/1.2424932.
- [420] J. C. Yang, M. D. Bharadwaj, G. Zhou, and L. Tropa, “Surface Kinetics of Copper Oxidation Investigated by In Situ Ultra-high Vacuum Transmission Electron Microscopy,” *Microscopy and Microanalysis*, vol. 7, no. 6, pp. 486–493, 2001, doi: 10.1007/s10005-001-0018-y.
- [421] I. Platzman, R. Brenner, H. Haick, and R. Tannenbaum, “Oxidation of polycrystalline copper thin films at ambient conditions,” *Journal of Physical Chemistry C*, vol. 112, no. 4, pp. 1101–1108, 2008, doi: 10.1021/jp076981k.
- [422] J.-W. Lim, Y. Ishikawa, K. Miyake, M. Yamashita, and M. Isshiki, “Influence of Substrate Bias Voltage on the Properties of Cu Thin Films by Sputter Type Ion Beam Deposition,” 2002.

- [423] J. W. Lim, K. Mimura, K. Miyake, M. Yamashita, and M. Isshiki, “Effect of substrate bias voltage on the purity of Cu films deposited by non-mass separated ion beam deposition,” *Thin Solid Films*, vol. 434, no. 1–2, pp. 30–33, 2003, doi: 10.1016/S0040-6090(03)00541-8.
- [424] J. W. Lim, K. Mimura, and M. Isshiki, “Application of glow discharge mass spectrometry for direct trace impurity analysis in Cu films,” *Appl Surf Sci*, vol. 227, no. 1–4, pp. 300–305, 2004, doi: 10.1016/j.apsusc.2003.12.007.
- [425] D. G. Mukhambetov and O. V Chalaya, “On the mechanism of self-deceleration of the thin oxide film growth,” *Journal of Vacuum Science & Technology A: Vacuum, Surfaces, and Films*, vol. 20, no. 3, pp. 839–842, 2002, doi: 10.1116/1.1471353.
- [426] B. Krishnamurthy, R. E. White, and H. J. Ploehn, “Electric field strength effects on time-dependent passivation of metal surfaces,” *Electrochim Acta*, vol. 47, no. 15, pp. 2505–2513, 2002, doi: 10.1016/S0013-4686(02)00110-X.
- [427] C. Dong, H. Zhong, T. Kou, J. Frenzel, G. Eggeler, and Z. Zhang, “Three-dimensional Cu foam-supported single crystalline mesoporous Cu₂O nanothorn arrays for ultra-highly sensitive and efficient nonenzymatic detection of glucose,” *ACS Appl Mater Interfaces*, vol. 7, no. 36, pp. 20215–20223, 2015, doi: 10.1021/acsami.5b05738.
- [428] Z. Li, Y. Chen, Y. Xin, and Z. Zhang, “Sensitive electrochemical nonenzymatic glucose sensing based on anodized CuO nanowires on three-dimensional porous copper foam,” *Sci Rep*, vol. 5, no. November, pp. 1–8, 2015, doi: 10.1038/srep16115.
- [429] D. Su, X. Xie, S. Dou, and G. Wang, “CuO single crystal with exposed {001} facets-A highly efficient material for gas sensing and Li-ion battery applications,” *Sci Rep*, vol. 4, pp. 1–9, 2014, doi: 10.1038/srep05753.
- [430] R. Ahmad, M. Vaseem, N. Tripathy, and Y. B. Hahn, “Wide linear-range detecting nonenzymatic glucose biosensor based on CuO nanoparticles inkjet-printed on electrodes,” *Anal Chem*, vol. 85, no. 21, pp. 10448–10454, 2013, doi: 10.1021/ac402925r.
- [431] M. B. Gawande *et al.*, “Cu and Cu-Based Nanoparticles: Synthesis and Applications in Catalysis,” *Chem Rev*, vol. 116, no. 6, pp. 3722–3811, 2016, doi: 10.1021/acs.chemrev.5b00482.
- [432] X. Wang, E. Liu, and X. Zhang, “Non-enzymatic glucose biosensor based on copper oxide-reduced graphene oxide nanocomposites synthesized from water-isopropanol solution,” *Electrochim Acta*, vol. 130, pp. 253–260, 2014, doi: 10.1016/j.electacta.2014.03.030.

- [433] J. M. Marioli and T. Kuwana, “Electrochemical characterization of carbohydrate oxidation at copper electrodes,” *Electrochim Acta*, vol. 37, no. 7, pp. 1187–1197, 1992, doi: 10.1016/0013-4686(92)85055-P.
- [434] Y. Zhang *et al.*, “Ultrasensitive and selective non-enzymatic glucose detection using copper nanowires,” *Biosens Bioelectron*, vol. 31, no. 1, pp. 426–432, 2012, doi: 10.1016/j.bios.2011.11.006.
- [435] F. Caballero-Briones, J. M. Artés, I. Díez-Pérez, P. Gorostiza, and F. Sanz, “Direct observation of the valence band edge by in situ ECSTM-ECTS in p-type Cu₂O layers prepared by copper anodization,” *Journal of Physical Chemistry C*, vol. 113, no. 3, pp. 1028–1036, 2009, doi: 10.1021/jp805915a.
- [436] A. M. S. El Din and F. M. A. El Wahab, “The behaviour of the copper electrode in alkaline solutions upon alternate anodic and cathodic polarization,” *Electrochim Acta*, vol. 9, no. 1, pp. 113–121, Jan. 1964, doi: 10.1016/0013-4686(64)80010-4.
- [437] N. A. Hampson, J. B. Lee, and K. I. Macdonald, “Oxidations at copper electrodes. Part 2. a study of polycrystalline copper in alkali by linear sweep voltammetry,” *J Electroanal Chem Interfacial Electrochem*, vol. 32, no. 2, pp. 165–173, Sep. 1971, doi: 10.1016/S0022-0728(71)80183-3.
- [438] J. Teichert, T. Doert, and M. Ruck, “Mechanisms of the polyol reduction of copper(ii) salts depending on the anion type and diol chain length,” *Dalton Transactions*, vol. 47, no. 39, pp. 14085–14093, 2018, doi: 10.1039/c8dt03034k.
- [439] X. Lin, Y. Wang, W. He, Y. Ni, and S. Kokot, “Nano-composite of Co₃O₄ and Cu with enhanced stability and catalytic performance for non-enzymatic electrochemical glucose sensors,” *RSC Adv*, vol. 7, no. 86, pp. 54460–54467, 2017, doi: 10.1039/c7ra11540g.
- [440] H. Wei, J. J. Sun, L. Guo, X. Li, and G. N. Chen, “Highly enhanced electrocatalytic oxidation of glucose and shikimic acid at a disposable electrically heated oxide covered copper electrode,” *Chemical Communications*, no. 20, pp. 2842–2844, 2009, doi: 10.1039/b904673a.
- [441] B. Li, Y. Fan, C. Li, X. Zhao, K. Liu, and Y. Lin, “Online Electrochemical Monitoring of Glucose in Rat Brain with Acanthosphere-like CuOOH Nanospheres-based Electrochemical Sensor as Non-enzymatic and O₂-independent Detector,” *Electroanalysis*, vol. 30, no. 6, pp. 1033–1040, 2018, doi: 10.1002/elan.201700574.
- [442] V. B. Juska, A. Walcarius, and M. E. Pemble, “Cu Nanodendrite Foams on Integrated Band Array Electrodes for the Nonenzymatic Detection of Glucose,”

- ACS Appl Nano Mater*, vol. 2, no. 9, pp. 5878–5889, 2019, doi: 10.1021/acsanm.9b01325.
- [443] J. Wang, T. T. Wang, F. Bin Wang, D. Y. Zhang, K. Wang, and X. H. Xia, “Exploration of the Copper Active Sites in Electrooxidation of Glucose on a Copper/Nitrogen Doped Graphene Nanocomposite,” *Journal of Physical Chemistry C*, vol. 120, no. 29, pp. 15593–15599, Jul. 2016, doi: 10.1021/acs.jpcc.5b05142.
- [444] W. Xu *et al.*, “Nanorod-aggregated flower-like CuO grown on a carbon fiber fabric for a super high sensitive non-enzymatic glucose sensor,” *J Mater Chem B*, vol. 3, no. 28, pp. 5777–5785, 2015, doi: 10.1039/c5tb00592b.
- [445] Y. Li, Y. Zhong, Y. Zhang, W. Weng, and S. Li, “Carbon quantum dots/octahedral Cu₂O nanocomposites for non-enzymatic glucose and hydrogen peroxide amperometric sensor,” *Sens Actuators B Chem*, vol. 206, pp. 735–743, 2015, doi: 10.1016/j.snb.2014.09.016.
- [446] Y. Cudennec and A. Lecerf, “The transformation of Cu(OH)₂ into CuO, revisited,” *Solid State Sci*, vol. 5, no. 11–12, pp. 1471–1474, 2003, doi: 10.1016/j.solidstatesciences.2003.09.009.
- [447] L. P. Xia, L. Liu, N. Deng, Y. W. Zhu, and J. B. He, “Cu(III)-independent oxidation and sensing of glucose on multi-layer stacked copper nanoparticles,” *Microchimica Acta*, vol. 182, no. 7–8, pp. 1289–1295, 2015, doi: 10.1007/s00604-015-1447-2.
- [448] R. Ahmad *et al.*, “Highly Efficient Non-Enzymatic Glucose Sensor Based on CuO Modified Vertically-Grown ZnO Nanorods on Electrode,” *Sci Rep*, vol. 7, no. 1, pp. 1–10, 2017, doi: 10.1038/s41598-017-06064-8.
- [449] S. Sun, X. Zhang, Y. Sun, S. Yang, X. Song, and Z. Yang, “Facile water-assisted synthesis of cupric oxide nanourchins and their application as nonenzymatic glucose biosensor,” *ACS Appl Mater Interfaces*, vol. 5, no. 10, pp. 4429–4437, 2013, doi: 10.1021/am400858j.
- [450] F. Largeaud, K. B. Kokoh, B. Beden, and C. Lamy, “On the electrochemical reactivity of anomers: electrocatalytic oxidation of α - and β -d-glucose on platinum electrodes in acid and basic media,” *Journal of Electroanalytical Chemistry*, vol. 397, no. 1–2, pp. 261–269, Nov. 1995, doi: 10.1016/0022-0728(95)04139-8.
- [451] K. S. Ryu, C. Kim, C. Park, and B. S. Choi, “NMR analysis of enzyme-catalyzed and free-equilibrium mutarotation kinetics of monosaccharides,” *J Am Chem Soc*, vol. 126, no. 30, pp. 9180–9181, 2004, doi: 10.1021/ja047911j.

- [452] B. Beden, F. Largeaud, K. B. Kokoh, and C. Lamy, “Fourier transform infrared reflectance spectroscopic investigation of the electrocatalytic oxidation of D-glucose: Identification of reactive intermediates and reaction products,” *Electrochim Acta*, vol. 41, no. 5 SPEC. ISS., pp. 701–709, Apr. 1996, doi: 10.1016/0013-4686(95)00359-2.
- [453] X. Niu, Y. Li, J. Tang, Y. Hu, H. Zhao, and M. Lan, “Electrochemical sensing interfaces with tunable porosity for nonenzymatic glucose detection: A Cu foam case,” *Biosens Bioelectron*, vol. 51, pp. 22–28, 2014, doi: 10.1016/j.bios.2013.07.032.
- [454] J. Luo, S. Jiang, H. Zhang, J. Jiang, and X. Liu, “A novel non-enzymatic glucose sensor based on Cu nanoparticle modified graphene sheets electrode,” *Anal Chim Acta*, vol. 709, pp. 47–53, 2012, doi: 10.1016/j.aca.2011.10.025.
- [455] H. B. Hassan and Z. A. Hamid, “Electrodeposited Cu-CuO composite films for electrochemical detection of glucose,” *Int J Electrochem Sci*, vol. 6, no. 11, pp. 5741–5758, 2011.
- [456] L. D. Burke, G. M. Bruton, and J. A. Collins, “The redox properties of active sites and the importance of the latter in electrocatalysis at copper in base,” *Electrochim Acta*, vol. 44, no. 8–9, pp. 1467–1479, 1998, doi: 10.1016/S0013-4686(98)00270-9.
- [457] H. Lee *et al.*, “Wearable/disposable sweat-based glucose monitoring device with multistage transdermal drug delivery module,” *Sci Adv*, vol. 3, no. 3, 2017, doi: 10.1126/sciadv.1601314.
- [458] D. A. Skoog, F. J. Holler, and S. R. Crouch, *Principles of instrumental analysis*. Cengage learning, 2017.
- [459] A. J. Bard and L. R. Faulkner, *Electrochemical methods Fundamentals and applications*, 2nd ed. Wiley New York, 2001.
- [460] H. Siampour, S. Abbasian, A. Moshaii, K. Omidfar, M. Sedghi, and H. Naderi-Manesh, “Seed-mediated Electrochemically Developed Au Nanostructures with Boosted Sensing Properties: An Implication for Non-enzymatic Glucose Detection,” *Sci Rep*, vol. 10, no. 1, pp. 1–11, 2020, doi: 10.1038/s41598-020-64082-5.
- [461] L. Tian and B. Liu, “Fabrication of CuO nanosheets modified Cu electrode and its excellent electrocatalytic performance towards glucose,” *Appl Surf Sci*, vol. 283, pp. 947–953, 2013, doi: 10.1016/j.apsusc.2013.07.048.

- [462] L. Wang, J. Fu, and Y. Song, “A facile strategy to prepare Cu₂O/Cu electrode as a sensitive enzyme-free glucose sensor,” *Int J Electrochem Sci*, vol. 7, no. 12, pp. 12587–12600, 2012.
- [463] H. Yoon *et al.*, “A chemically modified laser-induced porous graphene based flexible and ultrasensitive electrochemical biosensor for sweat glucose detection,” *Sens Actuators B Chem*, vol. 311, no. 5, p. 127866, May 2020, doi: 10.1016/j.snb.2020.127866.
- [464] J. Klode, L. Schöttler, I. Stoffels, A. Körber, D. Schadendorf, and J. Dissemond, “Investigation of adhesion of modern wound dressings: A comparative analysis of 56 different wound dressings,” *Journal of the European Academy of Dermatology and Venereology*, vol. 25, no. 8, pp. 933–939, Aug. 2011, doi: 10.1111/j.1468-3083.2010.03886.x.
- [465] K. Ren, J. Zhou, and H. Wu, “Materials for microfluidic chip fabrication,” *Acc Chem Res*, vol. 46, no. 11, pp. 2396–2406, 2013, doi: 10.1021/ar300314s.
- [466] A. Gangopadhyay, “Gold Thin-Film on Porous Flexible Polyester Membrane for Bio-Electronic Applications,” 2016.
- [467] S. Lin *et al.*, “Noninvasive wearable electroactive pharmaceutical monitoring for personalized therapeutics,” *Proc Natl Acad Sci U S A*, vol. 117, no. 32, pp. 19017–19025, 2020, doi: 10.1073/pnas.2009979117.
- [468] X. Niu, X. Li, J. Pan, Y. He, F. Qiu, and Y. Yan, “Recent advances in non-enzymatic electrochemical glucose sensors based on non-precious transition metal materials: Opportunities and challenges,” *RSC Adv*, vol. 6, no. 88, pp. 84893–84905, 2016, doi: 10.1039/C6RA12506A.
- [469] P. Si, Y. Huang, T. Wang, and J. Ma, “Nanomaterials for electrochemical non-enzymatic glucose biosensors,” *RSC Adv*, vol. 3, no. 11, pp. 3487–3502, 2013, doi: 10.1039/c2ra22360k.
- [470] T. Choi *et al.*, “Synthesis of carbon nanotube–nickel nanocomposites using atomic layer deposition for high-performance non-enzymatic glucose sensing,” *Biosens Bioelectron*, vol. 63, pp. 325–330, Jan. 2015, doi: 10.1016/J.BIOS.2014.07.059.
- [471] K. Qiu *et al.*, “Facile Preparation of Nickel Nanoparticle-Modified Carbon Nanotubes with Application as a Nonenzymatic Electrochemical Glucose Sensor,” <http://dx.doi.org/10.1080/00032719.2015.1076829>, vol. 49, no. 4, pp. 568–578, Mar. 2016, doi: 10.1080/00032719.2015.1076829.

- [472] R. Prasad and B. R. Bhat, “Multi-wall carbon nanotube–NiO nanoparticle composite as enzyme-free electrochemical glucose sensor,” *Sens Actuators B Chem*, vol. 220, pp. 81–90, Dec. 2015, doi: 10.1016/J.SNB.2015.05.065.
- [473] R. Ouyang *et al.*, “Excellent electrocatalytic performance of a Ni²⁺-loaded multiwalled carbon nanotube composite in glucose oxidation,” *Journal of Solid State Electrochemistry*, vol. 21, no. 10, pp. 2887–2898, Oct. 2017, doi: 10.1007/S10008-017-3603-6/METRICS.
- [474] I. Shackery *et al.*, “Sensitivity Enhancement in Nickel Hydroxide/3D-Graphene as Enzymeless Glucose Detection,” *Electroanalysis*, vol. 27, no. 10, pp. 2363–2370, Oct. 2015, doi: 10.1002/ELAN.201500009.
- [475] W.-Y. Jeon, Y.-B. Choi, H.-H. Kim, N. Jaffrezic-Renault, and M. Mcshane, “Disposable non-enzymatic glucose sensors using screen-printed nickel/carbon composites on indium tin oxide electrodes,” *mdpi.com*, 2015, doi: 10.3390/s151229846.
- [476] “Electrochemical properties of a novel Ni-doped nanoporous carbon,” *Elsevier*, Accessed: Apr. 10, 2023. [Online]. Available: <https://www.sciencedirect.com/science/article/pii/S0167577X15303578>
- [477] R. H.-B. and Bioelectronics and undefined 2013, “Amperometric glucose sensor based on nickel nanoparticles/carbon Vulcan XC-72R,” *Elsevier*, vol. 47, pp. 248–257, 2013, doi: 10.1016/j.bios.2013.02.044.
- [478] “Heteroatom-enriched porous carbon/nickel oxide nanocomposites as enzyme-free highly sensitive sensors for detection of glucose,” *Elsevier*, Accessed: Apr. 10, 2023. [Online]. Available: <https://www.sciencedirect.com/science/article/pii/S0925400515301854>
- [479] S. Premalatha, P. Sivasakthi, and G. N. K. Ramesh Bapu, “Electrodeposition of a 3D hierarchical porous flower-like cobalt–MWCNT nanocomposite electrode for non-enzymatic glucose sensing,” *RSC Adv*, vol. 5, no. 91, pp. 74374–74380, Sep. 2015, doi: 10.1039/C5RA12316J.
- [480] R. Prasad and B. R. Bhat, “Self-assembly synthesis of Co₃O₄/multiwalled carbon nanotube composites: an efficient enzyme-free glucose sensor,” *New Journal of Chemistry*, vol. 39, no. 12, pp. 9735–9742, Nov. 2015, doi: 10.1039/C5NJ01447F.
- [481] S. Hu, E. L. Ribeiro, S. A. Davari, M. Tian, D. Mukherjee, and B. Khomami, “Hybrid nanocomposites of nanostructured Co₃O₄ interfaced with reduced/nitrogen-doped graphene oxides for selective improvements in electrocatalytic and/or supercapacitive properties,” *RSC Adv*, vol. 7, no. 53, pp. 33166–33176, Jun. 2017, doi: 10.1039/C7RA05494G.

- [482] S. Ci, S. Mao, T. Huang, Z. Wen, D. A. Steeber, and J. Chen, “Enzymeless Glucose Detection Based on CoO/Graphene Microsphere Hybrids,” *Electroanalysis*, vol. 26, no. 6, pp. 1326–1334, Jun. 2014, doi: 10.1002/ELAN.201300645.
- [483] S. J. Li, J. M. Du, J. Chen, N. N. Mao, M. J. Zhang, and H. Pang, “Electrodeposition of cobalt oxide nanoparticles on reduced graphene oxide: A two-dimensional hybrid for enzyme-free glucose sensing,” *Journal of Solid State Electrochemistry*, vol. 18, no. 4, pp. 1049–1056, Dec. 2014, doi: 10.1007/S10008-013-2354-2/METRICS.
- [484] P. Liang, M. Sun, P. He, L. Zhang, and G. Chen, “Determination of carbohydrates in honey and milk by capillary electrophoresis in combination with graphene–cobalt microsphere hybrid paste electrodes,” *Food Chem*, vol. 190, pp. 64–70, Jan. 2016, doi: 10.1016/J.FOODCHEM.2015.05.059.
- [485] R. Madhu, V. Veeramani, S. M. Chen, A. Manikandan, A. Y. Lo, and Y. L. Chueh, “Honeycomb-like Porous Carbon-Cobalt Oxide Nanocomposite for High-Performance Enzymeless Glucose Sensor and Supercapacitor Applications,” *ACS Appl Mater Interfaces*, vol. 7, no. 29, pp. 15812–15820, Jul. 2015, doi: 10.1021/ACSAMI.5B04132.
- [486] H. Yu, J. Jin, X. Jian, Y. Wang, and G. C. Qi, “Preparation of Cobalt Oxide Nanoclusters/Overoxidized Polypyrrole Composite Film Modified Electrode and Its Application in Nonenzymatic Glucose Sensing,” *Electroanalysis*, vol. 25, no. 7, pp. 1665–1674, Jul. 2013, doi: 10.1002/ELAN.201300035.
- [487] Y. Su, B. Luo, and J. Z. Zhang, “Controllable Cobalt Oxide/Au Hierarchically Nanostructured Electrode for Nonenzymatic Glucose Sensing,” *Anal Chem*, vol. 88, no. 3, pp. 1617–1624, Feb. 2016, doi: 10.1021/ACS.ANALCHEM.5B03396/ASSET/IMAGES/MEDIUM/AC-2015-03396V_0011.GIF.
- [488] S. Yang, G. Li, G. Wang, J. Zhao, X. Gao, and L. Qu, “Synthesis of Mn₃O₄ nanoparticles/nitrogen-doped graphene hybrid composite for nonenzymatic glucose sensor,” *Sens Actuators B Chem*, vol. 221, pp. 172–178, Dec. 2015, doi: 10.1016/J.SNB.2015.06.110.
- [489] Y. Zhang *et al.*, “Electrospun graphene decorated MnCo₂O₄ composite nanofibers for glucose biosensing,” *Biosens Bioelectron*, vol. 66, pp. 308–315, Apr. 2015, doi: 10.1016/J.BIOS.2014.11.040.
- [490] M. M. Rahman, A. J. S. Ahammad, J. H. Jin, S. J. Ahn, and J. J. Lee, “A comprehensive review of glucose biosensors based on nanostructured metal-

- oxides,” *Sensors*, vol. 10, no. 5, pp. 4855–4886, May 2010, doi: 10.3390/S100504855.
- [491] M. F. Al-Kuhaili, “Characterization of copper oxide thin films deposited by the thermal evaporation of cuprous oxide (Cu_2O),” *Vacuum*, vol. 82, no. 6, pp. 623–629, Feb. 2008, doi: 10.1016/j.vacuum.2007.10.004.
- [492] M. T. S. Nair, L. Guerrero, O. L. Arenas, and P. K. Nair, “Chemically deposited copper oxide thin films: structural, optical and electrical characteristics,” *Appl Surf Sci*, vol. 150, no. 1, pp. 143–151, Aug. 1999, doi: 10.1016/S0169-4332(99)00239-1.
- [493] T. Maruyama, “Copper oxide thin films prepared by chemical vapor deposition from copper dipivaloylmethanate,” *Solar Energy Materials and Solar Cells*, vol. 56, no. 1, pp. 85–92, Sep. 1998, doi: 10.1016/S0927-0248(98)00128-7.
- [494] K. H. Yoon, W. J. Choi, and D. H. Kang, “Photoelectrochemical properties of copper oxide thin films coated on an n-Si substrate,” *Thin Solid Films*, vol. 372, no. 1–2, pp. 250–256, Sep. 2000, doi: 10.1016/S0040-6090(00)01058-0.
- [495] F. A. Akgul, G. Akgul, N. Yildirim, H. E. Unalan, and R. Turan, “Influence of thermal annealing on microstructural, morphological, optical properties and surface electronic structure of copper oxide thin films,” *Mater Chem Phys*, vol. 147, no. 3, pp. 987–995, 2014, doi: 10.1016/j.matchemphys.2014.06.047.
- [496] A. O. Musa, T. Akomolafe, and M. J. Carter, “Production of cuprous oxide, a solar cell material, by thermal oxidation and a study of its physical and electrical properties,” *Solar Energy Materials and Solar Cells*, vol. 51, no. 3–4, pp. 305–316, Feb. 1998, doi: 10.1016/S0927-0248(97)00233-X.
- [497] D. Barreca, A. Gasparotto, and E. Tondello, “CVD Cu_2O and CuO Nanosystems Characterized by XPS,” *Surface Science Spectra*, vol. 14, no. 1, pp. 41–51, 2007, doi: 10.1116/11.20080701.
- [498] J. Ghijsen *et al.*, “Electronic structure of Cu_2O and CuO ,” *Phys Rev B Condens Matter*, vol. 38, no. 16, pp. 11322–11330, 1988, doi: 10.1103/PHYSREVB.38.11322.
- [499] B. Vincent Crist, “Handbooks of Monochromatic XPS Spectra Volume 1 - The Elements and Native Oxides,” *Handbook of The Elements and Native Oxides*, vol. 1, no. January, pp. 1–87, 1999, [Online]. Available: Handbooks of Monochromatic XPS Spectra

- [500] M. M. Alam and M. M. R. Howlader, “Nonenzymatic electrochemical sensors via Cu native oxides (CuNO_x) for sweat glucose monitoring,” *Sens Biosensing Res*, vol. 34, no. September, 2021, doi: 10.1016/j.sbsr.2021.100453.
- [501] M. R. Johan, M. S. M. Suan, N. L. Hawari, and H. A. Ching, “Annealing effects on the properties of copper oxide thin films prepared by chemical deposition,” *Int J Electrochem Sci*, vol. 6, no. 12, pp. 6094–6104, 2011.
- [502] H. Huo, C. Guo, G. Li, X. Han, and C. Xu, “Reticular-vein-like Cu@Cu₂O/reduced graphene oxide nanocomposites for a non-enzymatic glucose sensor,” *RSC Adv*, vol. 4, no. 39, pp. 20459–20465, May 2014, doi: 10.1039/C4RA02390K.
- [503] J. Tu *et al.*, “A wireless patch for the monitoring of C-reactive protein in sweat,” *Nature Biomedical Engineering* 2023, pp. 1–14, Jun. 2023, doi: 10.1038/s41551-023-01059-5.
- [504] J. Min *et al.*, “Skin-Interfaced Wearable Sweat Sensors for Precision Medicine,” *Chem Rev*, vol. 123, no. 8, pp. 5049–5138, Apr. 2023, doi: 10.1021/ACS.CHEMREV.2C00823/ASSET/IMAGES/MEDIUM/CR2C00823_0046.GIF.
- [505] “Wearable autonomous biomimetic sweat sensor for precision nutrition,” May 2022.
- [506] J. Kim *et al.*, “Skin-interfaced wireless biosensors for perinatal and paediatric health,” *Nature Reviews Bioengineering* 2023, pp. 1–17, Jul. 2023, doi: 10.1038/s44222-023-00090-0.
- [507] T. Z. Redhwan, Y. Ali, M. M. R. Howlader, and Y. M. Haddara, “Electrochemical Sensing of Lead in Drinking Water Using Copper Foil Bonded with Polymer,” *Sensors* 2023, Vol. 23, Page 1424, vol. 23, no. 3, p. 1424, Jan. 2023, doi: 10.3390/S23031424.
- [508] M. M. R. Howlader, M. Iwashita, K. Nanbu, K. Saijo, and T. Suga, “Enhanced Cu/LCP adhesion by pre-sputter cleaning prior to Cu deposition,” *IEEE Transactions on Advanced Packaging*, vol. 28, no. 3, pp. 495–502, Aug. 2005, doi: 10.1109/TADVP.2005.848522.
- [509] T. Suga, A. Takahashi, M. Howlader, K. Saijo, and S. Oosawa, “A lamination technique of LCP/Cu for electronic packaging,” *2nd International IEEE Conference on Polymers and Adhesives in Microelectronics and Photonics, POLYTRONIC 2002 - Conference Proceedings*, pp. 177–182, 2002, doi: 10.1109/POLYTR.2002.1020205.

